A Study of the Creeping Motion of a Sphere Normal to a Deformable Fluid-Fluid Interface: Deformation and Breakthrough

Thesis by

Anthony S. Geller

in Partial Fulfillment of the Requirements

for the Degree of

Doctor of Philosophy

California Institute of Technology

Pasadena, California

1986

(Submitted April 29, 1986)

To my parents

Acknowledgment

I would like to express my appreciation to my research advisor Professor L. Gary Leal for suggesting this research topic and for his patient guidance and instruction throughout the course of this investigation. I have benefitted greatly from my contact with him.

I would also like to acknowledge the contribution of the other members of Prof. Leal's research group with whom I have had contact. Barry Bentley and David Dandy have provided notable assistance. Numerous discussions relating to this research and other topics have clarified my own thoughts as well as providing the inspiration for new ideas. Conversations with Ed Ascoli, Clarke Berdan, Jim Stoos and Howard Stone have been particularly helpful. Chris Chow, Rohit and Debbie Khanna, and Ken Reardon have made my stay at Caltech more interesting and enjoyable. Finally, I would like to thank all those people who have spent ninety minutes a day with me with our heads under water for making the last three years the experience it was.

Abstract

The creeping motion of a sphere normal to a deformable fluid-fluid interface has been studied using numerical and experimental techniques. A numerical method based on the distribution of point force singularities at fluid surfaces, the boundary integral method, has been applied to sphere motion in the presence of an interface subject to the constraint of either constant velocity normal to the interface, or constant non-hydrodynamic body force normal to the plane of the undeformed interface. Cases for several values of the viscosity ratio, density difference, and interfacial tension between the two fluids are considered. Calculations reveal two distinct modes of interface deformation: a film drainage mode in which fluid drains away in front of the sphere leaving an ever thinning film, and a tailing mode where the sphere passes several radii beyond the plane of the initially undeformed interface, while remaining encapsulated by the original surrounding fluid which is connected with its main body by a thin thread-like tail behind the sphere. We consider the influence of the viscosity ratio, density difference, interfacial tension and starting position of the sphere in determining which of these two modes of deformation will occur.

Experiments were performed for a rigid sphere translating normal to a deformable fluid-fluid interface with large capillary number. The motion of fluid at the interface in both the axial and radial directions was recorded as was the total force on the sphere. The experimental results were compared to boundary integral calculations of the interface position and force on the sphere, employing both a fully mobile and completely immobile model for interfacial dynamics. These comparisons indicate significant reduction in the interface mobility for the experimental system.

In order to increase our understanding of the actual breakthrough process, a third model for interfacial dynamics was developed. The latest model includes the disjoining pressure in the normal stress jump boundary condition. Preliminary

calculations indicate that dispersion forces can result in a change in the calculated mode of breakthrough, converting tailing cases to the film drainage mode. Further, for the range of parameters studied here, the effect of dispersion forces was relatively small until the sudden onset of motion of the interface toward the sphere caused breakthough.

Contents Page

Dedication ii

Acknowledgment iii

Abstract iv.

CHAPTER I. Introduction 1

References 16

Figure Captions 18

Figures 19

CHAPTER II. The Creeping Motion of a Spherical Particle Normal to a Deformable Interface 22

Abstract 24

I. Introduction 25

II. Mathematical formulation 29

(a) Governing Equations and Boundary Conditions 29

(b) Numerical Procedure 32

III. Preliminary Results 37

IV. Results for the Motion of a Sphere from a Large Distance at Constant Velocity 41

V. Results for the Motion of a Sphere from a Large Distance Due to a Constant Body Force on the Sphere 56

VI. Effect of Sphere Starting Position 64

(a) Initial Starting Position, $l_0 = 1.2$ 65

(b) Initial Position, l_0, Corresponding to the Thickness of the Film at Large deformation 66

VII. Conclusions 67

Appendix 70

References 72

Figure Captions 75

Figures 78

CHAPTER III. An Experimental Study of the Motion of a Sphere Normal to a Deformable Interface: High Capillary Number Results. 107

I. Introduction 108

II. Experimental Apparatus and Procedure 113

(a) Experimental Apparatus 113

(b) Experimental Procedure 117

III. Numerical Model for Inhibited Tangential Motion at the Interface and Tracer Particle Movement 119

IV. Experimental Results 125

(a) Data Evaluation for Theoretical Comparisons 125

(b) Comparison of Experimental and Numerical Results 130

References 136

Figure Captions 138

Figures 140

Appendix A. Derivation of the Linear System for the Motion of a Sphere Normal to a Deformable Interface 151

Appendix B. Data from Experimental Runs 162

CHAPTER IV. The Effect of London-van der Waals Dispersion Forces on the Motion of a Sphere Normal to a Deformable Interface 188

I. Introduction 189

II. Mathematical Formulation 191

III. Numerical Results 196

IV. Conclusions 201

References 203

Figure Captions 204

Figures 206

CHAPTER I

Introduction

The creeping motion of bubbles, drops, and particles through a viscous medium near a fluid-fluid interface has long been of interest in industrial applications. The resistance of emulsions to coalescence, the removal of contaminants in a liquid by flotation, and the mixing of liquid polymers are examples where an understanding of the behavior of a body near a deformable interface is central to predicting the performance of the larger system. One class of this group of problems involves the motion of a particle or drop near a plane, deformable interface separating two immiscible Newtonian fluids. The case of small body moving toward a large drop can also be represented by this system. If the particle or drop is moving toward the interface, the body may pass through the interface into the second fluid. Such a process is called coalescence when the body is a drop of the second fluid, and breakthrough when a rigid particle or a drop of some third fluid is involved.

The generalized coalescence problem including both drops and particles is of interest in many important processes. The stability of a suspension of liquid drops depends primarily on the ability of the drops to resist coalescence. Also, the final phase separation stages of a liquid-liquid extraction process involve droplets of one liquid, A, rising toward a stationary interface through another liquid, B, and B settling through A. The capture of particles by a fibrous mat collector onto which a layer of liquid has condensed is an example of a relevant breakthrough process. Although the analysis of such problems is extremely complex, we feel that the case of a single rigid sphere moving near a deformable, plane interface through a quiescent fluid is a valid prototype of the more involved phenomena mentioned above. For example, using a sphere and a flat interface to model the case of a small sphere approaching a much larger one introduces an error of order R_s/R_l, where R_s and R_l are the radii of the small and large sphere, respectively. Also, drops that are small enough behave essentially as rigid spheres, Maru, Wasan, and Kintner (1971).

The movement of the body may be a result of the action of any of several forces;

gravity, bouyancy and viscous forces are the ones most commonly considered, but the body might also be affected by electrostatic or magnetic forces to name only two. Furthermore, if the body is very close to the interface, there are short range forces between the body and interface (for example, London-van der Waals and electrical double layer forces) which may play a role.

Shah, Wasan, and Kintner (1972) consider the passage of a liquid drop through an interface to occur in six stages, namely:

1. An accelerating zone where the drop attains its terminal velocity.
2. A free fall zone where the drop moves at terminal velocity and there is little interface deformation.
3. A decelerating zone where the presence of the interface causes the drop velocity to change.
4. A film drainage zone. The film drainage configuration is sketched in Fig. 1.
5. The rupture of the film.
6. the movement of the drop away from the interface in the second fluid.

Using this list as an outline for the entire process, many researchers have assumed that each step could be studied individually and the knowledge of behavior for each step then collected for an understanding of the process as a whole. Therefore, to examine step 4, for example, experiments were run which place a drop or rigid sphere very close to the interface initially, effectively beginning the the process with step 4; Hartland (1968), Princen (1963). In general, however, the entire history of motion affects the instantaneous behavior of the body and interface, and the

process *must* be considered from the start and not as individual, independent steps. Indeed, consideration of the full initial value problem of a particle moving toward the interface from "far" out in one of the fluids shows that a thin film corresponding to step 4 does not even form in all cases as the particle passes from one fluid to another. For certain values of the interfacial tension, density difference and viscosity ratio between the two fluids, the sphere or drop may pass several radii beyond the plane of the undeformed interface carrying the original surrounding fluid with it. This fluid will then form a tail behind the sphere. A sketch of the "so-called" tailing mode is shown in Fig. 2. Breakthrough or coalescence could result from instabilities in this extending fluid thread before the film in front thins enough to rupture. The existence of breakthrough without film drainage has also been demonstrated experimentally for a rigid sphere approaching an initially flat interface at moderate Reynolds number, Maru, Wasan, and Kintner (1971). In Chapter II, we will examine whether the tailing mode is a valid solution to the governing equations and boundary conditions for vanishing Reynolds number, and if so, under what circustances this type of behavior occurs.

Early investigators of the coalescence phenomenon apparently felt that a particle or drop would always move relatively quickly toward an interface until an extremely thin film of fluid separated it from the interface. The drop or sphere would then stay at this position for some time until suddenly the film would rupture and the body would move rapidly into the second phase, Charles and Mason (1960). These conclusions were likely a consequence of using spheres or drops in the early experiments which always had a density equal to or only slightly different from that of the fluid into which the body would pass. In Chapter II, a force balance on a body with density intermediate to the two continuous fluids shows that *only* a film drainage configuration can result in such a situation. Since the early experiments revealed that most of the coalescence or breakthrough process was concentrated in

this quasi-static film drainage configuration, most researchers focused their efforts on understanding this one part of the overall process.

The resulting analyses and experiments of the film drainage process may be summarized as follows. H.M. Princen (1963) considered the shape of a fluid drop at a liquid-liquid interface in the "film drainage" configuration sketched in Fig. 1, but restricted his analysis to static conditions which were assumed to exist as a consequence of an unspecified repulsive force between the drop and the interface. The result was a prediction of "equilibrium" shapes of the interface for a wide range of Bond numbers, resulting from a balance between hydrostatic pressure and interfacial tension induced pressure differences, but no information about the time required for the coalescence process. Also, because interfacial tension and bouyancy forces are the only ones relevant in a "static" configuration, Princen's solution depends only on the dimensionless parameter $\Delta\rho\, g a^2/\gamma$, where a is a characteristic length scale of the problem, usually the sphere or undeformed drop radius, and $\Delta\rho$ is the difference in density between the upper and lower fluids, but does not include the effect of the viscosity of each fluid or the velocity of the body as it approaches the interface. To model film thinning, Princen applied Reynolds's lubrication result for plane parallel disks of equal area. The contact area and force applied to the disks were taken from the equilibrium calculations. This approximation is crude at best, as is admitted by the authors.

In subseqent papers, Princen and Mason (1965a) (1965b) tested these predictions experimentally and found good agreement between the experimental and numerical results. Although this agreement indicates Princen's analysis is correct, the agreement does not show that such a static analysis is valid for the dynamic coalescence phenomenon. Princen and Mason's experiments were carried out by lowering a drop at the end of a buret to the interface until the film configuration was established, and then releasing the drop at rest. Photographs were then taken

of the drop so its shape could be measured.

The concept of equilibrium shapes was expanded by Hartland (1968) to allow for a better calculation of particle motion. Using the equilibrium position and interface shape as his initial condition, Hartland solved the equations of motion subject to the following assumptions:

1. The thickness of the film and its variation with angular position are both small relative to the radius of the sphere or undeformed drop, up to some critical angle ϕ_c.

2. The point at which the film starts to tail off, ϕ_c, does not change with time.

3. Flow in the film occurs only in the direction tangential to the sphere; there is no radial pressure gradient.

4. Electrical double layers, van der Waal's forces and other short range forces are neglected.

5. A no-slip boundary condition is imposed at the sphere or drop surface, and the interface is either a stress free or no-slip boundary.

Because of assumption 5, Hartland's solution does not allow motion in the bulk fluid across the interface, and the viscosity ratio, λ, does not appear in his results. Nevertheless, Hartland was able to derive an equation for the film thickness, δ, as a function of angular position and time with Ca/Cg as a dimensionless parameter ($Ca = \mu U/\gamma$, $Cg = \mu U/\Delta\rho g a^2$). This equation was numerically integrated by Hartland using an experimental profile as the initial shape. A similar analysis was also reported by Shah, Wasan, and Kintner (1972) for a drop in which the correct boundary condition was employed at the drop surface, but still prohibiting motion

in the second continuous fluid phase. The results of these analyses, though correct for the stated assumptions, force one to accept a model of the interface which is usually unrealistic as it prohibits any consideration of circulation in the second fluid. In addition, no consideration was given to the possibility that the particle or drop could move into the second fluid without first establishing a film drainage configuration.

A more satisfactory analysis of the film drainage model was reported by Jones and Wilson (1978), who carried out an asymptotic expansion for the sphere position and interface shape using the ratio of gap thickness to sphere radius as the small parameter. Their results are the first to include the effects of viscosity ratio. Furthermore, Jones and Wilson were able to demonstrate the effect of assumptions made by earlier workers, for example, a no-slip surface slows down the drainage time compared to a case where circulation in the second fluid is considered. This treatment was further improved by Smith and Van de Ven (1984) who added the effect of gravity on the thin film to their solution.

The chief shortcoming of this work, however, is the assumption that a draining film will occur in all cases, and that the static, equilibrium shape for the spherical cap in front of the sphere is an adequate initial condition. A preliminary attempt to explore the possibility of the alternative tail configuration was reported by Maru, Wasan, and Kintner (1971). These authors used a macroscopic balance in an attempt to determine whether a stable configuration in the quasi-static sense used by Hartland (1968, 1969), Princen (1963), and Princen and Mason (1965a,b) can exist for a rigid sphere approaching the interface under the action of bouyancy, or whether the sphere continues moving through the interface. In this analysis, conditions for existence of an equilibrium position were examined by assuming the presence of a surface tension force acting upward on the sphere balanced by body and pressure forces acting downward. The authors found that for spheres with density interme-

diate to the two fluids, a stable configuration always exists at the interface. For spheres heavier than the lower fluid or lighter than the upper fluid, however, Maru, Wasan, and Kintner find there is a critical radius for which the sphere will not pass through the interface; only spheres larger than this radius will be able to counteract the surface tension force to pass into the other phase. However, there are errors in this analysis, most notably in the assumption of a surface tension force acting directly on the sphere in the absence of a contact line. The surface tension at the interface is assumed to act on the sphere at the point where the breakaway region begins. If the sphere had been resting on the interface, there would be a contact line, and a force of the type assumed would support the sphere. The particle, however, is not resting on the interface but is settling through the liquid. The correct formulation of the problem is to include a pressure jump in the gap region caused by the curvature of the interface which acts to increase the pressure on this part of the sphere and slow its motion toward the interface.

To this point, all the analyses mentioned imply that the time for coalescence after establishment of the film drainage configuration has a unique value. However, the experiments of Charles and Mason (1960) on drop coalescence show a Gaussian distribution for the time the sphere remains in the film drainage state. This observation leads to the conclusion that there must be some step in the process triggered by a random event. Lang and Wilke (1971) carried out a linear stability analysis for an infinite plane fluid film bounded above and below by semi-infinite fluids. They reached the conclusion that whenever a lighter fluid lies under a heavier one, the system will be unstable with respect to small random perturbations at the interface, while fluid fluid layers with the heavier on the bottom will be stable. Therefore, considering only hydrodynamic forces, a drop approaching an interface will always create an unstable film, but a rigid sphere will produce a stable configuration. Although the film drainage configuration is stable for the motion of a rigid particle,

the tailing configuration introduces a new question of stability. The photographs of Maru *et al.* (1971) show the growth of a varicose disturbance on the fluid thread until ultimately, the tail breaks apart. The configuration of the tail differs significantly from the classical cases of surface tension instabilities in stationary threads treated by Rayleigh (1892) and Mikami, Cox, and Mason (1975) to name only two. There is a complicated flow in the tail with fluid draining at the surface of the thread and being drawn up in the center. The net flow changes from positive as the volume of fluid II across the plane of the undeformed interface is increasing, to negative as the tail volume decreases, draining under the force of gravity. Also, there is an extensional nature to the flow in the tail as a consequence of the increasing distance between the sphere and position of the undeformed interface. The effect of this stretching is to stabilize the thread compared to the "stationary" case.

The experimental data on coalescence and breakthrough at low Reynolds number is quite limited. Experimental studies which try to investigate the entire process; Kirkpatric and Lockett (1974), Narayanan, Gossens, and Kosen (1974); rather than look at a single step, film drainage, for example, have tended to focus on the effects of the disturbance flow caused by drops on each other. Therefore, the most meaningful results have come from the work mentioned in the earlier part of this section. Princen (1963), Hartland (1969), Maru *et al.* (1971) and Shah *et al.* (1972) ran virtually the same experiment, all that was changed were the details of the apparatus and the method of taking data. In this experiment, a drop or sphere was held near the interface for some time and then released. The shape of the interface and position of the sphere were recorded by some means usually photographic, although Hartland uses a capacitance technique to measure the gap thickness. This procedure resulted in a narrow gap between the body and interface at the time of release. The detailed results, given this initial condition, may differ substantially from what would occur when the body is released several radii from the position of

the undeformed interface.

The history of the study of the film drainage problem shows that starting from very restricted models which eliminated almost all physical factors, researchers considered systems of increasing complexity in which additional features of the true physical system were incorporated. This progression continued until Smith and Van de Van (1984) solved the film drainage problem for all hydrodynamic effects. The process of paring from the full complex problem factors believed by the researchers not to dominate the behavior was also applied to the overall problem of a sphere approaching an interface. Early workers divided the problem into independent steps and studied the problem by focusing on what they believed to be the most important, the "film drainage" problem. Only later did workers begin to consider whether film drainage was always the rate determining step (the basic treatment by Maru *et al.*).

The problem of ultimate interest, of course, is to understand the factors which control the mechanism and dynamics of the breakthrough process. This investigation continues the study of the model problem of a sphere moving normal to deformable fluid-fluid interface by applying a numerical technique which allows us to solve for the motion of the sphere and interface as a single integrated process without prior assumptions about the behavior or configuration of the system. The numerical method is based on the fundamental solutions of Stokes equation, developed by Ladyzhenskaya (1963), in terms of a distribution of singularities over the bounding surfaces of the fluid. The method of solution thus involves evaluating the single and double layer strengths at the boundaries of the fluid, that is, at the sphere surface and the interface, and is particularly convenient since the single and double layer strengths are directly related to the velocity and stress components on these surfaces.

Youngren and Acrivos used this technique to calculate the slow viscous flow

of an unbounded fluid past a particle of arbitrary shape. Later, they extended the technique to solve for the steady state deformation of an inviscid drop in an extensional flow, Youngren and Acrivos (1976). More recently, Rallison and Acrivos (1978) considered drops of arbitrary viscosity. In our research group, Lee and Leal (1982) have used this method to determine the drag on a sphere moving at constant velocity toward a slightly deformable interface. Berdan and Leal (1982) have carried out similar calculations for translation of a sphere at constant velocity parallel to the interface.

In the work reported here, we apply the same technique to motion of a sphere normal to a deformable interface with the constraint that either the force on the sphere remains constant or the sphere moves with fixed velocity. Fig. 3 gives a schematic view of the system showing the sphere moving through fluid II toward fluid I (a convention we use consistently throughout this work) with velocity U. The Reynolds number for the system, $Re = \rho_2 U a/\mu_2$, is assumed small enough that Stokes equation is valid for each fluid. In dimensionless form the equations are:

$$\begin{aligned} 0 &= -\nabla p_1 + \lambda \nabla^2 \mathbf{u}_1 \\ 0 &= \nabla \cdot \mathbf{u}_1 \qquad \text{in fluid 1,} \end{aligned} \tag{1}$$

$$\begin{aligned} 0 &= -\nabla p_2 + \nabla^2 \mathbf{u}_2 \\ 0 &= \nabla \cdot \mathbf{u}_2 \qquad \text{in fluid 2.} \end{aligned} \tag{2}$$

Here $\lambda = \mu_1/\mu_2$. The boundary conditions for the system are as follows. There is no bulk flow in the fluids,

$$\mathbf{u}_1, \mathbf{u}_2 \rightarrow 0 \qquad \text{as } |\mathbf{x}| \rightarrow \infty, \tag{3}$$

and at the interface, $\mathbf{x} \in S_I$ the velocity is continuous.

$$\mathbf{u}_1 = \mathbf{u}_2 \tag{4}$$

The kinematic condition describes the time evolution of the interface shape function,

$$\mathbf{n} \cdot \mathbf{u}_1 = \mathbf{n} \cdot \mathbf{u}_2 = \frac{1}{|\nabla H|} \frac{\partial f}{\partial t}. \tag{5}$$

Here the interface shape is denoted as $z = f(r,t)$ and the outward pointing normal $\mathbf{n}$ at the interface is $\mathbf{n} = \nabla H/|\nabla H|$ with $H \equiv z - f(r,t)$. The final condition at the interface is the stress jump across the fluid I-fluid II interface. This work considers several forms for the stress jump. Chapter II uses the form

$$(\lambda \mathbf{n} \cdot \mathbf{T}_1 - \mathbf{n} \cdot \mathbf{T}_2) = -\frac{1}{Ca} (\nabla \cdot \mathbf{n})\mathbf{n} + \frac{1}{Cg} f\mathbf{n}, \tag{6}$$

which includes all hydrodynamic effects but not short range forces, or effects due to interfacial viscosity or surface tension gradients. In Chapter III, the form

$$(\lambda \mathbf{n} \cdot \mathbf{T}_1 - \mathbf{n} \cdot \mathbf{T}_2) = -\frac{1}{Ca} (\nabla \cdot \mathbf{n})\mathbf{n} + \frac{1}{Cg} f\mathbf{n} + \beta(\mathbf{x})\mathbf{t} \tag{7}$$

which includes a term for the tangential stress jump, magnitude $\beta(\mathbf{x})\mathbf{t}$, due to interfacial tension gradients at the interface is adopted for the model. In both cases, the dimensionless groups Ca and Cg give the ratio of viscous forces tending to deform the interface to a restoring force; for Ca the restoring force is interfacial tension, and the relevant restoring force for Cg is the body force due to a density difference between the two fluids.

In Chapter IV, the effect of the London-van der Waals dispersion force between the sphere and the fluid I phase is considered in addition to the purely hydrodynamic forces treated in Chapter II. The dispersion force is an attractive body force resulting from the mutual polarizability of the two materials, and, as was the case with the gravitational force, can be expressed as the gradient of a potential. For the dispersion force, the potential goes as r^{-6} where r is the separation between two material points. Furthermore, just as the hydrostatic pressure could be incorporated into the governing differential equation or removed from the definition of the stress

to appear in the normal stress boundary condition, so too, can the dispersion force be applied either in the governing equation or the boundary conditions, in which case the term disjoining pressure is also used. We chose the latter approach as it allows us to use the same potential solutions for Stokes equation as had been used in Chapters II and III. As a result, for the case of a disjoining pressure between the sphere and fluid I, the normal stress jump at the interface is

$$(\lambda \mathbf{n} \cdot \mathbf{T}_1 - \mathbf{n} \cdot \mathbf{T}_2) = -\frac{1}{Ca}(\nabla \cdot \mathbf{n})\mathbf{n} + \frac{1}{Cg} f\mathbf{n} + \frac{1}{Cl} F_{Disp}\,\mathbf{n}. \tag{8}$$

Where Cl is a dimensionless dispersion force number,the ratio of viscous forces to attractive dispersion forces; F_{Disp} is a function of the system geometry giving the magnitude of the attractive pressure at a point on the interface. The magnitude of F_{Disp} is $O(1/\text{the sphere-interface separation})$.

The remaining boundary condition is for the surface of the sphere. The no-slip condition which applies at the sphere surface in all cases is that the fluid velocity equals the velocity of the sphere. In the case of a constant velocity, U_∞, this is simply

$$\mathbf{u}_2 = \mathbf{i}_z \qquad \text{at} \qquad \mathbf{x} \in S_P. \tag{9a}$$

For the constant force problem, a force balance on the sphere yields the constraint on the solution

$$\int_0^\pi T_{nz}^P \sin\theta \partial\theta = 3, \tag{9b}$$

which determines the particle velocity at any instantaneous position.

We are thus able to treat steps $1-4$ of Shah *et al.*'s scheme in a single numerical simulation, and consider several models for the behavior of the fluid-fluid interface. The second chapter of this work applies the numerical technique to the sphere-interface system considering purely hydrodynamic effects with a constant interfacial tension at the surface dividing the two fluids. Constant velocity calculations are

used to explore the role of the physical parameters of the system in controlling the degree and type of deformation, exploring the role of interfacial tension and density difference as well as the effect of the viscosity ratio between the two fluids on the behavior of the system. Although the calculations for a solid sphere with constant velocity show the existence of breakthrough into the second fluid with the sphere dragging a tail of the original surrounding fluid with it for a wide range of conditions, it is not evident that this is representative of the case for constant force. In the latter circumstance, the sphere will clearly decelerate in the vicinity of the interface, and this might seem to favor establishment of the film drainage configuration. Thus, one primary objective is to determine the conditions under which a film drainage configuration will be established, and those when the sphere continues moving into the second fluid dragging a tail of the original surrounding fluid behind it. As time for breakthrough or coalescence changes greatly depending on which mode is followed, such information is needed in modelling any of the processes mentioned earlier. By applying a constant force boundary condition on the sphere, we solve for a settling sphere to determine when a film drainage configuration arises and when a slender tail of fluid forms behind the sphere.

Chapter III deals with experimental results for high interfacial tension cases. Berdan, (1982), reported on experiments performed with a tethered sphere moving at constant velocity toward a deformable interface. In his results, good agreement between experiment and numerical results were observed for cases of moderate to low interfacial tension, $Ca = O(1)$ or greater, but for the case of large γ the agreement broke down and significant differences were seen between the two results. Chapter III reports on our efforts to understand the cause of this discrepancy both by performing additional experiments, and also, by modifying the numerical model as described earlier in this section.

Chapter IV reports on the development of a model for and a preliminary study

of the effect of London-van der Waals dispersion forces on the behavior of the sphere-interface system. The numerical technique used to study the effect of viscosity ratio, interfacial tension, and density difference between the two fluids was modified to use the form for the normal stress jump which includes disjoining pressure, Eq. (8). The results of this calculation showed that the attraction between the sphere and the interface could lead to breakthrough via the film drainage mechanism by increasing the rate at which the interface moved toward the sphere.

References

Berdan II, C. 1982 Ph D. Dissertation California Institute of Technology.

Berdan II, C. and Leal L. G. 1982 Motion of a sphere in the presence of a deformable interface. Part 3: Numerical study of the translation of a sphere parallel to an interface. *J. Coll. and Interface Sci.* **87**, 62.

Charles, G.E. and Mason, S.G. 1960 The coalescence of liquid drops with flat liquid/liquid interfaces. *J. Coll. Sci.* **15**, 236.

Hartland, S. 1968 The approach of a rigid sphere to a deformable liquid/liquid interface *J. Coll. and Interface Sci.* **26**, 383.

Hartland, S. 1969 The profile of a draining film between a rigid sphere and a deformable fluid-liquid interface. *Chem. Eng. Sci.* **24**, 987.

Jones, A. F. and Wilson, S. D. R. 1978 The film drainage problem in droplet coalescence. *J. Fluid Mech.* **87**, 263.

Kirkpatric, R. D. and Lockett, M.J. 1974 The influence of approach velocity on bubble coalescence. *Chem. Eng. Sci.* **29**, 2363

Lang, S. B. and Wilke, C. R. 1971 A hydrodynamic mechanism for the coalescence of liquid drops. I: Theory of coalescence at a planar interface. *I. and E. C. Fundamentals* **10**, 329.

Ladyzhenskaya, O. A. 1963 *The Mathematical Theory of Viscous Incompressible Flow.* Gordon and Breach, New York.

Lee, S. H. and Leal, L.G. 1982 Motion of a sphere in the presence of a deformable interface. Part 2: Numerical study of the translation of a sphere normal to an interface. *J. Coll. and Interface Sci.* **87**, 81.

Maru, H. C., Wasan, D. T. and Kintner, R. C. 1971 Behavior of a rigid sphere at a liquid-liquid interface. *Chem. Eng. Sci.* **26**, 1615.

Mikami, T., Cox, R. G. and Mason, S.G. 1975 Breakup of extending liquid threads. *Int. J. of Multiphase Flow* **2**, 113.

Narayaran, S., Gossens, L. H. J. and Kossen, N. W. F. 1974 Coalescence of two bubbles rising in line at low Reynolds number. *Chem. Eng. Sci.* **29**, 2071.

Princen, H.M. 1963 Shape of a fluid drop at a liquid-liquid interface. *J. Coll. Sci.* **18**, 178.

Princen, H.M. and Mason, S.G. 1965a Shape of a fluid drop at a fluid-liquid interface. I. Extension and test of two phase theory. *J. Coll. Sci.* **20**, 156.

Princen, H.M. and Mason, S.G. 1965b Shape of a fluid drop at a fluid-liquid interface. II. theory for three phase systems. *J. Coll. Sci.* **20**, 246.

Rayleigh, Lord 1892 On the instability of a cylinder of viscous liquid under capillary force. *Phil. Mag.* **34**, 145.

Rallison, J.M. and Acrivos, A. 1978 A numerical study of the deformation and burst of a viscous drop in an extensional flow. *J. Fluid Mech.* **89**, 191.

Shah, S. T., Wasan, D. T. and Kintner, R. C. 1972 Passage of a liquid drop through a liquid-liquid interface. *Chem. Eng. Sci.* **27**, 881.

Smith, P. G. and Van de Ven, T. G. M. 1984 The effect of gravity on the drainage of a thin liquid film between a solid sphere and a liquid/fluid interface. *J. Coll. Interface Sci.* **100**, 456.

Youngren, G.K. and Acrivos, A. 1975 Stokes flow past a particle of arbitrary shape: a numerical method of solution. *J. Fluid Mech.* **69**, 377.

Figure Captions

Figure 1: Film drainage configuration for a sphere at a deformable interface.

Figure 2: Tailing configuration for a sphere at a deformable interface.

Figure 3: Schematic sketch of the system for numerical calculations.

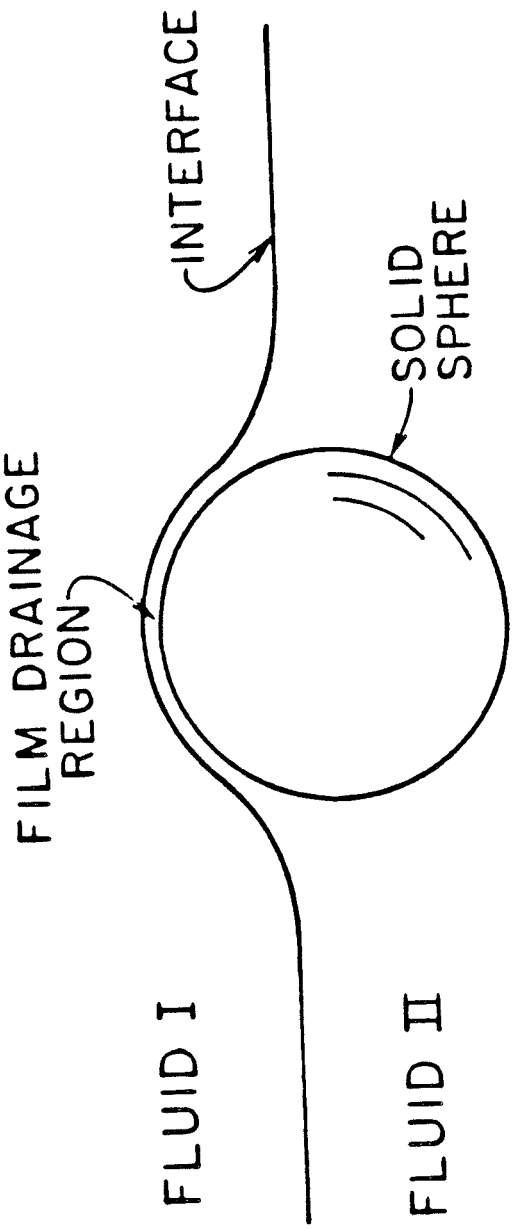
INTERFACE
SOLID SPHERE
FILM DRAINAGE REGION
FLUID I
FLUID II

Figure 1.

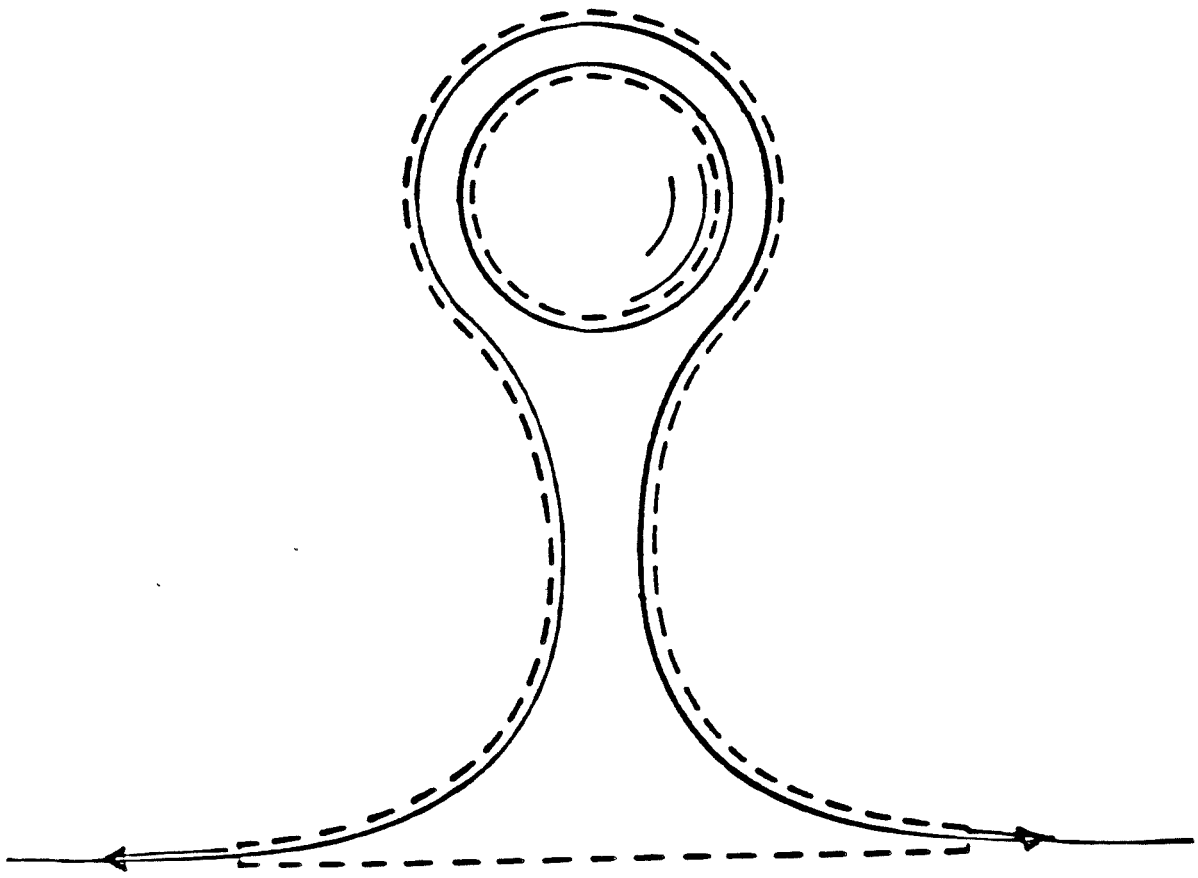

Figure 2.

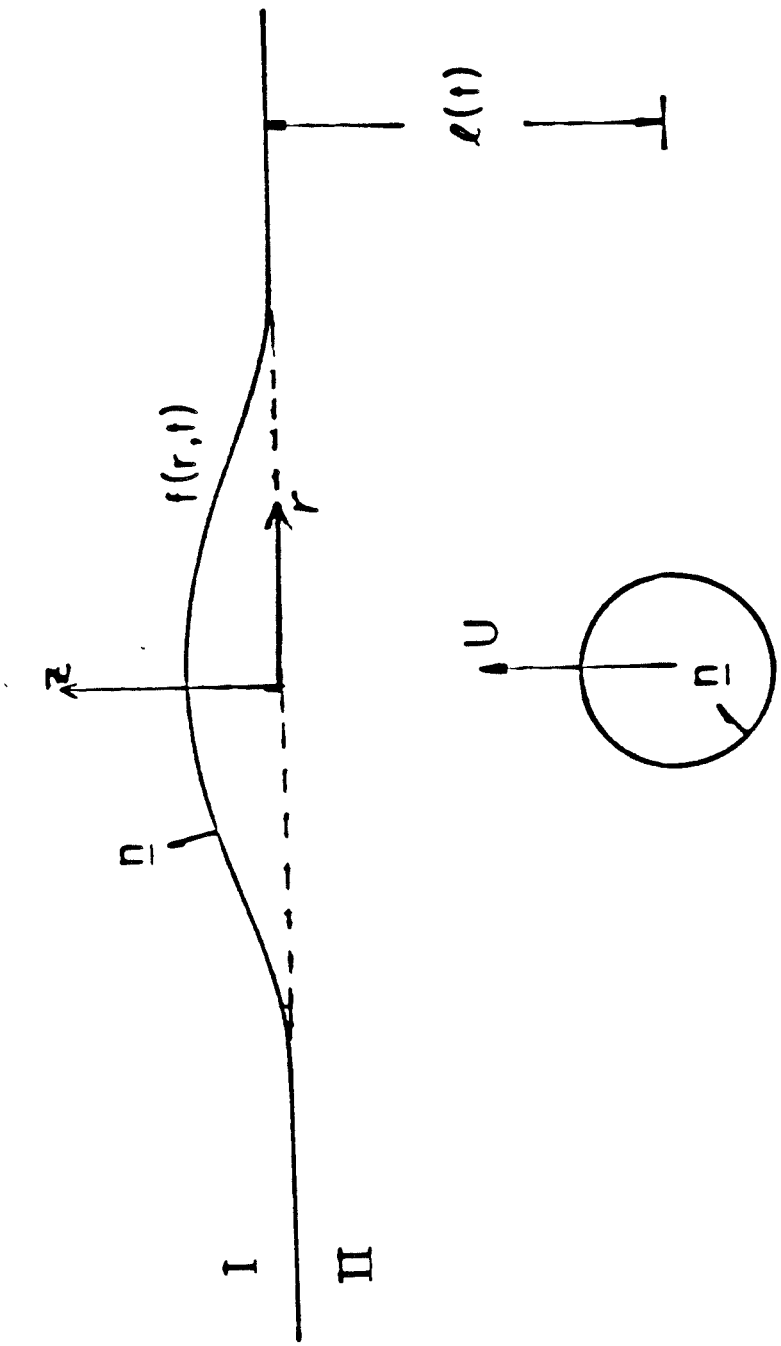

Figure 3.

Chapter II

The Creeping Motion of a Spherical Particle Normal to a Deformable Interface

The text of Chapter II consists of an article which has been accepted for publication in the *Journal of Fluid Mechanics*

The Creeping Motion of a Spherical Particle Normal to a Deformable Interface

by

A.S. Geller, S.H. Lee † and L.G. Leal

Department of Chemical Engineering
California Institute of Technology
Pasadena, California 91125

† Present address: Chevron Oil Field Research Co., La Habra, CA 90631

Abstract

In this paper, numerical results are presented for the approach of a rigid sphere normal to a deformable fluid-fluid interface in the velocity range for which inertial effects may be neglected. Both the case of a sphere moving with constant velocity, and that of a sphere moving under the action of a constant non-hydrodynamic body force are considered for several values of the viscosity ratio, density difference and interfacial tension between the two fluids. Two distinct modes of interface deformation are demonstrated: a film drainage mode in which fluid drains away in front of the sphere leaving an ever thinning film, and a tailing mode where the sphere passes several radii beyond the plane of the initially undeformed interface, while remaining encapsulated by the original surrounding fluid which is connected with its main body by a thin thread-like tail behind the sphere. We consider the influence of the viscosity ratio, density difference, interfacial tension and starting position of the sphere in determining which of these two modes of deformation will occur.

I. INTRODUCTION

When a fluid droplet or rigid spherical particle moves in one fluid bounded either above or below by a second fluid, the presence of the fluid-fluid interface will affect the motion of the body, and the interface will in turn be deformed by the disturbance flow caused by the sphere or drop. If the particle or drop is moving toward the interface, the body may pass through the interface into the second fluid. Such a process is called coalescence when the body is a drop of the second fluid and breakthrough for a rigid particle or a drop of some third fluid.

The generalized coalescence or breakthrough problem is of interest in many important processes. The stability of a suspension of liquid drops depends primarily on the ability of the drops to resist coalescence. The final separation stages of a liquid-liquid extraction process involve droplets of one liquid, A, rising toward a stationary interface through another liquid, B, and B settling through A, Figure 1. The capture of particles by a fibrous mat collector onto which a layer of liquid has condensed is an example of a relevant breakthrough process. A logical problem for initial investigation of the complicated phenomena inherent in these applications is a single rigid sphere moving through a quiescent fluid near a deformable, initially plane interface. Indeed, this problem has already been the subject of intensive study and is commonly identified as "the" coalescence problem. With one exception, however, (Maru, Wasan and Kintner, 1971), these earlier investigators have assumed that the passage of a particle or drop from one fluid to the other always occurs via the film drainage configuration, depicted in Fig. 2, with "film drainage" as the slowest step in an overall process in which each step can (it is assumed) be studied independently of the others.

In general, however, the prior history of motion affects the instantaneous behavior of the body and interface so that the total process must be considered from the start and not as individual, independent steps. Indeed, we shall see that con-

sideration of the full initial value problem of a particle moving toward an interface from "far" out in one of the fluids shows that the film formation and drainage are not even always steps relevant to the passage of a body from one fluid to another. [See also Leal and Lee (1981) which contains a preliminary version of some of the material that is reported here.] For certain values of the interfacial tension, density difference and viscosity ratio between the two fluids, a long slender tail may form behind the body as it passes through the original plane of the undisturbed interface, and breakthrough or coalescence could then result from instabilities in this extending thread. The existence of breakthrough by this mode has, in fact, been demonstrated experimentally, but only for a single case of a rigid sphere approaching an initially flat interface at moderate Reynolds number (Maru, Wasan and Kintner 1971).

The emphasis of earlier investigators on the film drainage configuration seems to have resulted from the fact that the sphere or drop used in the early experiments generally had a density either equal to that of the fluid into which it would pass, or between the density of the two fluids. As we shall see, a force balance on a body with density intermediate to the two suspending fluids shows that only a film drainage configuration can result in such a situation. Since most of the time for coalescence or breakthrough in these cases is concentrated in the quasi-static film drainage configuration, most researchers focused their efforts on this portion of the overall process.

A large number of analyses of the film drainage configuration have been reported in the literature. Many of these were reviewed by Jeffreys and Davies (1971). However, the most satisfactory analysis of the film drainage configuration is that of Jones and Wilson (1978), who carried out an asymptotic expansion for the sphere position and interface shape using the ratio of gap thickness to sphere radius as the small parameter. This treatment was improved by Smith and Van de Ven (1984)

who also included the effect of gravity on the thin film. The chief shortcoming of previous theoretical work, in our opinion, is the implicit assumption that a draining film will occur in *all* cases. The only theoretical attempt to explore the possibility of the alternative tail configuration was reported by Maru, Wasan and Kintner (1971), but this work contains conceptual errors [see Geller (1986), and section V of this paper].

Experimental data on coalescence and breakthrough at low Reynolds number is surprisingly limited. Studies which tried to investigate the entire coalescence process; Kirkpatric and Lockett (1974), Narayaran, Gossens and Kossen (1974); rather than looking at a single step, e.g., film-drainage, have tended to focus on the effects of the disturbance flow caused by drops on each other. A number of very similar film drainage experiments were reported by Princen (1963), Hartland (1968, 1969), Maru *et al.* (1971) and Shah *et al.* (1972)

In these latter experiments, a drop or sphere was held near the interface for some time and then released. This procedure resulted in a narrow gap between the body and interface at the time of release, and yields a film drainage configuration. However, the detailed results may differ substantially from what would occur if the body were released several radii from the undeformed interface. The shape of the interface and the position of the sphere were usually recorded photographically, although Hartland used a capacitance technique to measure the gap thickness. Table I shows the conditions in terms of the relevant dimensionless parameters for which experiments have been run with rigid spheres. It is evident that although only a few cases were reported, a fairly wide range of values for the parameters has been covered, albeit with a restricted range of initial conditions.

This paper reports on a *numerical* study of a rigid sphere moving normal to an initially flat deformable interface subject to one of two conditions on the sphere motion; either the sphere is moving with a constant velocity or it is moving under

TABLE I. Published experimental results

(photographs or numerical data)

	λ	Ca	Cg	Re
Hartland (1968)	4.76	0.753	0.133	3.62
Hartland (1968)	45.88	0.470	0.090	3.62
Hartland (1969)	0.022	0.465	0.089	0.003
Hartland (1969)	0.210	0.150	0.026	0.045
Maru *et al.* (1971)	0.434	3.830	1.972	15.19
Shah *et al.* (1972)	0.440	2.545	1.782	800.76

the action of a constant body force, such as buoyancy. Only gravity, interfacial tension and viscous forces are considered in the force balance on the sphere; the effect of Van der Waal's and other electroviscous forces will be considered in a future study. Earlier work in this research group has examined the case of a sphere moving with constant velocity both normal to the interface, Lee and Leal (1982), and parallel to it, Berdan (1982) but only under conditions of small or moderate deformation. The present study extends the range of solutions to include large interface deformation for the constant velocity case, and to obtain corresponding solutions under the condition of constant force which was not considered in the earlier work. Our objectives are: to expose those factors which control the details of interface deformation in this purely hydrodynamics problem; to provide a basis for comparison with experimental results so that (a) the influence of nonhydrodynamic factors can be recognized and (b) the effects of such factors as fluid inertia or non-Newtonian rheology can be evaluated; and, finally, in the case of the constant force problem, to determine conditions for establishment of a tailing configuration, rather than a draining film.

The problem of ultimate interest, of course, is to understand the factors which

control the mechanism and dynamics of the breakthrough process. However, at the level of analysis represented by the work reported here, we can investigate this question only in the context of purely hydrodynamic, continuum mechanisms. If, for example, breakthrough should occur by rupture of a thin film due to instabilities associated with London-van der Waals forces, or even by a purely molecular mechanism where the "film thickness" is of a molecular (noncontinuum) scale, we could not determine that fact in the context of the present theory. Indeed, even if a purely hydrodynamic instability were relevant, its existence might require finer spatial or temporal resolution than is possible with the present methods of solution. What we can determine, however, are the conditions when the combination of viscous, capillary and body forces will lead to a conformation in which a film (or tail) is present. The stability of each configuration must ultimately be treated, including all relevant contributions to the local force balance (i.e., at least electroviscous effects) to judge exactly where and when breakthrough occurs. As indicated above, the effects of van der Waals and other electroviscous forces will be reported in a future communication.

Let us now turn to the main problem of this paper — namely, the generation of solutions to the full dynamical problem of a sphere moving towards an initially flat, but deforming fluid interface. The mathematical formulation, including the basic governing equations and an outline of the method of solution via the so-called boundary integral technique of low Reynolds number hydrodynamics will be presented in the next section. The rest of the paper is concerned with the results and interpretation of our numerical calculations.

II. Mathematical Formulation

(a) Governing Equations and Boundary Conditions

We consider the translation of a rigid sphere normal to an initially flat but deformable interface between two immiscible, Newtonian fluids. The governing equations and boundary conditions are identical for the sphere falling through the lighter fluid or rising through the heavier fluid; we choose (arbitrarily) to present our analysis and results for the latter case. Figure 3a shows a schematic view of the system for a rising sphere. The analysis which we consider is predicated on the neglect of inertia effects in the fluids and in the motion of the sphere. Thus, we assume

$$\frac{U_\infty a \rho_2}{\mu_2} \ll 1 \tag{1}$$

where we have chosen the velocity of the sphere, U_∞, in an unbounded fluid 2 as the characteristic velocity, and the radius of the sphere as the characteristic length scale. In the constant velocity formulation of the problem, U_∞ is simply the sphere velocity. When the sphere is assumed to move under the action of buoyancy, $U_\infty = (2/9) \cdot (ga^2(\rho_s - \rho_2)/\mu_2)$ and this is the maximum velocity of the sphere. In this case, Eq. (1) is a conservative estimate of conditions necessary for neglect of inertial effects when the sphere is near the interface.

The governing differential equations, in dimensionless form were previously given by Lee and Leal (1982), and they are simply restated here for convenience.

$$\begin{aligned} 0 &= -\nabla p_1 + \lambda \nabla^2 \mathbf{u}_1 \\ 0 &= \nabla \cdot \mathbf{u}_1 \qquad \text{in fluid 1} \end{aligned} \tag{2}$$

$$\begin{aligned} 0 &= -\nabla p_2 + \nabla^2 \mathbf{u}_2 \\ 0 &= \nabla \cdot \mathbf{u}_2 \qquad \text{in fluid 2} \end{aligned} \tag{3}$$

$$\mathbf{u}_1, \mathbf{u}_2 \rightarrow 0 \qquad \text{as } |\mathbf{x}| \rightarrow \infty \tag{4}$$

and at the interface $\mathbf{x} \in S_I$

$$\mathbf{u}_1 = \mathbf{u}_2 \tag{5}$$

$$(\lambda \mathbf{n} \cdot \mathbf{T}_1^I - \mathbf{n} \cdot \mathbf{T}_2^I) = -\frac{1}{Ca}(\nabla \cdot \mathbf{n})\mathbf{n} + \frac{1}{Cg} f\mathbf{n} \tag{6}$$

$$\mathbf{n} \cdot \mathbf{u}_1 = \mathbf{n} \cdot \mathbf{u}_2 = \frac{1}{|\nabla H|}\frac{\partial f}{\partial t} \quad , \tag{7}$$

where the interface shape is denoted as $z = f(r,t)$ and the outward pointing normal $\mathbf{n}$ at the interface is $\mathbf{n} = \nabla H/|\nabla H|$ with $H \equiv z - f(r,t) = 0$. The stress $\mathbf{T}_i$ is the total stress minus the hydrostatic contribution and this is the reason why the body force term appears in the boundary condition (6), rather than in the differential equations (2) and (3). It is convenient for formulation purposes to utilize a cylindrical coordinate system, as indicated in Fig. 3a, with $z = 0$ corresponding to the plane of the underformed interface, and the z-axis passing through the center of sphere at $z = -l(t)$. Three dimensionless parameters result from the non-dimensionalization, the viscosity ratio, $\lambda = \mu_1/\mu_2$; the capillary number $Ca \equiv \mu_2 U_\infty/\gamma$, and $Cg \equiv \mu_2 U_\infty/a^2 g(\rho_2 - \rho_1)$. The latter two represent ratios of the characteristic viscous stress at the interface relative to surface tension and buoyancy forces, respectively.

The no-slip condition which applies at the sphere surface in all cases is that the fluid velocity equal the velocity of the sphere. In the case of a constant velocity, U_∞, this is simply

$$\mathbf{u}_2 = \mathbf{i}_z \qquad \text{at} \qquad \mathbf{x} \in S_P. \tag{8a}$$

For the constant force problem, a force balance on the sphere yields the constraint on the solution

$$\int_0^\pi T_{nz}^P \sin\theta \partial\theta = 3, \tag{8b}$$

which determines the particle velocity at any instantaneous position.

The problem then is to solve (2) and (3), subject to the conditions (4)-(8), for the velocity and pressure fields and the interface shape as a function of time and/or

particle position.

(b) Numerical Procedure

Although the problem in general is non-linear, the non-linearity arises from the presence of the unknown shape function f, in the boundary conditions; the governing differential equations are themselves linear. Therefore, it is possible to use a fundamental solution for the differential equation, and reduce the calculation to one of finding the particular form of the solution which satisfies the boundary conditions. Following the earlier work of Lee and Leal (1982), we use the general solution of Stokes' equations due to Ladyzhenskaya (1963) in which point singularities are distributed over the bounding surfaces of the fluid resulting in an integral representation for the pressure and velocity at any arbitrary point in that fluid, $\mathbf{x}$:

$$\mathbf{u}(\mathbf{x}) = \frac{1}{8\pi}\int_S \left[\frac{\mathbf{I}}{R} + \frac{(\mathbf{x}-\eta)(\mathbf{x}-\eta)}{R^3}\right]\cdot\mathbf{T}(\eta)\cdot\mathbf{n}\,dS_\eta - \frac{3}{4\pi}\int_S\left[\frac{(\mathbf{x}-\eta)(\mathbf{x}-\eta)(\mathbf{x}-\eta)}{R^5}\right]\cdot\mathbf{u}(\eta)\cdot\mathbf{n}\,dS_\eta \tag{9}$$

$$p(\mathbf{x}) = \frac{1}{2\pi}\int_S\left[\frac{1}{R} - \frac{3(\mathbf{x}-\eta)(\mathbf{x}-\eta)}{R^5}\right]\cdot\mathbf{u}(\eta)\cdot\mathbf{n}\,dS_\eta + \frac{1}{4\pi}\int_S\left[\frac{(\mathbf{x}-\eta)}{R^3}\right]\cdot\mathbf{T}(\eta)\cdot\mathbf{n}\,dS_\eta \tag{10}$$

where

η = position on bounding surface, variable of integration

$$R \equiv |\mathbf{x} - \eta|$$

Here S represents the boundary of the fluid domain. Thus, when (9) and (10) are applied to fluid 2, S includes both the sphere surface and the interface. In fluid 1, the only boundary is the interface. It will be noted that the weighting functions

in the integrals are just the velocity and stress components at the fluid boundaries. Thus, the basic idea is to use the boundary conditions (4)-(8) and the limiting forms of (9) and (10) at the boundaries to obtain a coupled set of integral equations for the boundary velocity and stress components which are unknown. Once these integral equations are solved for boundary values of the velocity and stress, the formulae (9) and (10) can be evaluated to obtain the velocity and pressure at any point in the fluid domain where these quantities are desired. Frequently, however, the only quantities of interest are the particle motion and interface shape and, for this, we need only the surface values of velocity and stress.

The details of applying (9) and (10) together with the boundary conditions at the interface to obtain integral equations for the boundary velocity and stress components has been outlined previously by Lee and Leal (1982). Here, we content ourselves with merely reporting the results. At the interface we obtain

$$\frac{1}{2}\mathbf{u}^I(\mathbf{x}) = -\frac{3}{4\pi}\int_{S_I}\frac{\mathbf{rrr}}{R^5}\cdot\mathbf{u}^I\cdot\mathbf{n}\,dS_I + \frac{1}{8\pi}\int_{S_I}\left[\frac{\mathbf{I}}{R}+\frac{\mathbf{rr}}{R^3}\right]\cdot\mathbf{T}_2^I\cdot\mathbf{n}\,dS_I$$
$$+\frac{1}{8\pi}\int_{S_P}\left[\frac{\mathbf{I}}{R}+\frac{\mathbf{rr}}{R^3}\right]\cdot\mathbf{T}_2^P\cdot\mathbf{n}\,dS_P\ , \quad \mathbf{x}\in S_I \tag{11}$$

and

$$\frac{1}{2}(\lambda+1)\mathbf{u}^I(\mathbf{x}) = \frac{3}{4\pi}(\lambda-1)\int_{S_I}\frac{\mathbf{rrr}}{R^5}\mathbf{u}^1\cdot\mathbf{n}\,dS_I + \frac{1}{8\pi}\int_{S_P}\left[\frac{\mathbf{I}}{R}+\frac{\mathbf{rr}}{R^3}\right]\cdot\mathbf{T}_2^P\cdot\mathbf{n}\,dS_P$$
$$-\frac{1}{8\pi}\int_{S_I}\left[\frac{\mathbf{I}}{R}+\frac{\mathbf{rr}}{R^3}\right]\cdot\mathbf{F}(f)\,dS_I\ , \quad \mathbf{x}\in S_I \tag{12}$$

where the function $\mathbf{F}(f)$ is the stress difference at the interface,

$$\mathbf{F}(f) \equiv \lambda\mathbf{n}\cdot\mathbf{T}_1^I - \mathbf{n}\mathbf{T}_2^I = -\frac{1}{Ca}\left[\frac{K}{r}\frac{\partial f}{\partial r}+K^3\frac{\partial^2 f}{\partial r^2}\right]\mathbf{n}+\frac{1}{Cg}f\mathbf{n}, \tag{13}$$

here expressed in cylindrical coordinates. The superscripts I and P refer to the surface of the interface and sphere, respectively; the vector $\mathbf{r}$ is defined as $\mathbf{r}\equiv\mathbf{x}-\eta$; and $\mathbf{T}_i^I$ is the stress tensor evaluated as the interface is approached from fluid i. K

is defined as $1/|\nabla H|$ with the shape function H defined in Eqs. (15a,b,c). Finally, on the surface of the sphere

$$\mathbf{u}^P(\mathbf{x}) = -\frac{3}{4\pi}\int_{S_I}\frac{\mathbf{rrr}}{R^5}\cdot\mathbf{u}^I\cdot\mathbf{n}\,dS_I + \frac{1}{8\pi}\int_{S_I}\left[\frac{\mathbf{I}}{R}+\frac{\mathbf{rr}}{R^3}\right]\cdot\mathbf{T}_2^I\cdot\mathbf{n}\,dS_I$$
$$+\frac{1}{8\pi}\int_{S_P}\left[\frac{\mathbf{I}}{R}+\frac{\mathbf{rr}}{R^3}\right]\cdot\mathbf{T}_2^P\cdot\mathbf{n}\,dS_P, \quad \mathbf{x}\in S_P \tag{14}$$

Following the precedent of Lee and Leal (1982), the problem to this point has been described entirely in terms of the cylindrical coordinate system sketched in Fig. 3a. Although this representation appears as the "natural" description in view of the axisymmetric nature of the problem, it can lead to very large values of $\partial f/\partial r$ and $\partial^2 f/\partial r^2$ when the interface approaches a "tailing" configuration and it was the loss of numerical accuracy associated with this fact which was largely responsible for termination of Lee and Leal's earlier solutions at relatively modest levels of deformation. In order to overcome this deficiency and insure maximum numerical accuracy in the calculation of spatial derivatives, we divide the interface into three sections with the interface shape function H represented by a different coordinate system in each section (Fig. 3b).

$$H_1(\mathbf{x}) = \rho - f_1(\theta,t) = 0, \quad \mathbf{x}\in S_1^I \quad (0\le\theta\le\theta_{\max}) \tag{15a}$$

$$H_2(\mathbf{x}) = r - f_2(z,t) = 0, \quad \mathbf{x}\in S_2 \quad (z_{\min}\le z\le z_{\max}) \tag{15b}$$

$$H_3(\mathbf{x}) = z - f_3(r,t) = 0, \quad \mathbf{x}\in S_3^I \quad (r_{\min}\le r) \tag{15c}$$

Equation (15a) locates the interface in terms of the distance from the center of the sphere as a function of the angle from vertical. In Eq. (15b), the interface shape is expressed in terms of the distance from the z-axis as a function of z. The "original" cylindrical coordinate system is used to describe the interface shape as a function of r in (15c). Although (15b) and (15c) are both written in cylindrical coordinates,

different functional representations of the interface are used in the two cases. The vector function $\mathbf{F}(\mathrm{f})$ is then given by

$$\mathbf{F}(f_1) = -\frac{1}{Ca}\left(\frac{2}{k_1 r} - \frac{1}{k_1^3 r^2}\frac{\partial^2 f_1}{\partial\theta^2} - \frac{1}{k_1 r^2}\frac{\partial f_1}{\partial\theta}\cot\theta + \frac{1}{k_1^3 r^3}\left(\frac{\partial f_1}{\partial\theta}\right)^2\right)\mathbf{n}_1 + \frac{1}{Cg}z\mathbf{n}_1 \ , \quad \text{for} \quad \mathbf{x}\in S_1^I$$

$$\mathbf{F}(f_2) = -\frac{1}{Ca}\frac{1}{k_2}\left(\frac{1}{r} - \frac{1}{k_2^2}\frac{\partial^2 f}{\partial z^2}\right)\mathbf{n}_2 + \frac{1}{Cg}z\mathbf{n}_2 \ , \quad \text{for} \quad \mathbf{x}\in S_2^I$$

$$\mathbf{F}(f_3) = -\frac{1}{Ca}\frac{1}{k_3}\left(\frac{1}{r}\frac{\partial f}{\partial r} + \frac{1}{k_3^2}\frac{\partial^2 f}{\partial r^2}\right)\mathbf{n}_3 + \frac{1}{Cg}z\mathbf{n}_3 \ , \quad \text{for} \quad \mathbf{x}\in S_3^I$$

where

$$k_1 = \left[1 + \frac{1}{r^2}\left(\frac{\partial f_1}{\partial\theta}\right)^2\right]^{1/2} \ , \quad \mathbf{n}_1 = \frac{1}{k_1}\left(\mathbf{i}_r - \frac{1}{r}\frac{\partial f_1}{\partial\theta}\mathbf{i}_\theta\right) \ ,$$

$$k_2 = \left[1 + \left(\frac{\partial f_2}{\partial z}\right)^2\right]^{1/2} \ , \quad \mathbf{n}_2 = \frac{1}{k_2}\left(\mathbf{i}_r - \frac{\partial f_2}{\partial z}\mathbf{i}_z\right) \ ,$$

$$k_3 = \left[1 + \left(\frac{\partial f_3}{\partial r}\right)^2\right]^{1/2} \ , \quad \mathbf{n}_3 = \frac{1}{k_3}\left(\mathbf{i}_z - \frac{\partial f_3}{\partial r}\mathbf{i}_r\right) \ ,$$

The derivatives in the equation for the normal stress jump junction $\mathbf{F}(f)$ were evaluated by use of a cubic spline polynomial. A spline function was fit through the center points of the interface segments in each of the three regions and differentiated analytically at the node points to give $\partial f_i/\partial x_i$ ($x_i = \theta,\ z,\ r$). The spline function was also used to prevent the node points from convecting along the interface as the calculation progressed so that the original segment distribution was maintained throughout a numerical run.

When the sphere velocity is known so that Eq. (8a) applies, Eqs. (11, 12 and 14) give three integral equations for the unknown quantities $\mathbf{u}^I$, $\mathbf{T}_2^I$ and $\mathbf{T}^p$,

provided the interface shape and sphere position are known. When we consider the constant force problem, on the other hand, Eq. (8b) applies and we have four integral equations for $\mathbf{u}^I$, $\mathbf{u}^P$, $\mathbf{T}_2^I$ and $\mathbf{T}^P$. Having solved these equations in either case for some specified initial shape, the kinematic condition, Eq. (7), can be used to calculate $\partial f/\partial t$. This allows the interface shape to be determined at some later time by adding $\partial f/\partial t\, \Delta t$ to the present shape. The position of the sphere is also changed by an increment $\mathbf{u}^P \cdot \Delta t$ and the process is repeated using the new sphere position and interface shape. In this way, the sphere is "marched" forward from any given initial condition.

As the problem of motion normal to the interface is axisymmetric, the surface integrals can be simplified greatly by analytically integrating in the azimuthal direction to reduce the surface integrals to line integrals. Equations (11, 12 and 14) then yield seven linear integral equations in the seven unknowns u_r^I, u_z^I, u_z^P, $T_{2_{nr}}^I$, T_{nz}^P, T_{nr}^P. Following the work of Lee and Leal (1982), these equations were solved numerically using a simple collocation method. This technique converts the integral equations into a system of linear algebraic equations. The surface of the sphere and interface were divided into segments small enough that $\mathbf{u}^I$, $\mathbf{u}^P$, $\mathbf{T}_2^I$ and $\mathbf{T}^P$ could be approximated throughout the segment by the value at the center of the segment. The criteria used here to determine the size of these segments is discussed in the following section. The integrations were then carried out by Simpson's rule. This procedure converts the seven integral equations into a system of $(4N_I + 2N_P + 1)$ linear algebraic equations where N_I is the number of segments on the interface and N_P is the number of segments on the sphere. This system is readily solved by Gaussian elimination. One complication is that the integrands in (11), (12) and (14) become singular when $\mathbf{x} \to \eta$ [see Eq. (9) for definitions of $\mathbf{x}$ and η]. Thus integration over a small neighborhood of $\mathbf{x}$ was carried out analytically using a linear expansion of the integrands in Eq. (11)-(14) so that all terms remain

bounded during the numerical integration.

The solutions generated by this numerical scheme are time-dependent through the kinematic condition Eq. (7), although the governing equations for the fluids are the steady Stokes equations. All of the equations and boundary conditions (2)-(7) are based upon the assumption of a characteristic time scale

$$t_c = \frac{a}{U_\infty} .$$

Thus, any motion, including a time-dependent instability, which evolves on a time scale of this order or slower will be resolved by the numerical solution scheme. Surface tension driven flows, with a length scale l, will be characterized by a time scale

$$t^* = \frac{\mu_2 l}{\sigma} .$$

Hence, such motions will be resolved if

$$0\left(\frac{\mu_2 l}{\sigma}\right) \geq 0\left(\frac{a}{U_\infty}\right) .$$

This condition can be written in the alternative form

$$\frac{l}{a} Ca \geq 0(1)$$

Thus, any surface tension driven disturbance with a length scale $l = 0(a)$ or larger will be resolved for systems with $Ca = 0(1)$. Very small wavelength disturbances, or disturbances in systems with a large interfacial tension will not be resolved.

III. Preliminary Results

The solution to the problem formulated in the previous section will generally depend on both the initial location of the sphere and the initial shape of the interface.

Therefore, a new set of calculations is required, in principle, for every combination of initial conditions. In an attempt to circumvent this considerable complication, Lee and Leal (1982) pursued the concept of "limiting solutions" in which the characteristic time for displacement of the sphere is either very much larger or very much smaller than an intrinsic measure of the characteristic timescale for interface motion. These two cases correspond to an interface that remains flat for the fast moving sphere, or one which reaches a steady state deformation, i.e., $\mathbf{u} \cdot \mathbf{n} = 0$ at each instantaneous position of the sphere in the case of "slow" transition. In either of these cases, the velocity of the sphere and the interface shape (or velocity) would depend only on λ, Ca, Cg and the instantaneous position of the sphere, thereby removing the prior history of sphere motion and interface shape as a factor in the solution. Unfortunately, comparison with exact numerical solutions showed that only relatively few combinations of λ, Ca, Cg and initial sphere position corresponded accurately to these limiting cases.

In the present paper, we therefore have considered further the dependence of the solution on the initial position of the sphere. It is intuitively evident that a starting position which is sufficiently large should have a small effect on the solution when the sphere is near the interface. This is illustrated in Figs. 18 and 20 for results obtained under the condition of a constant force, Eq. (8b). In these figures, interface shapes are plotted in a reference frame moving with the sphere so that the interface appears to be sweeping past the sphere for starting positions, l_o, of 3, 5, and 10 radii from an undeformed interface, with $\lambda = 1$, $Ca = 1$, $Cg = 1$ and $\lambda = 10$, $Ca = 1$, $Cg = 1$. We shall discuss these results in some detail in section V. For present purposes, it is sufficient to note that the interface shapes for starting positions of 5 and 10 appear to be identical by the time the sphere reaches a position 3 radii away from the original interface position. The case starting at 3 also produces deformation equal to the other two cases once the sphere reaches $l = 0.75$. Figure

20 indicates that for a higher viscosity ratio, it takes longer for the three cases to converge to the same shape, but after $l = 0.10$, the results for the various starting positions are indistinguishable. Plots of sphere velocity versus position for these cases are given in Figs. 19 and 21. Again, the results for the three cases converge as the sphere reaches a position straddling the interface. Finally, Fig. 5 gives the same type of plot for the constant velocity case with $\lambda = 1$, $Ca = 1$, $Cg = 1$ with the same qualitative results. It is evident that a starting position $l_o = 3$ is large enough to produce solutions which are qualitatively (and over most of the trajectory quantitatively) representative of the solution for a sphere approaching an interface from any large distance, and we use the value $l_0 = 3$ for many of the computations that are reported in this paper. Solutions with a *smaller* initial separation between the sphere and the interface can, however, exhibit important qualitative differences from these "large initial separation" solutions, as we shall consider later in some detail.

Another aspect of the numerical calculation which should be discussed prior to the detailed results is the fact that the domain of numerical integration along the interface in Eqs. (13, 14 and 16) is necessarily truncated at some finite distance R_0, from the centerline. Numerical and asymptotic justification for this procedure was provided by Lee and Leal (1982) for the case of sphere motion at a constant velocity. Figure 4 demonstrates the effect of increasing R_0 on the sphere velocity for the constant force problem at three different sphere positions. All other calculations in this study were carried out with $R_0 \geq 12$. It may also be noted that the truncation is equivalent to assuming $\mathbf{u}^I$ and $\mathbf{T}^I = 0$ for $r > R_0$. Thus, additional justification of the truncation procedure can be achieved by comparing the calculated values of $\mathbf{u}^I$ and $\mathbf{T}^I$ near the point of truncation with values near the centerline. Generally, several orders of magnitude difference existed between these two sets of values.

Although it is a fairly straightforward procedure to decide on a reasonable lower

bound for R_0, deciding on the segment sizes along the sphere and interface surfaces is a more complex problem. Of course, placing more segments on the surface comes closer to representing the process of integration, but adding segments to the surface increases computation time and cost. The number of segments necessary is strongly influenced by the details of the weighting function distribution along the surface. In the collocation method used here, it is assumed that $\mathbf{u}^I$ and $\mathbf{T}^I$ or $\mathbf{T}^P$ are constant at the center-point value within each segment; thus, the density of segments must be largest in regions where the values of these variables change most rapidly. Also, the contribution from any segment decreases at least as fast as $1/r^2$ as r increases, so larger segment increments can be used as the distance along the interface increases. The solutions are axisymmetric and we have already indicated that the azimuthal angle ϕ has been integrated out from the full integral Eqs. (13)-(16) to obtain the equations which are solved here. Thus the collocation "segments" on the sphere are actually "strips" around the sphere, with the sphere surface incremented in terms of the polar angle θ. Following Lee and Leal (1982) a uniform segment distribution in θ was chosen for the sphere, with 10 increments in θ covering the sphere surface when the interface deformation was small or moderate, increasing to 16 for large deformations and/or small sphere-interface separations.

A nonuniform distribution of segment sizes was used along the interface. The number of segments (which again are strips encircling the $r = 0$ axis) was taken as 14 for "stiff" interfaces, i.e., those that showed slight deformation, and 16 to 35 for interfaces with large deformation, again the number increasing as the deformation grew.

When the three coordinate system representation was used to describe the interface, two additional parameters were specified, Θ_{max} and z_{min}. These were chosen to correspond to the end of the spherical cap and tail regions, respectively, as illustrated qualitatively in Fig. 3b. As a result, in each of the three basic regions the

interface closely followed a coordinate surface except in the area where one representation changed over into another, and the partial derivatives of the shape functions in each region had small magnitudes in the chosen coordinate representation.

The final parameter of the numerical algorithm was the time step used in incrementing the interface shape and sphere position. This marching was carried out by simply multiplying the instantaneous velocity of the sphere or interface segment, calculated by the collocation technique, by the timestep. In other words, the exact equation for sphere position $l = l_o + \int_{t_o}^{t} u^P dt$ is approximated by $l = l_o + \sum_{i=1}^{n} u_i^P \Delta t_i$ where a new u_i^P is calculated at each time step, and similarly for the interface. The largest non-dimensional time step, $\Delta t = \Delta t'/(a/U_\infty)$ used was 0.05 and this value was decreased as the rate of change of the sphere position or interface shape increased. Also, for both constant force and constant velocity calculations, a shorter time step is needed as the distance between two surfaces (for example the sphere and the interface) decreases. Although this time marching procedure is accurate only to $0(\Delta t)$, the requirement that Δt decrease as bounding surfaces approach necessitates a small enough time step that it is not necessary to employ higher order methods. Whenever a new time step was introduced, an overlap region with the old larger time step was included in the calculation. The shapes and velocities in this region were compared for the two cases and if the differences had been greater than 2%, the small time step would have been introduced at an earlier point until the difference was within 2%. In all cases, however, the difference actually computed was less than 0.5% when the new time step was introduced.

IV. Results for Motion of a Sphere from a Large Distance at Constant Velocity

The numerical scheme described in the preceding two sections has been used

to investigate the motion of a sphere normal to a deformable interface. We first consider the case where the sphere moves with a constant velocity from a large distance. The results presented in this section complement Lee and Leal (1982) who considered the same problem but were limited to calculations for moderate deformation only. Using the three coordinate system representation, we have now been able to numerically consider cases where the interface shows large deformation, continuing in some cases to the point where the sphere has passed many radii beyond the plane of the undeformed interface. A feature of the numerical algorithm is that the maximum allowable time step becomes smaller as the thickness of either the film of liquid in front of the sphere or the tail becomes thinner. Thus, the present computations were terminated when the cost to further increment the sphere position by a small distance became unacceptably large. In no case was this computational termination point coincident with the onset of instability of the film or tail, or of "contact" between the sphere and the interface. Thus, as noted earlier, a definitive conclusion was never possible as to the final mode of breakthrough. In some cases, however, the rates of change of the film or tail thickness do provide strong circumstantial evidence to support either film rupture or tail rupture as the likely mechanism of breakthrough.

In order to provide a framework for discussion of the results, it is useful to begin by reviewing the expected role of viscous, capillary and body forces in determining the degree of interface deformation for the case of sphere motion at a constant velocity. From a macroscopic point of view, a basic energy balance at any moment will exist between the rate of working, FU, by the particle on the fluid (where U is the particle velocity and F is the hydrodynamic drag which, at steady state, is equal in magnitude to the applied force necessary to maintain the constant velocity U), and the rate of conversion to internal and potential energy. When the particle is far from the interface, the rate of working, FU, is converted entirely to heat via

viscous dissipation. As the particle approaches the interface, however, the force, F, required to maintain the velocity U increases, partly as a consequence of an increase in the rate of viscous dissipation and partly to balance the increase in potential energy of the system as the interface begins to deform so that the heavier fluid is carried across the plane, $z = 0$, of the undeformed interface and the surface area is increased. If we focus on the region above $z = 0$ that is occupied by fluid II, as illustrated and considered in detail for a tailing configuration in the Appendix, an approximate balance exists between the rate of working FU, the rate of increase of potential energy as the volume of fluid is increased by "entrainment" into the tail, the rate of increase of surface energy as the interfacial area is increased, the rate of working by surface stresses at the exterior boundaries of the film plus tail and the rate of viscous dissipation in the film plus tail.

The *details* of interface deformation can only be determined by solving the full problem outlined in the previous section, and we shall present results of this type very shortly. Some general features can be understood, however, on the basis of the approximate energy balance in the film plus tail that we have just outlined. Let us consider initially the case $\lambda = 0$. Now, for any given λ, the rate at which the interface deforms for a given rate of input of mechanical energy, FU, is determined by the incremental increase of potential energy that is required due to the increase of surface area and the increased volume of heavy fluid above the $z = 0$ plane. Since the potential energy increase is proportional to the surface tension and the density difference between the two fluids, and Ca and Cg measure the characteristic magnitude of viscous forces relative to capillary and buoyancy forces, it is evident in the constant velocity case that a decrease in Ca and/or Cg will tend to *reduce* the *rate* of interface deformation. Thus, for a given position of the sphere, the interface will tend to be less deformed for smaller values of Ca or Cg. Of course, some of the mechanical energy is converted irreversibly to heat even for $\lambda = 0$, but

as λ increases both the rate of dissipation within the film plus tail and the rate of working by viscous stresses at the boundary of the tail-film region will increase. Consequently, for fixed Ca and Cg (roughly, fixed FU), we may expect that the rate of deformation will decrease with increase of λ since an increased fraction of the input energy is being dissipated to heat. Thus, again, for a given instantaneous position of the sphere, the interface will be less deformed as λ increases. An upper bound on the amount of fluid which the sphere can carry across the $z = 0$ plane corresponds to the case when viscous effects are negligible and the interfacial free energy is zero ($Ca = \infty$). In this case, the maximum volume of entrained fluid will be determined by a balance between the force applied to the fluid from the sphere, F, and the total buoyancy force on the fluid in the film plus tail region. We shall see shortly, from our detailed solutions, that this balance is very closely approached for $\lambda = 0$ even when $Ca = 0(1)$. This is illustrative of the fact that interfacial tension acts primarily to moderate the rate of entrainment across the interface at any moment by affecting the shape of the interface in an attempt to minimize the area (or curvature), but does not itself control the total amount of fluid which can be carried across the plane by entrainment. Indeed, as the density difference becomes very small (i. e., $Cg \to \infty$), the maximum degree of interface deformation will become very large for any level of interfacial tension (Berdan and Leal, 1982). The role of nonzero values for the viscosity ratio, λ, is similar to interfacial tension in the sense that the interface deformation (and rate of entrainment) is decreased at any instant, relative to its value for $\lambda = 0$, but a nonzero viscosity ratio does not in itself control the total maximum volume of fluid which can be entrained across the $z = 0$ plane, this still being determined by the balance between drag and the net body force.

It is important to recognize that the constant velocity problem considered in this section is special in that a tailing configuration of interface deformation must

ultimately be achieved in all cases in the absence of hydrodynamic instabilities leading to rupture of the interface (the exception being $Ca = Cg = 0$, corresponding to a solid wall). For very small (but nonzero) values of Ca and/or Cg, the interface will remain virtually flat until the sphere begins to penetrate the plane $z = 0$, and the minimum dimension of the film which then forms will be exceedingly small compared to the radius of the sphere. Furthermore, the force required to move the sphere at constant velocity will become exceedingly large. Nevertheless, a film and tail must ultimately form. Whether such an extremely thin film could actually be realized in the "real" problem, where additional effects such as van der Waals forces are present is doubtful, but that is a question which cannot be answered in the present context where only hydrodynamic, surface tension and body forces are considered. In addition, as a practical matter, the present numerical scheme is not well suited to cases involving extremely thin films (or tails) and we are thus forced (by the cost of obtaining a solution) to stop some calculations involving small values of Ca and/or Cg before the sphere moves a significant distance across the $z = 0$ plane. In these cases, it is important to recognize that the "inability" to proceed further with the solution does not mean that a tailing configuration will not ultimately appear in the constant velocity case (assuming of course that no hydrodynamic instability is encountered). It is only the inability of our present scheme to generate the solution with reasonable economics for small Ca and/or Cg which prevents our demonstrating the tailing configuration which must inevitably occur. The constant velocity problem does not, therefore, contribute directly to our understanding of the conditions for existence of the film drainage or tailing configurations which can occur in the case of motion under the action of a constant force. It does provide the simplest forum for understanding, in detail, the physics controlling interface deformation and that is its most important role. In addition, however, the constant velocity case provides an essential basis for high resolution

experimental observations over a wide range of Ca and Cg as are necessary to expose the role in the coalescence process of effects such as non-Newtonian rheology or inertia which cannot be studied easily by a theoretical (numerical) analysis (Geller, Berdan, and Leal, 1986).

Let us now consider the results obtained from the numerical calculations in detail for the case of sphere motion at a constant velocity. The first case treated is $\lambda = 1$, $Ca = Cg = 1$. We choose to begin with this case because the "characteristic" measures of viscous, surface tension and gravity forces are all of equal magnitude and thus these forces should be expected to have a roughly equivalent role in the behavior of the sphere and interface. Profiles showing the interface shape at equal increments of time (or particle displacement) are plotted in Fig. 5. The most obvious feature of this solution is the long, slender tail which evolves behind the sphere and the rather considerable volume of fluid which is carried across the interface by the sphere. The "film" over the front portion of the sphere does thin slowly, but in none of the cases shown in the figure is it particularly thin compared to the sphere radius. It is also noteworthy that none of the interface shapes drawn in Fig. 5 exhibits any indication of hydrodynamic or capillary instability, although the spatial resolution of our solution algorithm is such that disturbances on the scale of either the tail diameter or minimum sphere-interface separation could be detected if they were present. It may be noted in this regard that the linear stability analysis of Lang and Wilke (1971) leads to the conclusion that the "film" in front of a rigid sphere approaching an interface should be stable in the absence of van der Waals forces. On the other hand, the experimental observations of Maru *et al.* (1971) show the onset and growth of a varicose disturbance on the "tail" which does cause it to break apart, but only after the tail is approximately 120 particle radii in length, far beyond the final configuration which is attainable at reasonable cost with the current method of solution. The obvious alternative would seem to be a detailed stability analysis

for a draining, extending tail, such as that shown in Fig. 5. Unfortunately, none of the existing analyses of "thread" stability is directly applicable, and an improved analysis does not appear viable to us at the present time due to the complicated and "unknown" nature of the "base" geometry and flow. The classical analyses of Rayleigh (1892) and Tomotika (1935) for surface tension driven instability of a stationary thread "neglect" the nonuniform geometry, the draining flow in the tail, and, most importantly the extension of the tail with time, which is known from both experimental and theoretical studies to increase stability, cf. Grace (1971), Chin and Han (1979) and Olbricht and Leal (1983). A problem which more closely resembles the situation in the tail is the stability of an infinite thread that is aligned with the symmetry axis of a uniaxial straining flow, treated by Mikami, Cox and Mason (1975). Their analysis includes the effect on stability of extension and of a decrease in thread diameter, but in a controlled manner determined by the assumed uniaxial straining flow (which is not present in the tail behind the sphere). These researchers predicted a fastest growing wavelength which depends on the instantaneous radius but which reaches an asymptotic limit with time. For the case $\lambda = 1, Ca = 1$, this asymptotic limiting wavelength is approximately 35 thread radii (or roughly 15 sphere radii for our case); our calculations go as far as a length of about 6.5 for the tail region, considerably less than the wavelength for instability predicted by Mikami *et al.*, and much less than seen experimentally by Maru *et al.* (1971). If, as said before, extension and thinning of the fluid cylinder are factors "stabilizing" the growth of capillary waves, Mikami's results may provide an upper bound on the length that the tail can achieve since the flow assumed in their calculations provides the greatest extensional character.

An examination of the governing equations and boundary conditions, Eqs. (2)-(8), indicates that the interface shape will depend on the parameters λ, Ca, and Cg. Lee and Leal (1982) have previously discussed the role of each of λ, Ca and

Cg on the behavior of the deforming interface at small and moderate deformations. In the remainder of this section, we focus on the large deformation behavior of the interface beginning with the influence of the viscosity ratio λ. The effect of the viscosity ratio can be seen by comparing the results in Fig. 5 with those in Figs. 6 and 7, where we consider the same values of $Ca = Cg = 1$, but $\lambda = 0$ and 10, respectively. It is visually evident on the basis of the film thickness at the front stagnation point of the sphere that the amount of deformation for a given position of the sphere is decreased in the early part of the deformation process as the viscosity ratio, λ is increased. This visual impression is confirmed if we actually measure the volume of fluid in the film + tail region above the $z = 0$ plane as a function of particle position, though the differences on this basis between the cases $\lambda = 0$ and $\lambda = 1$ are very small. This can be seen in Fig. 8 where we have plotted (for reasons to be discussed shortly) the total volume of the fluid region plus sphere normalized by $6\pi a^2$. We have argued earlier that the influence of increased viscosity in the upper fluid should be primarily one of controlling the rate and details of interface deformation rather than the maximum amount of fluid which can be carried across the $z = 0$ plane. This conjecture is confirmed for $\lambda = 0$ and 1 by the results in Fig. 8, where a maximum is obvious in the volume which is approximately independent of λ, though occurring somewhat later (i.e., for more negative values of l) for $\lambda = 1$ than for $\lambda = 0$. Beyond the point of maximum volume, the film + tail region begins to lose fluid by "drainage", though this process is also slower for $\lambda = 1$ than for $\lambda = 0$. The case $\lambda = 10$, which initially begins with a much smaller volume of entrained fluid (for $l > 0$) has not yet yielded a maximum in the volume of entrained fluid by the time that the calculation was stopped due to the thinness of the film at the front of the sphere, but the total volume of fluid entrained is similar to the other cases at intermediate values of l. In all of the general features described above, the numerical solutions illustrated in Figs. 5-7 confirm the qualitative physical picture

(outlined at the beginning of this section) of the role of λ in the interface deformation process. Certain detailed features of interface shape could not be predicted by the qualitative arguments, however, and these are also of interest here.

First, it is evident that the portion of the tail plus film region which changes shape most rapidly once the total volume begins to decrease by drainage is strongly dependent on λ. In particular, for $\lambda = 0$, the film region barely thins at all but instead is carried along in almost rigid motion by the sphere. All of the loss of fluid volume occurs in the tail, which thins rapidly both because it is being stretched and because there is no flow entering the tail from the film to compensate for this stretching and for the drainage of fluid back across the $z = 0$ plane. For $\lambda = 1$, on the other hand, the film is thinned more rapidly as a consequence of viscous stresses at the interface, the fluid in the tail drains more slowly and the result is a marked decrease in the rate at which the tail decreases in radius. The fact that the "film" barely thins at all when viscous stresses are removed from the interface (in setting $\lambda = 0$) shows that neither capillary nor body forces plays a significant role in this process, at least for $Ca = Cg = 0(1)$. Finally, although we have indicated previously that the mode of "breakthrough" cannot generally be established in the absence of a thorough study of possible hydrodynamic instabilities, and/or other phenomena associated with the existence of colloidal forces between the interface and sphere surface, or between the interface and itself (for example, across the thin tail), a simple comparison of the rate of decrease of the film and tail "thickness" in the case $\lambda = 0$ is strongly suggestive that "breakthrough" will occur in that case by a necking failure in the tail, leading presumably to a sphere in fluid 1 surrounded by a layer of fluid 2 (though this cannot represent an equilibrium configuration, see Johnson and Sadhal, 1985).

A final point of interest, with regard to these first three solutions, is the variation of the hydrodynamic drag on the particle as a function of its position. The

numerically calculated values of the drag ratio (i.e., the drag/$6\pi\mu_2 aU$) for the cases $\lambda = 0$, 1 and 10 with $Ca = Cg = 1$, are shown as a function of particle position by the solid lines in Fig. 8. The deviation in the drag from Stokes' law obviously increases with λ. Furthermore, the results for $\lambda = 0$ and $\lambda = 1$ show a definite maximum in the drag at a position where the particle has passed beyond the plane of the undisturbed interface. This maximum in the drag appears to occur primarily because of a corresponding maximum in the volume of fluid in the complete column consisting of the film and tail. To demonstrate this fact, let us consider the net body force on the fluid column excluding the sphere which is simply $(\rho_1 - \rho_2)g(v_f + v_s)$, where v_f is the total volume of fluid in the column (i.e., film plus tail), and v_s is the volume of the sphere. If the contributions of viscous stresses and interfacial tension were completely negligible in the macroscopic energy balance described earlier, this net body force should exactly balance the hydrodynamic force from the particle to the fluid. In this case,

$$Drag\ ratio = \frac{v_f + v_s}{6\pi a^3} Cg^{-1} \tag{16}$$

Thus, for $Cg = 1$

$$Drag\ ratio = \frac{v_f + v_s}{6\pi a^3}$$

and it would follow that any variation in the drag ratio with particle position should be reflected in temporal variations of $v_f + v_s$. In order to test this conclusion, values of $v_s + v_f$ were measured from the numerical solutions, and $(v_s + v_f)/6\pi a^3$ was plotted in Fig. 8 for comparison with the numerically calculated drag ratio. It is evident that the drag ratio and $(v_f + v_s)/6\pi a^3$ agree extremely well for the case $\lambda = 0$. Apparently, any contributions of viscous dissipation or the increase in surface energy due to increased surface area to the overall energy balance (from which the simple "force balance" of (30) is "derived") are negligible for $\lambda = 0$, $Ca = Cg = 1$. On the other hand, as λ increases, the drag ratio considerably exceeds $(v_s + v_f)/6\pi a^3$, though the position of the maximum in the drag ratio still appears

to agree well with the position of the maximum in $(v_f + v_s)$. We believe that the difference between the drag ratio and $(v_s + v_f)/6\pi a^3$ for $\lambda > 0$ is primarily a consequence of the increased rate of working by viscous stresses at the interfacial boundary of the columnar region. The quantitative comparison for $\lambda = 0$ provides strong evidence for the validity of the qualitative picture, based on an overall energy balance, that was outlined at the beginning of this section.

In the remainder of this section, we consider the detailed effects of variations in Ca and Cg on the large deformation behavior of the interfaces. We first consider two cases of small Ca and Cg. Figure 9 shows interface shapes for the case $\lambda = 1$, $Ca = Cg = 0.1$ and Fig. 10 presents the results for $\lambda = 1$, $Ca = Cg = 10^{-3}$ both with the center of the sphere initially 3 radii away from a flat interface. The asymptotic limiting case, $Ca \ll 1$, $Cg \ll 1$, corresponds to very large surface tension and gravitational forces relative to viscous forces, and is known to yield asymptotically small deformations of the initially flat interface provided only that the sphere has not begun to penetrate the plane of the undisturbed interface. Although it is not known precisely how small Ca and Cg must be for this asymptotic behavior to manifest itself, it might be supposed that simple dominance of surface tension or gravitational forces (corresponding to Ca or $Cg < 1$) would be enough. It is evident from Fig. 9 that this is not the case. Even for $Ca = Cg = 0.1$, there is considerable deformation before the sphere comes close to the $z = 0$ plane. The role of viscous forces is small in this case relative to surface tension and gravity effects so we see, (as was also true for $\lambda = 0$), that there is only very slow thinning in the film ahead of the sphere in spite of the fact that $\lambda = 1$. The important effects are taking place in the tail behind the sphere. Unlike the earlier results, a long tail is not formed behind the sphere. What is evident from Fig. 9 is that once the interface has been deformed by the sphere, say, between $l = -1$ and -2, the relatively large surface tension tends to drive the interface toward a minimum energy configuration, namely

a spherical shell encapsulating the particle with a flat interface below. At the same time, the relatively strong capillary forces, in combination with the increased density difference between the two fluids, causes rapid drainage and a "pinching off" of the tail behind the sphere. In the second case, $\lambda = 1$, $Ca = Cg = 10^{-3}$, the magnitude of the surface tension and density difference is such that the interface appears nearly rigid at the point where the computation is terminated. Breakthrough, in this case, undoubtedly occurs in real systems by rupture of the thin film on the front portion of the body. Nevertheless, if we were to continue the present calculations for a sufficiently long time, a tail would eventually develop.

Figure 11 shows the drag ratio versus position for $\lambda = 1$, $Ca = Cg = 1$, 0.1 and 10^{-3}. The points which appear with the plot for $Ca = Cg = 10^{-3}$ are exact analytical results for sphere motion towards a *flat* interface with $\lambda = 1$ calculated by Lee and Leal (1980). The present numerical results can be seen to agree very well with these analytical results. It should be noted that this comparison provides a fairly critical test of the accuracy of the numerical scheme because the numerical solution difficulties are most severe where sphere-interface separation becomes very small. The generalities discussed with regard to Fig. 8 (such as the existence of a maximum in the drag) are seen to apply in these cases as well; however, the increased restoring force associated with the decrease of Ca and Cg causes a very substantial increase in the magnitude of the drag ratio.

Finally, three constant velocity cases were considered in which λ and Cg were held equal to 1.0, but Ca was varied to examine the effects of surface tension in more detail. In one of these cases, we took $Ca = 10^{-2}$, with the result that the interface deformed very little, and a deformation mode was observed similar to $Ca = Cg = 10^{-3}$ but with slightly increased amplitude of deformation. In the interest of space conservation, this case is not shown here but will be available in Geller (1986). The second case, $\lambda = 1, Cg = 1$ and $Ca = \infty$ is depicted in Fig. 12.

Here, the surface tension is zero. As the viscosity ratio is the main factor controlling the film thickness for either Ca or $Cg = 0(1)$, the thinning of fluid in front of the sphere is almost identical to that shown in Fig. 5 for $\lambda = Cg = Ca = 1$. The difference in interface shapes between these two cases is in the thickness of the tail behind the sphere. In the present case without any surface tension, the tendency of the tail to "pinch off" is reduced, and a broader tail results.

The final case we present in the series illustrating the role of surface tension is $Ca = 10^{-1}$ ($\lambda = 1$, $Cg = 1$), shown in Fig. 13. In this case, Ca is small enough to have a very strong influence on the behavior of the interface and yet not so small as to inhibit all deformation prior to the sphere crossing the $z = 0$ plane. Examination of Fig. 13 shows that for the early stages of deformation, $l = 3$ to 0, surface tension acts to broaden the deformed part of the interface by flattening it, and thereby minimizing the total curvature. This broadening can be seen by comparison with the result for $Ca = 1$ in Fig. 5. In spite of this "broadening" effect, however, the total volume of fluid carried across the plane of the initially undeformed interface is nearly equal for the two cases consistent with the predictions from the macroscopic balance on the sphere-tail system. Furthermore, though the resistance of the interface to deformation caused by the large value of γ initially results in a rapid thinning of the thin film in front of the particle, this film does not continue to drain as the sphere moves but eventually reaches a steady thickness equal to that for $Ca = 1$, $Cg = 1$, $\lambda = 1$ as expected based on our earlier discussion of the role of the viscosity ratio in the formation the film. As the sphere moves across the initial plane of the interface, $l = 0$ to -3, the interface must deform in front of the sphere, and the interface shape near the sphere is almost identical to the case (Fig. 5) where $Ca = 1$. However, the effect of surface tension is still to keep the interface as flat as possible, and the interface does not drop back to the $z = 0$ plane as near to the centerline as for the $Ca = 1$ case. As a consequence, the volume of fluid entrained

with the sphere for $Ca = 10^{-1}$ is somewhat larger during this period ($l = 0$ to -3) than for $Ca = 1$ (as is the drag ratio). From $l = 0$ to -3, a transition is also beginning from one low energy configuration to another. Through $l = -3$, surface tension acts to broaden the deformation in order to reduce the interfacial area. After this point, however, the deformation is great enough that the interface begins to move rapidly toward the other low energy shape of an encapsulated sphere with the tail pinched off at the rear. Unlike the case presented earlier in which both Ca and Cg were 10^{-1}, the primary mechanism driving the constriction in the present case is capillary forces, and it can be seen by comparison of Figs. 9 and 13 that the drainage occurs less rapidly. Nevertheless, drainage for $Ca = 10^{-1}$, $Cg = 1$ does occur faster than for the $Ca = Cg = 1$ case, with 40% of the entrained volume being lost between $l = -4$ and -5 for the former case, and only 50% from $l = -4$ to -8 in the latter. The rapid change from one low-energy configuration to another causes a rapid "pinching" of the interface in the tail region so that the likely cause of breakthrough for cases like Figs. 9 and 13 with $Ca = 10^{-1}$ would seem to be "pinch off" in which the thickness of the tail goes to "zero", rather than the growth of a hydrodynamic instability in the tail as seems likely for $\lambda = 1$, $Ca = 1$, $Ca = 1$.

The final constant velocity case we present is for $\lambda = 1$, $Ca = 1$, $Cg = 10^{-1}$. This is a case where the role of the density difference between the two fluids dominates over that of the viscosity ratio or surface tension. Figure 14 presents the interface shapes calculated for this system. The most noticeable feature of these shapes is that without surface tension to broaden the deformation, the interface falls back to the $z = 0$ plane relatively near the centerline. In most cases, the interface is flat beyond $r = 1.5$. Also, although the magnitude of the drag ratio for this case is comparable to that for $\lambda = 1$, $Ca = 10^{-1}$, $Cg = 1$ (Fig. 15); consistent with the results of the macroscopic balance (Eq. 30), the volume of fluid carried across the $z = 0$ plane is an order of magnitude smaller for the $Cg = 10^{-1}$ case. A noticeable

difference in the drag ratio for the case $Cg = 10^{-1}$, $Ca = 1$ relative to the other two cases shown in Fig. 15 is that the drag ratio appears to be leveling off after $l = -3$, while the drag continues to decrease for the other two cases. This difference is attributable to the different mechanisms causing fluid to drain from the region behind the sphere. In the case where the density difference between the two fluids is the dominant driving force for drainage, the particle is almost entirely encapsulated and this combined body of a sphere and fluid film is moving as a single unit. This conclusion is supported not only by the interface shapes of Fig. 14, but also by the u_z and u_r values calculated for the interface in the encapsulated region. Behind the sphere, the fluid column is apparently no longer being supported by the viscous forces and so does not contribute to the drag on the sphere. In this case, C_D levels off near the value for an isolated sphere-film combination moving through fluid I. In the cases where surface tension is the major cause of drainage (Fig. 13), or is equal in importance to the density difference (Fig. 9), a significant force is being exerted on fluid II at the interface. In the film region in front of the sphere, the force due to surface tension acts in the direction opposite to sphere motion as the inward normal has a downward pointing z-component. After the sphere begins to become encapsulated, part of the interface near the sphere has an inward pointing normal whose z component is in the same direction as the sphere's motion, and in this region the z component of the normal force due to interfacial tension will be directed along the line of sphere motion thereby lowering the drag. As the area of the interface with upward pointing z component of n is growing (unlike the film region which has a downward pointing component of the normal but is stable in size), the net effect is for the drag on the sphere resulting from interfacial tension to decrease with time as the pinching continues. Since the pinching process will not stop until the sphere is entirely encapsulated and, as shown above, the drag following from the density difference levels off, the drag ratio continues to decrease

for these two cases.

The results of this section provide definite evidence of a "tailing" configuration as the sphere passes across the plane of the undisturbed interface. The dynamics of the layer of fluid immediately adjacent to the sphere appears to be dominated by viscous forces, with gravitational forces also playing a role, but to be only weakly influenced by interfacial tension forces. The dynamics of the tail, on the other hand, appear to be more strongly influenced by interfacial tension forces, these tending to pinch off the tail as the system is eventually driven toward a second minimum free energy configuration in which the sphere is surrounded by a thin fluid layer of constant thickness and the interface reverts to a flat, undeformed configuration. In the next two sections we explore the effects of motion under the action of a constant force, rather than motion at constant velocity as in this section, and also consider the influence of the initial configuration for values $l_o < 3$.

V. Results for Motion from a Large Distance Due to a Constant Body Force on the Sphere

In this section, we describe our results for the case of motion under the action of a constant external body force. Our goals are twofold. First, we wish to determine whether the conclusions of the preceding section, relating to the roles of λ, Ca and Cg in controlling the shape of the interface, carry over from the constant velocity to the constant force problem. Also, we are concerned with the conditions for the establishment of the tailing and film drainage configurations. Unlike the constant velocity situation discussed in the previous section, where a tail will necessarily develop provided a large enough force is exerted on the sphere, in the constant force case, either a tailing mode or film drainage behavior might result. The constant force problem is fundamentally different from the earlier case in that here the ve-

locity decreases as the sphere approaches the interface hence Ca and Cg decrease effectively as well. It is possible that the particle force is not great enough at these lower velocities to carry it across the plane $z = 0$ and form a tail with the result being that film draining is the exhibited mode of breakthrough. Finally, we wish to compare the results of our numerical solutions against those of earlier theories and experiments. To accomplish the latter goal, two calculations were carried out corresponding to published experimental runs. One was for a case which experimentally exhibited film drainage, the other where a tail configuration was reported.

Before proceeding to discuss numerical results, however, we note that it can be shown without use of a numerical procedure that only one mode of deformation is possible for a certain subclass of the constant force problem. In particular, in cases where the force responsible for sphere motion is buoyancy-induced, film-drainage is the only possible configuration when the particle density is intermediate between the densities of the two fluids. This result is demonstrated easily by showing that any configuration in which the particle passes beyond the plane of the initial flat interface, is inconsistent with a macroscopic "equilibrium" force balance when the sphere density is between that of the two fluids. The details of this calculation are shown in the Appendix. The condition of an intermediate sphere density is satisfied whenever $Cg < 2/9$. The fact that no inconsistency arises for sphere densities which are not intermediate to the two fluids (i.e., for $Cg > 2/9$) does not, of course, prove that a tailing configuration will actually arise in a dynamical calculation (or experiment). It shows only that such a configuration is possible.

We consider one case for which the macroscopic balance predicts film drainage, i.e., $Cg < 2/9$. This is for the set of parameters $\lambda = 0.022$, $Ca = 0.464$, $Cg = 0.089$. These parameters correspond to an aluminum sphere falling through golden syrup toward liquid parafin, the system used in Hartland's (1969) experiments. The associated Reynold's number for this system is 0.003. A feature predicted in the

film drainage theories for this case is the pinch point described by Hartland (1969) and given a physical explanation by Jones and Wilson (1978). Calculated interface shapes for the sphere starting at $l_o = 3.0$ are shown in Fig. 16. The mode of interface deformation is clearly film drainage. Fig. 17 is an enlargement of the film region showing the pinching of the interface as predicted by Jones and Wilson (1978). Also shown are the results from Hartland's (1969) experiments. Although the calculated shapes are qualitatively close to the measured interface positions, the quantitative agreement is not particularly good. We feel that this is most likely a manifestation of different initial configurations in the two cases. The initial condition for the numerical work has already been discussed. The sphere is placed with its center 3 radii away from a flat interface and released subject to the condition of a constant applied force. Hartland is less clear about his initial conditions. In fact, the only evidence given is the interface shape for $t = 1.89$. For the case $l_o = 3$, calculated numerically, it takes a time of 5.50 to reach a film thickness at the center line corresponding to this measured interface shape. From this, we conclude that the experimental run by Hartland started with the sphere closer to the interface than $l_o = 3$, but we cannot be sure exactly where the experiment did start.

We now consider the more interesting cases ($Cg > 2/9$) where a tailing configuration is possible and address the question of when tails actually occur. For the case of the sphere moving with constant velocity, U, the parameters Ca and Cg are defined in terms of U. In the present situation, however, the velocity of the sphere does not have a fixed value but changes with position. An appropriate characteristic velocity scale for dimensional analysis (cf. Eqs. 2-8) is the Stokes velocity for motion of the sphere under the same force in an unbounded fluid (i.e., sufficiently far from the interface). Values of Ca and Cg defined in terms of this velocity are then used to compare results with the constant velocity case for the same values of Ca and Cg. However, the actual instantaneous sphere velocity varies with position,

as already noted, and is generally less than the Stokes velocity. Thus, the values of Ca and Cg defined in terms of the Stokes velocity overestimate the magnitude of viscous forces relative to capillary or gravitational (buoyancy) forces for any given instantaneous position of the sphere. For some purposes, it is therefore useful to consider "effective" values of Ca and Cg (denoted as Ca_{eff} and Cg_{eff}) based on the instantaneous sphere velocity. The differences between characteristic values of Ca and Cg, and their "effective" or instantaneous values, Ca_{eff} and Cg_{eff}, are important in understanding the difference between motion at a constant velocity and motion with a constant applied force. Fig. 18 shows the interface shape for $\lambda = 1$, $Ca = Cg = 1$ and $l_o = 3$ with a constant applied force on the sphere, while the instantaneous sphere velocity is plotted in Fig. 19. It is evident that the sphere velocity is strongly decreased in the presence of the interface when moving under the action of a constant force. Thus, the deformation at any point in time is less than in the corresponding constant velocity case, as may be seen by comparing Figs. 5 and 18.

However, there is no question that the deformation process (and thus, presumably, time to breakthrough) will be much longer for a given value of Ca and Cg in the constant force problem. What is in doubt is the mode of deformation and ultimately breakthrough. For the purpose of answering this question and providing a more meaningful comparison of the constant force and constant velocity cases, interface shapes should be compared at the same positions of the sphere relative to the plane of the undeformed interface rather than at equal increments of time. Furthermore, based on the reduction in sphere velocity shown in Fig. 19, the instantaneous or effective values of Ca and Cg in the case $\lambda = 1$, $Ca = 1$, $Cg = 1$ range between initial values of $Ca = Ca_{eff}$, $Cg = Cg_{eff} = 1$, and minimum values $Ca_{eff} = Cg_{eff} = 0.09$ at $t \approx 15$. Thus, one might expect to find interface shapes which lie somewhere between the constant velocity case $\lambda = 1$, $Ca = 1$, $Cg = 1$

and $\lambda = 1$, $Ca = 10^{-1}$, $Cg = 10^{-1}$ that were shown in Figs. 5 and 9, respectively. Comparison of Figs. 5, 9 and 18 shows that this is, indeed, the case. Compared with the interface shape at the same sphere position for the constant velocity problem with $Ca = Cg = 1$, it is evident that the "film" is initially thinner in the constant force solution, but that there is a stronger tendency later in the deformation process for the short "tail" behind the sphere to pinch off to produce a film of constant thickness over the majority of the sphere surface. Although this latter behavior is strongly reminiscent of the constant velocity case with $Ca = Cg = 0.1$ (Fig. 9), the "film" thickness is considerably larger in the constant force problem reflecting the relatively small forces resisting deformation at earlier times in the process when Ca_{eff} and Cg_{eff} are larger than 0.1. Although calculations for $t > 15$ were not carried out, it appears very likely on the basis of comparison with the constant velocity problem that the mode of breakthrough will be "pinching off" of the fluid tail behind the sphere.

Additional evidence for the existence of "tailing" modes of interface deformation in the case of sphere motion with a constant applied force will be presented shortly. It is apparent, however, that the rapid decrease in Ca_{eff} and Cg_{eff} which occurs as the sphere slows down does lead to much shorter tails for given values of Ca and Cg than occured in the constant velocity problem. The possiblity exists that a given set of parameters which gave a high drag ratio and a broad tail behind the sphere for constant velocity could yield a film drainage configuration in the constant force case even for $Cg > 2/9$.

Fig. 20 shows the interface configuration for the constant force problem with $Ca = Cg = 1$, $\lambda = 10$, a case which did give a broad tailing configuration in the constant velocity case. The sphere velocity is plotted against time in Fig. 21. Comparing Figs. 20 and 7 one sees that the broad tail of the constant velocity plot has become a film drainage configuration in the constant force problem. At $t = 33$,

the sphere velocity has dropped to 0.04 of the corresponding Stokes' velocity, and thus $Ca_{eff} = Cg_{eff} = 0.04$. With such large restoring forces *relative* to the viscous forces, further deformation is difficult so one expects the remaining fluid to merely drain away between the sphere and the interface.

Maru *et al.* previously attempted to develop an "a priori" criteria for existence of a tailing configuration. The existence of serious shortcomings in this work have been mentioned in an earlier section. Here, comparison of present results for the various values of λ points to one of the problems with their work and all others who use a quasi-static force balance to calculate sphere and interface motion. By failing to consider the shear stress on the surface of the interface, these authors do not have any way of judging the time scale of sphere motion relative to drainage of the film, and so cannot differentiate between systems with different viscosity ratios. In effect, they assume a film drainage configuration as the initial condition and neglect the interface beyond the point where it begins to break-away from the sphere. Fig. 18 shows that the film region is established early and remains essentially the same after $t = 8$ for $l_o = 3$; whereas, the interface in the break-away region continues to deform creating a tail configuration. For the large viscosity ratio case and the same values of Ca and Cg, the film again is essentially formed at $t = 8$ but the interface past $r = 1.5$ shows much less deformation. As a consequence of their analysis, Maru, Wasan and Kintner (1971) predict that film drainage will never be observed for $Ca = Cg = 1$, while our results give strong indications to the contrary depending upon the viscosity ratio, λ.

The results of the constant force cases described above demonstrate how the qualitative nature of the interface deformation changes relative to the constant velocity case. In both of the constant force cases examined so far for $Cg > 2/9$, the dramatic decrease in sphere velocity (and thus of Ca and Cg) results in the absence of long slender tails behind the sphere as were found in the case of constant

velocity. To determine whether such a configuration is possible or if the deceleration of the sphere will always prohibit the formation a long tail in creeping flow, a set of calculations was run duplicating an experiment of Maru, Wasan and Kintner which produced a long tail behind the sphere, albeit at finite Reynolds number. Using a 3 mm. glass sphere falling through cyclohexanol with a 62.5% glycerine-water solution as the fluid 1 phase, Maru *et al.* observed a tail which reached a length of 120 sphere radii before exhibiting significant disturbances on its surface. The parameters of this system are $\lambda = 0.434$, $Ca = 3.83$, $Cg = 1.97$; the Reynolds number is 15.19. With such a large Reynolds number, inertial effects are certainly not negligible, and it is by no means obvious that a long slender tail should be expected in the creeping flow regime. However, Fig. 22 shows the calculated interface shapes versus position for this case and a long thin tail has very definitely developed. Fig. 23 shows how the sphere velocity changes with position. Note that a minimum is observed at $l = -2.0$ (i.e., at $t = 7.5$), which is related to the maximum found in the drag coefficient for motion for constant velocity. As the sphere becomes more encapsulated under the effect of surface tension, the velocity increases, eventually going above 1.00, the value in an unbounded region of fluid 2. The sphere would have a velocity of 2.304 in an unbounded domain of fluid 1, but this velocity will never be achieved until breakthrough as the surrounding fluid 2 increases the density of the composite body above that of the sphere alone. The results of this calculation confirm the existence of a long slender tail for the case of a sphere moving under a constant bouyancy force. The comparison with published results can be of only a qualitative nature as no quantitative data on the interface shapes or sphere velocity were given by Maru *et al.* (1971).

As a further demonstration of the existence of tails in the constant force problem, results for the case $\lambda = 1$, $Ca = 1$, $Cg = 10$ are presented in Fig. 24. This case again shows the definitive formation of a relatively long, slender tail. The ve-

locity as a function of position is included in Fig. 23. At the minimum point, the velocity is approximately 0.4 times the Stokes' velocity. Thus, Ca_{eff} and Cg_{eff} span the ranges 0.2-1 and 2-10, respectively. The nearest constant velocity case would thus appear to be $\lambda = 1$, $Ca = Cg = 1$ and $\lambda = 1$, $Ca = 10^{-1}$, $Cg = 1$. Indeed, the interface shows many characteristics of the constant velocity results for the latter case. The broad deformation and surface tension driven constriction are both features which reappear in the constant force result. The rapid constriction of the tail which occured in the constant velocity problem, however, is not present here. As the sphere continues past $l = -3$ and begins to accelerate, the interface behaves more like the $\lambda = 1$, $Ca = 1$, $Cg = 1$ constant velocity case. For this set of parameters, the surface tension force driving constriction is decreased and this is reflected by the deceleration of pinching in the tail after $t = 13$. Also, the increased viscous force is able to support the fluid in the tail.

The most interesting comparison, however, is with the results shown earlier for motion with a constant force at $\lambda = 1$, $Ca = Cg = 1$. The increase in Cg from 1 to 10 means that the effect of body forces on interface deformation should be relatively unimportant compared to capillary forces in the case $\lambda = 1$, $Ca = 1$, $Cg = 10$, and the comparison with $\lambda = 1$, $Ca = Cg = 1$ further allows us to observe the way in which interfacial tension and density differences influence deformation. Comparing the results of Figs. 18 and 24, the chief difference at early times when the sphere velocity is not too strongly influenced by the interface (so that the Ca_{eff} values are similar) is that the deformation produced is broader in the case $Cg = 10$. This is a consequence of the fact that the smaller density difference in this case yields less resistance to the tendency of interfacial tension to produce a broad, flat deformation — i.e., the system, all else being equal can support a larger volume of fluid II across the $z = 0$ plane when Cg is increased.

As the sphere continues to move, an increasing volume of the heavy fluid is

carried across the $z = 0$ plane until finally, the force applied from the sphere can no longer support such a large volume of fluid, drainage accelerates and a tail configuration results. Obviously, for larger Cg values, a larger volume of fluid can be supported and this clearly reflected in comparing results from Figs. 18 and 24, though comparison is difficult due, in part, to the fact that the changes in sphere velocity are different in the two cases. As was true for the constant velocity systems, once the tail configuration appears, the role of interfacial tension changes from one of tending to preserve the flat interface to one of minimizing the surface area in the tail region by producing a spherical shell around the sphere with the tail pinched off. This is demonstrated dramatically in the $\lambda = 1$, $Ca = 1$, $Cg = 1$ results where the significantly lower value of Ca_{eff} from the case of Fig. 24 (0.1 vs. 0.4) causes a much more rapid pinching of the fluid in the tail region.

VI. Effect of Sphere Starting Position

Previously, we have discussed the effect of starting positions greater than or equal to three sphere radii from the undeformed interface. These results were presented to show that if one is interested in the behavior of the sphere-interface system some time after the sphere begins to approach the interface, results for all calculations begun at a distance greater than $l_o = 3$ will appear identical. Here, we discuss another aspect of the initial starting point question: the effect of starting the sphere very close to the flat interface. Two groups of calculations have been carried out. In the first, a series of cases were run in which the sphere center was initially 1.2 radii from a flat interface. In the second, initial starting positions were chosen so that the minimum initial gap between the sphere and a flat interface was comparable to the film thickness at large times when the initial position was $l_o \rightarrow 3$. These second calculations were done only for sets of parameters which displayed tailing

with a fairly stable film thickness in front of the sphere when started with $l_o = 3.0$. This type of calculation more closely duplicates the experiments described in the Introduction where a drop was brought close to an interface and then released, and may reveal cases where the starting position causes a change from the tailing configuration to one of film drainage (as was observed in all of the experiments other than Maru *et al.*, 1971).

(a) Initial Starting Position, $l_o = 1.2$.

Calculations with starting positions $l_o = 1.2$ were performed for several cases. These included for constant velocity $\lambda = 1$, $Ca = Cg = 0.10$, a tailing case; and the constant force cases $\lambda = 1$, $Ca = Cg = 0.10$, and $\lambda = 0.022$, $Ca = 0.465$, $Cg = 0.089$ which represent a tailing and a film drainage configuration, respectively. In all of these cases, the calculated values for the velocities, stress and position of the interface at some value of l came to within 1% of the values calculated when the initial position was 3.0. When this occurred, the calculations were stopped. The quasi-steady assumption made in deriving Eqs. (13)-(16) insures that for a given set of parameters, only the current position of the sphere and interface influence the future behavior of the system; the prior history of the calculation will thus influence future results only through its effect on the current interface shape and sphere position. Therefore, when the positions of the sphere and interface in the $l_o = 1.2$ calculation are the same as in the $l_o = 3.0$ case, all future results will be identical as well. Fig. 25 shows the $l_o = 1.2$ results for $\lambda = 1$ $Ca = Cg = 0.10$ with a constant sphere velocity, and this may be compared to Fig. 9 which gives results for the same λ, Ca and Cg values, but $l_o = 3.0$. The specific time it takes for the $l_o = 1.2$ and $l_o = 3.0$ interface shapes to become equal depends on the dimensionless parameters of the system; however, these results demonstrate that no change in the mechanism of breakthrough occurs when an initial gap thickness of 0.2 is used rather than 2.0 corresponding to the $l_o = 3.0$ calculations.

(b) Initial Position, l_o, Corresponding to the Thickness of the Film at Large Deformation.

This calculation differs significantly from all those discussed previously. In all the cases presented to this point, film and tail formation first occurred simultaneously, then film drainage took place as the tail lengthened and narrowed. The present situation is one in which a thin film is present from the onset of the calculation, whereas the tail still must be formed from the flat interface. The implication of this in the constant velocity problem is that the sphere may move across the interface before a tail has time to form. In the case of constant applied force, the probability of this happening is enhanced by the fact that the small gap between the sphere and interface will produce high velocity gradients right from the beginning of the calculation and so a large contribution to the drag on the sphere. This results in a lower initial sphere velocity and a corresponding decrease in the effective values of Ca and Cg. Small values for Ca_{eff} and Cg_{eff} tend to inhibit deformation of the flat interface and result in film drainage for breakthrough.

The constant velocity case chosen was $\lambda = 1.0$ $Ca = Cg = 0.10$. For $l_o = 3.0$, this case displays a short, pinched tail and narrow film surrounding the sphere. The fact that the tail is short suggests that tail formation is likely to be suppressed in going to the close starting position. The thickness of the film after formation of the tail remains relatively constant at 0.05 and this was the separation between the sphere and interface at the start of the calculation, i.e., $l_o = 1.05$. Comparing Figs. 9, 25 and 26 for $l_o = 3$, 1.2 and 1.05, respectively, it can be seen that the interface shapes are fairly similar; however, in the $l_o = 1.05$ case, calculations would simply not converge much past $l = 0.0$, i.e., the sphere straddling the interface, in spite of the fact that the convergence had been achieved in other cases with even thinner films between the sphere and interface. It is possible that no solution exists beyond the point of convergence for this case with $l_o = 1.05$. In this case, the

change in starting position of the sphere would have caused a change in the mode of breakthrough for $\lambda = 1$, $Ca = Cg = 0.1$. However, the solution technique utilized here does not allow a definitive case that the lack of convergence is not simply a failure of the numerics.

For a constant force problem, the case of $\lambda = 1$ $Ca = 1$ $Cg = 10$ was run with $l_o = 1.10$ corresponding to the film thickness seen in the $l_o = 3.0$ result. The results of this calculation are shown in Fig. 27. One sees that the two cases agree in the film region but the results for $l_o = 1.1$ show a narrower tail than for the $l_o = 3.0$ result. Also, although a tail is formed, the total deformation of the interface in the $l_o = 1.10$ case is much less than for the large starting distance. That is, the interface for $l_o = 1.10$ lies below that for $l_o = 3.0$ at equal sphere positions. The result of starting from $l_o = 1.10$ is that tailing is enhanced in the constant force case and so rather than changing the mode of breakthrough, the close starting positions hastens breakthrough in the existing mode.

The effect of starting the sphere close to the interface may be summarized by saying that the initial conditions influence the deformation for some time after the calculation is begun. For the case when $l_o = 1.2$, the departure of the calculation from the $l_o = 3.0$ result diminishes with time until the results are identical. For a starting position corresponding to the film thickness after a tail has been established, the departure from the $l_o = 3.0$ result may be significant enough to cause a change in the breakthrough for the constant velocity case $\lambda = 1$ $Ca = Cg = 0.10$ and does cause a departure in the interface shape for the constant force case $\lambda = 1$ $Ca = 1$ $Ca = 10$ for a long time after the calculation is started.

VII. CONCLUSIONS

We have used the boundary-integral technique to numerically study the creep-

ing axisymmetric motion of a sphere normal to an initially flat fluid-fluid interface under the constraint that the sphere moves either with a constant velocity or under the action of a constant buoyancy force.

Our calculations show the existence of two distinct modes of interface deformation for the constant force problem which we have designated as film draining and tailing. The parameters controlling which mode will occur are Ca and Cg, reflecting the relative magnitudes of the interfacial tension and the density difference between the two fluid phases; the forces associated with these two properties tend to maintain the interface in its initially flat configuration. Thus, when these restoring forces are large relative to the viscous forces generated by the motion of the sphere, i.e., Ca, $Cg << 1$, film drainage behavior occurs. When the inverse is true, i.e., Ca, Cg approximately order 0.1 or greater, a tailing configuration appears. A further statement about the possibility of tailing for the constant buoyancy force case can be made: no tails can occur when the density of the sphere is intermediate to those of the two fluids.

A significant difference in the behavior of the constant force and constant velocity problems is the shortening of the tails in the former case for moderate Ca and Cg. This follows from the decrease of the instantaneous effective deforming forces as the sphere approaches the interface. As the sphere comes closer to the interface, its velocity decreases, thereby increasing the strength of interfacial tension and density body forces due to the density difference relative to viscous forces. The increased relative strength of the restoring forces makes further deformation more difficult, with the final outcome being the suppressed extension of the tail and more film drainage occurring between the sphere and interface. The viscosity ratio acts not to restore the interface to its initial flat shape, but controls the rate at which fluid drains from the space between the sphere and interface.

Comparison of our results with published experimental data was carried out

with fair agreement. These differences which do exist are believed to be a consequence of differences in the initial conditions used, but as the experimental descriptions did not state these initial conditions, this area cannot be explored presently. Calculations using small interface-sphere separations showed that changes in initial conditions could significantly influence results, especially at early times.

Appendix

Macroscopic Force Balance for a Sphere Several Radii

Beyond an Initially Undeformed Interface

To prove that a sphere moving under a constant body force cannot cross the plane of the initially undeformed interface when the body force is gravity alone, a macroscopic force balance is carried out for a sphere which is assumed to have crossed the plane $z = 0$, carrying a body of fluid II with it in the form of a film plus tail. We shall see that a contradiction is reached in this balance if the density of the sphere is between that of the two fluids, thus showing that a configuration of the tailing type is impossible for this case.

We begin by stating the force balance for the sphere alone

$$F_{ext} - \rho_s g V_s - \int_{S_p} (\mathbf{T}_2 \cdot \mathbf{n}) \cdot \mathbf{k} \, \partial S_p + \rho_2 g V_s = 0 \qquad (A1)$$

where ρ_2 is the density of the fluid in which the sphere is immersed.

$\mathbf{T}_2$ is the dynamic stress tensor in fluid 2 (i.e., the total stress minus hydrostatic pressure contributions).

$\mathbf{n}$ is the outer unit normal to the sphere.

$\mathbf{k}$ is a unit normal in the vertical (z) direction.

S_p is the volume of the sphere,$(4/3)\pi a^3$.

F_{ext} is any external force on the sphere in addition to gravity.

A similar balance on the fluid region ("control volume") marked inside the dashed lines of Fig. A1 gives

$$\rho_1 g V_t - \rho_2 g V_t + \int_{S_p} (\mathbf{T}_2 \cdot \mathbf{n}) \cdot \mathbf{k} \partial S_p - \rho_2 g V_s + \int_{S_I} (\mathbf{T}_1 \cdot \mathbf{n}) \cdot \mathbf{k} \partial S_I = 0 \qquad (A2)$$

where

v_f is the volume of fluid 2 in the tail + film region inside the dashed lines of Fig. 4.

V_t is the sum of v_f and v_s.

$\mathbf{T}_1$ is the dynamic stress tensor in fluid 1.

S_I is the portion of the surface of the control volume defined by the interface between fluids 1 and 2.

S^* is the portion of the surface of the control volume which is coincident with the initial plane of the interface.

If we neglect the contribution due to $\mathbf{T}_2$ at S^*,† and assume $\lambda = 0$ so that $\int_{S_I}(\mathbf{T}_1 \cdot \mathbf{n}) \cdot \mathbf{k}\, \partial S_I = 0$, the balance Eqs. (1) and (2) can be combined to yield

$$\frac{V_t}{v_s} = \frac{\rho_2 - \rho_s}{\rho_2 - \rho_1} + \frac{F_{ext}}{g(\rho_2 - \rho_1)V_s} \qquad (A3)$$

We consider the case $F_{ext} = 0$ in which the only "external" force on the sphere is due to buoyancy. Now, it is obvious that $V_t/V_s > 1$. On the other hand, $(\rho_2 - \rho_s)/(\rho_2 - \rho_1) < 1$ unless $\rho_s < \rho_1$. Hence, we conclude that the configuration represented by Fig. A1 is impossible unless $\rho_s < \rho_1$. No such inconsistency arises if we apply the same force balance concepts to a film drainage configuration with $\rho_1 < \rho_2$. The presence of viscosity in fluid I, $\lambda \neq 0$, would act to slow the drainage of the fluid in the tail, but could not provide a force to actually overcome gravity. Therefore, the conclusions from Eq. (A3) would hold even for a viscous fluid I.

---

† The mass flux at S^* is seen to be small after calculating the change in tail volume with time. Furthermore, the velocity and velocity gradients in this region are also small.

References

Berdan II, C. 1982 Ph D. Dissertation California Institute of Technology.

Berdan II, C. and Leal L. G. 1982 Motion of a sphere in the presence of a deformable interface. Part 3: Numerical study of the translation of a sphere parallel to an interface. *J. Coll. and Interface Sci.* **87**, 62.

Chin, H. B. and Han, C. D., 1979, Studies on droplet deformation and breakup. I. Droplet deformation in extensional flow. *J. Rheol.* **23**, 557.

Geller, A. S. 1986 Ph.D. Dissertation, California Institute of Technology.

Geller, A. S., Berdan II, C. and Leal, L. G. 1986 An experimental study of the motion of a sphere normal to a deformable fluid-fluid interface. In preparation.

Grace, H. P., 1971, Eng. Foundation 3rd Res. Conf. on Mixing, Andover, N.H.

Hartland, S. 1968 The approach of a rigid sphere to a deformable liquid/liquid interface *J. Coll. and Interface Sci.* **26**, 383.

Hartland, S. 1969 The profile of a draining film between a rigid sphere and a deformable fluid-liquid interface. *Chem. Eng. Sci.* **24**, 987.

Jeffreys, G. V. and Davies, G. A. 1971 in *Recent Advances in Liquid/Liquid Extraction* (ed. C. Hanson), p. 495, Pergamon Press.

Johnson, R. E. and Sadhal, S. S. 1985 Fluid mechanics of compound multiphase drops and bubbles. *Ann. Rev. Fluids* **17**, 289.

Jones, A. F. and Wilson, S. D. R. 1978 The film drainage problem in droplet coalescence. *J. Fluid Mech.* **87**, 263.

Kirkpatric, R. D. and Lockett, M.J. 1974 The influence of approach velocity on bubble coalescence. *Chem. Eng. Sci.* **29**, 2363

Lang, S. B. and Wilke, C. R. 1971 A hydrodynamic mechanism for the coalescence of liquid drops. I: Theory of coalescence at a planar interface. *I. and E. C. Fundamentals* **10**, 329.

Ladyzhenskaya, O. A. 1963 *The Mathematical Theory of Viscous Incompressible Flow* . Gordon and Breach, New York.

Leal and Lee 1981 "Proceedings of IUTAM-IUTPAC Symposium on 'Interactions of Particles in Colloid Dispersions'. Canberra, Australia. March 16-21, 1981

Lee, S. H., Chadwick, R. S. and Leal, L. G. 1979 Motion of a sphere in the presence of a plane interface. Part 1: An approximate solution by generalization of the method of Lorentz. *J. Fluid Mech.* **93**, 705.

Lee, S. H. and Leal, L.G. 1980 Motion of a sphere in the presence of a plane interface. Part 2: An exact solution in bipolar coordinates *J. Fluid Mech.* **98**, 193.

Lee, S. H. and Leal, L.G. 1982 Motion of a sphere in the presence of a deformable interface. Part 2: Numerical study of the translation of a sphere normal to an interface. *J. Coll. and Interface Sci.* **87**, 81.

Maru, H. C., Wasan, D. T. and Kintner, R. C. 1971 Behavior of a rigid sphere at a liquid-liquid interface. *Chem. Eng. Sci.* **26**, 1615.

Mikami, T., Cox, R. G. and Mason, S.G. 1975 Breakup of extending liquid threads. *Int. J. of Multiphase Flow* **2**, 113.

Narayaran, S., Gossens, L. H. J. and Kossen, N. W. F. 1974 Coalescence of two bubbles rising in line at low Reynolds number. *Chem. Eng. Sci.* **29**, 2071.

Olbricht, W. L. and Leal, L. G. 1983 The creeping motion of immiscible drops through a converging/diverging tube. *J. Fluid Mech.* **134**, 329.

Princen, H.M. 1963 Shape of a fluid drop at a liquid-liquid interface. *J. Coll. Sci.* **18**, 178.

Rayleigh, Lord, 1892 On the instability of a cylinder of viscous liquid under capillary force. *Phil Mag.* **34**, 145.

Shah, S. T., Wasan, D. T. and Kintner, R. C. 1972 Passage of a liquid drop through a liquid-liquid interface. *Chem. Eng. Sci.* **27**, 881.

Smith, P. G. and Van de Ven, T. G. M. 1984 The effect of gravity on the drainage of a thin liquid film between a solid sphere and a liquid/fluid interface. *J. Coll. Interface Sci.* **100**, 456.

Tomotika, S. 1936 Breaking up of a drop of viscous liquid immersed in another viscous fluid which is extending at a uniform rate. *Proc. Roy. Soc. Lond.* **A153**, 302.

Figure Captions

Figure 1: Schematic sketch of the final stages of phase separation following liquid-liquid extraction between two immiscible liquids.

Figure 2: Film drainage configuration for a sphere at a deformable interface.

Figure 3: (a) Schematic sketch of the system for numerical calculations. (b) The three-function representation of the interface shape.

Figure 4: Sphere velocity as a function of R_0 for the limiting case of slow sphere motion (i.e., $\mathbf{u}^I \cdot \mathbf{n} = 0$). $l = 1,\ 3,\ 5;\ \lambda = 10,\ Ca = Cg = 1$ for the constant force problem ($\times$ results from calculations).

Figure 5: Interface shape as a function of sphere position (drawn in a reference frame in which the sphere is fixed) for $\lambda = 1,\ Ca = 1,\ Cg = 1$; —— shapes for sphere initially at $l_0 = 3$; - - - $l_0 = 5$; - - - - - $l_0 = 10$. Constant velocity case.

Figure 6: Interface shape as a function of sphere position for $\lambda = 0,\ Ca = 1,\ Cg = 1,\ l_o = 3$. Constant velocity case.

Figure 7: Interface shape as a function of sphere position for $\lambda = 10,\ Ca = 1,\ Cg = 1,\ l_o = 3$. Constant velocity case.

Figure 8: Drag ratio versus sphere position for $Ca = Cg = 1,\ \lambda = 0, 1$ and 10: —— numerically calculated values; volume of the tail plus sphere measured from the numerically calculated interface profiles divided by $6\pi a^3$, + $(\lambda = 0)$, $\bigcirc(\lambda = 1)$, $\Delta(\lambda = 10)$.

Figure 9: Interface shape as a function of sphere position for $\lambda = 1,\ Ca = 0.1,\ Cg = 0.1,\ l_o = 3$. Constant velocity case.

Figure 10: Interface shape as a function of sphere position for $\lambda = 1$, $Ca = 10^{-3}$, $Cg = 10^{-3}$, $l_o = 3$. Constant velocity case.

Figure 11: Drag ratio versus sphere position for $Ca = Cg = 1, 0.1, 10^{-3}$, $\lambda = 1$, constant velocity case. Values calculated from Lee and Leal (1980), (0).

Figure 12: Interface shape as a function of sphere position for $\lambda = 1$, $Ca =$ inf, $Cg = 1$, $l_o = 3$. Constant velocity case.

Figure 13: Interface shape as a function of sphere position for $\lambda = 1$, $Ca = 0.1$, $Cg = 1$, $l_0 = 3$. Constant velocity case.

Figure 14: Interface shape as a function of sphere position for $\lambda = 1$, $Ca = 1$, $Cg = 0.1, l_o = 3$. Constant velocity case.

Figure 15: Drag ratio versus sphere position for $\lambda = 1$; $Ca = 1$, $Cg = 0.1$; $Ca = 0.1$, $Cg = 1$; $Ca = Cg = 0.1$.

Figure 16: Interface shape as a function of sphere position for $\lambda = 0.022$, $Ca = 0.465$, $Cg = 0.089, l_o = 3$. Constant force case.

Figure 17: Detail of film region for $\lambda = 0.022$, $Ca = 0.465$, $Cg = 0.089, l_o = 3$: —— numerical calculations, – – – experimental results from Hartland (1969).

Figure 18: Interface shape as a function of sphere position for $\lambda = 1$, $Ca = 1$, $Cg = 1$: —— shapes for sphere initially at $l_o = 3$; – – – $l_o = 5$; - - - $l_o = 10$. Constant force problem.

Figure 19: Velocity as a function of sphere position for $\lambda = 1$, $Ca = 1$, $Cg = 1$: —— $l_o = 3$; – – – $l_o = 5$; - - - $l_o = 10$.

Figure 20: Interface shapes as a function of sphere position for $\lambda = 10$, $Ca = 1$, $Cg = 1$: —— $l_o = 3$; – – – $l_o = 5$; - - - - - $l_o = 10$. Constant force problem.

Figure 21: Velocity as a function of sphere position for $\lambda = 10,\ Ca = 1,\ Cg = 1$: —— $l_o = 3$; – – – $l_o = 5$; - - - - - $l_o = 10$.

Figure 22: Interface shape as a function of sphere position for $\lambda = 0.434,\ Ca = 3.831,\ Cg = 1.972,\ l_o = 3$. Constant force case.

Figure 23: Velocity as a function of sphere position for constant force cases.

Figure 24: Interface shape as a function of sphere position for $\lambda = 1,\ Ca = 1,\ Cg = 10,\ l_o = 3$. Constant force case.

Figure 25: Interface shape as a function of sphere position for $\lambda = 1,\ Ca = Cg = 0.10,\ l_o = 1.2$. Constant velocity case.

Figure 26: Interface shape as a function of sphere position for $\lambda = 1,\ Ca = Cg = 0.10,\ l_o = 1.05$. Constant velocity case.

Figure 27: Interface shape as a function of sphere position for $\lambda = 1,\ Ca = 1,\ Cg = 10, l_o = 1.10$. Constant velocity case.

Figure A1: Schematic sketch of control volume for an overall force balance on the fluid in the tail plus film.

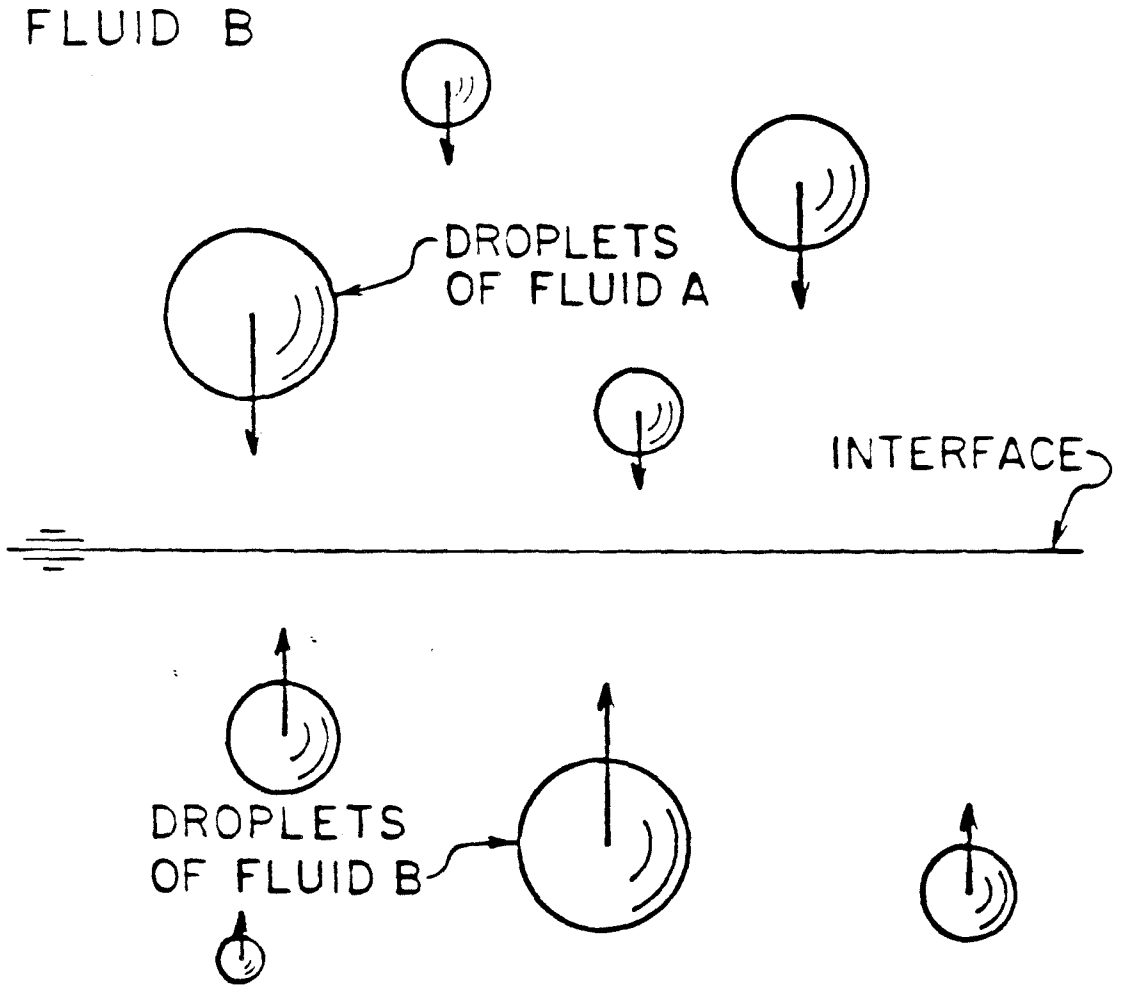
FLUID B
DROPLETS
OF FLUID A
INTERFACE
DROPLETS
OF FLUID B
FLUID A

Figure 1.

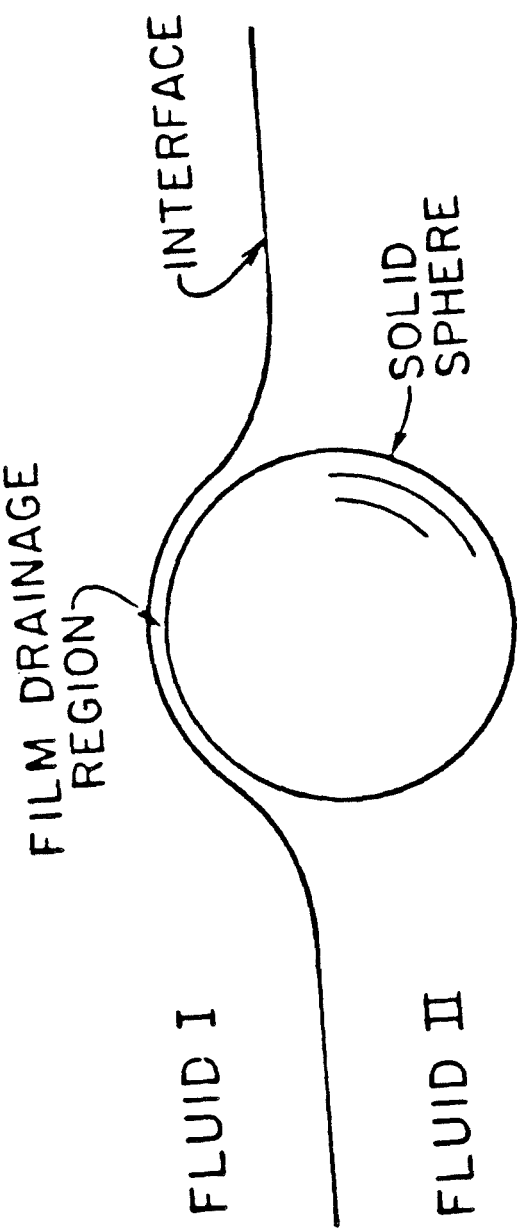
INTERFACE
SOLID SPHERE
FILM DRAINAGE REGION
FLUID I
FLUID II

Figure 2.

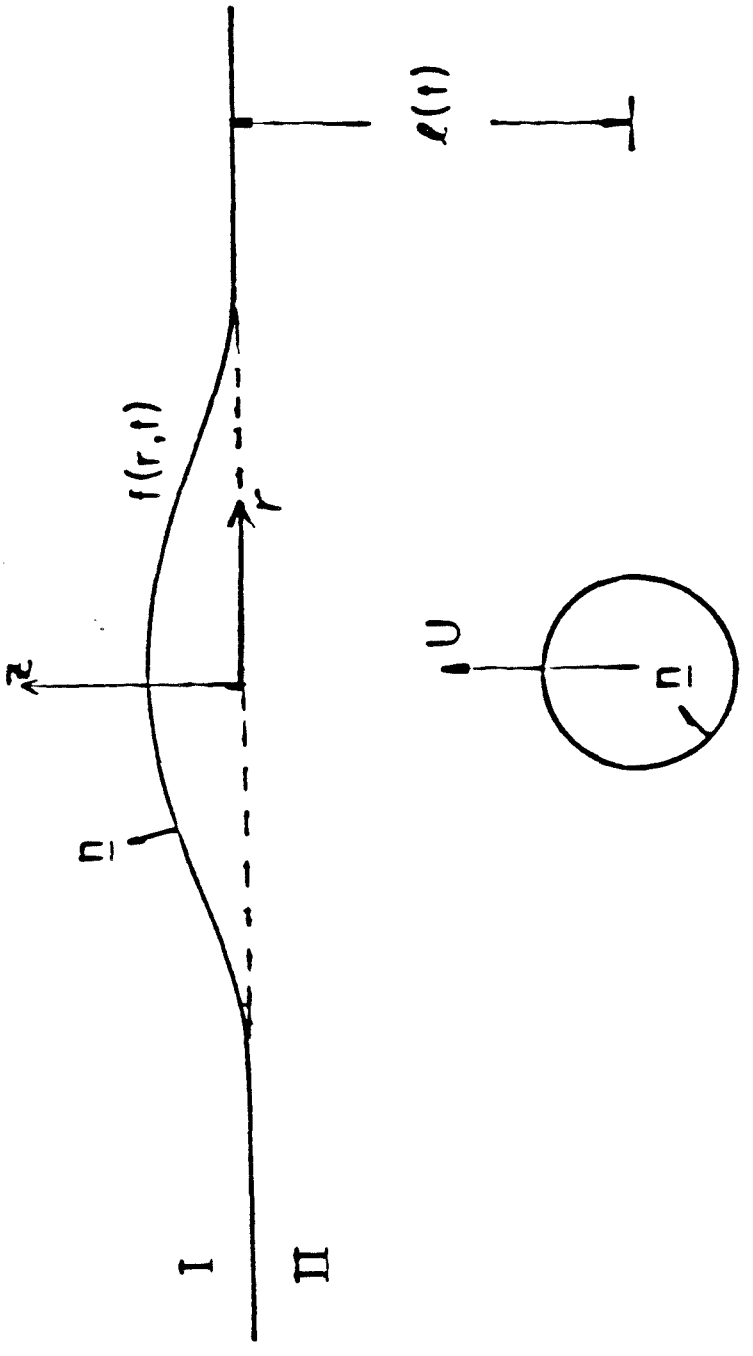

Figure 3a.

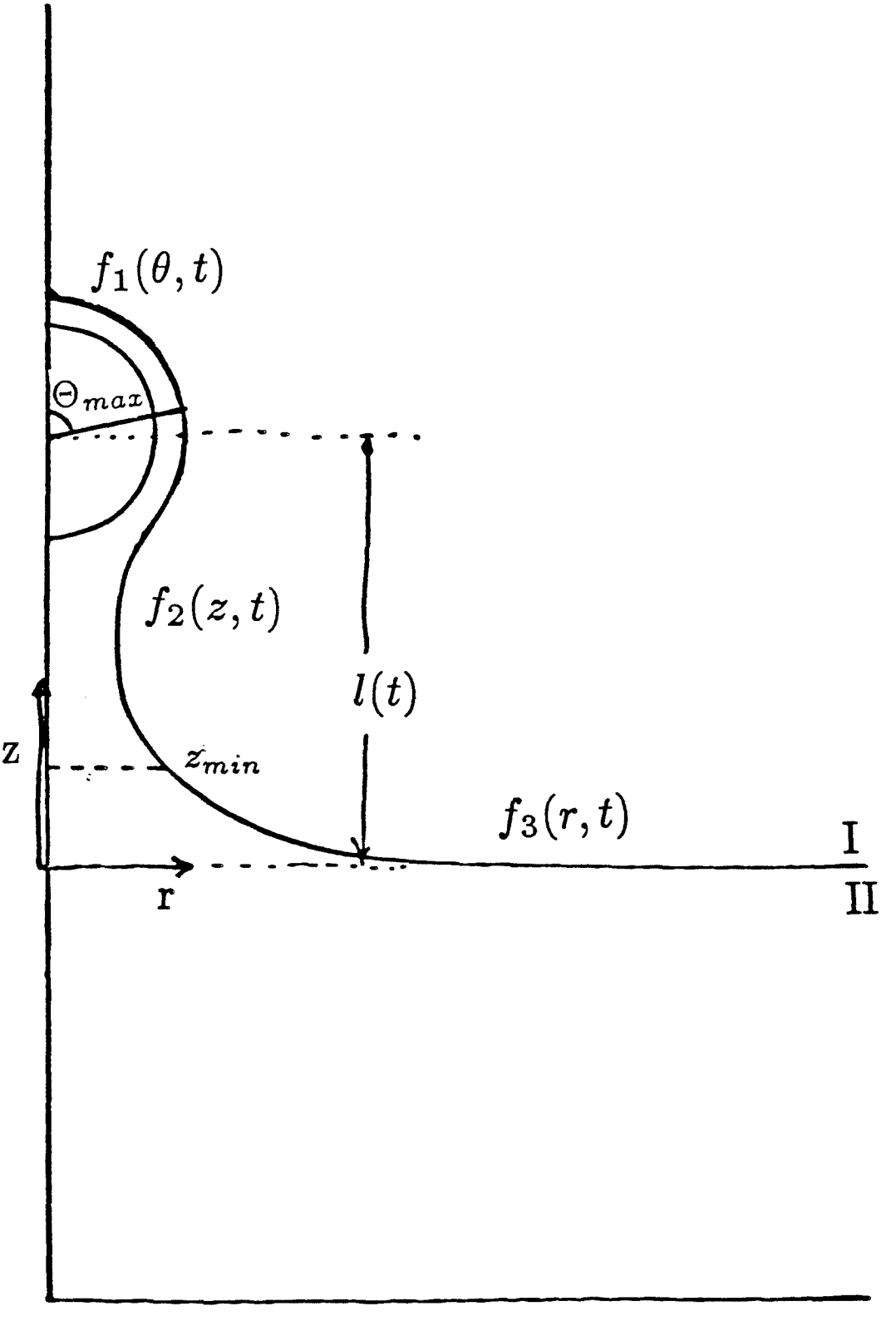

Figure 3b.

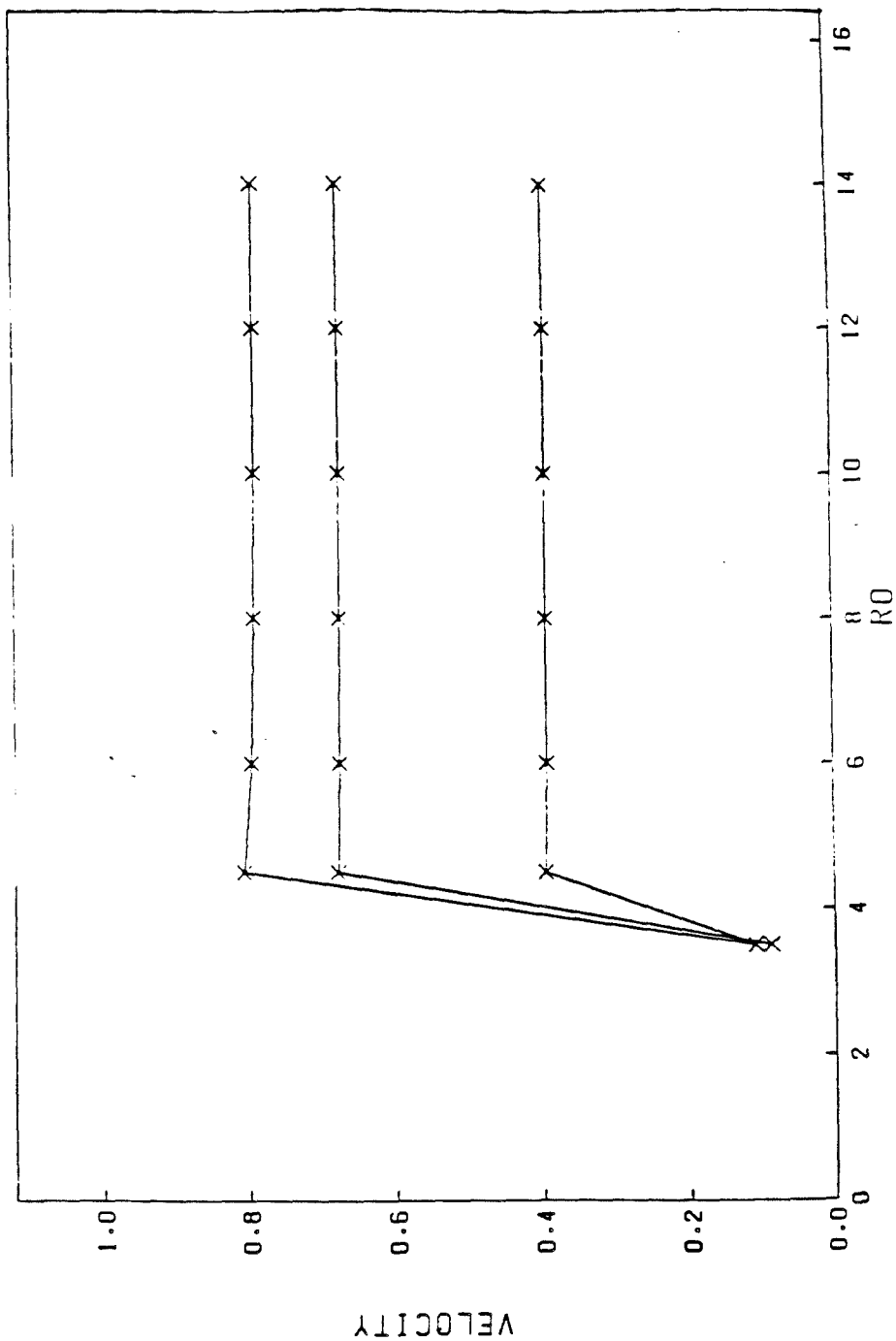

Figure 4.

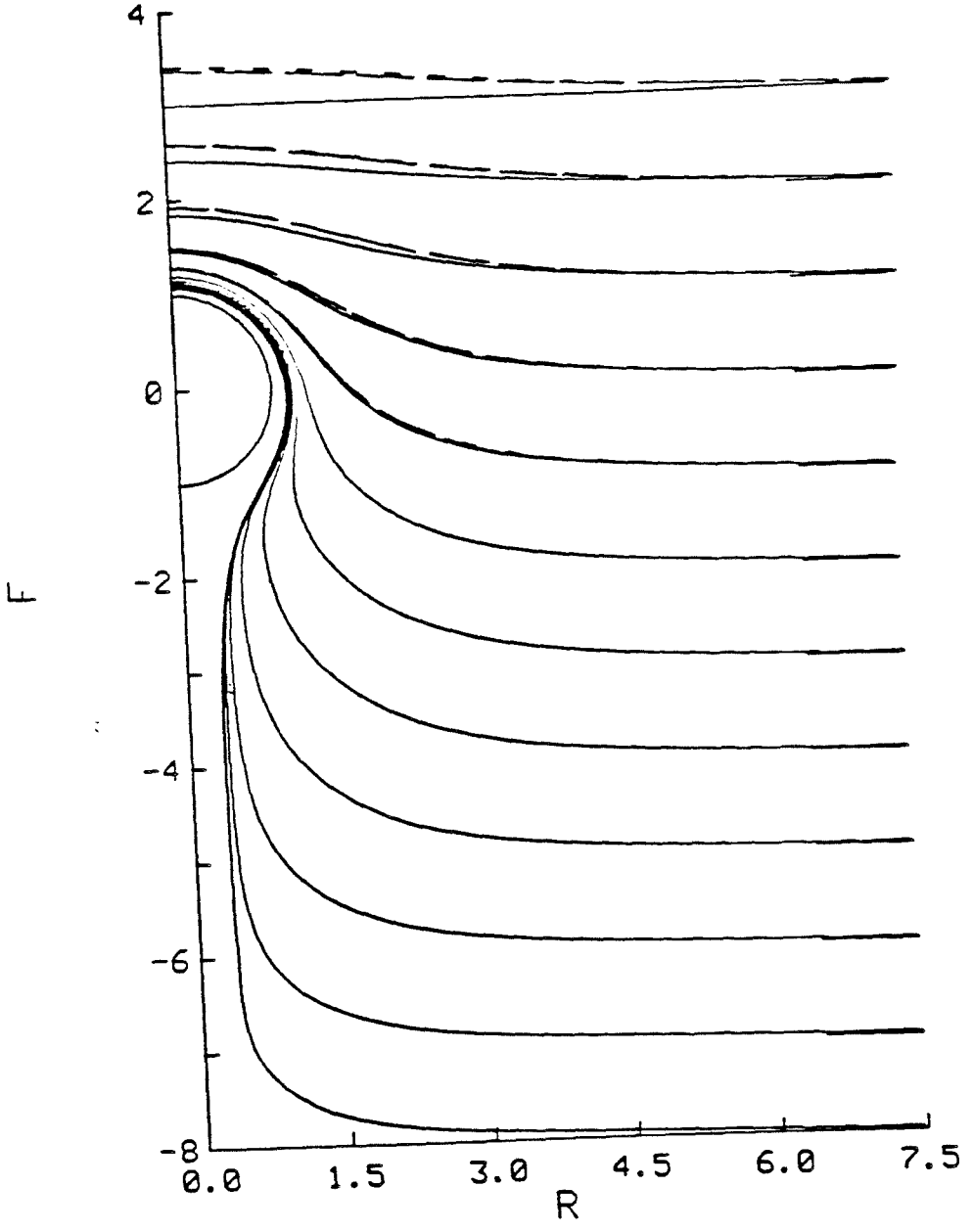

Figure 5.

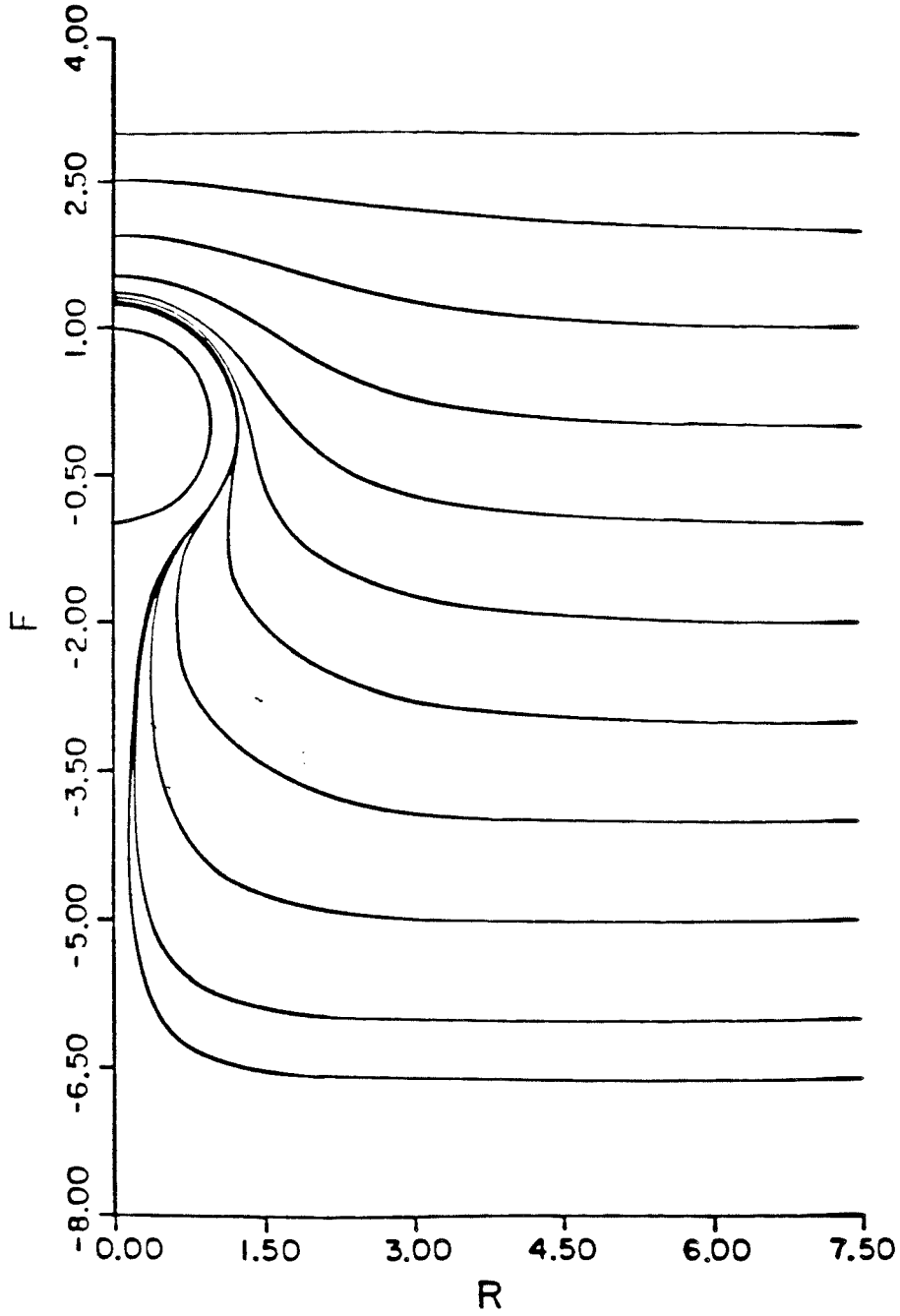

Figure 6.

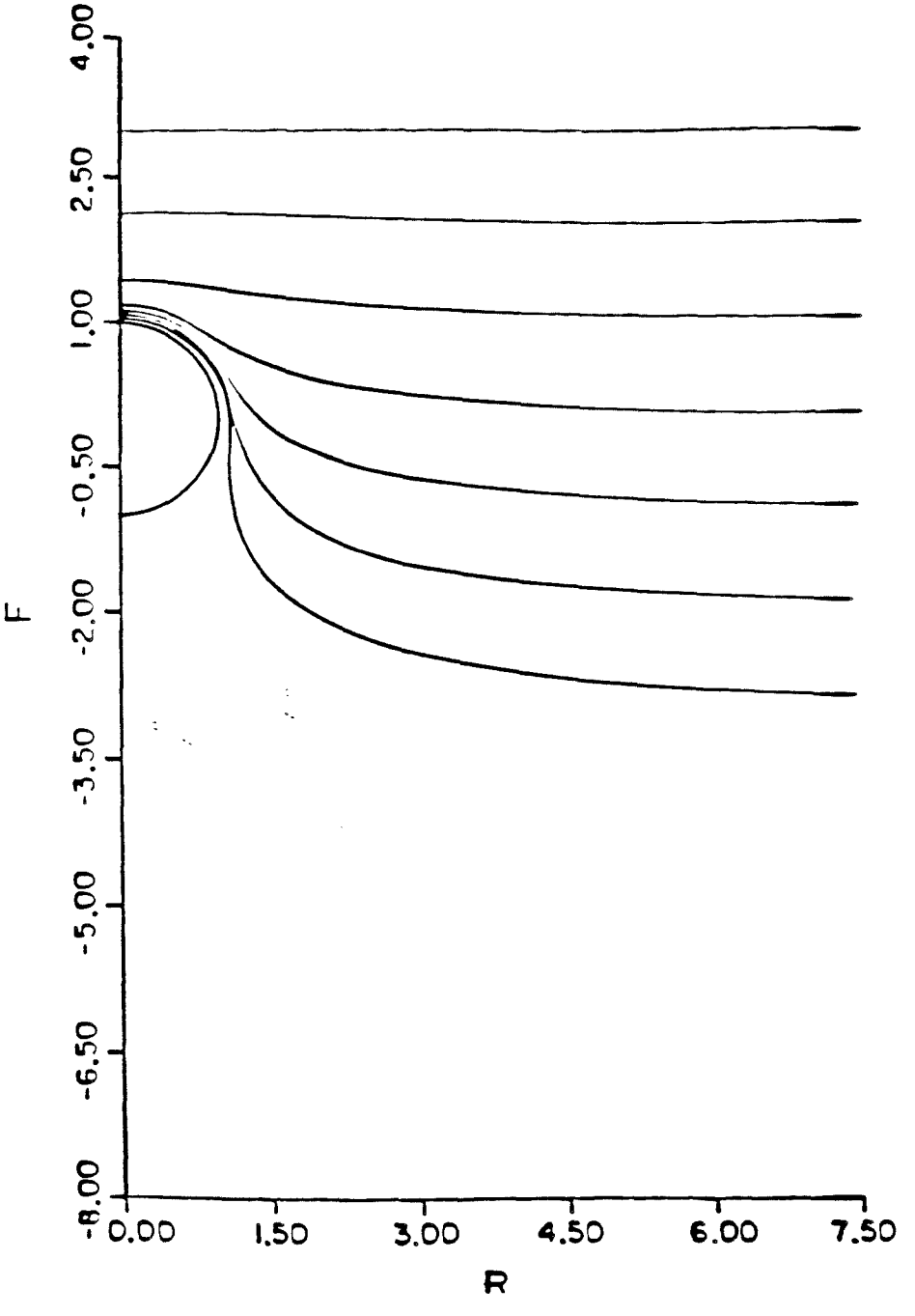

Figure 7.

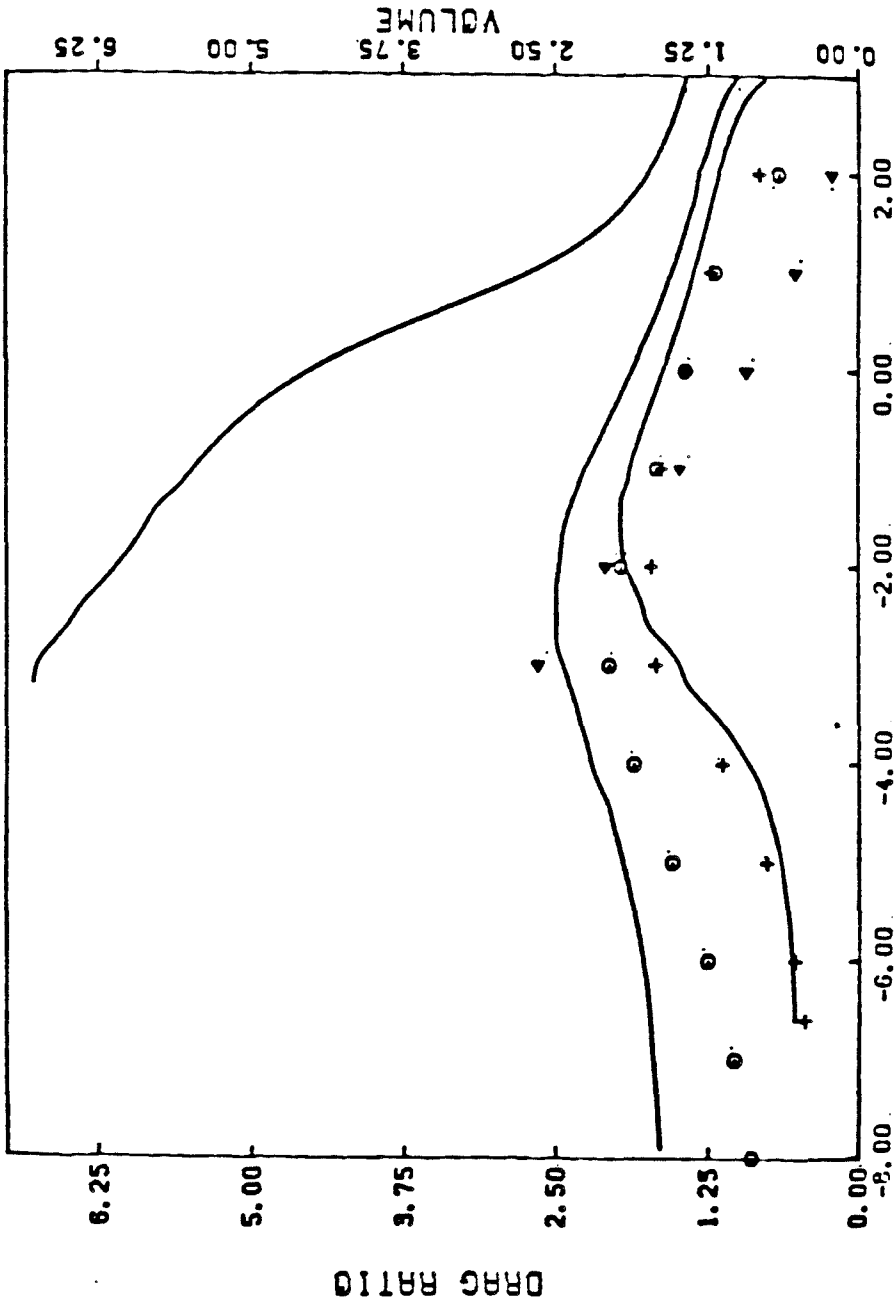
ORAG RATIO
6.25
5.00
3.75
2.50
1.25
0.00
-8.00
-6.00
-4.00
-2.00
0.00
2.00
L
VOLUME
0.00
1.25
2.50
3.75
5.00
6.25

Figure 8.

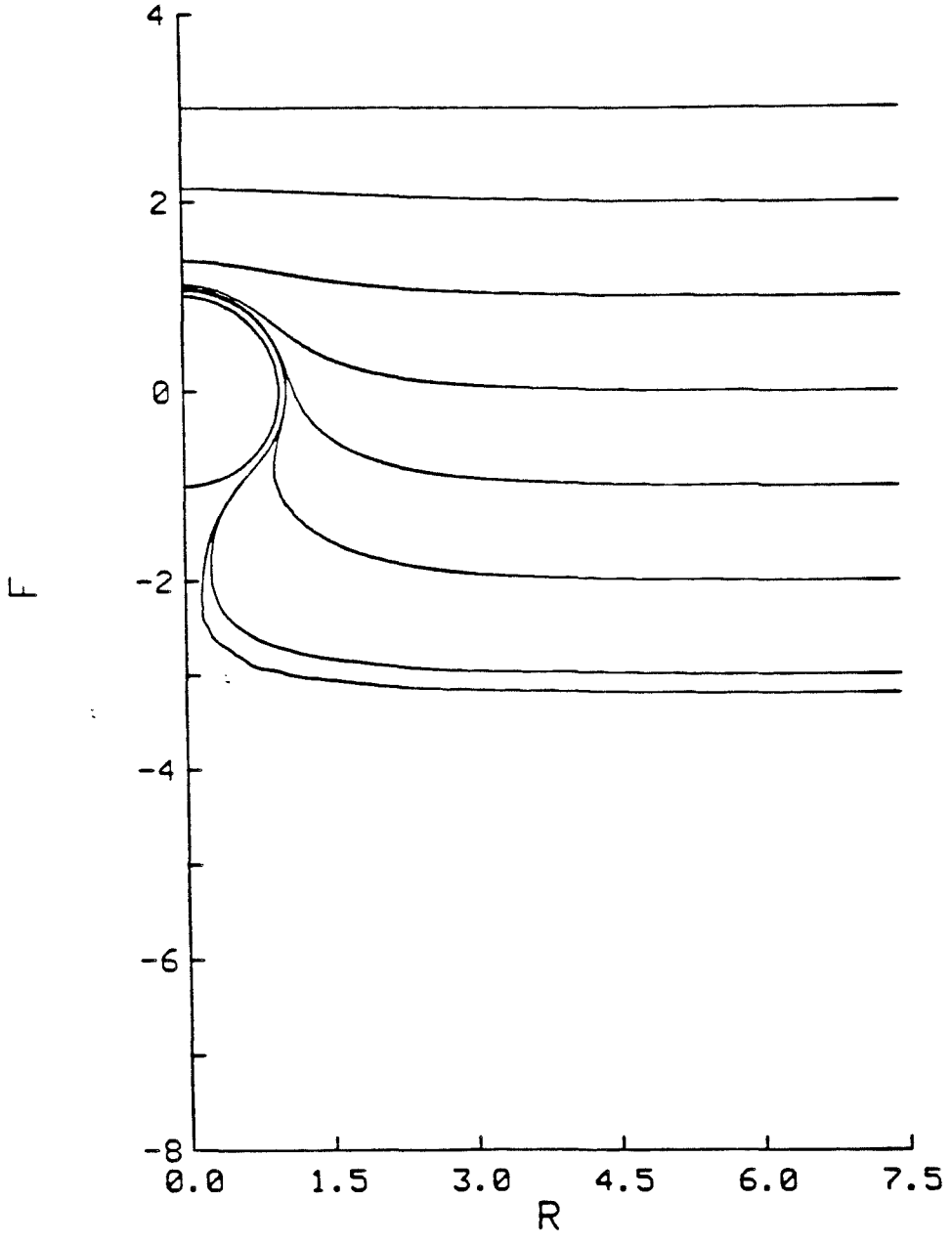

Figure 9.

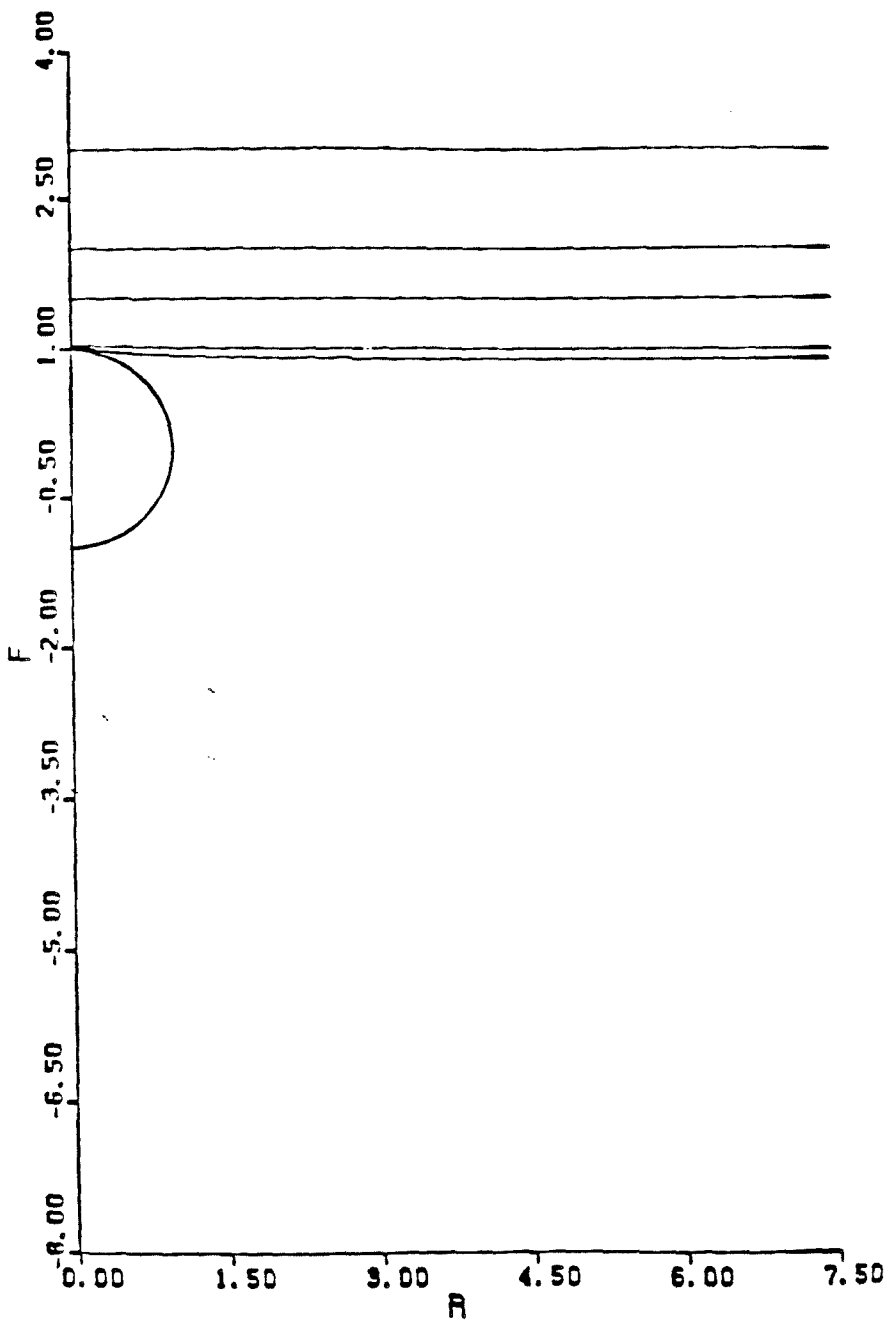

Figure 10.

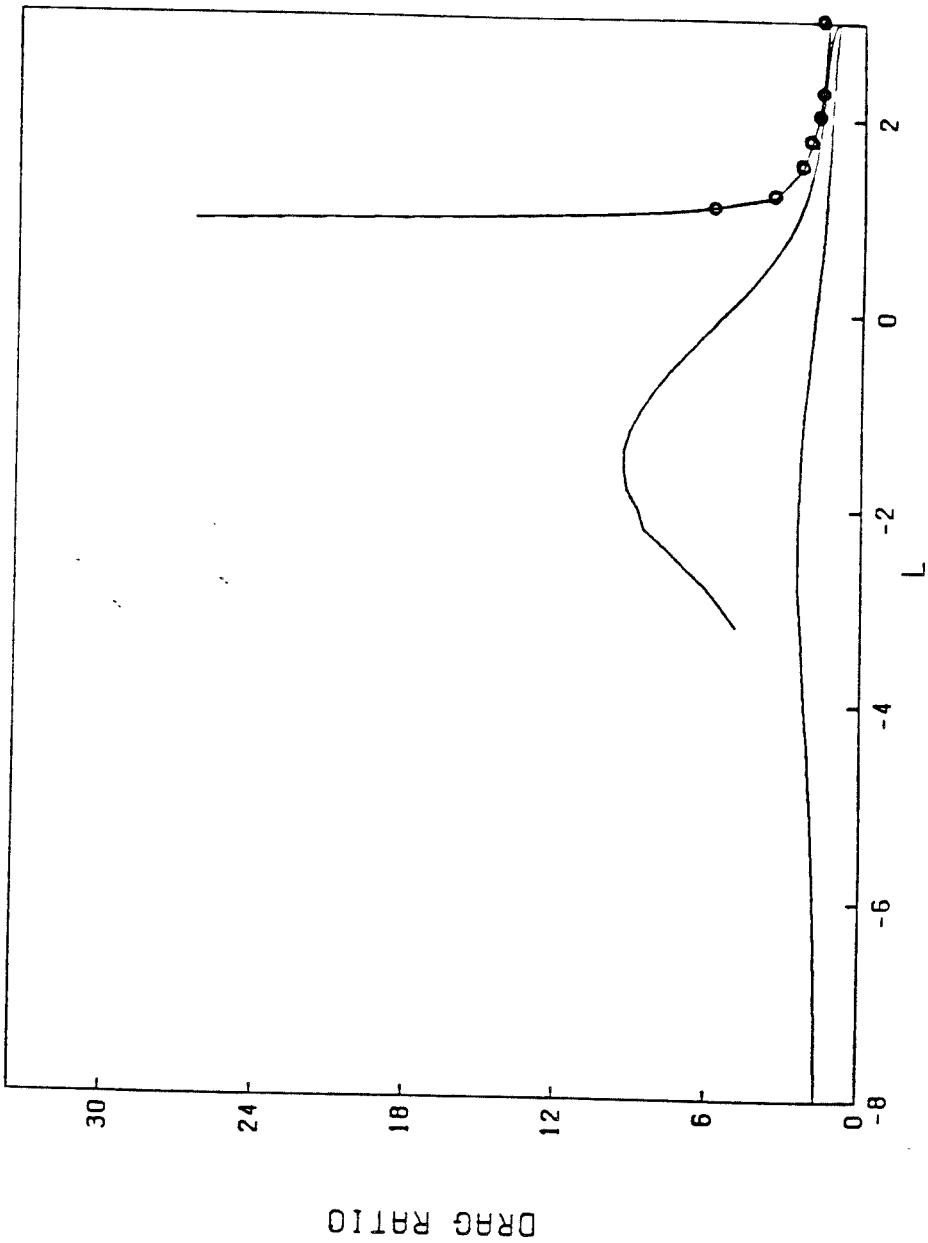

Figure 11.

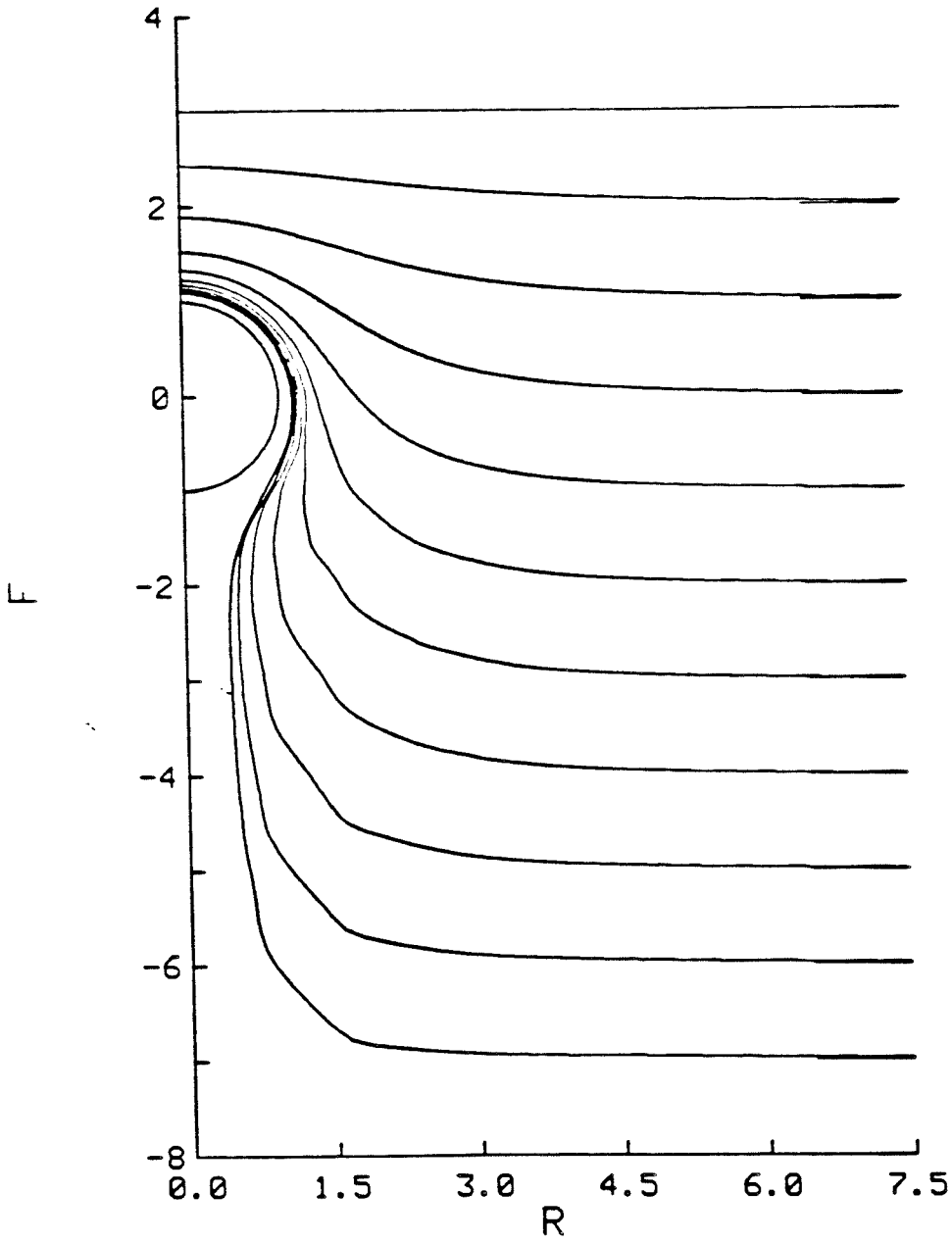

Figure 12.

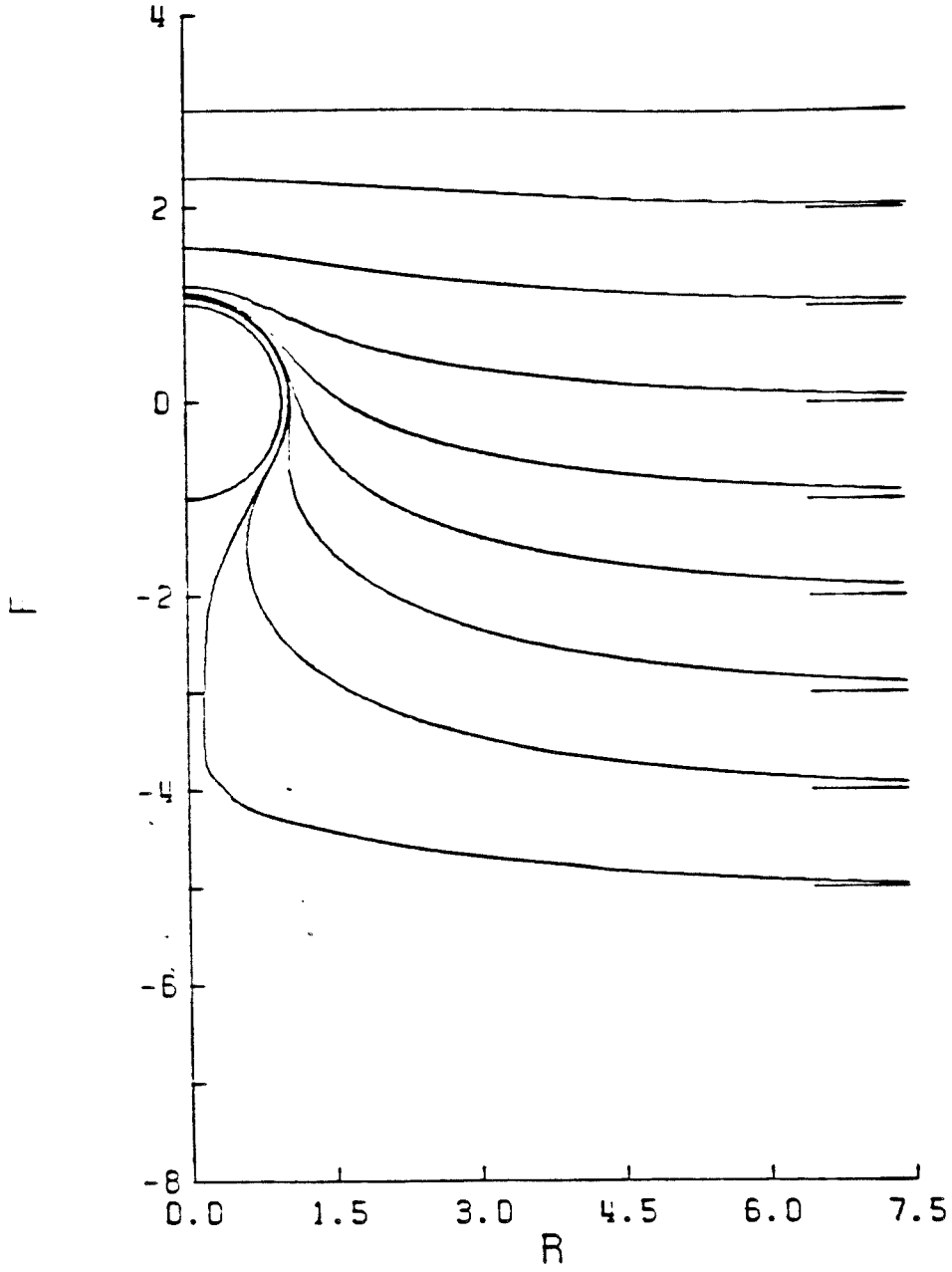

LAMBDA = 1.000 CA = 0.100 CG = 1.000

Figure 13.

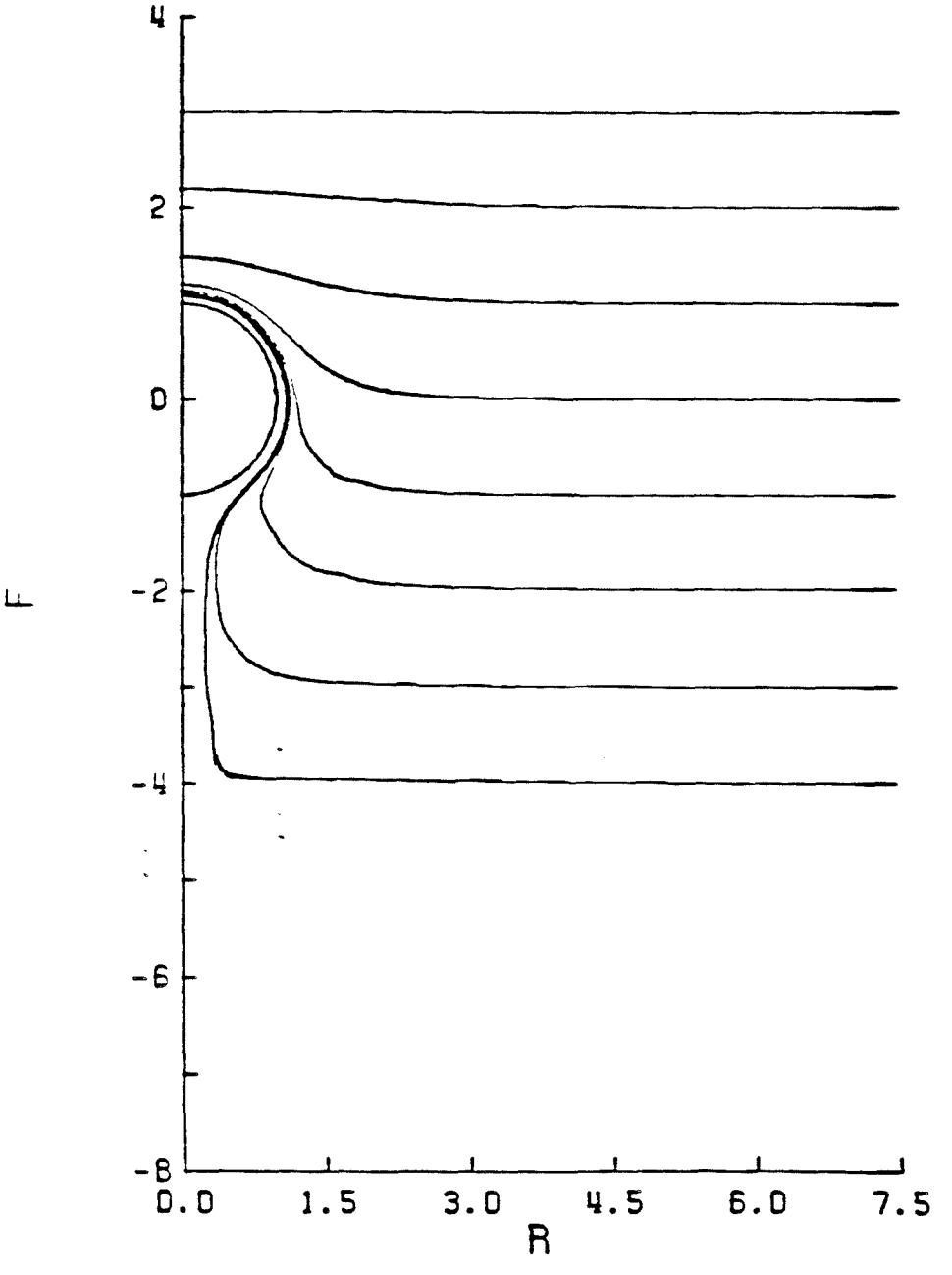

LAMBDA = 1.000 CA = 1.000 CG = 0.100

Figure 14.

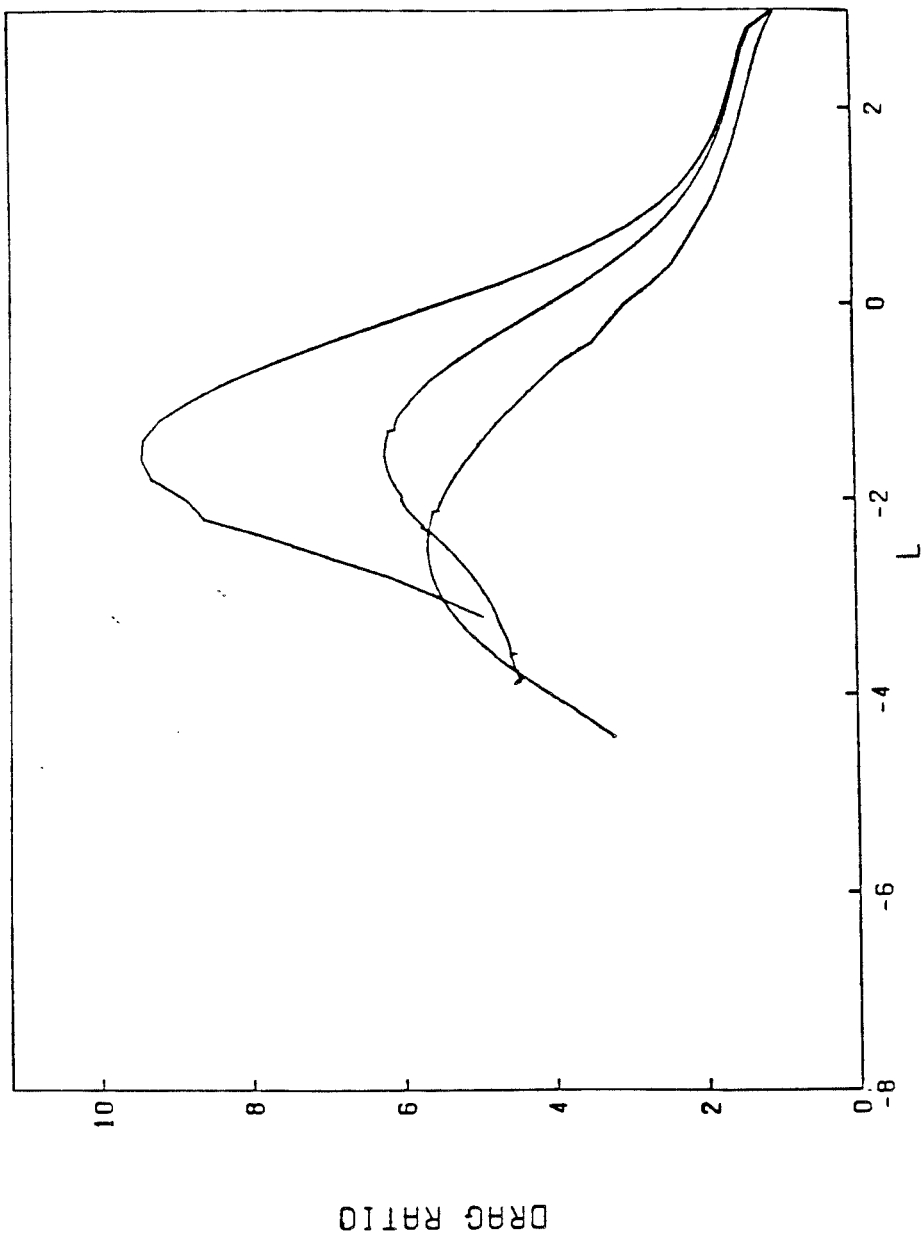

Figure 15.

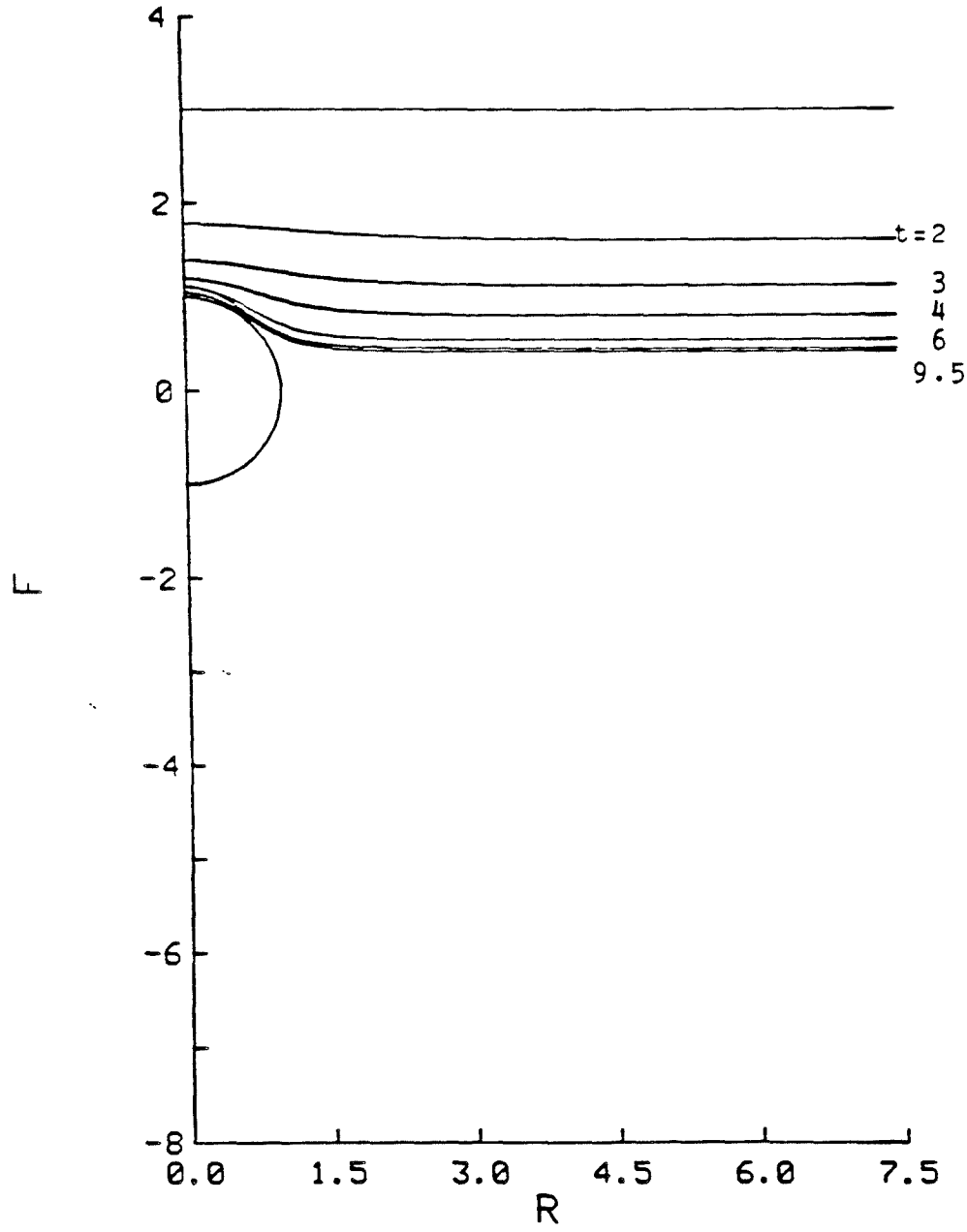
4
2
0
-2
-4
-6
-8
F
0.0
1.5
3.0
4.5
6.0
7.5
R
t = 2
3
4
6
9.5
LAMBDA = 0.022
CA = 0.465
CG = 0.089

Figure 16.

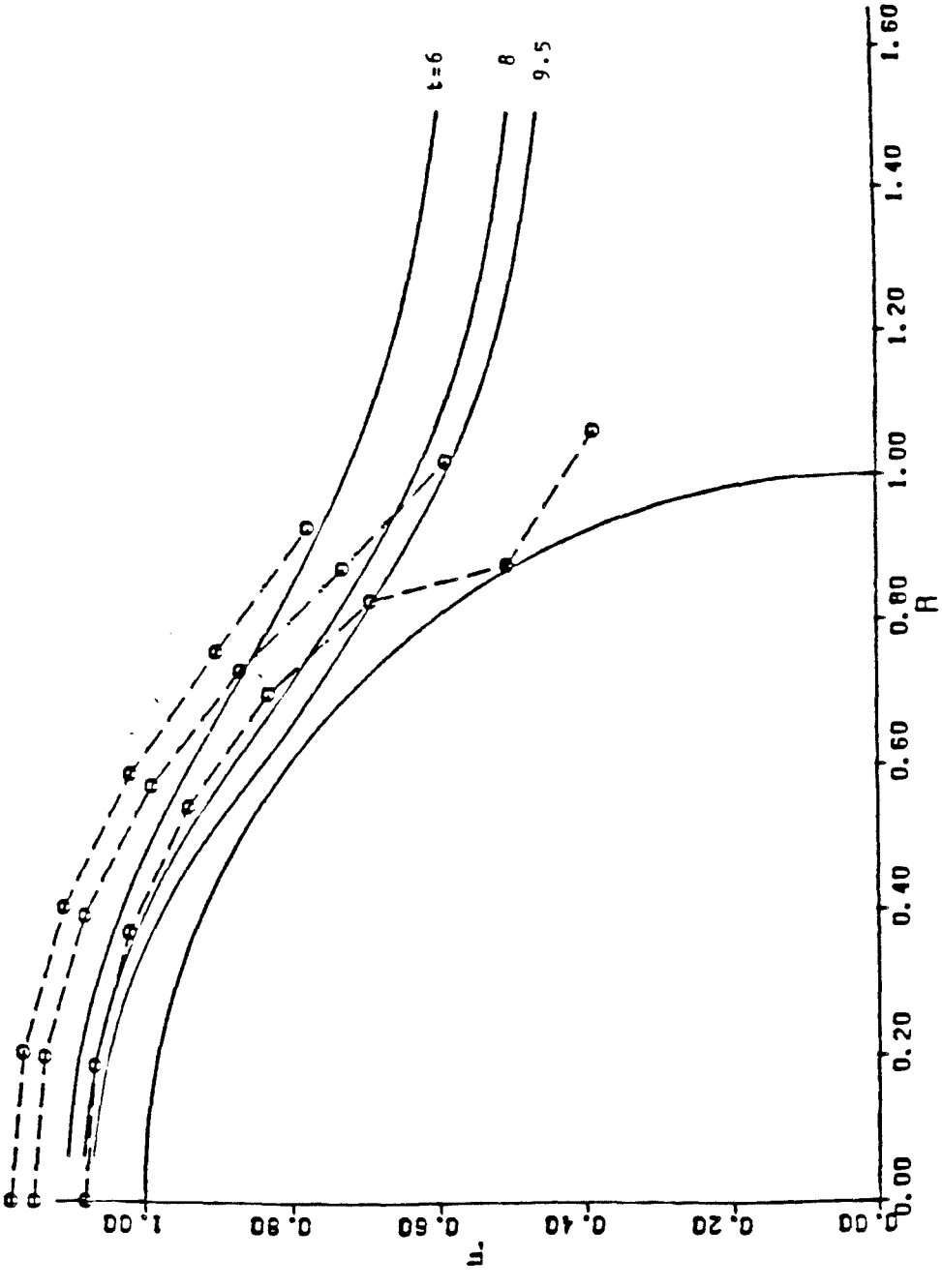
t=6
8
9.5
0.00
0.20
0.40
0.60
0.80
1.00
1.20
1.40
1.60
R
0.00
0.20
0.40
0.60
0.80
1.00
π

Figure 17.

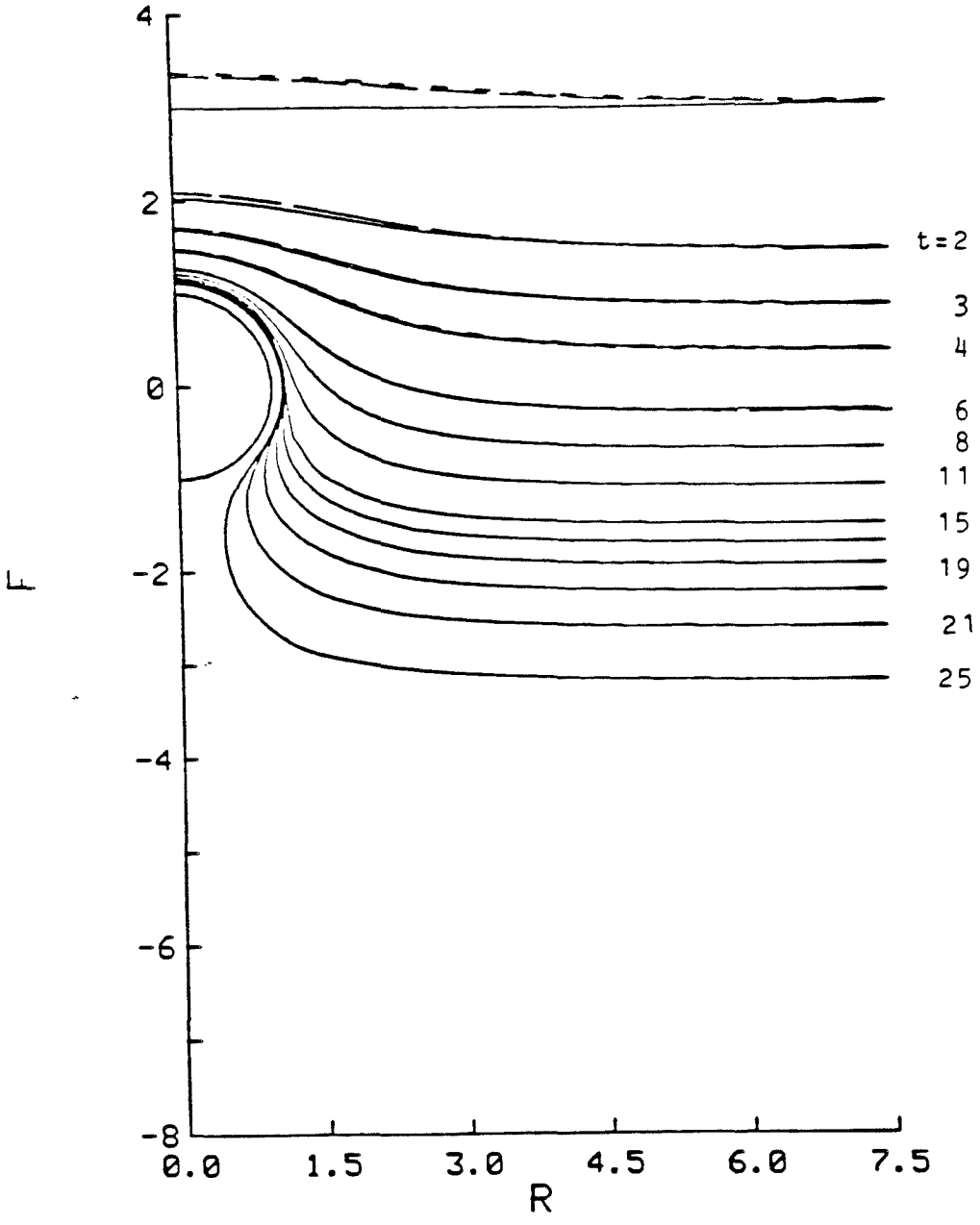
4
2
0
-2
-4
-6
-8
F
0.0
1.5
3.0
4.5
6.0
7.5
R
t=2
3
4
6
8
11
15
19
21
25
LAMBDA = 1.000 CA = 1.000 CG = 1.000

Figure 18.

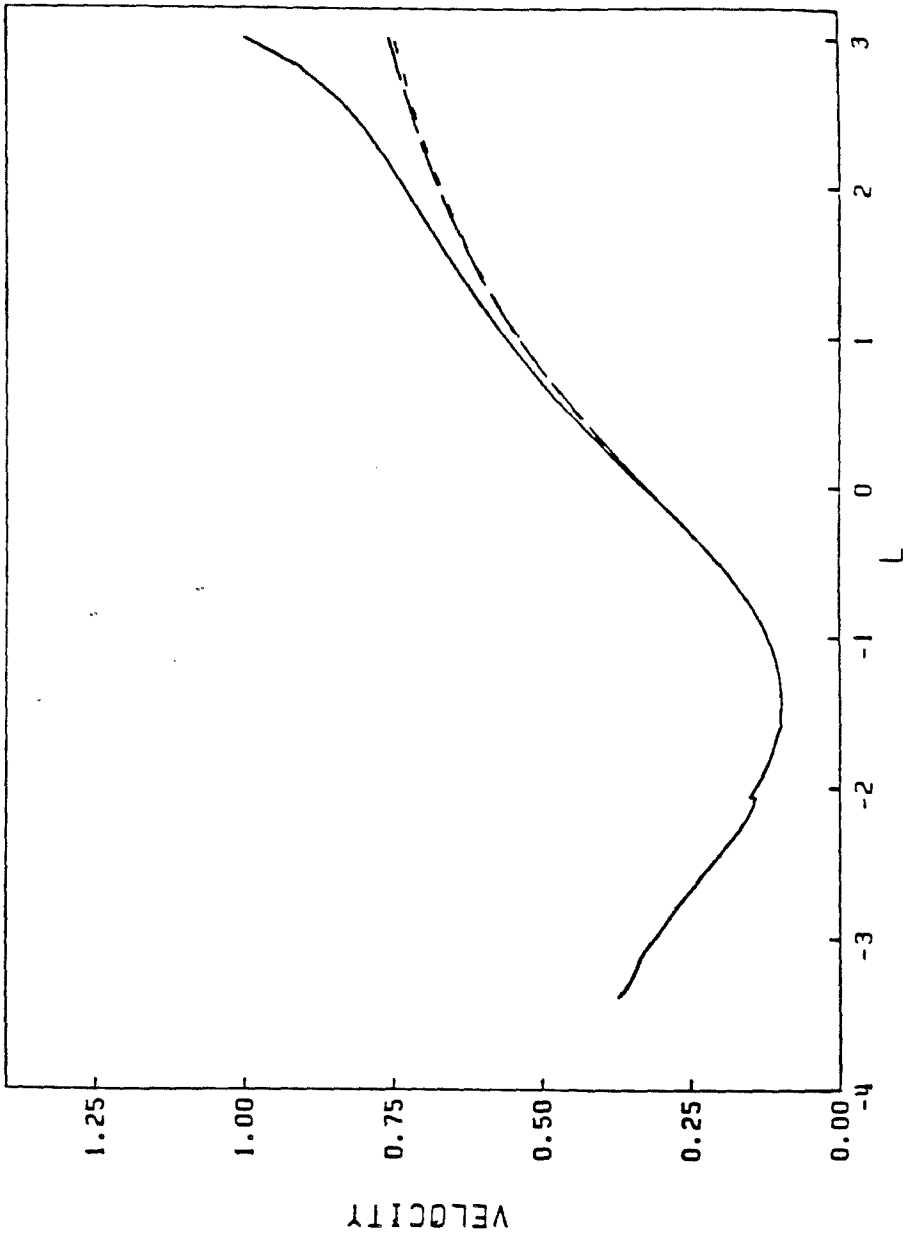

Figure 19.

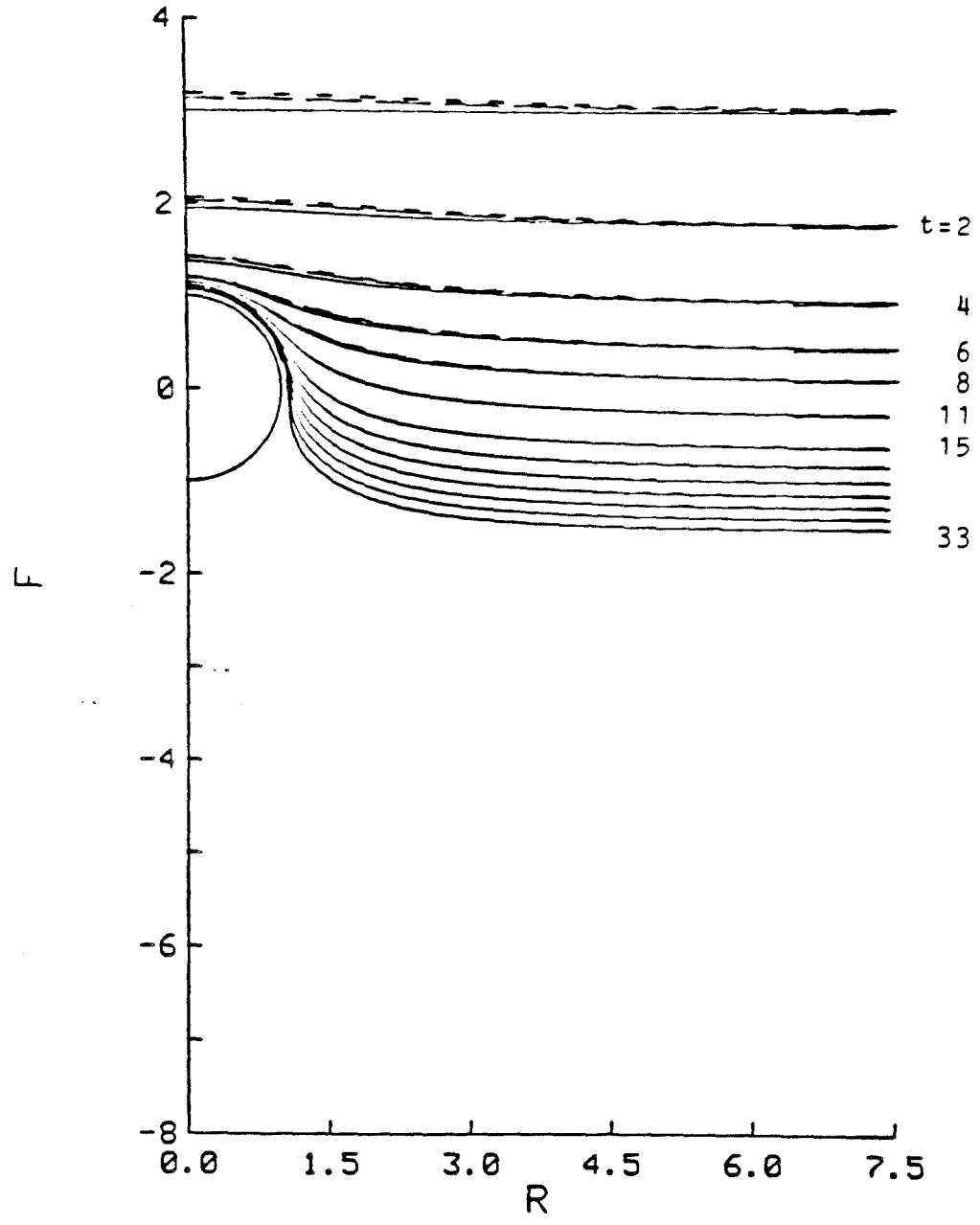
4
2
0
-2
-4
-6
-8
F
0.0
1.5
3.0
4.5
6.0
7.5
R
t=2
4
6
8
11
15
33
LAMBDA = 10.000 CA = 1.000 CG = 1.000

Figure 20.

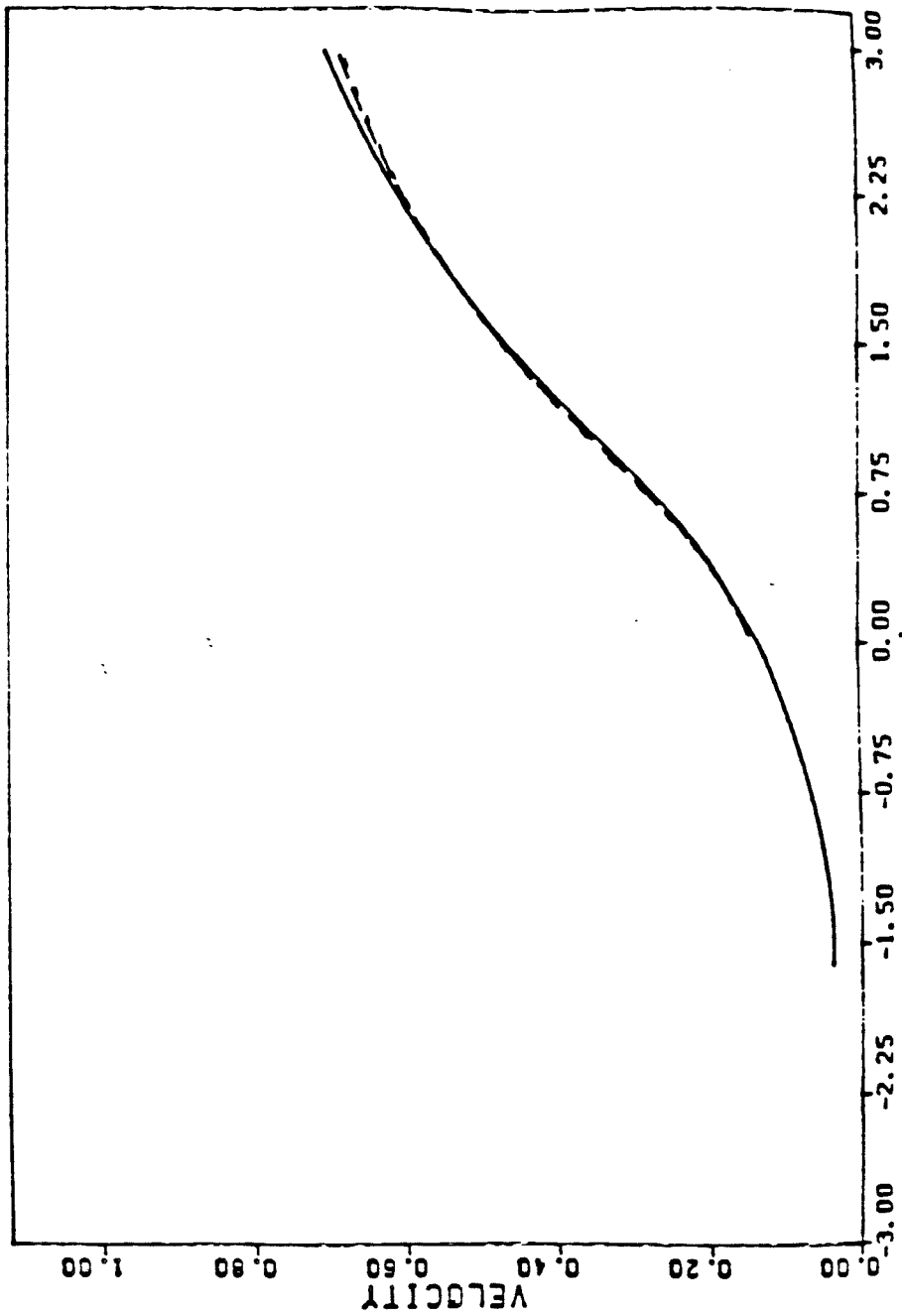
VELOCITY
0.00
0.20
0.40
0.60
0.80
1.00
-3.00
-2.25
-1.50
-0.75
0.00
0.75
1.50
2.25
3.00
L

Figure 21.

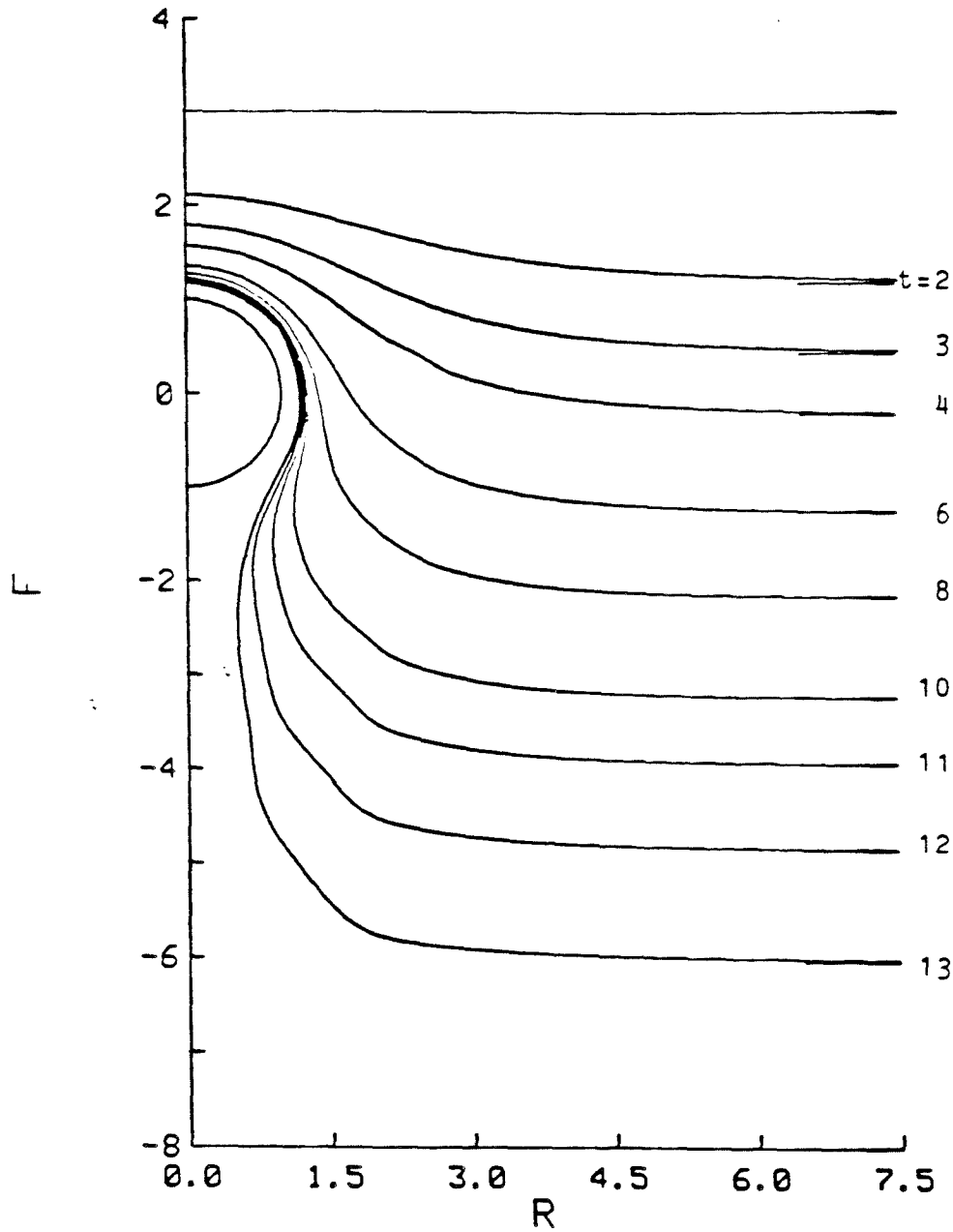

LAMBDA = 0.434 CA = 3.831 CG = 1.972

Figure 22.

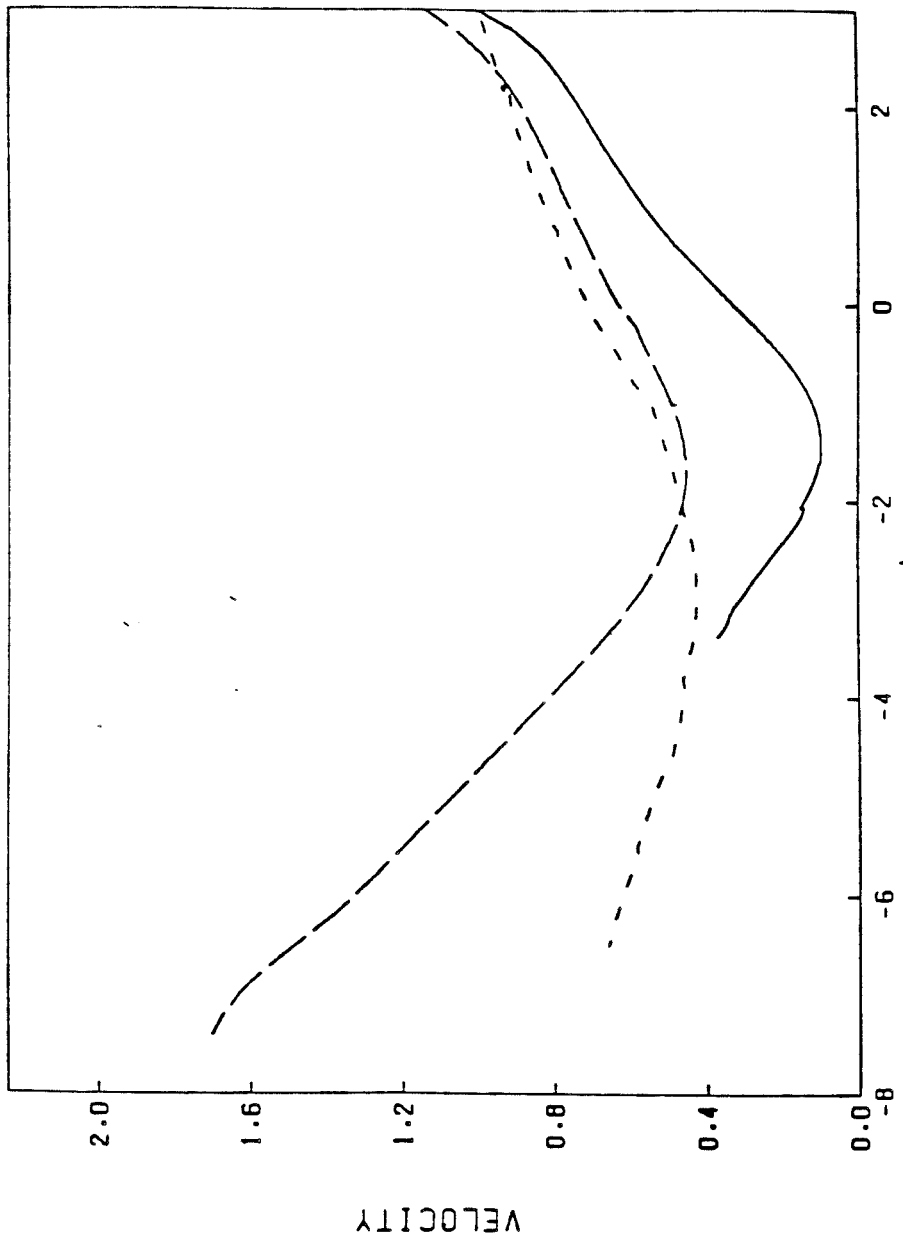

Figure 23.

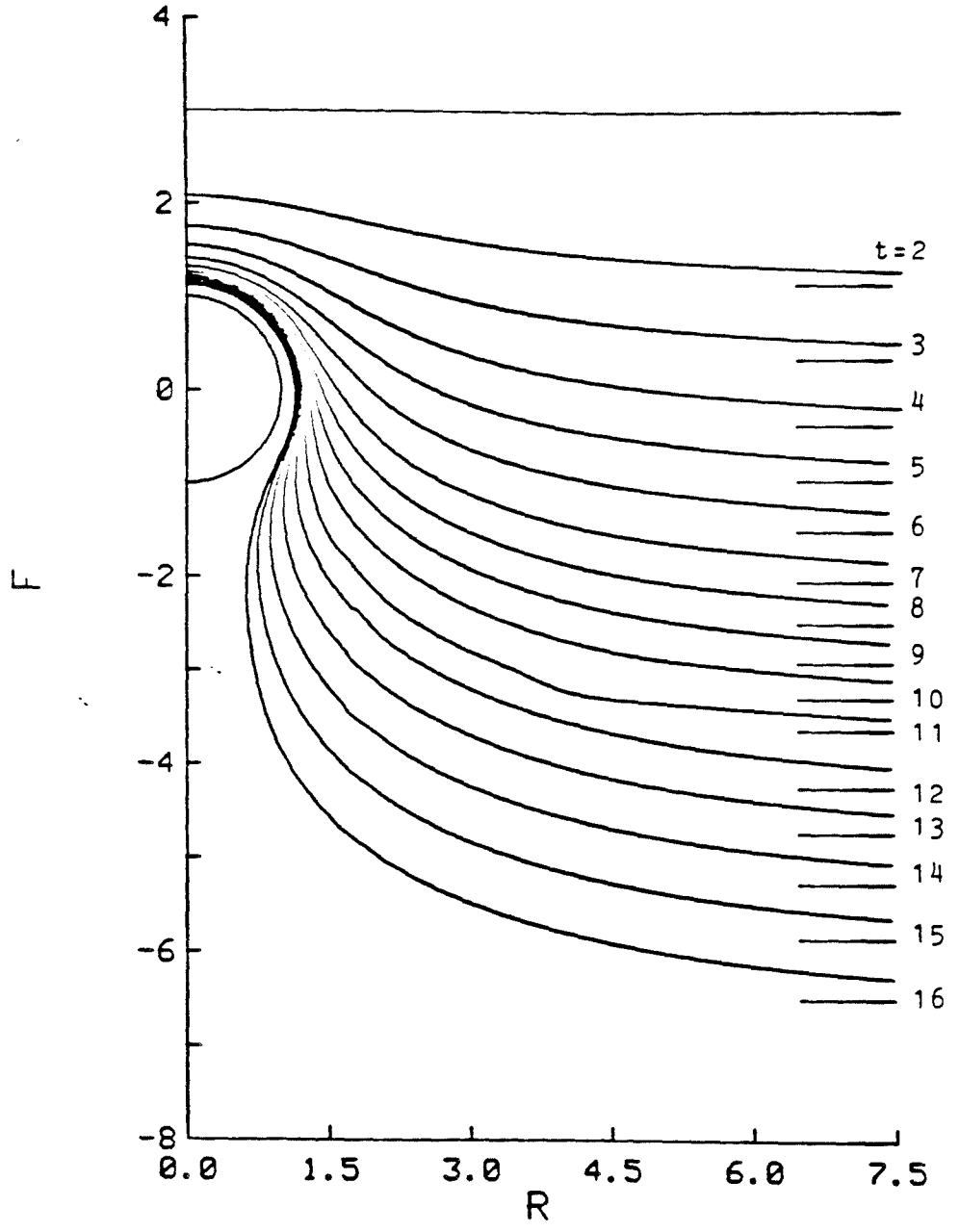

LAMBDA = 1.000 CA = 1.000 CG = 10.000

Figure 24.

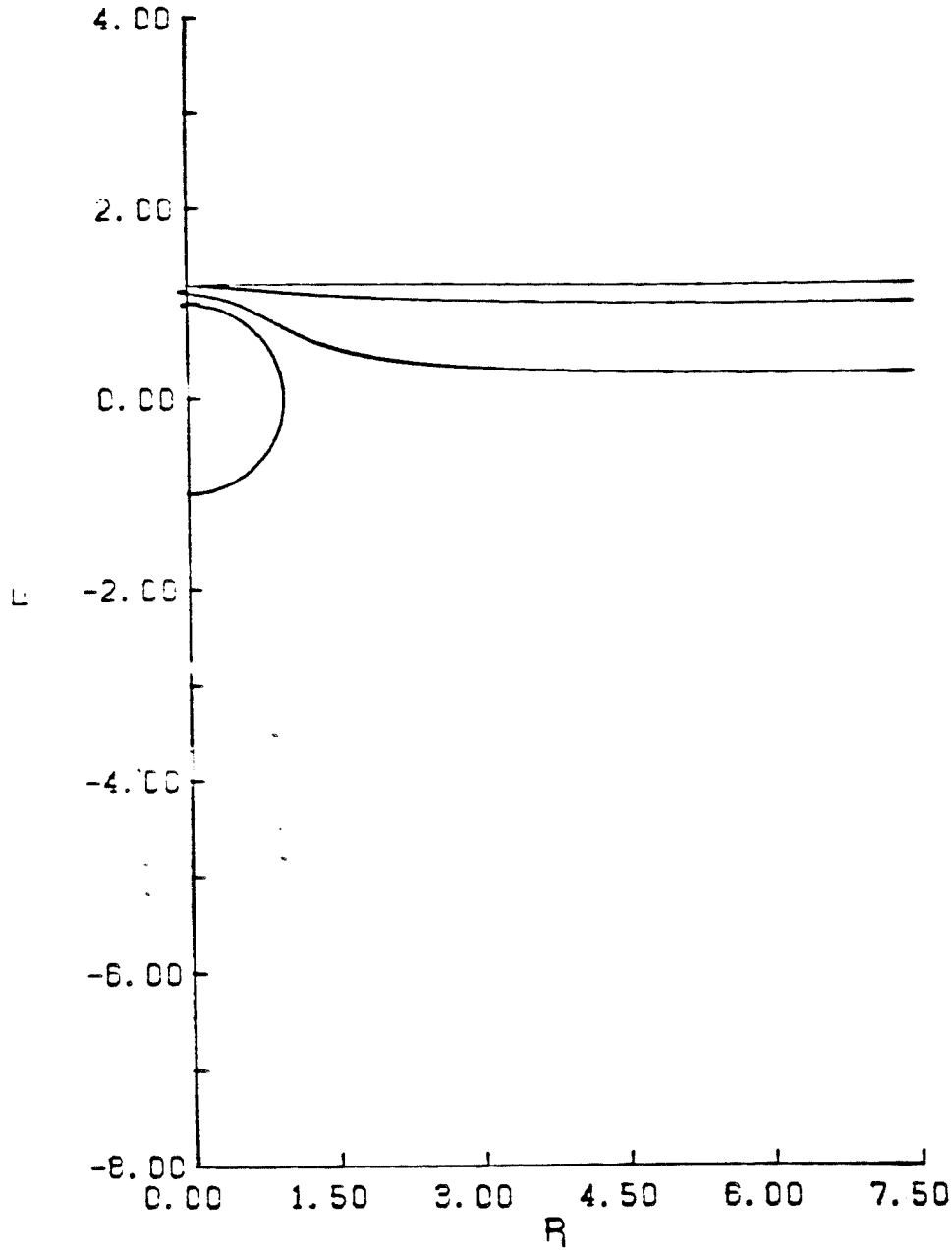

Lambda = 1.000 Ca = 0.100 Cg = 0.100

Figure 25.

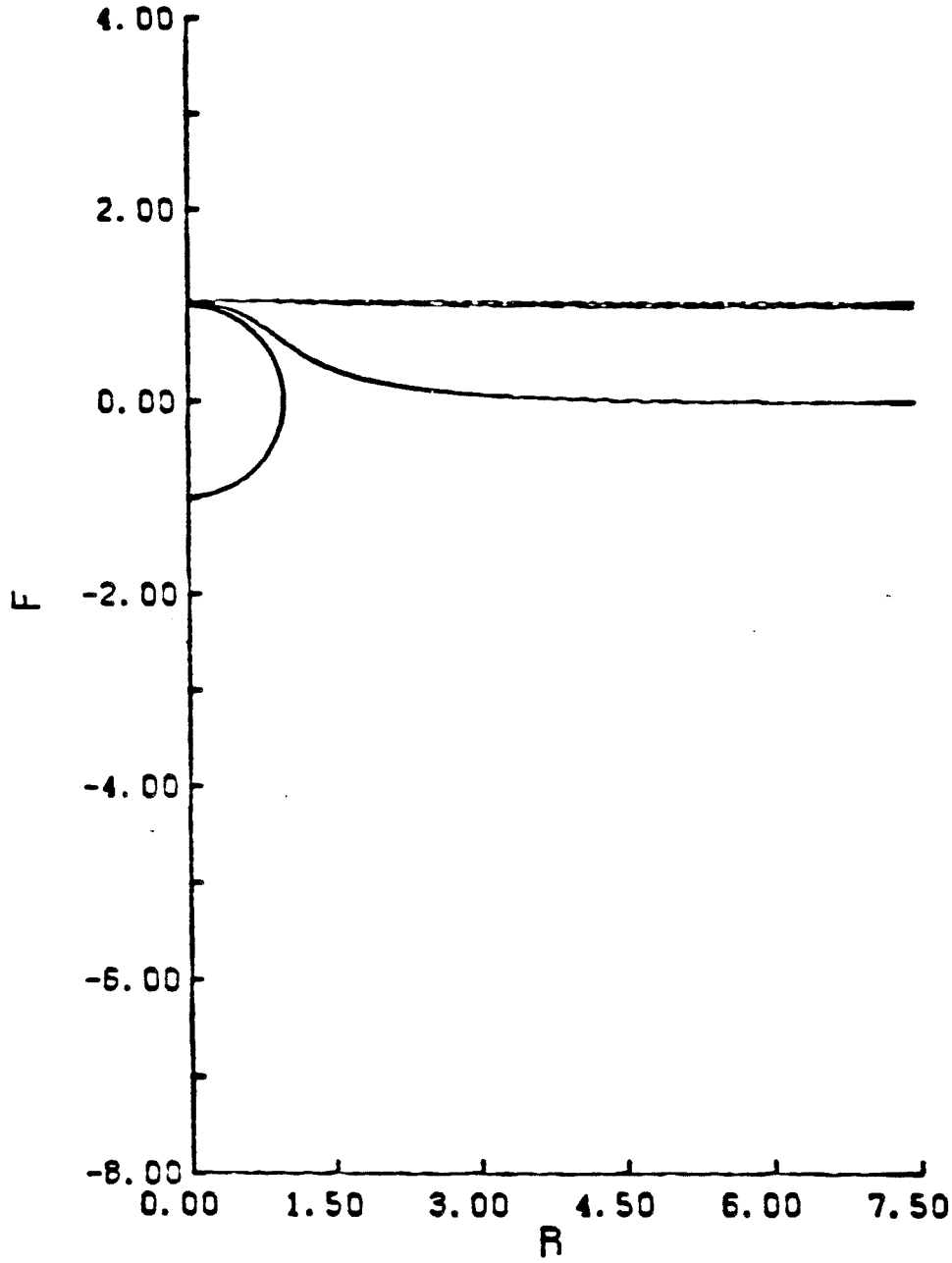

Lambda = 1.000 Ca = 0.100 Cg = 0.100

Figure 26.

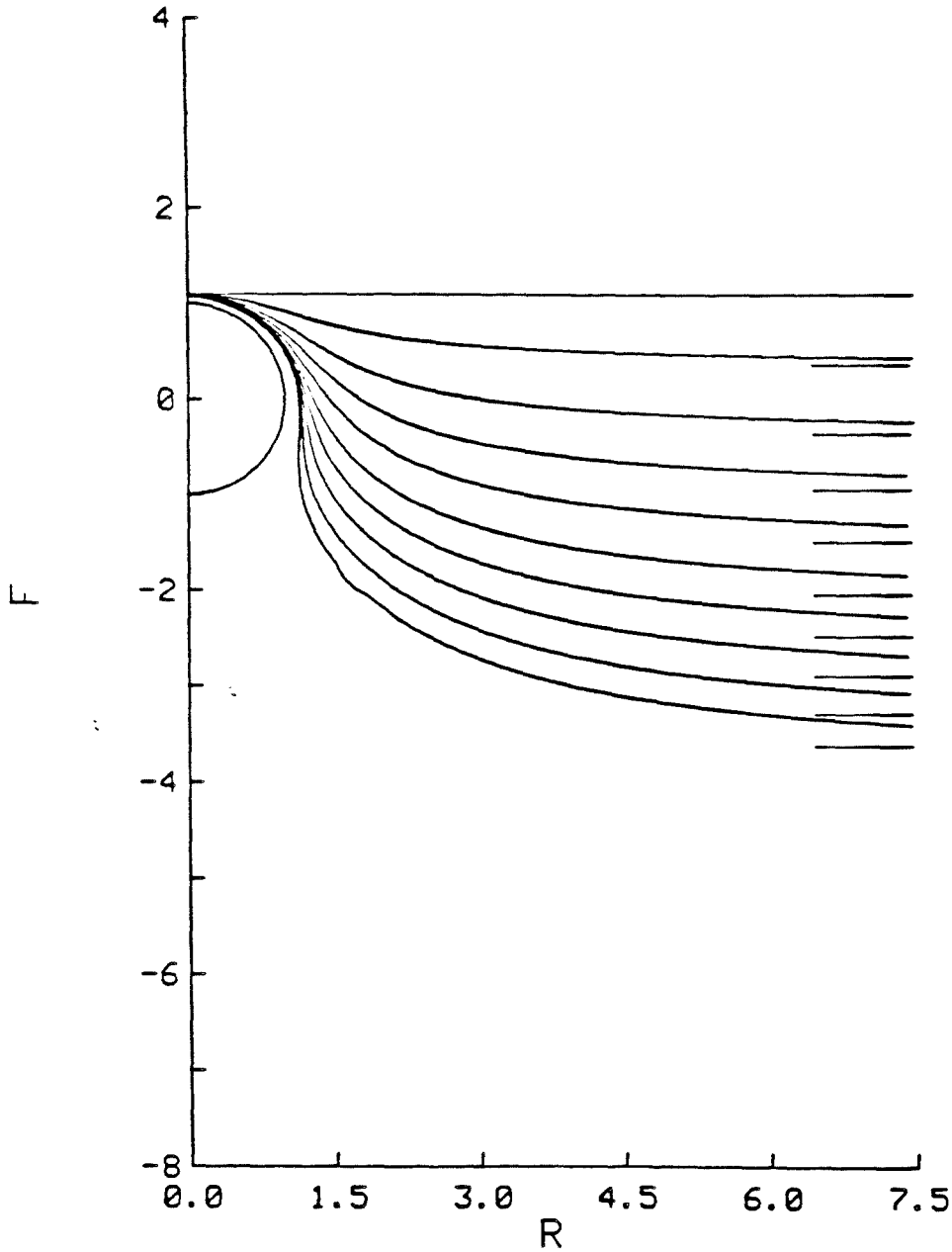

Figure 27.

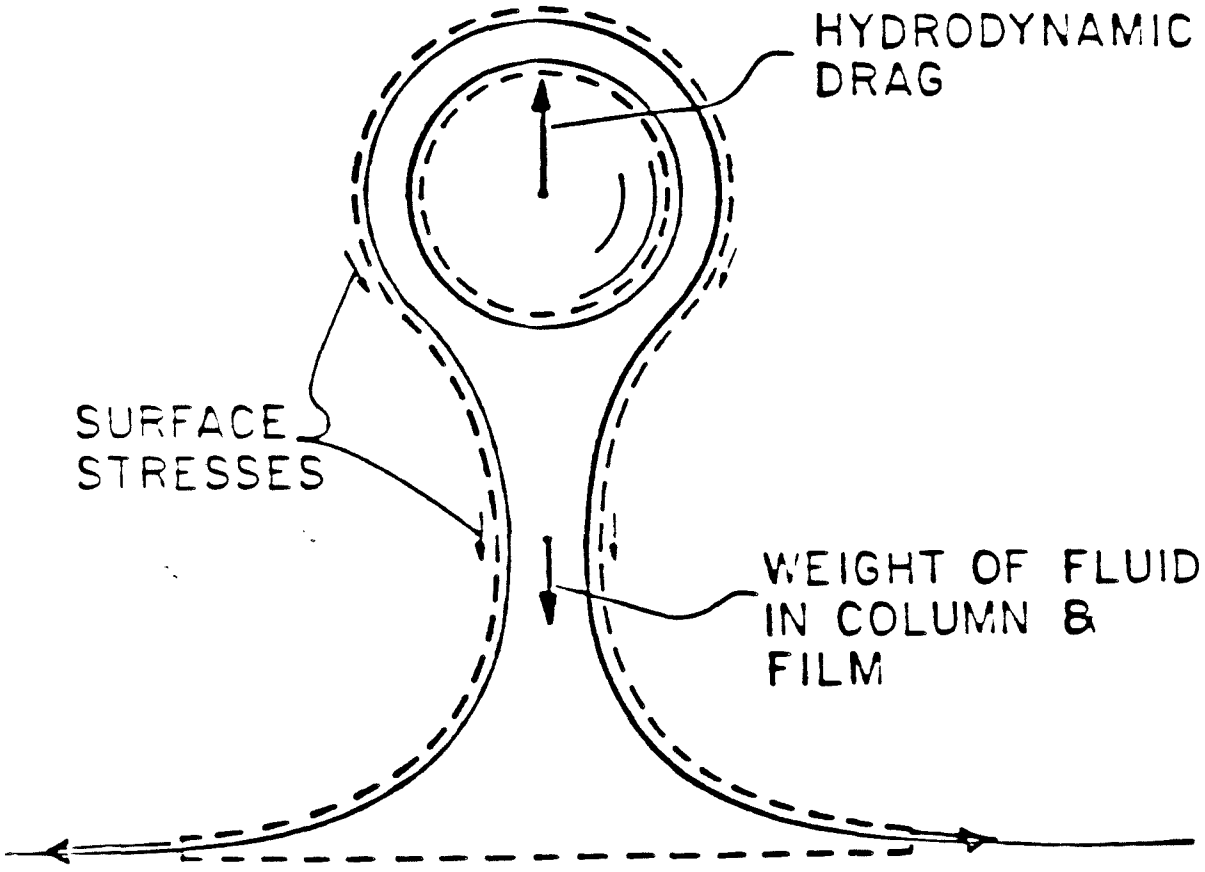
HYDRODYNAMIC
DRAG
SURFACE
STRESSES
WEIGHT OF FLUID
IN COLUMN &
FILM

Figure A1.

Chapter III

An Experimental Study of the Motion of a Sphere Normal to a Deformable Interface: High Capillary Number Results

I. Introduction

In the previous chapter, the problem of a sphere moving at zero Reynolds number under the condition of constant velocity or experiencing a constant body force, normal to a deformable, infinite fluid-fluid interface was examined using the boundary integral technique. This numerical procedure predicted the deformation and stress at the interface and the drag on the sphere or its velocity as it moved toward the interface. In that chapter comparisons between numerical results and two previously published experimental cases were drawn showing reasonable qualitative agreement between the two. However, more extensive comparisons of this type were made by Berdan (1982) where the results of experiments performed specifically for such comparisons are given. The objectives of Berdan's experiments were to verify earlier numerical results and also to show that the experimental system was able to reproduce the behavior of an infinite fluid domain at zero Reynolds number as a preliminary to its use in studying the same problem at finite Reynold's number or for non-Newtonian fluids.

Berdan presents results of experiments performed in a plexiglass tank in which a sphere was lowered toward an initially flat interface at a fixed velocity by a tether wire. The drag which would have existed alone on the sphere was then inferred by attempting to take into account for the presence of walls and the wire on the sphere-interface system. Berdan's experiments covered a range of physical parameters involving cases of low, medium and high values of viscosity ratio, interfacial tension and density difference between the two fluids in many combinations. The magnitudes of these physical parameters are again described by the three dimensionless groups; viscosity ratio, $\lambda = \mu_1/\mu_2$; capillary number, $Ca = \mu_2 U/\gamma$ and a density difference number, $Cg = \mu_2 U/(\rho_1 - \rho_2)ga^2$, as was the case in Chapter II. The results of Berdan's experiments showed very good quantitative agreement with the numerical calculations for the 10 cases involving low or moderate values

of γ (Ca order one or greater). In the remaining two cases, however, for which $Ca \approx 0.34$, significant departure from the calculations was seen in the experiments.

In order to confirm the ability of the experiments to reproduce the case of a sphere moving toward an interface in an infinite fluid, it is neccessary to understand the source of the discrepancy between the experiments and calculations for the low Ca cases. It is possible that there was some sort of error in performing the experiments reported by Berdan (only one run was performed for each set of parameters) or that some physical effect played an important role in the behavior of the system which was not accounted for in the numerics; electroviscous effects, for example. A final possibility is that the simple geometric difference between the numerical system (infinite fluids and interface, isolated falling sphere) and the experiments (finite fluids and interface, presence of walls, sphere-wire combination), is somehow responsible for the difference between experimental and theoretical results. This work adresses the first two possibilities by repeating Berdan's experiments for the two $Ca \approx 0.34$ cases, and considering how restricted tangential mobility at the interface due to surfactant effects might have effected the results. Tangential mobility at the interface is explored both experimentally and numerically. The former is done by following the motion of tracer particles at the interface, the latter by modifying the numerical technique of the preceding chapter to include restricted mobility.

In the boundary integral method of Chapter II, a form for the stress jump across the interface was needed. The simplest form for this stress jump and the one employed in Chapter II is that the tangential stress is continuous and the normal stress shows a discontinuity proportional to the local curvature, with the constant of proportionality equal to the interfacial tension, γ. Although this simple model is used often and generally provides accurate results, it should be remembered that it is just one of several limiting forms of Scriven's general equation for the stress

discontinuity across an interface (Scriven, 1960).

$$[\![\mathbf{n}\cdot\mathbf{T}]\!] = -\nabla_s\gamma + (\epsilon+\kappa)\nabla_s^2\mathbf{u} + \epsilon\,[2K(\mathbf{u}-\mathbf{n}\mathbf{n}\cdot\mathbf{u}) + \mathbf{n}\times\nabla_s(\mathbf{n}\cdot\nabla_s\times\mathbf{u}) + 2\,(\mathbf{n}\times\nabla_s\mathbf{n}\times\mathbf{n})\cdot\nabla_s(\mathbf{n}\cdot\mathbf{u})] + \mathbf{n}\,[2H\gamma + 2H(\epsilon+\kappa)\nabla_s\cdot\mathbf{u} - 2\epsilon\,(\mathbf{n}\times\nabla_s\mathbf{n}\times\mathbf{n}):\nabla_s\mathbf{u}] \quad , \qquad (1)$$

where

$$2H = -\nabla_s\cdot\mathbf{n}$$

$$2K = -\,(\mathbf{n}\times\nabla_s\mathbf{n}\times\mathbf{n}):\nabla_s\mathbf{n} \quad .$$

Representing the behavior of the interface by the single constant parameter, γ, neglects the contribution of interfacial shear, ϵ, and dilational, κ, viscosities as well as the role of interfacial tension gradients. These additional terms become more important as the capillary number decreases and the concentration of surfactants increases. Both changes result in an increase of ϵ and κ thereby giving greater weight to the geometric terms they multiply. Also, increasing γ or the concentration of surfactants allows for a greater potential for variation in γ and so $-\nabla_s\gamma$ may increase as well.

A number of previous investigations have been carried out to explore the effects of interface rheology and surfactant nonuniformity on fluid dynamics. In the case of falling drops, the role of ϵ and κ have been studied by Wei, Schmidt and Slattery (1974). The effect of surface tension nonuniformity on the dynamics of drops has been studied for both the case where the surfactant is insoluble in the bulk phases and quickly leads to a no slip region on the interface (Davis and Acrivos, 1966), and for soluble surfactants where there is a non-zero velocity over the entire surface (LeVan and Newman, 1976). Holbrook and LeVan, (1983a, b) consider cases intermediate to these two extremes. More closely related to the present investigation is the analysis of Shail and Gooden (1983) who examine the problem of a solid

sphere translating normal to a fluid-fluid interface with a surfactant film, but with the restriction that the interface remains flat, that is, $\mathbf{u} \cdot \mathbf{n} = 0$ on the interface. This restriction implies that either the sphere-interface separation is large or else Ca and/or Cg is asymptotically small. Also, unlike Holbrook and LeVan (1983a, b), who solve the mass transfer problem for coupled transport mechanisms, Shail and Gooden assume that one of the mechanisms (surface convection, surface diffusion, or diffusion from the bulk fluid to the surface) limits surfactant transport and so solve the problem separately for each of these limiting processes. Further, although Shail and Gooden apply Scriven's expression for the stress jump at the interface, the restriction that the surface remains planar causes all curvature dependent terms to vanish. Nevertheless, Shail and Gooden were able to demonstrate the role of a surfactant film in determining the drag on a sphere approaching a liquid-liquid interface. Unfortunately, our experimental results for the drag on the sphere cannot be compared to Shail and Gooden's calculations. The authors' condition that the interface remains flat means that the two parameters Ca and Cg do not appear in either their governing equations or boundary conditions. Instead, Shail and Gooden have a system characterized by parameters relating interfacial transport mechanisms. Thus, we have no basis for comparison of the two types of results in the fluid region before the sphere meets the plane of the undeformed interface, the domain where Shail and Gooden's solution overlaps our own (even assuming we choose to ignore the obviously significant deformation of the interface in the cases presented here). The macroscopic balances of the appendix to Chapter II shows that in the range of Ca and Cg for the experiments, the drag on the sphere depends very heavily on the volume of fluid carried across the plane of the initially flat interface, and Shail and Gooden's treatment of the problem does not allow for this contribution to the drag.

The full surfactant problem requires treating all modes of surfactant transport

at the interface simultaneously with solution of the fluid flow problem. Shail and Gooden treat several limiting cases where some of these transport modes may be neglected; and further, all cases are linearized with respect to surface concentration. A greater simplification is to remove consideration of surfactant transport entirely. The fluids used for the experiments described by Berdan (1982) and reported here contain surfactants in the form of chemical contaminants and dust particles which are observed at the fluid-fluid interface. It is the presence of these surfactants which we believe cause the disparity between Berdan's experiments and his calculations. The unknown nature and concentration of these surfactants, though, makes it impossible to apply any rigorous theory to the interfacial behavior of the experimental system. However, we can apply a limiting theory for the dynamics of the interface which will take into account the presence of surfactants.

It has been recognized that the presence of surface active agents in fluids can make small drops behave as rigid spheres by inhibiting all tangential motion, thereby changing the drop-fluid interface to a no-slip surface (Davis and Acrivos, 1966). The reduction in mobility of fluid at the drop surface is the result of a jump in the tangential component of the stress across the interface brought about by interfacial tension gradients. As a second limiting case complementing the freely mobile interface result, for comparison to the experimental results, we adopt a model for flow at the fluid-fluid interface which has no tangential component for the fluid velocity, $\mathbf{u} \cdot \mathbf{t} = 0$. This allows us to replace the mass transfer problem of finding the concentration of surfactant at each point on the interface with the solution for the tangential stress jump necessary to inhibit all tangential motion. The expression for the stress jump in the boundary integral calculation is modified to include a term for the strength of the interfacial tension gradients, and rather than determine the value of this term by solving for the transport of surfactant at the interface; the term is given the magnitude consistent with vanishing tangential velocity in accord

with the conclusions of Davis and Acrivos (1966).

The use of this ad hoc assumption about the surfactant concentration and immobility of the interface is not unprecedented. In Sadhal and Johnson's treatment of flow past a drop with a stagnant cap (1983), a surfactant film was assumed to exist a priori over the rising drop from the rear stagnation point to some cap angle θ in front of which the interface was treated as fully mobile. Sadhal and Johnson show that if the Peclet number in each fluid phase and at the interface vanishes, or if there is a strong adsorption barrier to the surfactant flux from the bulk phase to the interface, tangential motion on the drop surface will cease.

In this chapter, we will present additional experimental results for the anomalous cases in Berdan's work and apply a zero tangential velocity condition at the interface to the boundary integral method of Chapter II to show how removing tangential mobility affects the calculations for interface deformation and sphere drag. By comparing experimental results to the two limiting calculations (immobile and fully mobile interface), we are able to determine the degree to which the interface is made immobile by surfactants and the ability of the model to accurately simulate the experiments.

II. Experimental Apparatus and Procedure

(a) Experimental Apparatus

The equipment used to perform the experiments outlined in the introduction consists of three main parts, and will be considered in detail later. Briefly, however, the three are: a large plexiglass tank containing two immiscible, Newtonian fluids, a rigid sphere and translation assembly to lower the sphere at a fixed velocity as well as measure its position, and finally, instruments to record the shape of the interface and the force on the submerged body (sphere-wire combination). A sketch

of the experimental system is shown in Fig. 1. All experiments, Berdan's as well as our own, used the same equipment to give as great a degree of reproducibility as possible, but of course, fresh fluid was used for the present runs.

The plexiglass tank was constructed of 1/2 inch plexiglass and measured 15″ across and 36″ deep. The lower phase (corresponding to fluid I of the preceding chapter) was water; the upper phase was a silicon oil blend consisting of two grades of Dow Corning Silicon Oil 200 fluid with 28.9% 30,000 cs. grade and 71.1% 1000 cs. grade. Both fluids are Newtonian (Olbricht, 1981). The silicon oil blend is hydrophobic and so is immiscible with the water phase; also, its physical properties are unaffected by changes in humidity. The physical properties of the fluids were measured to insure that they agreed with Berdan's results. The densities of the liquids were measured with a standard calibrated hydrometer in a temperature bath stable to $\pm 0.06°$ C. The viscosities of the fluids were measured using a Cannon-Fenske viscometer calibrated to ASTM Std. (D-445) in the same temperature bath. The surface tension between the two fluids was measured using a du Nouy balance following ASTM Std. (D-971). In all cases the results agreed with Berdan's earlier measurements. These values for density and viscosity of the two fluids and for surface tension are presented in Table I.

TABLE I. Physical Properties of Liquids Used in Experiments

Fluid	μ (poise)	ρ (gm/cm^3)	γ (dynes/cm)
silicon oil blend	33.83	0.97075	37
water	9.74×10^{-3}	0.99792	–

The particle in the experiments was a polished bronze sphere, spherical to ± 0.0002 inches. Spheres with two different diameters were used in the experiments; one with radius 0.4747 cm and the other with $a = 1.2697$ cm. This gives a minimum

sphere wall separation of 14 radii. Results of Chapter II show that for this distance, fluid motion at the interface should have effectively gone to zero and the effect of the wall on the sphere should be small. The sphere was connected to the translation system via a stainless steel wire 32 inches long with diameter of 0.0041 inches. This wire is an important component of the translation system. It must be small enough in diameter to minimize the disturbance caused to the flow field but must not experience a change in length during an experiment as this would introduce error into the sphere position measurement. Furthermore, stretching or coiling will cause the wire to act like a spring, thus introducing error into the force measurement. Using the elastic modulus of the present stainless steel wire, the maximum change in length due to stretching is calculated at 0.06% of its total length. To prevent the wire from coiling, it was straightened mechanically so that it would hang vertically under its own weight.

A mechanical translation system performed the function of lowering the sphere toward the interface at a fixed speed. This assembly consisted of an aluminum bar which was constrained to move vertically with no rotation by a centering guide that also functioned to position the sphere in the tank. A 1/50 hp. motor rated at 38 in. lbs. maximum torque raises and lowers the bar by winding or unwinding a steel cable attached to the aluminum bar around a 6 in. take up spool. The motor has a continuous setting feedback controller to insure constant velocity. A ruler attached to the guide bar served to indicate the relative position of the sphere. Before an experiment was performed, it was necessary to correlate the height of the sphere in the tank with the reading on the ruler.

The final component of the experimental apparatus is the data acquisition system. To measure the reduction in tension in the wire as the sphere approached the interface a very sensitive measuring device was needed. This consisted of a ring force transducer sending signals to an Omni-Scribe model A-5141-5 multi-span

strip chart recorder (span 0.001 to 10 volts full scale). The recorder is equiped with a manual event marker so at least one position per experiment on the chart recorder could be correlated to the sphere position. The ring force transducer fitted with a semiconductor bridge is the most accurate small deflection transducer available that could give output sufficiently high for the small forces and changes in forces produced during the experiments. The strain in the ring causes changes in the resistances of the individual legs of the bridge and so a change in the voltage across the bridge. It is this voltage which is recorded by the chart recorder. The transducer gain was $620 \pm 2\mu V$ per gram and during operation the transducer output could be read to $\pm 2\mu V$. Because of changes in the resistance due to temperature fluctuations, the ring tensiometer was thermally isolated from the surroundings. It was fixed rigidly to the guide bar of the translation system by a thermally isolating coupling and surrounded by an insulated housing. To insure thermal equilibrium during an experiment, the transducer was warmed up under load for an hour before starting a run.

The remaining experimental data including interface shape, tracer particle position, sphere position, and time were recorded on a single video tape via two video cameras. One camera was always mounted to record simultaneously the position of the ruler attached to the guide bar and the display of a digital stopwatch. This allowed us not only to record the relative position of the sphere; but also, by combining the time and position data calculate an average velocity over short periods during a run. Table BI presents the results of these measurements. The maximum velocity fluctuation for any run was 4% and the average fluctuation less than 1.40%. The other camera was mounted to view the motion of the interface. Two camera positions were used to record different types of interface motion. When mounted horizontally in the plane of the water-silicon oil interface, the camera recorded the vertical deformation of the interface as the sphere approached. This was the same

view recorded by Berdan, and also obtained most easily from the boundary integral calculations. For some runs, however, the camera was mounted below the tank and focused up at the plane of the interface. In this case, the plane was illuminated from the side with a thin horizontal plane of light produced by a 300 W projector bulb shined through a deep channel formed from two parallel aluminum plates. Dust particles at the interface reflected this light and acted as tracer particles to allow the r-component of motion at the interface to be visualized as the sphere approached (the lens on the video camera had a depth of field long enough to show the tracer particles throughout an experiment). For the slightly deformed interface, this will nearly be the tangential component of velocity. A screen spliter combined the images from the two cameras, one focused on the guide bar, the other on the interface, in a single frame so both sets of data could be recorded on the single video tape.

(b) Experimental Procedure

The plexiglass tank was filled with the lower fluid, water, to a depth of 7.725 inches (dimensionless distance 15.45, 41.32 depending on sphere diameter) after having been cleaned with distilled water and allowed to dry. The silicon oil phase was added on top of the water by slowly pouring it down the outside of a tygon tube placed in the corner of the tank. This procedure was employed so that mixing of the two fluids was kept to a minimum during the tank filling operation. Even though there was minimal mixing of the fluids, they were allowed to sit in the tank for several days to insure that separation of the two phases was complete and a sharp discontinuity rather than a zone of mixed fluids existed at the interface. The depth of the upper phase was approximately 21″ and we will have more to say about the depth of this fluid when we discuss how the data taken during an experiment was converted to the drag ratio for the sphere.

At least one hour before a run, the tether wire and one of the two spheres was

attached to the ring force transducer and a current passed across the transducer to allow it to warm up under strain. Once the transducer had been warmed up and the data acquisition equipment was operating, the sphere was lowered toward the interface at a velocity controlled to duplicate Berdan's values of Ca and Cg. It was not possible, though, to set a precise translation speed; therefore, the sphere velocities for these runs only approximate Berdan's. The variance ranges from -0.013 cm/sec to $+0.007$ cm/sec corresponding to a relative change of -3.4% to $+1.8\%$ relative to the velocities set by Berdan. The initial distance of the sphere to the interface was 48.03 radii for the 0.4747 cm sphere and 13.88 radii for the 1.2697 cm one. Even for the larger sphere, this distance was far enough away from the interface that any effects due to start-up motion died out long before the sphere was within even 10 radii of the water-silicon oil interface. At this distance, the effect of the interface was negligible (section VI of Chapter II gives a discussion of the start-up motion for the system). When the center of the sphere was several radii past the plane of the deformed interface, the effect of the tether wire on the flow in the tail of fluid II makes the results suspect so there was no reason to continue the experiment.

In all, eight experiments were performed, four with the large sphere for the parameters corresponding to what is called case C4 in Berdan (1982), and four with the 0.4747 cm sphere to duplicate case C11 in Berdan. The precise values for λ, Ca and Cg for all these runs are presented in Table II. For two runs in each case, the video camera was positioned horizontally at the interface, denoted by "s" after the run number, and for the remaining cases a bottom view of the tracer particles was used ("b" follows the run number for these cases). On two occasions, the output from the force transducer went off-scale on the chart recorder. Both instances were for experiments using the large sphere, corresponding to Berdan's case C4, and in those cases, data could only be taken to sphere position, $l, = 1.30$. For the other

two cases corresponding to Berdan's case C4; a sensitivity 10 times smaller was used on the recorder and force data was taken for all sphere positions, albeit with less sensitivity than the preceding two cases.

TABLE II. Dimensionless Parameters for Experimental Runs.

Run	a (cm)	U (cm/sec)	λ	Ca	Cg
1b	0.4747	0.371	2.88×10^{-4}	0.339	2.092
1s	0.4747	0.375	2.88×10^{-4}	0.343	2.116
2b	0.4747	0.365	2.88×10^{-4}	0.334	2.059
2s	0.4747	0.371	2.88×10^{-4}	0.339	2.092
3b	1.2697	0.368	2.88×10^{-4}	0.336	0.290
3s	1.2697	0.376	2.88×10^{-4}	0.344	0.297
4b	1.2697	0.388	2.88×10^{-4}	0.355	0.306
4s	1.2697	0.374	2.88×10^{-4}	0.342	0.295

III. Numerical Model for Inhibited Tangential Motion at the Interface And Tracer Particle Movement

Before presenting the results from the experiments described in the previous section, we will describe the details of the numerical technique that was used to simulate the behavior of the sphere-interface system under the assumption that the tangential velocity component of fluid II vanishes at the interface. To solve this problem, a boundary integral technique is again employed, as was done in Chapter II. To facilitate this approach, the problem was formulated so that the transistion in going from a fully mobile interface to one with no tangential velocity occurs in the stress jump at the interface. Hence, many of the details of Chapter II remain the

same for this case. In particular, the governing equation are once again all carried out under conditions for which $Re = \mu_2 Ua/\rho_2 \ll 1$):

$$\begin{aligned} 0 &= -\nabla p_1 + \lambda \nabla^2 \mathbf{u}_1 \\ 0 &= \nabla \cdot \mathbf{u}_1 \qquad\qquad \text{in fluid 1} \end{aligned} \tag{2}$$

$$\begin{aligned} 0 &= -\nabla p_2 + \nabla^2 \mathbf{u}_2 \\ 0 &= \nabla \cdot \mathbf{u}_2 \qquad\qquad \text{in fluid 2} \end{aligned} \tag{3}$$

with the boundary condition at infinity

$$\mathbf{u}_1, \mathbf{u}_2 \rightarrow 0 \qquad\qquad \text{as } |\mathbf{x}| \rightarrow \infty \tag{4}$$

and at the interface $\mathbf{x} \in S_I$

$$\mathbf{u}_1 = \mathbf{u}_2 \tag{5}$$

$$\mathbf{n} \cdot \mathbf{u}_1 = \mathbf{n} \cdot \mathbf{u}_2 = \frac{1}{|\nabla H|} \frac{\partial f}{\partial t} \ , \quad H = z - f(r,t) \tag{6}$$

The change comes in the form of the stress jump equation which is now expressed in the form,

$$(\lambda \mathbf{n} \cdot \mathbf{T}_1 - \mathbf{n} \cdot \mathbf{T}_2) = -\frac{1}{Ca} (\nabla \cdot \mathbf{n})\mathbf{n} + \frac{1}{Cg} f\mathbf{n} + \beta(\mathbf{x})\mathbf{t} \ . \tag{7}$$

Here the additional term, $\beta(\mathbf{x})$ is used to account for interfacial tension gradients and other surfactant effects which may inhibit tangential motion in the interface. In principle, by solving the coupled mass-momentum equations for fluid and surfactant molecules, one can obtain an expression for $\beta(\mathbf{x})$. Here, however, a simpler approach is taken. As described in the introduction, we assume that at each point on the

interface $\beta(\mathbf{x})$ has the value necessary for the tangential stress difference to cancel the fluid motion tangent to the interface in fluid II exactly .

$$\mathbf{t} \cdot \mathbf{u}_2 = 0 \qquad \mathbf{x} \in S_I \tag{8}$$

Of course it is not known "a priori" what value of β is needed at each point, and $\beta(\mathbf{x})$ is thus an additional unknown arising from the condition of interface immobility in the tangential direction. to obtain a solution, we need to solve for $\beta(\mathbf{x})$ along with the velocity and stress components at the boundaries of the fluids. The final boundary condition comes from the no-slip condition on the sphere. in particular, the sphere is moving with velocity $U\mathbf{i}_z$ or in non-dimensional terms:

$$\mathbf{u}_2 = \mathbf{i}_z \qquad \mathbf{x} \in S_P. \tag{9}$$

The velocity and pressure at a point in either fluid is again given by Ladyzhenskaya's singularity equation

$$\begin{aligned} \mathbf{u}(\mathbf{x}) \;=\; & \frac{1}{8\pi} \int_S \left[\frac{\mathbf{I}}{R} + \frac{(\mathbf{x} - \eta)(\mathbf{x} - \eta)}{R^3} \right] \cdot \mathbf{T}(\eta) \cdot \mathbf{n} \, \mathrm{dS}_\eta \\ & - \frac{3}{4\pi} \int_S \frac{(\mathbf{x} - \eta)(\mathbf{x} - \eta)(\mathbf{x} - \eta)}{R^5} \cdot \mathbf{u}(\eta) \cdot \mathbf{n} \, \mathrm{dS}_\eta \end{aligned} \tag{10}$$

$$\begin{aligned} p(\mathbf{x}) \;=\; & \frac{1}{2\pi} \int_S \left[\frac{1}{R} - \frac{3(\mathbf{x} - \eta)(\mathbf{x} - \eta)}{R^5} \right] \cdot \mathbf{u}(\eta) \cdot \mathbf{n} \, \mathrm{dS}_\eta \\ & + \frac{1}{4\pi} \int_S \frac{(\mathbf{x} - \eta)}{R^3} \cdot \mathbf{T}(\eta) \cdot \mathbf{n} \, \mathrm{dS}_\eta \end{aligned} \tag{11}$$

where

η = position on bounding surface, the variable of integration

$$\mathrm{R} \equiv |\mathbf{x} - \eta| = |\mathbf{r}|$$

(Ladyzhenskaya, 1963).

Now, however, when the integral form for the velocity on the fluid I side of the interface is subtracted from the equation for fluid II and the condition for continuity of velocity at the interface applied, Eq. (5), the result is:

$$\frac{1}{2}(\lambda+1)\mathbf{u}^I(\mathbf{x}) = \frac{3}{4\pi}(\lambda-1)\int_{S_I}\frac{\mathbf{rrr}}{R^5}\mathbf{u}^I\cdot\mathbf{n}\,\mathrm{dS_I} + \frac{1}{8\pi}\int_{S_P}\left[\frac{\mathbf{I}}{R}+\frac{\mathbf{rr}}{R^3}\right]\cdot\mathbf{T}_2^P\cdot\mathbf{n}\,\mathrm{dS_P}$$
$$-\frac{1}{8\pi}\int_{S_I}\left[\frac{\mathbf{I}}{R}+\frac{\mathbf{rr}}{R^3}\right]\cdot\mathbf{F}(f)\,\mathrm{dS_I}\quad,\quad \mathbf{x}\in S_I \tag{12}$$

where the function $\mathbf{F}(\mathrm{f})$ is the stress difference at the interface. With $K = 1/|\nabla H|$:

$$\mathbf{F}(f) \equiv \lambda\mathbf{n}\cdot\mathbf{T}_1^I - \mathbf{n}\mathbf{T}_2^I = -\frac{1}{Ca}\left[\frac{K}{r}\frac{\partial f}{\partial r}+K^3\frac{\partial^2 f}{\partial r^2}\right]\mathbf{n}+\frac{1}{Cg}f\mathbf{n}+\beta(\mathbf{x})\mathbf{t} \tag{13}$$

which is analogous to Eqs. (12) and (13) in Chapter II. The remaining integral equations derived in Chapter II are unaffected by the change in Eq. (7). Eq. (13) is written in the form used when a single coordinate system describes the interface shape function. As for the numerical technique of Chapter II, however, when the interface deformation became large, three functional representations were used to describe the surface of the interface. In this case, the proper form of Eq. (15) in Chapter II was used to represent the interface and the corresponding expression for $\mathbf{F}(f)$ in equation (16) was employed in evaluating the shape dependent terms of Eq. (13). Since $\beta(\mathbf{x})$ does not include any shape dependent terms (it is an unknown which is being solved for) it was not necessary to take the different coordinate representations into account when dealing with that term.

After invoking the collocation assumption and replacing the integrals with sums, the immobile interface condition adds an additional NI unknowns for the values of β at each node point but also provides NI additional equations from the tangential velocity constraint. Appendix A gives the full system of integral equations as well as the algebraic equations resulting from application of the collocation

assumption. The linear system was solved by Gaussian elimination and marched forward in time using an explicit integration of the kinematic condition, Eqn. (6). Figs. 2 and 3 show calculated results for both mobile and immobile interfaces and particular values of the dimensionless parameters. Specifically, Fig. 2 gives results for the case $\lambda = 2.88 \times 10^{-4}$, $Ca = 0.344$, $Cg = 0.297$ equal to the parameters of case $3s$ in the experimental work and corresponding to Berdan's case C4; while Fig. 3 corresponds to case C11 in Berdan with $\lambda = 2.88 \times 10^{-4}$, $Ca = 0.339$, $Cg = 2.092$. These are the parameters for experimental case $1b$. In both figures, as was done in the previous chapter, the results are plotted in a reference frame fixed on the sphere. The interface then appears to be sweeping past the fixed sphere.

Consideration of Figs. 2 and 3 shows a modest but clear difference between the interface shapes for mobile and immobile interface conditions. It is evident that the ability of the interface to support a tangential stress jump greatly effects the role of λ in controlling interface deformation. At first, $l > 0$, the $\mathbf{u} \cdot \mathbf{t} = 0$ cases show wider sphere-interface separation for $r = 0$ than is seen for a mobile interface. Later, in both these immobile cases, however, but most notably in the $Cg = 2.092$ calculation, the film in front of the sphere continues to thin, a phenomenon usually associated with $\lambda \gg 1$, rather than forming a thick film of approximately fixed width which translates with the sphere as occurs with a mobile interface for the present value of λ. The latter type of behavior was seen in the small λ results of Chapter II. By applying the concepts developed in the previous chapter for the mechanism of interface deformation in opposition to the restoring forces of density difference and interfacial tension, we can understand what factors cause this change in behavior. For an immobile interface, fluid II is forced into motion by the sphere, but can only move normal to the surface, and so will have a larger z-component of velocity, and thus show greater deformation, than the case when no surface active agents are present. This will be accompanied by a larger force on the sphere than

predicted by the mobile interface result.

However, the film thickness does not *remain* greater for the immobile case as the sphere continues to move past the $z = 0$ plane. Restoring forces continue to grow as the sphere moves and the interface deforms, and the particle cannot support this ever increasing volume of fluid II across the $z = 0$ plane. Therefore, fluid II must drain back below the plane of the flat interface, and there will be a region of the interface with a negative z-component of velocity. For $\lambda \ll 1$ and a mobile interface, interfacial tension drives a flow encapsulating the sphere creating a film that does not thin as the sphere continues to move with the excess fluid draining from the tail, and a $-z$ velocity in the portion of the interface outside the film. The flow over the portion of the interface encapsulating and moving with the sphere is parallel to the sphere surface, that is, tangential at the interface. Radial motion can not occur if the thickness of the film is maintained. For high λ cases, this tangential motion is opposed by the large energy required to cause fluid I to flow in order to maintain continuity of velocity at the interface; for the model of interface behavior applied here, such tangential motion is stopped entirely, preventing encapsulation. Therefore, in order to allow drainage of fluid II as the sphere moves further past $z = 0$, the film continues to thin for the surfactant problem.

In the previous chapter we explained how once a stable film is established around the sphere, the drag will eventually decrease; whereas, for a film thinning case, the drag increases monotonically. This same behavior will be seen for these cases in our discussion of the experimental results; although, the change in the qualitative behavior in the region ahead of the sphere is caused by the type of boundary condition applied for the stress jump at the interface rather than by varying the physical parameters as was done in Chapter II.

IV. Experimental Results

(a) Data evaluation for theoretical comparisons

As stated in the introduction, one purpose of performing these experiments was to compare the results to numerical calculations of the type described in Chapter II. This comparison is made to explore the degree to which experiments in the plexiglass tank with a sphere-tether wire combination body can be made to represent the problem solved in the previous chapter, that is, a sphere moving toward a mobile, infinite interface between two semi-infinite fluids. In order to perform this comparison, the results of the experiments, which of course, are all recorded in some standard dimension (inches, centimeters, volts, seconds) must be expressed as non-dimensional quantities; furthermore, the effect of the bounding walls and tether wire must be discounted from the sphere-interface results.

Three types of data are presented here from eight experiments with a sphere approaching the interface. For all cases, the force on the sphere-tether wire body was measured by the ring force tensiometer and the result recorded in volts by a strip chart recorder. For half the runs, the deformation of the interface in the z-coordinate (direction parallel to sphere motion) was recorded on videotape, and for the other half of the experiments, radial distance of tracer particles at the interface from the center of the tank was measured as a function of time. The interface deformation data stored on videotape in an analog form was digitized by tracing the shapes by hand onto a transparency and measuring the position of points on the interface in 1/10 inch increments. The tracings of the interface shapes were carried out as accurately as possible, but despite setting the brightness and contrast to the optimal position for each frame traced, the resolution of the monitor prevented the tracings from being accurate to more than ± 2 mm which translates to non-dimensional lengths of 0.14 for the smaller sphere and 0.06 for the larger. This resolution problem did not arise in following the tracer particles at the

interface as they were essentially pin points of light showing precisely against the dark background. The sphere diameter was also measured from a tracing and this length used to non-dimensionalize the position data for comparison with numerical results. Table B2 presents the z-coordinate data for the four side-view experiments as measured from the transparencies and after non-dimensionalization with respect to a. Table B3 gives the tracer particle data for those four experiments in the same way.

Treatment of the force data was more involved than a simple non-dimensionalization with respect to the characteristic force of Chapter II. For comparison purposes, it is necessary to account for any force or force modification arising in the experimental system which would not occur in the sphere-infinite interface system of the numerical work. This includes the force due to the wire, the correction to the force on the combined sphere-wire body relative to the sum of the individual forces on the wire and sphere, and wall corrections. Berdan (1982) discusses the theories which are applied to the experimental system to deduce what the force would be if the sphere were alone and the fluid was unbounded. Here, we use Berdan's procedure, as described below to treat the interactions as well.

We begin by considering the effect of the walls on the sphere's drag. Any wall correction can be written in the form

$$Drag\ Ratio = \frac{F}{F_\infty} = \frac{1}{1 - k\left(\frac{a}{h}\right) + 0\left(\frac{a}{h}\right)^3} \tag{14}$$

where F_∞ is Stokes drag on a sphere in an infinite fluid, $6\pi\mu Ua$, a is the sphere radius; h, the distance from the sphere center to the bounding surface and k, a geometry dependent coefficient For a fluid bounded by 1 plane wall, $K = 0.5625$ (Happel and Brenner, 1983); and for a fluid bounded by two parallel infinite walls, $k = 1.0040$ (Ho and Leal, 1973). There is also a result available for a circular cylindrical enclosure, $k = 2.1044$ (Happel and Brenner, 1983). However, no an-

alytic solution exists for k when a sphere moves enclosed by four perpendicular walls. One choice in handling the 4-wall correction is merely to double k for the two-wall problem and use $k = 2.0080$. Another choice is to apply the correction for a concentric cylinder with diameter equal to the width of the tank which will necessarily over correct for the wall effect as the inscribed cylinder will lie closer to the sphere than the four planar walls at all points but the four points of tangency. The difference in the drag ratio between using twice the two-wall correction and k for an inscribed cylinder is less than 0.8% for the value of a/h that applies for the larger sphere; for the smaller sphere, this difference drops to less than 0.3%. Clearly, the error associated with one choice over the other is very small. However, we choose the inscribed cylinder correction for the sphere-wall interaction in the work reported here. The determining factor in this choice is that exact theoretical results exist for the axial motion of concentric cylinders and this result can be used to correct the drag for the force on the wire.

To account for the drag on the wire, we modify Happel and Brenner's formula for the drag per unit length on a cylinder (radius b) which moves parallel to its axis with velocity U relative to a concentric outer cylinder with radius h. Multiplying their expression by the wire's length L, we get an expression for the force on the finite wire

$$F_{wire} = \frac{2\pi\mu UL}{\ln\left(\frac{h}{b}\right) - 1} \tag{15}$$

where we use the half-width of the tank for h.

We see from the preceeding discussion that we can easily account for the contribution to the "system" drag due to the motion of the wire through a bounded fluid (wire-fluid and wire-wall interactions), and the correction to the drag on a sphere due to sphere-wall interactions. We must finally consider the effect the wire and sphere have on each other. Clearly, the presence of the wire at the back of the

sphere should significantly effect the flow in that region with an associated change in the drag, while the presence of the sphere in front of the wire should moderate the flow seen by the wire and thus effect the force acting on it. As a result, the drag on the combination sphere-wire body will differ significantly from the sums of the drag on the sphere and wire separately. The problem of a sphere attached to a slender body of circular cross section is solved analytically by de Mester and Katz (1974) for motion of the body in an infinite fluid. The force on the sphere-slender body combination in that case is shown to depend on the sphere and slender body radii as well as the length of the slender body, the last in a highly non-linear way. To get an accurate measure of the length of the slender body (wire) in the experiments, the depth of the silicon oil was carefully measured before each experiment. In addition to the force on the sphere-slender body combination, de Mestre and Katz also give the force that each would experience if it moved independently through an infinite fluid. The ratio of the drag on the combination body to the individual contributions from the sphere and the slender body is called β. No one has considered the effect of *bounding* walls on the analytic results of de Mestre and Katz for the sphere-wire combination; thus to account for the presence of walls in the experiment, Berdan introduces an empirical factor α into de Mestre and Katz's result. This factor, α , is defined by the equation:

$$\alpha + \beta = \frac{\text{Drag on (sphere + wire) in tank}}{\text{drag on sphere in tank + drag on wire in tank}} \tag{16}$$

The correction term, α, modifies de Mestre and Katz's interaction factor, β, to account for the presence of the tank walls and the interface. As for the wall correction coefficient, k, α depends only on the geometry of the system, and so can, in principle, be determined once for all runs with a given sphere-wire radius ratio. Berdan evaluated α by finding the value which would yield a drag on the

sphere equal to Stokes drag when the sphere is far ($l \gg 10$) from the interface. In our present work, we also use Berdan's value for α, 0.03. Berdan's method of choosing α assumes that the effect of the interface and walls on the sphere-wire combination will be independent of distance from the interface. It is possible (or even likely) that the sphere-wire interaction will change as the sphere approaches the interface, and the value of α should be modified in some unknown manner. To check the appropriateness of the constant α assumption, Berdan compared experimental results for the sphere approaching a rigid wall to Brenner's theoretical result for an infinite plane wall (Brenner, 1961). In this case, the corrected experimental results with $\alpha = 0.03$ agreed to $\pm 5\%$ with the theoretical predictions. This gives some evidence of the appropriateness of the various corrections used to deduce the drag on the sphere in the presence of the wire and tank walls including the assumption of constant $\alpha = 0.03$. Presumably any departure from this assumption would be stronger for the rigid wall case than for the deformable interface that we consider here.

For comparison to the numerical drag results for an isolated sphere in an infinite two-fluid system, the corrections for the measured force just outlined were applied to the output from the ring force tensiometer as follows: $\alpha + \beta$ was calculated from the geometric information about the size and position of the sphere-wire body and the total *measured* force is then divided by that computed quantity. The resulting value is the sum of the forces on a sphere and a wire moving separately in a bounded fluid. Eq. (15) is evaluated for the force on the wire and this value is subtracted from the adjusted force, thus yielding the drag on the sphere in a bounded fluid. Finally, Eq. (14) is used to transform this force on the sphere in a bounded fluid into the drag which would have existed for the same sphere in an infinite domain. Table B4 presents the sphere drag data both in the raw form as read from the chart recorder (columns 1 and 2 where "position" refers to the x-coordinate measuring

time, and height is the y-coordinate, measuring the force), as well as the final scaled form for the distance to the interface in sphere radii and the drag which would exist on the sphere if the two fluid systems were unbounded, scaled with Stokes drag. Also included in this table are the total force in dynes and the force which would be experienced by the wire and sphere separately. The correction due to sphere-wire interactions is included under the heading "ratio". In the following section, we compare the corrected experimental results for a sphere approaching an unbounded interface with the results of boundary integral calculations.

(b) Comparison of experimental and numerical results

We begin by considering the deformation of the interface in the direction parallel to the sphere's motion. Fig. 4 illustrates the measured and predicted interface shapes for the high Cg and low Ca experimental case that was originally considered by Berdan. The parameters used for the sake of calculation were Berdan's original values of $\lambda = 0.003$, $Ca = 0.339$, $Cg = 2.029$. As discussed previously, however, it was not possible to duplicate these parameters precisely in the experiments. While the sphere velocity could be controlled at a fixed value with precision, the actual velocity could not be set accurately enough to match the previous experiments. This variation in the sphere velocity caused Ca and Cg to vary from the numerical values by $+1.2\%$ to -1.5% for the high Cg cases considered here (1,2) and from $+3.2\%$ to -2.3% for the low Cg cases (3,4) that will be considered shortly. These small differences in Ca and Cg might effect the results slightly but should not cause wide variations between cases. Far more significant was the the error introduced in tracing the interface position from the video monitor. Errors in reading the position of the $z = 0$ plane or the actual position of the interface, could result in errors on the order of $5 - 15\%$. In light of the magnitude of the possible errors that could potentially be introduced into the interface shapes, Fig. 4 shows good

reproducibility between the several experimental runs performed. For the low Cg, low Ca cases ($\lambda = 0.003$, $Ca = 0.344$, $Cg = 0.297$) shown in Fig. 5, the several experimental cases are in even better agreement; this is a result of the larger sphere size causing the relative error in reading the interface shape from the monitor to be smaller. One conclusion which we can draw from the results of Figs. 4 and 5, without reference to numerical data, is that the discrepancy reported by Berdan between experimental observation and theoretical calculations for a clean, mobile interface was not the result of an isolated error in his procedure nor a fault in the evaluation of physical constants for the fluids since his results were duplicated here in several experiments.

A comparison of the experimental results to the shapes predicted by numerical calculations for mobile and immobile interfaces is shown in Figs. 4 and 5. Fig. 5 shows that the experimental shapes for small Ca and Cg agree with the results of the calculations within the limits of our ability to read the interface position from the video monitor, but that the difference between the shapes for the mobile and immobile interfaces is of the same order as the experimental error. Therefore, we can only conclude that the experimental results for interface shape for $\lambda = 2.88 \times 10^{-4}$, $Ca = 0.344$, $Cg = 0.297$ are not inconsistent with either type of interface behavior. However, the continuous thinning of the fluid film in front of the sphere, which was seen in the discussion of Fig. 3 to be a feature of the *immobile* interface system, is demonstrated by the experimental results both for the low Cg case of Fig. 5 and to an even greater degree by the shapes shown in Fig. 4. The film thickness is equal to the height of the interface at $R = 0$ plus $(l - 1)$. This change in the behavior of the fluid film to that qualitatively associated with the immobile interface calculations tends to support the hypothesis that the difference between experimental and theoretical results in Berdan's work is a consequence of some surface active agent effecting the behavior of the interface. Although a consis-

tent difference between mobile and immobile results and experimental observations cannot be seen in the low Cg data of Fig. 5, the results shown in Fig. 4 reveal that the experimental interface shapes consistently lie above *both* sets of calculations to a degree which is beyond the error in reading interface shapes from the video monitor. The experimental results indicate that the simple model of a completely immobilized interface for the behavior of the interface when surface active species are present underpredicts the degree of deformation of the actual interface, though the numerical results are closer to experimental observation in this case than for the clean, mobile interface. Thus while these deformation results do provide circumstantial evidence of reduced interface mobility, they do not allow a definitive determination whether significant restriction of the tangential flow at the interface actually occurs.

In contrast, the tracer particle data which shows a direct image of motion in the interface, does provide conclusive evidence of a reduction in the r-component of fluid motion at the interface, and this corresponds directly to reduced tangential mobility. In particular, Fig. 6 shows the tracer particle results for the two experiments performed with the small sphere (cases 1b, 2b). The results show that the tracer particles follow very nearly the trajectories predicted by the *immobile* surface model, with perhaps only slight tangential motion. For the low Cg experiments (3b, 4b) whose results are shown in Fig. 7, the motion at the interface is intermediate to the two limiting cases but still shows a significant reduction in mobility. Again the results for two experiments are combined in the same figure and both show greatly reduced motion at the interface. From the data on the r and z-component of interface deformation for the eight experiments performed for this work, and the two done previously by Berdan, we believe that there is significant restriction of the tangential flow in the fluid I-fluid II interface, and that this is the primary source of discrepancy between the low Ca data and the predictions for a mobile interface

as originally hypothesized by Berdan. This restriction is manifested by a greatly reduced r-component of fluid velocity, and an increase in the amount of deformation in the z direction. Both these trends are qualitatively predicted by the simple immobile interface model that we use to account for surfactant effects; however, the model predicts the restriction in tangential motion more accurately than the increase in z deformation.

In order to complete the comparison between data and numerical predictions, we must compare the drag results from the experiments to the numerically calculated drag when the fluid-fluid interface allows no tangential velocity. This comparison is illustrated in Figs. 8 and 9. The insets in these figures show the results for the full range of L in the experiments; whereas, the main figure shows the drag ratio in the region where the sphere is close to the interface and suffers the greatest effect from its influence. The figures for the full experiment are included to demonstrate that the drag on the sphere inferred from our experiments does reduce to Stokes drag when the sphere is far away from the interface. This gives some extra confidence in our ability to accurately account for the extra forces in the experimental system. Both figures show that there is good reproducibility of results for the several experiments with the small degree of scatter attributable to the slight variations in Ca and Cg. The results demonstrate that although tangential motion is inhibited at the interface, the simple model of completely immobilized tangential motion, that is, $\mathbf{u} \cdot \mathbf{t} = 0$, does not accurately predict the drag on the sphere. In fact, although the experimental drag on the sphere is $\approx 40\%$ greater than the numerical value for the mobile interface case with $Ca = 0.344$, $Cg = 0.297$ and $\approx 60\%$ larger for the large Cg case, the *qualitative* behavior of the experimental systems for $l < 0$ follows that predicted for the *mobile* interface system. In Fig. 8, the rate at which the drag increases slows as the center of the sphere passes the plane of the flat interface. In Fig. 9, a maximum is displayed in the experimental drag ratio

which corresponds to the theoretically calculated predictions. Of course, too much emphasis should not be placed on the $l < 0$ results. In this region, wire-interface effects are likely to be significant, and theses interactions are not accounted for in our treatment of the experimental drag.

The fact that the experimental results behave qualitatively more like the mobile interface than the immobile one is most likely a result of the inability of the interface to produce a large enough tangential stress jump in the film region to completely inhibit tangential motion there. We have already shown how the results of our calculations for the immobile interface indicate the formation of a draining film in front of the sphere as it continues to move. Fig. 9 now shows how the force on the sphere continues increasing as this layer thins. The calculations also show the tangential stress jump needed to maintain $\mathbf{u} \cdot \mathbf{t} = 0$ grows with the thinning of the film. In the experiments, though, the surfactants present cannot produce a stress jump in this region large enough to overcome the high stress at the interface, and fluid will begin to move tangentially. From this point on, the interface will behave qualitatively like the mobile one in the film region, and the drag on the sphere will decrease as some encapsulation occurs. The stress at the interface outside the film region will be low enough that the surfactant will be able to maintain a stress jump to prevent tangential motion so the overall drag on the sphere will remain higher than the drag calculated for the mobile interface cases. There are no tracer particle results for the interface in the film region as it was not possible to see particles through the light reflected from the surface of the sphere. For the other cases presented by Berdan in which the experiments agreed with the mobile interface calculations, Ca was at least a full order of magnitude greater than for the cases discussed here. In those large Ca experiments, the interfacial tension gradient could never acheive a strength large enough to counteract the tangential flow, and good agreement between experiment and calculation resulted.

The conclusions we draw from all of the data taken for the experiments is that the experimental results for the low Ca system can be qualitatively represented by the simple model where all tangential motion at the interface is suppressed. Tracer particle data supports the conclusion of reduced interface mobility by directly showing a reduction in the r-component of fluid velocity at the interface. The quantitative comparison of the experiments with numerical results employing the immobile interface model, though, indicates that this simple model does not accurately represent the behavior at the interface nor accurately predict the force on the sphere in the presence of a real surfactant film. In order to bring experimental and numerical results into better agreement, a more sophisticated model must presumably be used to represent surfactant effects in the numerical scheme.

References

Berdan II, C. 1982 Ph. D. Dissertation California Institute of Technology.

Brenner, H. 1961 The slow motion of a sphere through a viscous liquid toward a plane surface. *Chem. Eng. Sci.* **10**, 242.

Davis, R.E. and Acrivos, A. 1966 The influence of surfactants on the creeping motion of bubbles. *Chem. Eng. Sci.* **21**, 681.

de Mestre, N.J. and Katz, D.F. 1974 Stokes flow about a sphere attached to a slender body. *J. Fluid Mech.* **64**, 817.

Happel, J. and Brenner, H. 1983 *Low Reynolds Number Hydrodynamics, 2nd ed.*, Martinus Nijhoff Publishers, The Hague.

Ho, B.P. and Leal, L.G. 1974 Inertial migration of rigid spheres in two-dimensional unidirectional flows. *J. Fluid Mech.* **65**, 365.

Holbrook, J.A. and LeVan, M.D. 1983a Retardation of droplet motion by surfactant. Part 1. Theoretical development and asymptotic solutions. *Chem. Eng. Commun.* **20**, 191.

Holbrook, J.A. and LeVan, M.D. 1983b Retardation of droplet motion by surfactant. Part 2. Numerical solutions for exterior diffusion, surface diffusion and adsorption kinetics *Chem. Eng. Commun.* **20**, 273.

Ladyzhenskaya, O.A. 1963 *The Mathematical Theory of Viscous Incompressible Flow.* Gordon and Breach, New York.

Lee, S. H. and Leal, L.G. 1982 Motion of a sphere in the presence of a deformable interface. Part 2: Numerical study of the translation of a sphere normal to an interface. *J. Coll. and Interface Sci.* **87**, 81.

LeVan, M.D. and Newman, J. 1976 The effect of surfactant on terminal and interfacial velocities of a bubble or drop. *A.I.Ch.E. J.* **22**, 695.

Olbricht, W.L. 1976 Ph. D. Dissertation California Institute of Technology.

Sadhal, S.S. and Johnson, R.E. 1983 Stokes flow past bubbles and drops partially coated with thin films. Part I. Stagnant caps of surfactant film - exact solution. *J. Fluid Mech.* **126**, 237.

Scriven, L.E. 1960 Dynamics of a fluid interface: Equations of motion for Newtonian surface fluids. *Chem. Eng. J.* **12**, 981.

Shail, R. and Gooden, D.K. 1983 On the slow translation of a solid submerged in a fluid with a surfactant film - II. *Int. J. Multiphase Flow.* **9**, 227.

Wei, L.Y.; Schmidt, W. and Slattery, J.C. 1974 Measurement of surface dilational viscosity. *J. Coll. and Interface Sci.* **48**, 1.

Figure Captions

Figure 1: Schematic view of experimental apparatus. a: variable speed motor; b: low pitch 6 inch aluminum take-up wheel; c:1/16 inch stainless steel cable with swivel fitting at lower connection; d: ruler; e: 3/4 inch square by 42 inch aluminum quide bar; f: 6 inch guide affixed rigidly to wall with 8 screw adjustments for vertical allignment of guide bar; g: mark for ruler readings, attatched to f; h: digital clock; i: ring force transducer with thermal isolation mounting to guide bar; j: thermal isolation housing for force transducer; k: 0.0041 inch straightened steel wire; l: polished bronze sphere; m: fluid I, water: n: fluid II, silicon oil blend; o: 15inch square by 36″ plexiglass tank; p: video camera with 6:1 zoom and 2 diopter close-up lens; q: video camera with 6:1 zoom and 2 diopter close-up lens; r: screen splitter and recorder to combine images from cameras p and q and record results; s: video monitor with interface from camera p in upper section and clock and ruler from camera q in lower section.

Figure 2: Interface shape as a function of sphere position (drawn in a reference frame in which the sphere is fixed) for $\lambda = 2.88\times10^{-4}$, $Ca = 0.344$, $Cg = 0.297$; —— shapes for mobile interface calculation; – – – shapes for immobile interface calculation. Constant velocity case.

Figure 3: Interface shape as a function of sphere position for $\lambda = 2.88\times10^{-4}$, $Ca = 0.339$, $Cg = 2.029$; —— shapes for mobile interface calculation; – – – shapes for immobile interface calculation. Constant velocity case.

Figure 4: Interface shape as a function of sphere position for $\lambda = 2.88\times10^{-4}$, $Ca = 0.339$, $Cg = 2.029$; —— shapes for mobile interface calculation; – – – shapes for immobile interface calculation; $\sqcup$ (Berdan's data); $\triangle$ (Case

1s); × (case 2s).

Figure 5: Interface shape as a function of sphere position for $\lambda = 2.88 \times 10^{-4}$, $Ca = 0.344$, $Cg = 0.297$; —— shapes for mobile interface calculation; – – – shapes for immobile interface calculation; □ (Berdan's data); △ (Case 3s); × (case 4s).

Figure 6: R trajectories of points on the interface for case corresponding to $\lambda = 2.88 \times 10^{-4}$, $Ca = 0.339$, $Cg = 2.029$; —— trajectory from mobile interface calculation; – – – trajectory from immobile interface calculation; △ position of tracer particles, case 1b × position of tracer particles, case 2b

Figure 7: R trajectories of points on the interface for case corresponding to $\lambda = 2.88 \times 10^{-4}$, $Ca = 0.344$, $Cg = 0.297$; —— trajectory from mobile interface calculation; – – – trajectory from immobile interface calculation; △ position of tracer particles, case 3b × position of tracer particles, case 4b

Figure 8: Drag ratio versus sphere position for the case $\lambda = 2.88 \times 10^{-4}$, $Ca = 0.344$, $Cg = 0.297$; —— results from mobile interface calculations; – – – results from immobile interface calculations. ○ (Case 3b); × (Case 3s); △ (Case 4b); □ (Case 4s); ◇ (Berdan's data).

Figure 9: Drag ratio versus sphere position for the case $\lambda = 2.88 \times 10^{-4}$, $Ca = 0.339$, $Cg = 2.029$; —— results from mobile interface calculations; – – – results from immobile interface calculations. ○ (Case 1b); × (Case 1s); △ (Case 2b); □ (Case 2s); ◇ (Berdan's data).

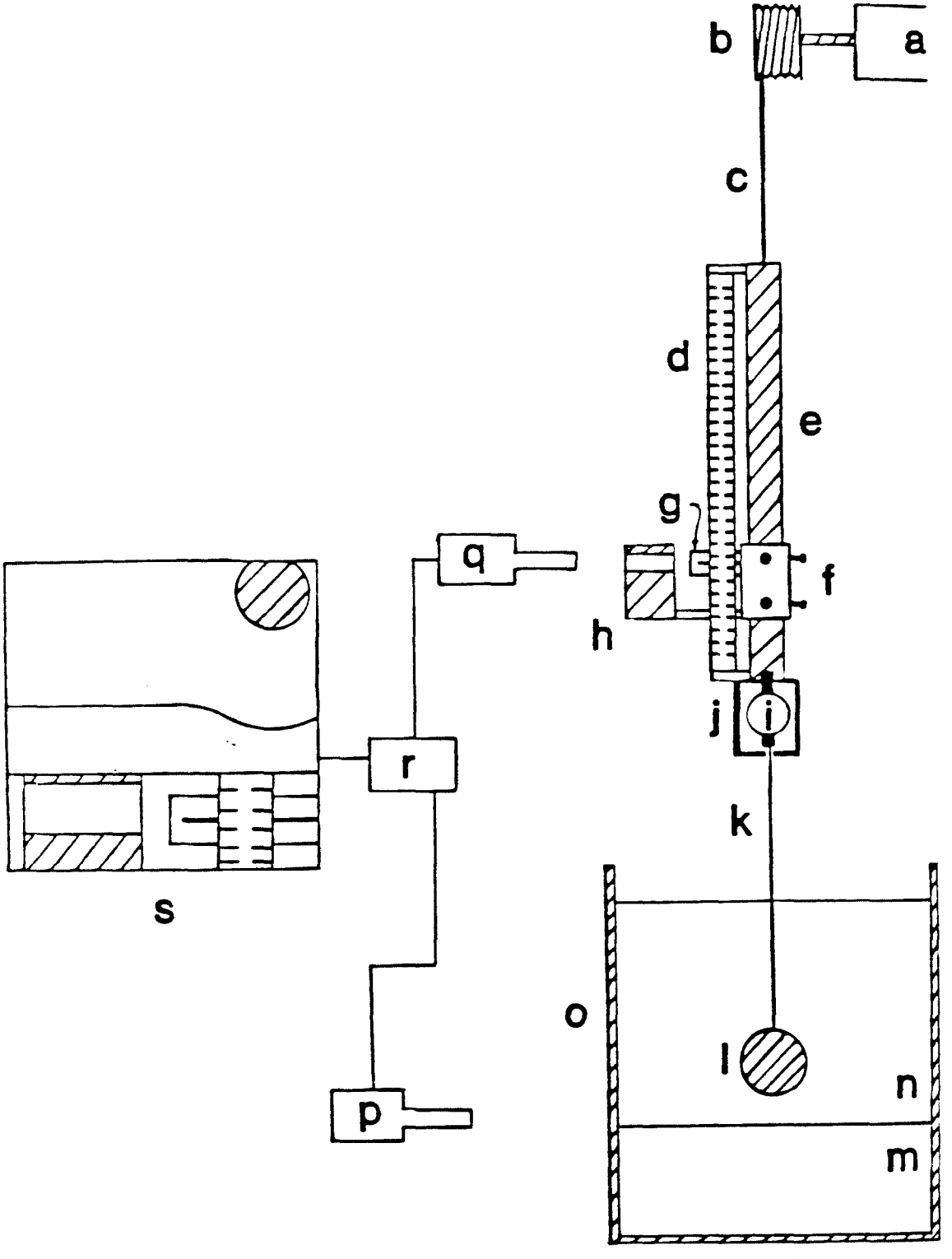

Figure 1.

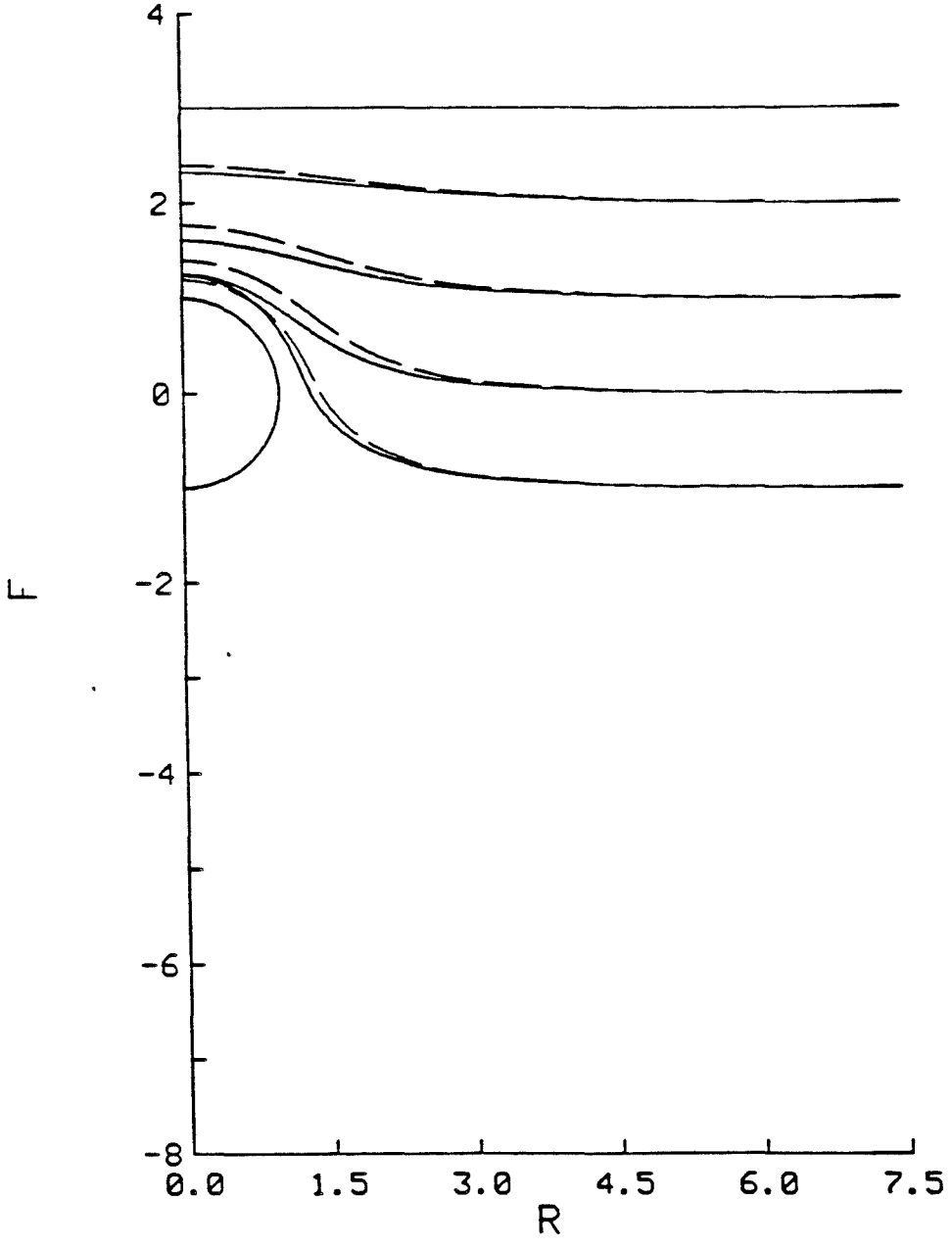

LAMBDA = 0.0003 CA = 0.344 CG = 0.297

Figure 2.

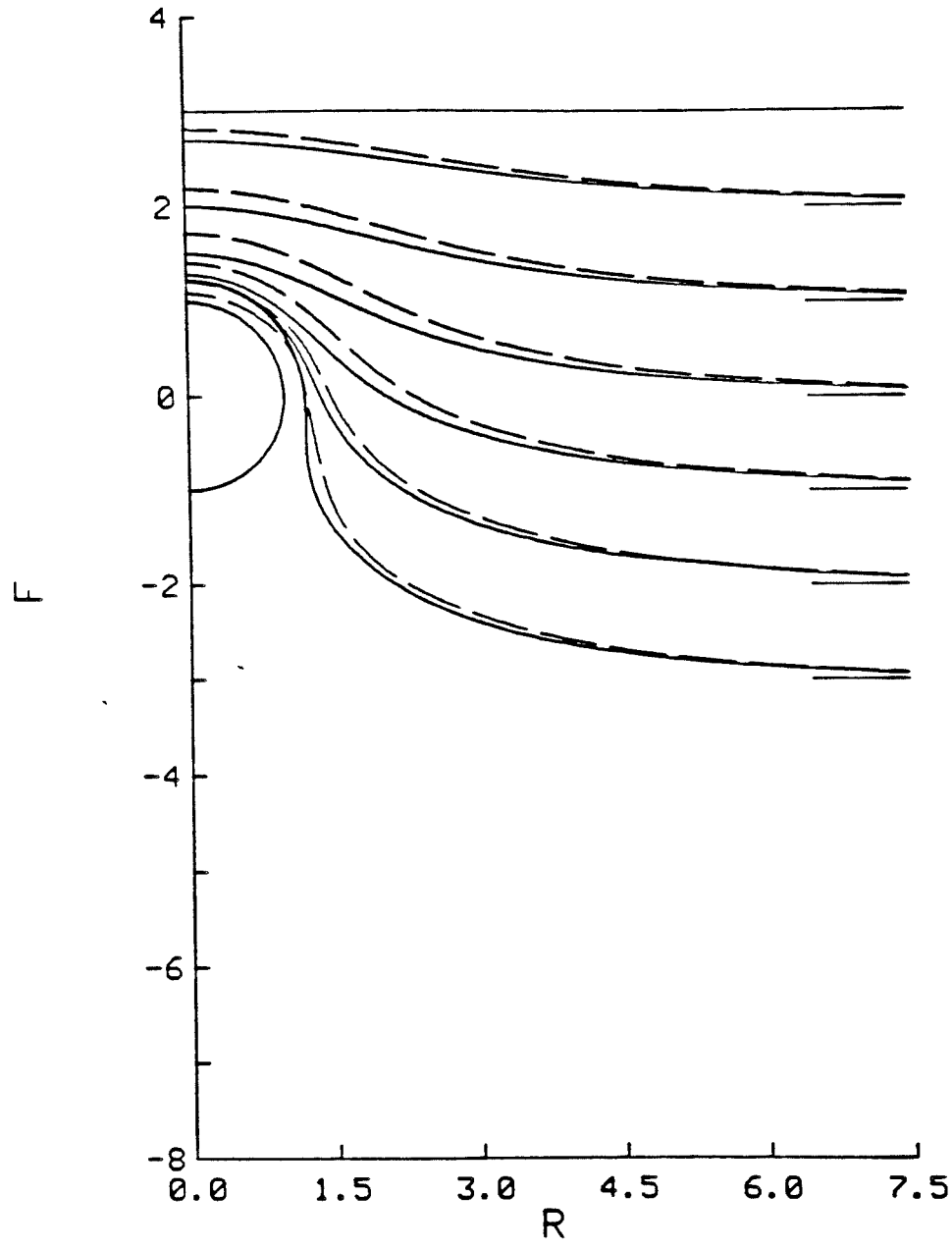

Figure 3.

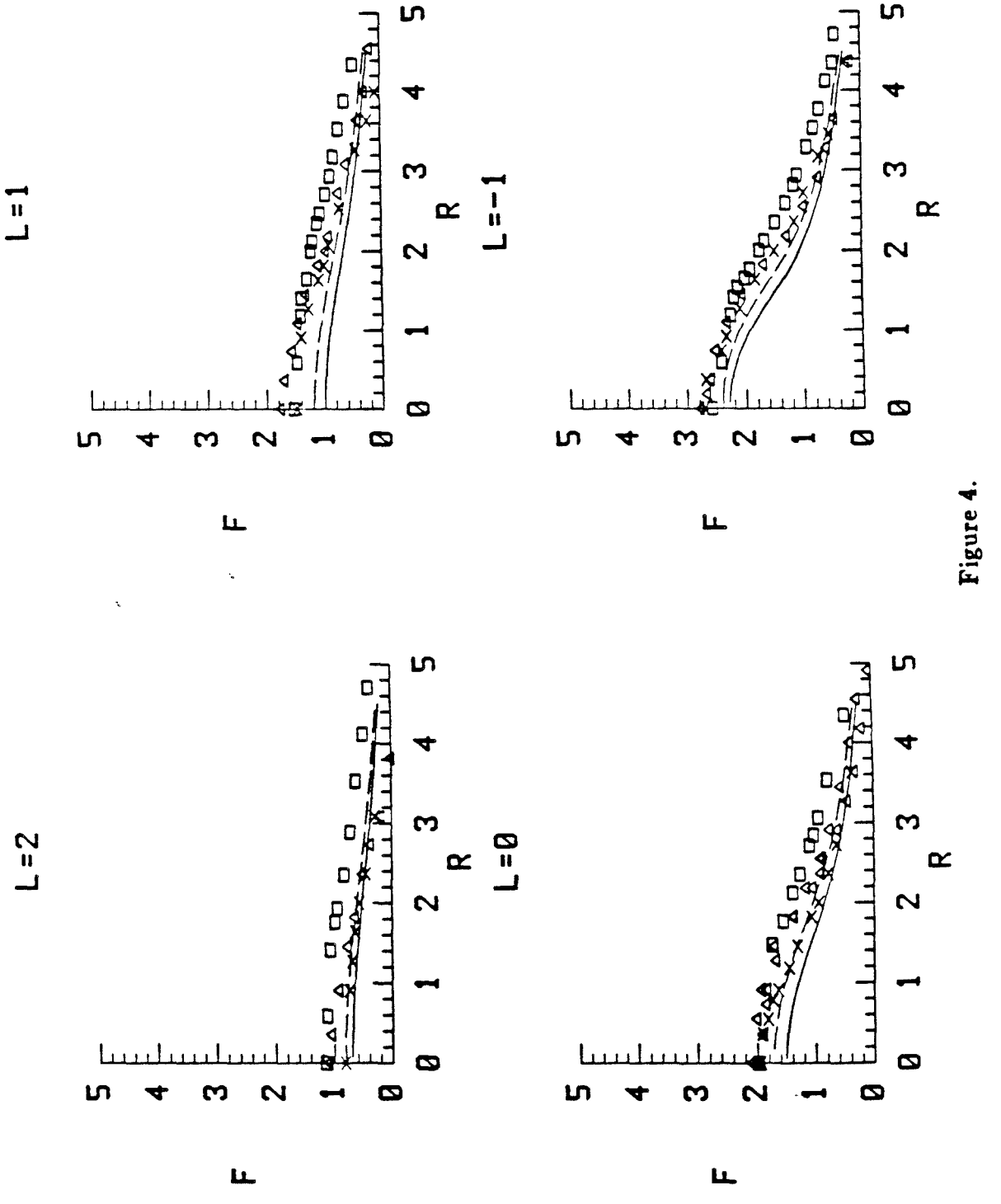

Figure 4.

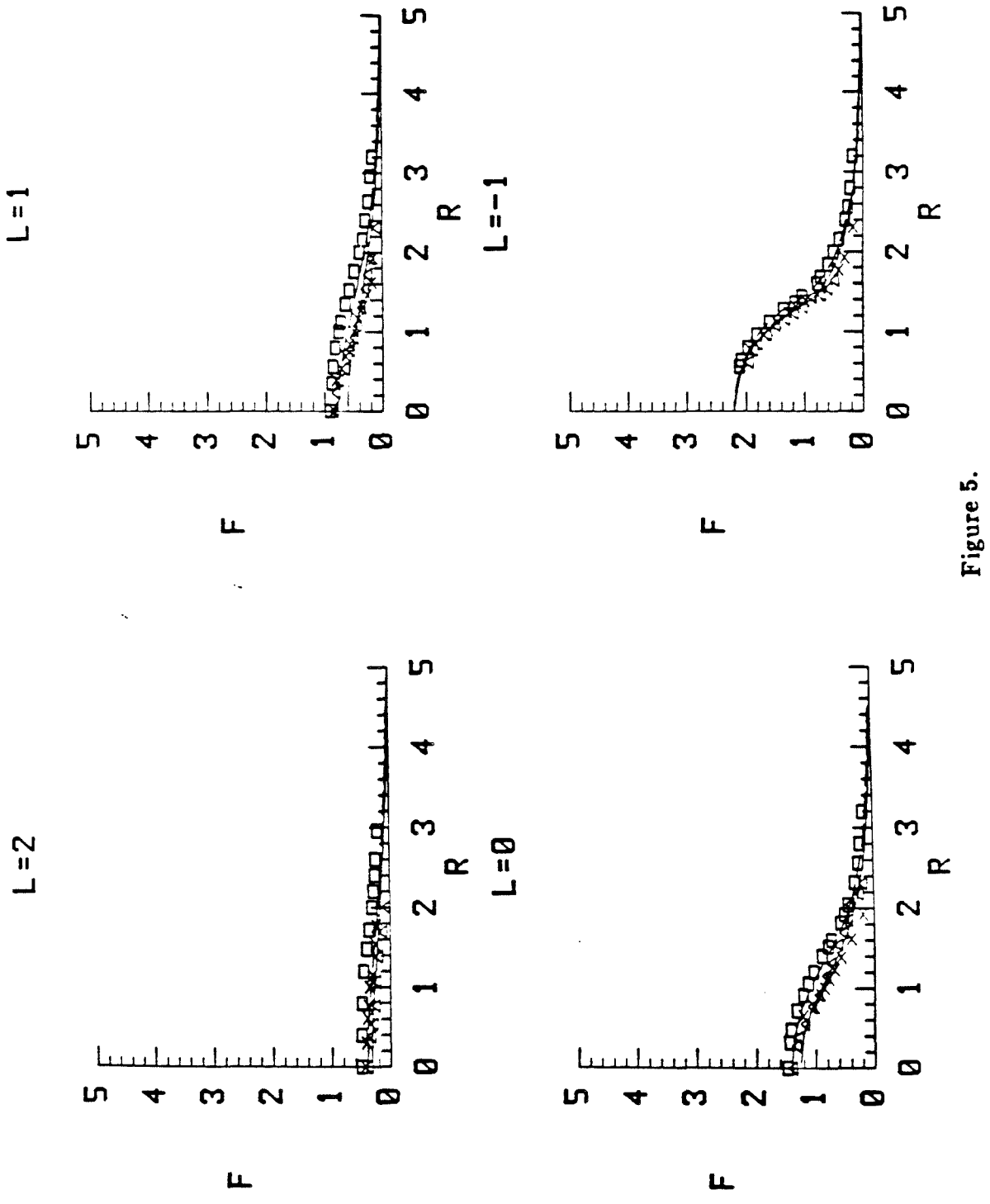

Figure 5.

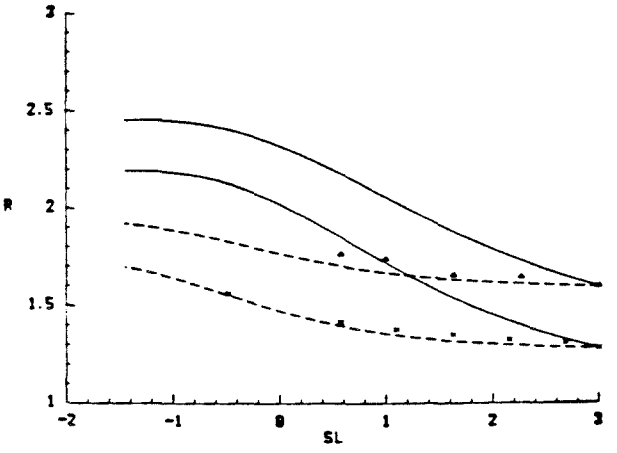

Figure 6a.

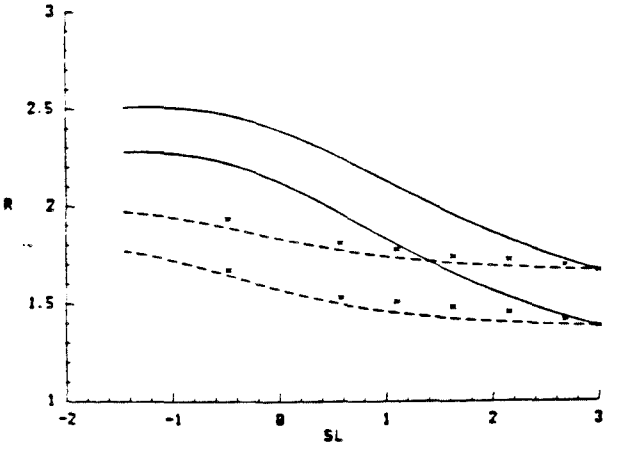

Figure 6b.

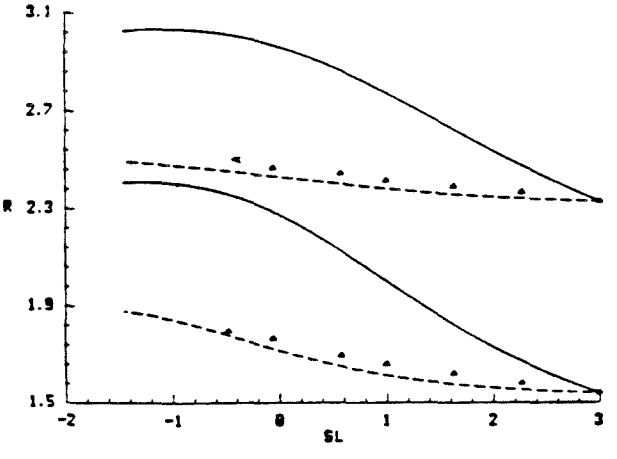

Figure 6c.

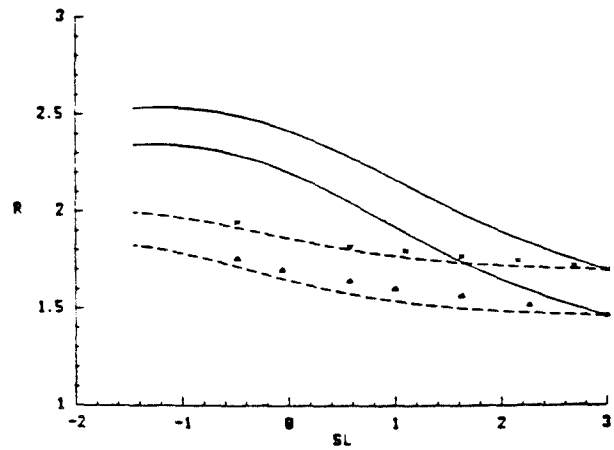

Figure 6d.

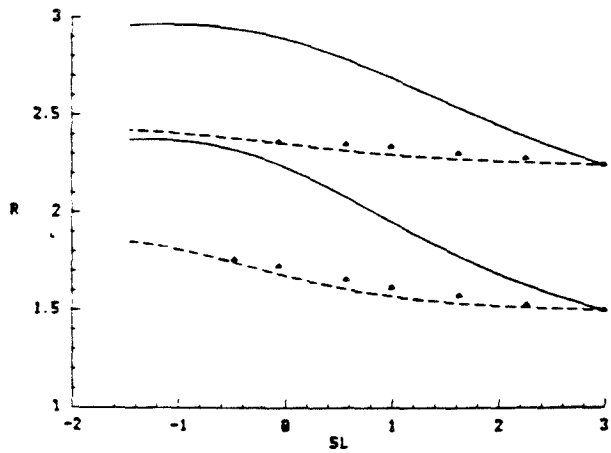

Figure 6e.

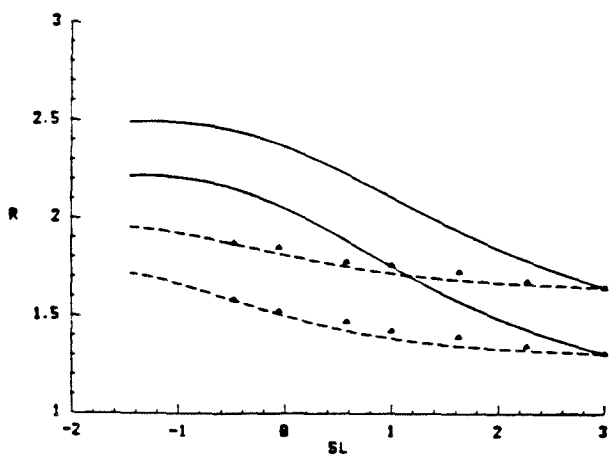

Figure 6f.

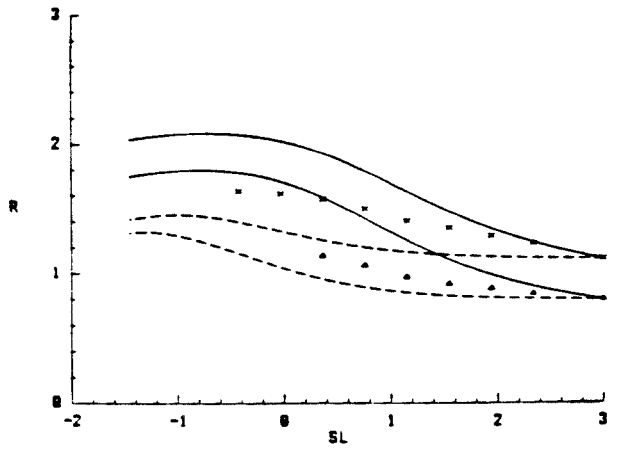

Figure 7a.

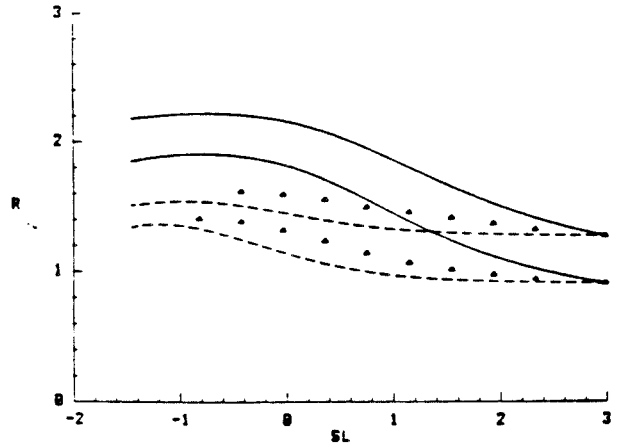

Figure 7b.

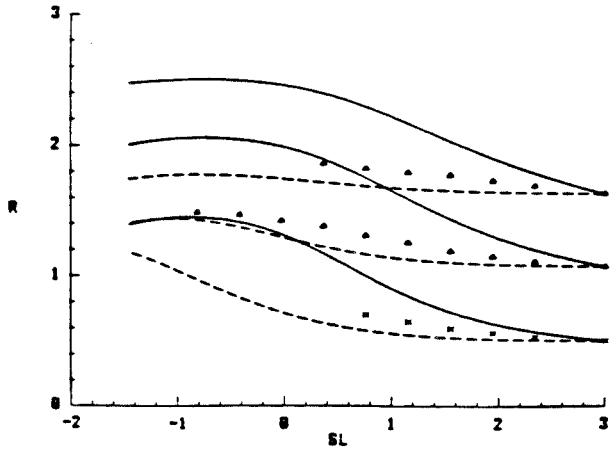

Figure 7c.

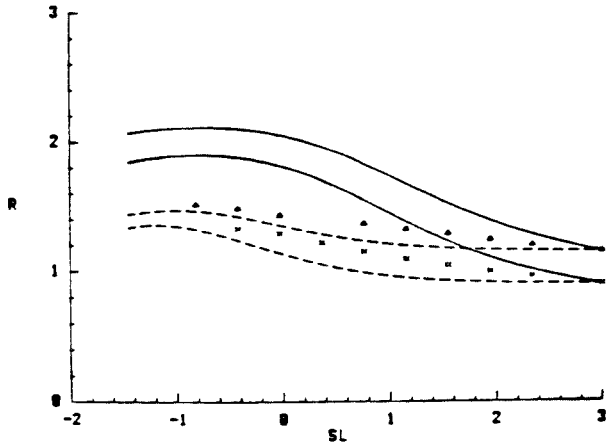

Figure 7d.

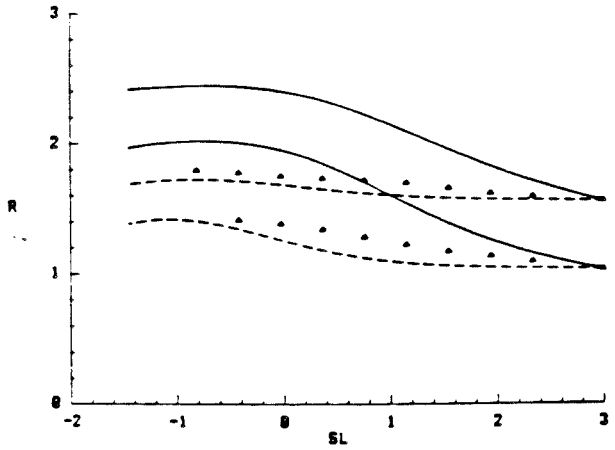

Figure 7e.

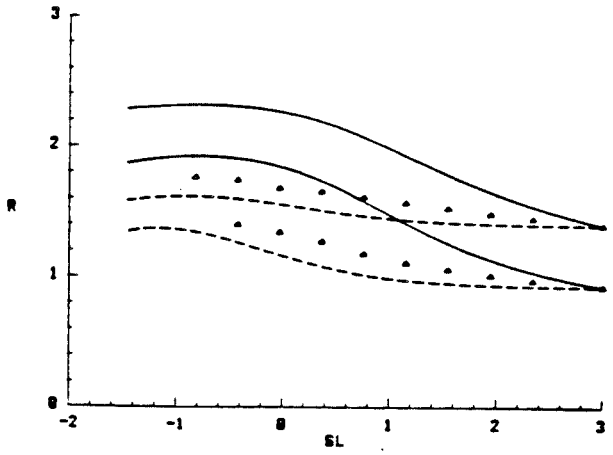

Figure 7f.

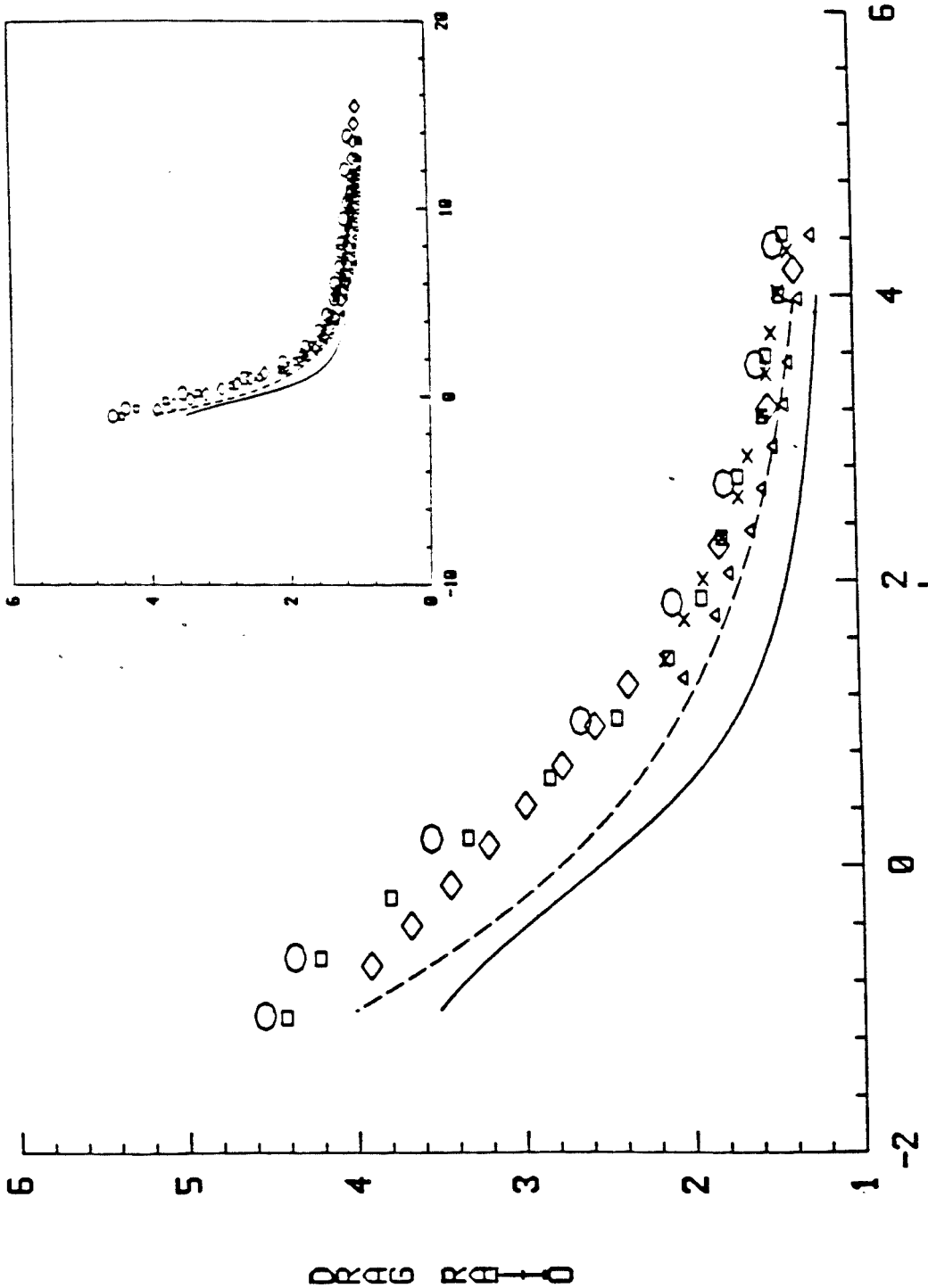

Figure 8.

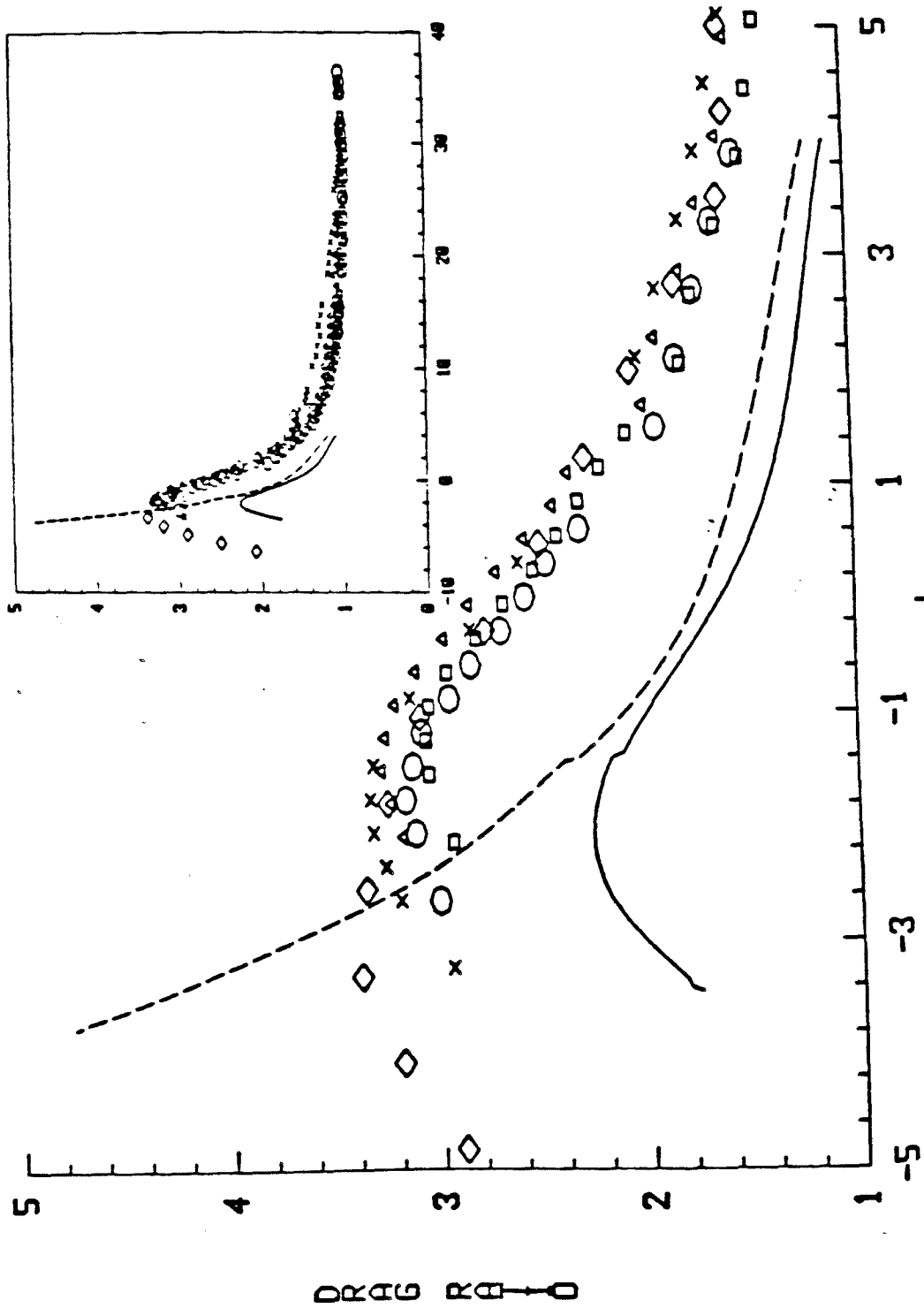

Figure 9.

Appendix A

Derivation of the linear system for the Motion of a Sphere Normal to a Deformable Surfactant Film Interface

This section gives, in detail, the derivation of the linear system used in the numerical scheme for the motion of a sphere normal to a deformable fluid-fluid interface which, due to the presence of surfactants, allows no tangential motion. In section III, the governing equations and boundary conditions for the system were given in Eq. (2)-(9). From Ladyzhenskaya, (1963), a solution to Stokes equation for the velocity of an element of fluid II on the interface is:

$$\frac{1}{2}\mathbf{u}^I(\mathbf{x}) = -\frac{3}{4\pi}\int_{S_I}\frac{\mathbf{rrr}}{R^5}\cdot\mathbf{u}^I\cdot\mathbf{n}\,dS_I + \frac{1}{8\pi}\int_{S_I}\left[\frac{\mathbf{I}}{R}+\frac{\mathbf{rr}}{R^3}\right]\cdot\mathbf{T}_2^I\cdot\mathbf{n}\,dS_I$$
$$+\frac{1}{8\pi}\int_{S_P}\left[\frac{\mathbf{I}}{R}+\frac{\mathbf{rr}}{R^3}\right]\cdot\mathbf{T}_2^P\cdot\mathbf{n}\,dS_P\ , \quad \mathbf{x}\in S_I \qquad (A1)$$

where the jump condition for the double layer integral has already been applied. On the surface of the sphere, the double layer integral vanishes so the result for the velocity is:

$$\mathbf{u}^P(\mathbf{x}) = -\frac{3}{4\pi}\int_{S_I}\frac{\mathbf{rrr}}{R^5}\cdot\mathbf{u}^I\cdot\mathbf{n}\,dS_I + \frac{1}{8\pi}\int_{S_I}\left[\frac{\mathbf{I}}{R}+\frac{\mathbf{rr}}{R^3}\right]\cdot\mathbf{T}_2^I\cdot\mathbf{n}\,dS_I$$
$$+\frac{1}{8\pi}\int_{S_P}\left[\frac{\mathbf{I}}{R}+\frac{\mathbf{rr}}{R^3}\right]\cdot\mathbf{T}_2^P\cdot\mathbf{n}\,dS_P, \quad \mathbf{x}\in S_P \qquad (A2)$$

Noting that $\mathbf{u}(\mathbf{x})$ as $\mathbf{x}\to S_I$ from fluid I equals $\mathbf{u}(\mathbf{x})$ as $\mathbf{x}\to S_I$ from fluid II (continuity of velocity at the interface, Eq. (5)), we can consider the interface from the fluid I side.

$$\frac{1}{2}\lambda\mathbf{u}^I(\mathbf{x}) = -\frac{3}{4\pi}\lambda\int_{S_I}\frac{\mathbf{rrr}}{R^5}\cdot\mathbf{u}^I\cdot\mathbf{n}\,dS_I$$
$$+\frac{1}{8\pi}\int_{S_I}\left[\frac{\mathbf{I}}{R}+\frac{\mathbf{rr}}{R^3}\right]\cdot\lambda\mathbf{T}_2^I\cdot\mathbf{n}\,dS_I\ , \quad \mathbf{x}\in S_I \qquad (A3)$$

Adding Eqs. (A1) and (A3) and using the continuity of velocity condition as well as the fact that the normal for the two fluids at the interface point in opposite directions, the result is Eq. (12)

$$\frac{1}{2}(\lambda+1)\mathbf{u}^I(\mathbf{x}) = \frac{3}{4\pi}(\lambda-1)\int_{S_I}\frac{\mathbf{rrr}}{R^5}\cdot\mathbf{u}^I\cdot\mathbf{n}\,dS_I + \frac{1}{8\pi}\int_{S_P}\left[\frac{\mathbf{I}}{R}+\frac{\mathbf{rr}}{R^3}\right]\cdot\mathbf{T}_2^P\cdot\mathbf{n}\,dS_P$$
$$-\frac{1}{8\pi}\int_{S_I}\left[\frac{\mathbf{I}}{R}+\frac{\mathbf{rr}}{R^3}\right]\cdot\left(\lambda\mathbf{n}\cdot\mathbf{T}_1^I-\mathbf{n}\cdot\mathbf{T}_2^I\right)dS_I \quad , \quad \mathbf{x}\in S_I \qquad (A4)$$

Eq. (7) gives a relation for the stress jump in terms of the interface shape function, and after making the substitution of Eq. (7) into (A4), the equation reads:

$$\frac{1}{2}(\lambda+1)\mathbf{u}^I(\mathbf{x}) = \frac{3}{4\pi}(\lambda-1)\int_{S_I}\frac{\mathbf{rrr}}{R^5}\cdot\mathbf{u}^I\cdot\mathbf{n}\,dS_I + \frac{1}{8\pi}\int_{S_P}\left[\frac{\mathbf{I}}{R}+\frac{\mathbf{rr}}{R^3}\right]\cdot\mathbf{T}_2^P\cdot\mathbf{n}\,dS_P$$
$$-\frac{1}{8\pi}\int_{S_I}\left[\frac{\mathbf{I}}{R}+\frac{\mathbf{rr}}{R^3}\right]\cdot\mathbf{F}(f)\,dS_I \quad , \quad \mathbf{x}\in S_I \qquad (A5)$$

where the function $\mathbf{F}(f)$ is the stress difference at the interface whose exact form depends on the coordinate system used to represent the interface shape.

$$\mathbf{F}(f) \equiv \lambda\mathbf{n}\cdot\mathbf{T}_1^I - \mathbf{n}\cdot\mathbf{T}_2^I$$

$$\mathbf{F}(f_1) = -\frac{1}{Ca}\left(\frac{2}{k_1 r}-\frac{1}{k_1^3 r^2}\frac{\partial^2 f_1}{\partial\theta^2}-\frac{1}{k_1 r^2}\frac{\partial f_1}{\partial\theta}\cot\theta+\frac{1}{k_1^3 r^3}\left(\frac{\partial f_1}{\partial\theta}\right)^2\right)\mathbf{n}_1$$
$$+\frac{1}{Cg}z\mathbf{n}_1+\beta(\mathbf{x}_1)\mathbf{t}_1 \ , \ \text{for} \ \mathbf{x}\in S_1^I \qquad (A6a)$$

$$\mathbf{F}(f_2) = -\frac{1}{Ca}\frac{1}{k_2}\left(\frac{1}{r}-\frac{1}{k_2^2}\frac{\partial^2 f}{\partial z^2}\right)\mathbf{n}_2+\frac{1}{Cg}z\mathbf{n}_2 \ , \quad \text{for} \quad \mathbf{x}\in S_2^I \qquad (A6b)$$

$$\mathbf{F}(f_3) = -\frac{1}{Ca}\frac{1}{k_3}\left(\frac{1}{r}\frac{\partial f}{\partial r}+\frac{1}{k_3^2}\frac{\partial^2 f}{\partial r^2}\right)\mathbf{n}_3+\frac{1}{Cg}z\mathbf{n}_3 \ , \quad \text{for} \quad \mathbf{x}\in S_3^I \qquad (A6c)$$

where

$$k_1 = \left[1 + \frac{1}{r^2}\left(\frac{\partial f_1}{\partial \theta}\right)^2\right]^{1/2} \quad , \quad \mathbf{n}_1 = \frac{1}{k_1}\left(\mathbf{i}_r - \frac{1}{r}\frac{\partial f_1}{\partial \theta}\mathbf{i}_\theta\right)$$

$$k_2 = \left[1 + \left(\frac{\partial f_2}{\partial z}\right)^2\right]^{1/2} \quad , \quad \mathbf{n}_2 = \frac{1}{k_2}\left(\mathbf{i}_r - \frac{\partial f_2}{\partial z}\mathbf{i}_z\right)$$

$$k_3 = \left[1 + \left(\frac{\partial f_3}{\partial r}\right)^2\right]^{1/2} \quad , \quad \mathbf{n}_3 = \frac{1}{k_3}\left(\mathbf{i}_z - \frac{\partial f_3}{\partial r}\mathbf{i}_r\right)$$

Eqs. (A1), (A2), and (A5) along with the condition of constant sphere velocity, $\mathbf{u}(\mathbf{x}) = i_z$, $\mathbf{x} \in S_P$, give 4 integral equations for the 4 unknowns: $\mathbf{u}^I$, $\mathbf{u}^P$, $\mathbf{T}^I \cdot \mathbf{n}$, $\mathbf{T}^P \cdot \mathbf{n}$, provided the interface shape and sphere position are known

The problem of normal motion is axisymmetric, so the surface integrals can be greatly simplified by integrating in the azimuthal direction. The result of that integration for Eqs. (A1), (A2), and (A5) along with the equation for no tangential velocity gives the system of linear integral equations we must solve.

$$\begin{aligned}\frac{1}{2}\begin{bmatrix} u_r^I(\mathbf{x}) \\ u_z^I(\mathbf{x}) \end{bmatrix} = &- \frac{3}{4\pi}\int_{S_I} \mathbf{C}(\mathbf{x},\eta)\cdot\begin{bmatrix} u_r^I \\ u_z^I \end{bmatrix}\eta_r(1+f'^2)^{1/2}d\eta_r \\ &+ \frac{1}{8\pi}\int_{S_I} \mathbf{B}(\mathbf{x},\eta)\cdot\begin{bmatrix} \mathbf{T}^I_{2nr} \\ \mathbf{T}^I_{2nz} \end{bmatrix}\eta_r(1+f'^2)^{1/2}d\eta_r \\ &+ \frac{1}{8\pi}\int_{S_P} \mathbf{B}(\mathbf{x},\Theta)\cdot\begin{bmatrix} \mathbf{T}^P_{nr} \\ \mathbf{T}^P_{nz} \end{bmatrix}\sin\Theta d\Theta \ , \quad \mathbf{x}\in S^I \end{aligned} \tag{A7}$$

$$\begin{aligned}\begin{bmatrix} u_r^P(\mathbf{x}) \\ u_z^P(\mathbf{x}) \end{bmatrix} = &- \frac{3}{4\pi}\int_{S_I} \mathbf{C}(\mathbf{x},\eta)\cdot\begin{bmatrix} u_r^I \\ u_z^I \end{bmatrix}\eta_r(1+f'^2)^{1/2}d\eta_r \\ &+ \frac{1}{8\pi}\int_{S_I} \mathbf{B}(\mathbf{x},\eta)\cdot\begin{bmatrix} \mathbf{T}^I_{2nr} \\ \mathbf{T}^I_{2nz} \end{bmatrix}\eta_r(1+f'^2)^{1/2}d\eta_r \\ &+ \frac{1}{8\pi}\int_{S_P} \mathbf{B}(\mathbf{x},\Theta)\cdot\begin{bmatrix} \mathbf{T}^P_{nr} \\ \mathbf{T}^P_{nz} \end{bmatrix}\sin\Theta d\Theta \ , \quad \mathbf{x}\in S^P \end{aligned} \tag{A8}$$

$$\frac{1}{2}(\lambda+1)\begin{bmatrix} u_r^I(\mathbf{x}) \\ u_z^I(\mathbf{x}) \end{bmatrix} = -\frac{3}{4\pi}(\lambda+1)\int_{S_I} \mathbf{C}(\mathbf{x},\eta)\cdot\begin{bmatrix} u_r^I \\ u_z^I \end{bmatrix}\eta_r(1+f'^2)^{1/2}d\eta_r$$
$$+\frac{1}{8\pi}\int_{S_I}\mathbf{B}(\mathbf{x},\eta)\cdot\begin{bmatrix} F_r \\ F_z \end{bmatrix}\eta_r(1+f'^2)^{1/2}d\eta_r$$
$$+\frac{1}{8\pi}\int_{S_P}\mathbf{B}(\mathbf{x},\Theta)\cdot\begin{bmatrix} \mathbf{T}^P_{nr} \\ \mathbf{T}^P_{nz} \end{bmatrix}\sin\Theta d\Theta\ , \quad \mathbf{x}\in S^I \qquad (A9)$$

$$t_r(\mathbf{x})u_r^I(\mathbf{x}) + t_z(\mathbf{x})u_z^I(\mathbf{x}) = 0 \quad \mathbf{x}\in S_I \qquad (A10)$$

Here

$$\mathbf{B}(\mathbf{x},\eta) = \begin{bmatrix} B_{rr} & B_{rz} \\ B_{zr} & B_{zz} \end{bmatrix} \text{ and } \mathbf{C}(\mathbf{x},\eta) = \begin{bmatrix} C_{rr} & C_{rz} \\ C_{zr} & C_{zz} \end{bmatrix}$$

The elements of **B** and **C** are given in Lee and Leal (1982)

To solve Eqs. (A7)-(A10) numerically, the collocation assumption is applied. Integration over the interface and sphere surface is broken down into integrals over segments of the surface with the values of the unknowns, u_i, T_{n_i}, and β_i, in that segment assumed to be constant. As a result, the unknowns can be taken outside the integrals and a system of linear equations results. For example, given NI points on the interface and NP on the sphere, Eqs. (A7)-(A9) become:

$$\frac{1}{2}u_r^I(\mathbf{x}_j) = -\frac{3}{4\pi}\sum_{i=1}^{NI} u_r^I(\mathbf{x}_i)\left[\int_{\eta_{i-1}}^{\eta_i} C_{rr}(\mathbf{x}_j,\eta)\eta_r(1+f'^2)^{1/2}d\eta_r\right]$$
$$-\frac{3}{4\pi}\sum_{i=1}^{NI} u_z^I(\mathbf{x}_i)\left[\int_{\eta_{i-1}}^{\eta_i} C_{rz}(\mathbf{x}_j,\eta)\eta_r(1+f'^2)^{1/2}d\eta_r\right]$$
$$+\frac{1}{8\pi}\sum_{i=1}^{NI} T^I_{2_{nr}}(\mathbf{x}_i)\left[\int_{\eta_{i-1}}^{\eta_i} B_{rr}(\mathbf{x}_j,\eta)\eta_r(1+f'^2)^{1/2}d\eta_r\right]$$
$$+\frac{1}{8\pi}\sum_{i=1}^{NI} T^I_{2_{nz}}(\mathbf{x}_i)\left[\int_{\eta_{i-1}}^{\eta_i} B_{rz}(\mathbf{x}_j,\eta)\eta_r(1+f'^2)^{1/2}d\eta_r\right]$$
$$+\frac{1}{8\pi}\sum_{i=1}^{NP} T^I_{nr}(\mathbf{x}_i)\left[\int_{\Theta_{i-1}}^{\Theta_i} B_{rr}(\mathbf{x}_j,\Theta)\sin\Theta d\Theta\right]$$

$$+\frac{1}{8\pi}\sum_{i=1}^{NP}T^I_{nz}(\mathbf{x}_i)\left[\int_{\Theta_{i-1}}^{\Theta_i}B_{rz}(\mathbf{x}_j,\Theta)\sin\Theta d\Theta\right]\ ,\quad \mathbf{x}_j\in S_I \quad (A11)$$

$$\begin{aligned}\frac{1}{2}u^I_z(\mathbf{x}_j) =& -\frac{3}{4\pi}\sum_{i=1}^{NI}u^I_r(\mathbf{x}_i)\left[\int_{\eta_{i-1}}^{\eta_i}C_{zr}(\mathbf{x}_j,\eta)\eta_r(1+f'^2)^{1/2}d\eta_r\right]\\ &-\frac{3}{4\pi}\sum_{i=1}^{NI}u^I_z(\mathbf{x}_i)\left[\int_{\eta_{i-1}}^{\eta_i}C_{zz}(\mathbf{x}_j,\eta)\eta_r(1+f'^2)^{1/2}d\eta_r\right]\\ &+\frac{1}{8\pi}\sum_{i=1}^{NI}T^I_{2_{nr}}(\mathbf{x}_i)\left[\int_{\eta_{i-1}}^{\eta_i}B_{zr}(\mathbf{x}_j,\eta)\eta_r(1+f'^2)^{1/2}d\eta_r\right]\\ &+\frac{1}{8\pi}\sum_{i=1}^{NI}T^I_{2_{nz}}(\mathbf{x}_i)\left[\int_{\eta_{i-1}}^{\eta_i}B_{zz}(\mathbf{x}_j,\eta)\eta_r(1+f'^2)^{1/2}d\eta_r\right]\\ &+\frac{1}{8\pi}\sum_{i=1}^{NP}T^I_{nr}(\mathbf{x}_i)\left[\int_{\Theta_{i-1}}^{\Theta_i}B_{zr}(\mathbf{x}_j,\Theta)\sin\Theta d\Theta\right]\\ &+\frac{1}{8\pi}\sum_{i=1}^{NP}T^I_{nz}(\mathbf{x}_i)\left[\int_{\Theta_{i-1}}^{\Theta_i}B_{zz}(\mathbf{x}_j,\Theta)\sin\Theta d\Theta\right]\ ,\quad \mathbf{x}_j\in S_I \quad (A12)\end{aligned}$$

$$\begin{aligned}u^P_r(\mathbf{x}_j) =& -\frac{3}{4\pi}\sum_{i=1}^{NI}u^I_r(\mathbf{x}_i)\left[\int_{\eta_{i-1}}^{\eta_i}C_{rr}(\mathbf{x}_j,\eta)\eta_r(1+f'^2)^{1/2}d\eta_r\right]\\ &-\frac{3}{4\pi}\sum_{i=1}^{NI}u^I_z(\mathbf{x}_i)\left[\int_{\eta_{i-1}}^{\eta_i}C_{rz}(\mathbf{x}_j,\eta)\eta_r(1+f'^2)^{1/2}d\eta_r\right]\\ &+\frac{1}{8\pi}\sum_{i=1}^{NI}T^I_{2_{nr}}(\mathbf{x}_i)\left[\int_{\eta_{i-1}}^{\eta_i}B_{rr}(\mathbf{x}_j,\eta)\eta_r(1+f'^2)^{1/2}d\eta_r\right]\\ &+\frac{1}{8\pi}\sum_{i=1}^{NI}T^I_{2_{nz}}(\mathbf{x}_i)\left[\int_{\eta_{i-1}}^{\eta_i}B_{rz}(\mathbf{x}_j,\eta)\eta_r(1+f'^2)^{1/2}d\eta_r\right]\\ &+\frac{1}{8\pi}\sum_{i=1}^{NP}T^I_{nr}(\mathbf{x}_i)\left[\int_{\Theta_{i-1}}^{\Theta_i}B_{rr}(\mathbf{x}_j,\Theta)\sin\Theta d\Theta\right]\\ &+\frac{1}{8\pi}\sum_{i=1}^{NP}T^I_{nz}(\mathbf{x}_i)\left[\int_{\Theta_{i-1}}^{\Theta_i}B_{rz}(\mathbf{x}_j,\Theta)\sin\Theta d\Theta\right]\ ,\quad \mathbf{x}_j\in S_P \quad (A13)\end{aligned}$$

$$
\begin{aligned}
u_z^P(\mathbf{x}_j) = &- \frac{3}{4\pi}\sum_{i=1}^{NI} u_r^I(\mathbf{x}_i)\left[\int_{\eta_{i-1}}^{\eta_i} C_{zr}(\mathbf{x}_j,\eta)\eta_r(1+f'^2)^{1/2}d\eta_r\right] \\
&- \frac{3}{4\pi}\sum_{i=1}^{NI} u_z^I(\mathbf{x}_i)\left[\int_{\eta_{i-1}}^{\eta_i} C_{zz}(\mathbf{x}_j,\eta)\eta_r(1+f'^2)^{1/2}d\eta_r\right] \\
&+ \frac{1}{8\pi}\sum_{i=1}^{NI} T_{2_{nr}}^I(\mathbf{x}_i)\left[\int_{\eta_{i-1}}^{\eta_i} B_{zr}(\mathbf{x}_j,\eta)\eta_r(1+f'^2)^{1/2}d\eta_r\right] \\
&+ \frac{1}{8\pi}\sum_{i=1}^{NI} T_{2_{nz}}^I(\mathbf{x}_i)\left[\int_{\eta_{i-1}}^{\eta_i} B_{zz}(\mathbf{x}_j,\eta)\eta_r(1+f'^2)^{1/2}d\eta_r\right] \\
&+ \frac{1}{8\pi}\sum_{i=1}^{NP} T_{nr}^I(\mathbf{x}_i)\left[\int_{\Theta_{i-1}}^{\Theta_i} B_{zr}(\mathbf{x}_j,\Theta)\sin\Theta d\Theta\right] \\
&+ \frac{1}{8\pi}\sum_{i=1}^{NP} T_{nz}^I(\mathbf{x}_i)\left[\int_{\Theta_{i-1}}^{\Theta_i} B_{zz}(\mathbf{x}_j,\Theta)\sin\Theta d\Theta\right], \quad \mathbf{x}_j \in S_P \quad (A14)
\end{aligned}
$$

$$
\begin{aligned}
\frac{1}{2}(\lambda+1)u_r^I(\mathbf{x}_j) = &- \frac{3}{4\pi}(\lambda+1)\sum_{i=1}^{NI} u_r^I(\mathbf{x}_i)\left[\int_{\eta_{i-1}}^{\eta_i} C_{rr}(\mathbf{x}_j,\eta)\eta_r(1+f'^2)^{1/2}d\eta_r\right] \\
&- \frac{3}{4\pi}(\lambda+1)\sum_{i=1}^{NI} u_z^I(\mathbf{x}_i)\left[\int_{\eta_{i-1}}^{\eta_i} C_{rz}(\mathbf{x}_j,\eta)\eta_r(1+f'^2)^{1/2}d\eta_r\right] \\
&+ \frac{1}{8\pi}\sum_{i=1}^{NI}\left[\int_{\eta_{i-1}}^{\eta_i} B_{rr}(\mathbf{x}_j,\eta)F_r\eta_r(1+f'^2)^{1/2}d\eta_r\right] \\
&+ \frac{1}{8\pi}\sum_{i=1}^{NI}\left[\int_{\eta_{i-1}}^{\eta_i} B_{rz}(\mathbf{x}_j,\eta)F_z\eta_r(1+f'^2)^{1/2}d\eta_r\right] \\
&+ \frac{1}{8\pi}\sum_{i=1}^{NP} T_{nr}^I(\mathbf{x}_i)\left[\int_{\Theta_{i-1}}^{\Theta_i} B_{zr}(\mathbf{x}_j,\Theta)\sin\Theta d\Theta\right] \\
&+ \frac{1}{8\pi}\sum_{i=1}^{NP} T_{nz}^I(\mathbf{x}_i)\left[\int_{\Theta_{i-1}}^{\Theta_i} B_{zz}(\mathbf{x}_j,\Theta)\sin\Theta d\Theta\right], \ \mathbf{x}_j \in S_I \quad (A15)
\end{aligned}
$$

$$
\frac{1}{2}(\lambda+1)u_r^I(\mathbf{x}_j) = - \frac{3}{4\pi}(\lambda+1)\sum_{i=1}^{NI} u_r^I(\mathbf{x}_i)\left[\int_{\eta_{i-1}}^{\eta_i} C_{zr}(\mathbf{x}_j,\eta)\eta_r(1+f'^2)^{1/2}d\eta_r\right]
$$

$$- \frac{3}{4\pi}(\lambda+1)\sum_{i=1}^{NI} u_z^I(\mathbf{x}_i)\left[\int_{\eta_{i-1}}^{\eta_i} C_{zz}(\mathbf{x}_j,\eta)\eta_r(1+f'^2)^{1/2}d\eta_r\right]$$

$$+ \frac{1}{8\pi}\sum_{i=1}^{NI}\left[\int_{\eta_{i-1}}^{\eta_i} B_{zr}(\mathbf{x}_j,\eta)F_r\eta_r(1+f'^2)^{1/2}d\eta_r\right]$$

$$+ \frac{1}{8\pi}\sum_{i=1}^{NI}\left[\int_{\eta_{i-1}}^{\eta_i} B_{zz}(\mathbf{x}_j,\eta)F_z\eta_r(1+f'^2)^{1/2}d\eta_r\right]$$

$$+ \frac{1}{8\pi}\sum_{i=1}^{NP} T_{nr}^I(\mathbf{x}_i)\left[\int_{\Theta_{i-1}}^{\Theta_i} B_{zr}(\mathbf{x}_j,\Theta)\sin\Theta d\Theta\right]$$

$$+ \frac{1}{8\pi}\sum_{i=1}^{NP} T_{nz}^I(\mathbf{x}_i)\left[\int_{\Theta_{i-1}}^{\Theta_i} B_{zz}(\mathbf{x}_j,\Theta)\sin\Theta d\Theta\right],\ \mathbf{x}_j \in S_I \quad (A16)$$

These equations can be rewritten in the form:

$$\frac{1}{2}u_r^I(\mathbf{x}_j) = \sum_{i=1}^{NI} -(CRR)_i\, u_r^I(\mathbf{x}_i) + \sum_{i=1}^{NI} -(CRZ)_i\, u_Z^I(\mathbf{x}_i)$$

$$+ \sum_{i=1}^{NI}(ACOS + BRR)_i\, T_{2_{nr}}^I(\mathbf{x}_i) + \sum_{i=1}^{NI}(BRZ)_i\, T_{2_{nz}}^I(\mathbf{x}_i)$$

$$+ \sum_{i=1}^{NP}(ACOS + BRR)_i\, T_{nr}^P(\mathbf{x}_i) + \sum_{i=1}^{NP}(BRZ)_i\, T_{nz}^P(\mathbf{x}_i) \quad (A17)$$

$$\frac{1}{2}u_z^I(\mathbf{x}_j) = \sum_{i=1}^{NI} -(CRZC)_i\, u_r^I(\mathbf{x}_i) + \sum_{i=1}^{NI} -(CZZ)_i\, u_Z^I(\mathbf{x}_i)$$

$$+ \sum_{i=1}^{NI}(BRZC)_i\, T_{2_{nr}}^I(\mathbf{x}_i) + \sum_{i=1}^{NI}(ACOS + BZZ)_i\, T_{2_{nz}}^I(\mathbf{x}_i)$$

$$+ \sum_{i=1}^{NP}(BRZC)_i\, T_{nr}^P(\mathbf{x}_i) + \sum_{i=1}^{NP}(ACOS + BZZ)_i\, T_{nz}^P(\mathbf{x}_i) \quad (A18)$$

$$u_r^P(\mathbf{x}_j) = \sum_{i=1}^{NI} -(CRR)_i\, u_r^I(\mathbf{x}_i) + \sum_{i=1}^{NI} -(CRZ)_i\, u_Z^I(\mathbf{x}_i)$$

$$+ \sum_{i=1}^{NI}(ACOS + BRR)_i\, T_{2_{nr}}^I(\mathbf{x}_i) + \sum_{i=1}^{NI}(BRZ)_i\, T_{2_{nz}}^I(\mathbf{x}_i)$$

$$+\sum_{i=1}^{NP}(ACOS+BRR)_i\,T^P_{nr}(\mathbf{x}_i)+\sum_{i=1}^{NP}(BRZ)_i\,T^P_{nz}(\mathbf{x}_i) \qquad (A19)$$

$$\begin{aligned}u^P_z(\mathbf{x}_j)=&\sum_{i=1}^{NI}-(CRZC)_i\,u^I_r(\mathbf{x}_i)+\sum_{i=1}^{NI}-(CZZ)_i\,u^I_Z(\mathbf{x}_i)\\&+\sum_{i=1}^{NI}(BRZC)_i\,T^I_{2_{nr}}(\mathbf{x}_i)+\sum_{i=1}^{NI}(ACOS+BZZ)_i\,T^I_{2_{nz}}(\mathbf{x}_i)\\&+\sum_{i=1}^{NP}(BRZC)_i\,T^P_{nr}(\mathbf{x}_i)+\sum_{i=1}^{NP}(ACOS+BZZ)_i\,T^P_{nz}(\mathbf{x}_i)\end{aligned} \qquad (A20)$$

$$\begin{aligned}\frac{1}{2}(\lambda+1)u^I_r(\mathbf{x}_j)=&\sum_{i=1}^{NI}(\lambda-1)(CRR)_i\,u^I_r(\mathbf{x}_i)+\sum_{i=1}^{NI}(\lambda-1)(CRZ)_i\,u^I_Z(\mathbf{x}_i)\\&+\sum_{i=1}^{NP}(ACOS+BRR)_i\,T^P_{nr}(\mathbf{x}_i)+\sum_{i=1}^{NP}(BRZ)_i\,T^P_{nz}(\mathbf{x}_i)\\&+\sum_{i=1}^{NI}\left[(ACOS+BRR)_i\,t_r+(BRZ)_i\,t_z\right]TSJ(\mathbf{x}_i)\\&-\left[(ACOS+BRR)_i\,F_r(\mathbf{x}_i)+(BRZ)_i\,F_z(\mathbf{x}_i)\right]\end{aligned} \qquad (A21)$$

$$\begin{aligned}\frac{1}{2}(\lambda+1)u^I_z(\mathbf{x}_j)=&\sum_{i=1}^{NI}(\lambda-1)(CRZC)_i\,u^I_r(\mathbf{x}_i)+\sum_{i=1}^{NI}(\lambda-1)(CZZ)_i\,u^I_Z(\mathbf{x}_i)\\&+\sum_{i=1}^{NP}(BRZC)_i\,T^P_{nr}(\mathbf{x}_i)+\sum_{i=1}^{NP}(ACOS+BZZ)_i\,T^P_{nz}(\mathbf{x}_i)\\&+\sum_{i=1}^{NI}\left[(BRZC)_i\,t_r+(ACOS+BZZ)_i\,t_z\right]TSJ(\mathbf{x}_i)\\&-\left[(BRZC)_i\,F_r(\mathbf{x}_i)+(ACOS+BZZ)_i\,F_z(\mathbf{x}_i)\right]\end{aligned} \qquad (A22)$$

In these equations, the substitution has been made:

$$CRR_i = \frac{3}{2\pi}\int_{\eta_{i-1}}^{\eta_i} C_{rr}(\mathbf{x}_j,\eta)\eta_r(1+f'^2)^{1/2}d\eta_r$$

$$CRZ_i = \frac{3}{2\pi}\int_{\eta_{i-1}}^{\eta_i} C_{rz}(\mathbf{x}_j,\eta)\eta_r(1+f'^2)^{1/2}d\eta_r$$

$$CZZ_i = \frac{3}{2\pi}\int_{\eta_{i-1}}^{\eta_i} C_{zz}(\mathbf{x}_j,\eta)\eta_r(1+f'^2)^{1/2}d\eta_r$$

$$CRZC_i = \frac{3}{2\pi}\int_{\eta_{i-1}}^{\eta_i} C_{zr}(\mathbf{x}_j,\eta)\eta_r(1+f'^2)^{1/2}d\eta_r$$

$$BRZ_i = \frac{1}{4\pi}\int_{\eta_{i-1}}^{\eta_i} B_{rz}(\mathbf{x}_j,\eta)\eta_r(1+f'^2)^{1/2}d\eta_r$$

$$BRZC_i = \frac{1}{4\pi}\int_{\eta_{i-1}}^{\eta_i} B_{zr}(\mathbf{x}_j,\eta)\eta_r(1+f'^2)^{1/2}d\eta_r$$

$$(ACOS+BRR)_i = \frac{1}{4\pi}\int_{\eta_{i-1}}^{\eta_i} B_{rr}(\mathbf{x}_j,\eta)\eta_r(1+f'^2)^{1/2}d\eta_r$$

$$(ACOS+BZZ)_i = \frac{1}{4\pi}\int_{\eta_{i-1}}^{\eta_i} B_{zz}(\mathbf{x}_j,\eta)\eta_r(1+f'^2)^{1/2}d\eta_r$$

$$TSJ(\mathbf{x}_i) = \beta(\mathbf{x}_i)$$

Eqs. (A17)-(A22) each involve $4\,NI+2\,NP$ unknowns $[NI\times u_r^I(\mathbf{x}_i)+NI\times u_z^i(\mathbf{x}_i)+NI \times T_{2_{nr}}^I(\mathbf{x}_i)+NI \times T_{2_{nz}}^I(\mathbf{x}_i)+NP \times T_{nr}^P(\mathbf{x}_i)+NP \times T_{nz}^P(\mathbf{x}_i)]$, and Eqs. (A21) and (A22) include NI additional unknowns for the values of $TSJ(\mathbf{x}_i)$. Thus there are $5\,NI + 2\,NP$ unknowns. By applying Eqs. (A17), (A18), (A21), (A22), and (A10) to each segment of the interface, and Eqs. (A19) and (A20) to the NP points on the sphere, $5\,NI + 2\,NP$ linear equations result for a well posed linear system. In matrix form, the system can be represented $A \cdot x = b$

$$
\begin{array}{c}
 \\
NI \\
NI \\
NI \\
NI \\
NP \\
NP \\
NI
\end{array}
\begin{array}{c}
\begin{array}{ccccccc}
NI & NI & NI & NI & NP & NP & NI
\end{array} \\
\begin{pmatrix}
(\lambda-1)CRR & (\lambda-1)CRZ & 0 & 0 & (ACOS+BRR) & BRZ & (ACOS+BRR)t_r+BRZ\,t_s \\
(\lambda-1)CRZC & (\lambda-1)CZZ & 0 & 0 & BRZC & (ACOS+BZZ) & BRZC\,t_r+(ACOS+BZZ)t_s \\
-CRR & -CRZ & (ACOS+BRR) & BRZ & (ACOS+BRR) & BRZ & 0 \\
-CRZC & -CZZ & BRZC & (ACOS+BZZ) & BRZC & (ACOS+BZZ) & 0 \\
-CRR & -CRZ & (ACOS+BRR) & BRZ & (ACOS+BRR) & BRZ & 0 \\
-CRZC & -CZZ & BRZC & (ACOS+BZZ) & BRZC & (ACOS+BZZ) & 0 \\
t_r & t_s & 0 & 0 & 0 & 0 & 0
\end{pmatrix}
\end{array}
$$

$$
\bullet
\begin{pmatrix}
u_r^I \\ u_s^I \\ T_{2_{nr}}^I \\ T_{2_{ns}}^I \\ T_{nr}^P \\ T_{ns}^P \\ TSJ(x_i)
\end{pmatrix}
=
\begin{pmatrix}
-|(ACOS+BRR)F_r+BRZ\,F_s| \\
-|BRZC\,F_r+(ACOS+BZZ)F_s| \\
0 \\ 0 \\ 0 \\ 1 \\ 0
\end{pmatrix}
$$

The symbols above and to the left of the matrix in Eq. (A23) indicate the number of times each column or row is to be repeated. In each row, the columns must include an element for each surface point, so there are $5\,NI + 2\,NP$ columns. Each row stands for the NI or NP equations for each surface point. This linear system is solved by Gaussian elimination for the unknown vector giving the velocity and stress at the interface and sphere surface.

Appendix B

Data From Experimental Runs

This appendix presents the data from the eight experimental runs performed for this work. Both dimensional and non-dimensional forms for this data are included.

TABLE BI. Time-Position Data and Calculated Sphere Velocity

Position	Time	Δt	U (cm/sec)	% Error*
21	950.5	–	–	–
22	953.2	2.70	0.370	1.33
27	966.7	13.50	0.370	1.33
30	974.7	8.00	0.375	–
37	993.3	18.60	0.376	0.267
42	1006.5	13.20	0.379	1.067
43	1009.2	2.70	0.370	1.333
44	1011.8	2.60	0.385	2.667

*avg.=0.375

a) Case 1s

TABLE BI. Time-Position Data and Calculated Sphere Velocity

Position	Time	Δt	U (cm/sec)	% Error*
21.0	13.8	–	–	–
22.5	18.0	4.20	0.357	3.775
25.0	24.7	6.70	0.373	0.539
27.0	30.2	5.50	0.364	1.887
31.0	41.0	10.80	0.370	0.270
32.5	45.0	4.00	0.375	1.078
36.0	54.5	9.50	0.368	0.809
40.0	65.1	10.60	0.377	1.617
42.5	71.8	6.70	0.373	0.539
45.0	78.4	6.60	0.379	2.156

*avg.=0.371

b) Case 1b

TABLE BI. Time-Position Data and Calculated Sphere Velocity

Position	Time	Δt	U (cm/sec)	% Error*
22.0	416.6	–	–	–
27.0	430.2	13.60	0.368	3.774
30.0	438.2	8.00	0.375	1.078
37.0	457.1	18.90	0.370	0.270
42.0	470.4	13.30	0.376	1.348
43.0	473.2	2.80	0.357	3.774
44.0	475.8	2.60	0.385	3.774

*avg.=0.371

c) Case 2s

TABLE BI. Time-Position Data and Calculated Sphere Velocity

Position	Time	Δt	U (cm/sec)	% Error*
21.0	71.1	–	–	–
22.5	75.3	4.20	0.357	2.192
25.0	82.2	6.90	0.362	0.822
27.0	87.8	5.60	0.357	2.192
31.0	98.7	10.90	0.367	0.548
32.5	102.9	4.20	0.357	2.192
36.0	112.3	9.40	0.372	1.918
40.0	123.1	10.80	0.370	1.370
42.5	129.9	6.80	0.368	0.822
45.0	136.6	6.70	0.373	2.192

*avg.=0.365

d) Case 2b

TABLE BI. Time-Position Data and Calculated Sphere Velocity

Position	Time	Δt	U (cm/sec)	% Error*
19.0	473.0	–	–	–
21.0	478.3	5.30	0.377	0.266
22.5	482.4	4.10	0.366	2.666
25.0	489.0	6.60	0.379	0.798
27.5	495.7	6.70	0.373	0.798
29.5	500.9	5.20	0.385	2.394
33.0	510.2	9.30	0.376	0.000
35.5	517.0	6.80	0.368	2.120

*avg.=0.376

e) Case 3s

TABLE BI. Time-Position Data and Calculated Sphere Velocity

Position	Time	Δt	U (cm/sec)	% Error*
18.0	42.6	–	–	–
19.5	46.8	4.20	0.357	2.989
23.0	56.4	9.60	0.365	0.815
25.0	61.8	5.40	0.370	0.543
29.0	72.6	10.80	0.370	0.543
30.5	76.6	4.00	0.375	1.902
34.0	86.1	9.50	0.368	–
36.5	92.9	6.80	0.368	–

*avg.=0.368

f) Case 3b

TABLE BI. Time-Position Data and Calculated Sphere Velocity

Position	Time	Δt	U (cm/sec)	% Error*
19.5	15.3	–	–	–
23.0	24.7	9.40	0.372	0.535
25.9	30.0	5.30	0.377	0.802
29.0	40.7	10.70	0.374	–
30.5	44.7	3.90	0.385	2.941
34.0	53.9	9.30	0.376	0.535
35.5	57.9	4.00	0.375	0.267

*avg.=0.374

g) Case 4s

TABLE BI. Time-Position Data and Calculated Sphere Velocity

Position	Time	Δt	U (cm/sec)	% Error*
18.0	23.3	–	–	–
19.5	27.3	4.0	0.375	3.350
23.0	36.3	9.00	0.389	0.258
25.0	41.4	5.10	0.392	1.031
29.0	51.7	10.30	0.388	–
30.5	55.5	3.80	0.395	1.804
34.0	64.5	9.00	0.389	–

*avg.=0.388

h) Case 4b

The shape data from experiments are:

TABLE BII. Interface Shape Data (in 1/10″ boxes)

$l = 0.9494$		$l = 0.4747$		$l = 0.000$		$l = -0.4747$	
R	F	R	F	R	F	R	F
0.0	6.0	0.0	9.7	0.0	11.5	0.0	15.3
2.0	5.7	2.0	9.3	3.0	11.0	1.0	14.7
5.0	5.0	4.0	8.6	5.0	10.3	2.0	14.3
8.0	4.2	6.0	8.0	8.0	9.3	4.0	13.8
10.0	3.5	8.0	7.2	10.0	7.6	6.0	12.7
13.0	2.8	10.0	6.0	12.0	5.7	8.0	11.2
15.0	2.0	11.0	5.3	13.0	5.0	10.0	9.2
17.0	1.0	12.0	5.0	14.0	4.8	12.0	7.0
21.0	0.0	15.0	4.0	16.0	3.4	14.0	5.5
		17.0	2.3	18.0	2.4	16.0	4.0
		20.0	2.2	20.0	1.7	18.0	3.2
		22.0	1.5	23.0	1.0	20.0	2.5
		25.0	0.0	27.0	0.3	24.0	1.3
				30.0	0.0	26.0	1.0
				32.0	0.4	35.0	0.0

a) Case 1s

TABLE BII. Interface Shape Data (in 1/10″ boxes)

$l = 0.9494$		$l = 0.4747$		$l = 0.000$		$l = -0.4747$	
R	F	R	F	R	F	R	F
0.0	4.5	0.0	8.2	0.0	10.7	0.0	15.0
5.0	4.0	5.0	7.7	2.0	10.5	2.0	14.8
7.0	3.8	7.0	7.0	3.0	10.0	4.0	13.3
9.0	3.5	9.0	6.0	4.3	9.5	5.0	12.8
11.0	3.1	10.0	5.5	5.0	9.0	7.0	11.5
13.0	2.5	11.9	5.0	6.5	8.0	9.0	10.0
17.0	1.6	14.0	4.0	8.0	7.2	11.0	8.2
		18.0	2.4	10.0	5.7	13.0	6.3
		20.0	1.3	11.0	5.2	15.0	5.4
		22.0	0.5	13.0	4.3	17.5	4.0
				15.0	3.5	19.0	3.0
				20.0	2.0		

b) Case 2s

TABLE BII. Interface Shape Data (in 1/10″ boxes)

$l = 2.5394$		$l = 1.2697$		$l = 0.000$		$l = -1.2697$	
R	F	R	F	R	F	R	F
0.0	4.7	0.0	10.6	0.0	17.8	8.0	25.0
5.0	4.0	3.0	10.2	3.7	17.0	10.0	24.0
7.0	3.4	5.0	9.4	5.0	16.4	11.0	23.0
10.0	3.0	7.0	8.2	7.2	15.0	12.5	21.0
14.0	2.8	10.0	6.9	10.0	13.5	14.0	19.1
18.0	2.3	12.0	6.1	12.0	12.0	15.0	17.0
22.0	1.4	14.0	5.4	15.0	10.3	16.0	15.0
26.0	0.6	17.0	4.5	17.0	9.2	17.0	13.0
		20.0	3.7	20.0	7.6	18.5	11.0
		22.3	3.0	22.0	6.4	19.0	9.0
		25.0	2.3	24.0	5.3	20.0	7.5
		30.0	1.0	26.6	5.0	21.3	6.0
				28.3	3.0		
				30.0	2.0		

c) Case 3s

TABLE BII. Interface Shape Data (in 1/10″ boxes)

$l = 2.5394$		$l = 1.2697$		$l = 0.000$		$l = -1.2697$	
R	F	R	F	R	F	R	F
0.0	5.7	0.0	11.0	8.5	15.7	10.0	25.0
4.0	5.3	5.0	10.5	10.0	13.3	11.0	23.8
8.0	5.1	7.0	9.2	12.0	11.9	12.5	22.0
10.0	4.9	9.0	8.3	13.0	11.0	13.3	21.0
13.0	4.6	11.0	7.4	14.5	10.0	14.5	19.0
15.0	4.0	13.0	6.4	16.0	8.8	16.0	16.5
20.0	3.3	15.0	5.5	18.0	7.3	17.0	15.0
23.0	3.0	17.0	4.5	21.0	5.0	18.0	12.8
		19.0	3.4	25.0	2.4	19.0	10.0
		21.0	2.4			20.0	8.2
		25.0	2.0			23.0	5.3
						25.0	4.0
						30.0	2.0

d) Case 4s

In dimensionless form these results are:

TABLE BIII. Dimensionless Interface Shape Data

$l = 2.00$		$l = 1.00$		$l = 0.00$		$l = -1.00$	
R	F	R	F	R	F	R	F
0.00	1.09	0.00	1.76	0.00	2.09	0.00	2.78
0.36	1.04	0.36	1.69	0.55	2.00	0.18	2.67
0.91	0.91	0.73	1.56	0.91	1.91	0.36	2.60
1.45	0.76	1.09	1.45	1.45	1.69	0.73	2.51
1.82	0.64	1.45	1.31	1.82	1.38	1.09	2.31
2.36	0.51	1.82	1.09	2.18	1.04	1.45	2.04
2.73	0.36	2.00	0.96	2.36	0.91	1.82	1.67
3.09	0.18	2.18	0.91	2.55	0.87	2.18	1.27
3.82	0.00	2.73	0.73	2.91	0.62	2.55	0.98
		3.09	0.60	3.27	0.44	2.91	0.73
		3.64	0.40	3.64	0.31	3.27	0.58
		4.00	0.27	4.18	0.18	3.64	0.45
		4.55	0.18	4.91	0.05	4.36	0.24
				5.45	0.00	4.37	0.18
				5.82	0.05	6.36	0.00

a) Case 1s

TABLE BIII. Dimensionless Interface Shape Data

$l = 2.00$		$l = 1.00$		$l = 0.00$		$l = -1.00$	
R	F	R	F	R	F	R	F
0.000	0.817	0.000	1.489	0.000	1.942	0.000	2.723
0.908	0.726	0.908	1.398	0.363	1.906	0.363	2.687
1.271	0.690	1.271	1.271	0.545	1.815	0.726	2.414
1.634	0.635	1.634	1.089	0.781	1.725	0.908	2.324
1.997	0.563	1.815	0.998	0.908	1.634	1.271	2.088
2.360	0.454	2.069	0.908	1.180	1.452	1.634	1.815
3.086	0.290	2.541	0.726	1.452	1.307	1.997	1.489
		3.267	0.436	1.815	1.071	2.360	1.144
		3.631	0.236	1.997	0.944	2.723	0.980
		3.994	0.091	2.360	0.781	3.177	0.726
				2.723	0.634	3.449	0.545
				3.631	0.363		

b) Case 2s

TABLE BIII. Dimensionless Interface Shape Data

$l = 2.00$		$l = 1.00$		$l = 0.00$		$l = -1.00$	
R	F	R	F	R	F	R	F
0.000	0.362	0.000	0.815	0.000	1.369	0.615	1.923
0.385	0.308	0.231	0.785	0.285	1.308	0.769	1.846
0.538	0.262	0.385	0.723	0.385	1.262	0.846	1.769
0.769	0.231	0.538	0.631	0.554	1.154	0.962	1.615
1.077	0.215	0.769	0.531	0.769	1.038	1.077	1.469
1.385	0.177	0.923	0.469	0.923	0.923	1.154	1.308
1.692	0.108	1.077	0.415	1.154	0.792	1.231	1.154
2.000	0.046	1.308	0.346	1.308	0.708	1.308	1.000
		1.538	0.262	1.538	0.585	1.423	0.846
		1.715	0.231	1.692	0.492	1.462	0.692
		1.923	0.177	1.846	0.408	1.538	0.577
		2.308	0.077	2.046	0.385	1.638	0.462
				2.177	0.231		
				2.308	0.154		

c) Case 3s

TABLE BIII. Dimensionless Interface Shape Data

$l = 2.00$		$l = 1.00$		$l = 0.00$		$l = -1.00$	
R	F	R	F	R	F	R	F
0.000	0.438	0.000	0.846	0.654	1.208	0.769	1.923
0.308	0.408	0.385	0.808	0.769	1.023	0.846	1.831
0.615	0.392	0.538	0.708	0.923	0.915	0.962	1.692
0.769	0.377	0.692	0.638	1.000	0.846	1.023	1.615
1.000	0.354	0.846	0.569	1.115	0.769	1.115	1.462
1.154	0.308	1.000	0.492	1.231	0.677	1.231	1.269
1.538	0.254	1.154	0.423	1.385	0.562	1.308	1.154
1.769	0.231	1.308	0.346	1.615	0.385	1.385	0.985
		1.462	0.262	1.923	0.185	1.462	0.769
		1.615	0.185			1.538	0.631
		1.923	0.154			1.769	0.408
						1.923	0.308
						2.308	0.169

d) Case 4s

The results of the tracer particle experiments are given in Table BIV:

TABLE BIV. Tracer Particle Data (in 1/10″ boxes)

l	a	b	c	d	e	f	g	h
41.8	26.2	28.0	22.3	25.5	38.2	24.9	39.6	27.2
42.2	26.9	28.5	22.9	26.0	38.8	25.9	40.2	28.0
42.5	27.5	29.3	23.7	26.8	39.2	26.6	40.6	28.2
42.8	28.2	29.9	24.2	27.5	39.8	27.2	41.0	29.6
43.0	28.2	30.2	25.0	28.2	40.0	27.9	41.5	30.0
43.3	30.0	31.4	27.1	29.3	41.9	28.8	41.9	
43.5	30.5	31.8	27.6	29.9		29.8		

a) Case 1b

TABLE BIV. Tracer Particle Data

(in 1/10″ boxes)

l	a	b	c	d
41.8	26.4	32.3	24.4	31.8
42.0	27.0	32.7	24.9	32.3
42.2	27.7	33.2	25.2	32.8
42.5	28.2	33.6	25.7	33.1
42.7	28.7	34.1	26.2	33.8
43.0	29.1	34.5	26.9	34.4
43.5	31.8	36.9	29.7	36.8

b) Case 2b

TABLE BIV. Tracer Particle Data (in 1/10″ boxes)

l	a	b	c	d	e	f	g	h	i
30.7	20.5	24.3	35.2	31.6	26.0	18.1	36.8	28.7	21.0
31.5	21.2	25.1	35.9	32.7	27.1	19.0	38.1	29.8	22.0
32.0	21.9	25.9	36.4	33.5	28.0	19.9	38.9	30.8	22.9
32.5	22.8	26.8	37.3	34.5	29.0	20.6	39.9	31.8	23.9
33.0	24.0	28.2	38.2	35.4	29.8	21.8	40.3	32.8	25.0
33.5	25.7	29.4	38.7	36.3	30.8	23.8	41.0	33.7	26.5
34.0	27.8	31.0	29.0	37.2		25.5	41.8	35.0	28.6
34.5	29.7	32.0	39.4	37.8	32.3			35.9	30.2
35.0	31.2	33.0	40.0	39.2	33.5			36.4	31.5
35.5	31.7	33.4	40.4	39.7	34.2				

c) Case 3b

TABLE BIV. Tracer Particle Data

(in 1/10″ boxes)

l	a	b	c	d
30.7	13.0	26.5	23.1	28.5
31.5	13.7	28.0	24.6	31.5
32.0	14.4	29.0	25.5	32.9
32.5	15.2	29.9	26.7	34.5
33.0	16.5	31.2	27.9	35.8
33.5	17.8	32.7	29.4	38.2
34.0		34.2	31.2	40.1
34.5		35.3	33.0	41.2
35.0		36.0	34.0	41.8
35.5			34.4	

d) Case 4b

In dimensionless form these results are:

TABLE BV. Dimensionless Tracer Particle Data

l	a	b	c	d	e	f	g	h
3.00	1.54	1.64	1.31	1.50	2.24	1.46	2.32	1.60
2.26	1.58	1.67	1.34	1.52	2.28	1.51	2.36	1.64
1.63	1.62	1.72	1.39	1.57	2.30	1.56	2.38	1.65
1.00	1.65	1.75	1.42	1.61	2.34	1.60	2.41	1.74
0.57	1.69	1.77	1.47	1.65	2.35	1.64	2.44	1.76
-0.05	1.76	1.85	1.59	1.72	2.46	1.69	2.46	
-0.47	1.79	1.87	1.62	1.76		1.75		

a) Case 1b

TABLE BV. Dimensionless Tracer Particle Data

l	a	b	c	d
3.00	1.38	1.70	1.28	1.67
2.68	1.42	1.72	1.31	1.70
2.15	1.45	1.74	1.32	1.72
1.63	1.48	1.76	1.35	1.74
1.10	1.51	1.79	1.37	1.77
0.57	1.53	1.81	1.41	1.81
-0.47	1.67	1.94	1.56	1.93

b) Case 2b

TABLE BV. Dimensionless Tracer Particle Data

l	a	b	c	d	e	f	g	h	i
3.00	0.91	1.08	1.56	1.40	1.15	0.80	1.63	1.27	0.93
2.33	0.94	1.11	1.59	1.45	1.20	0.84	1.69	1.32	0.97
1.94	0.97	1.15	1.61	1.48	1.24	0.88	1.72	1.36	1.01
1.55	1.01	1.19	1.65	1.53	1.28	0.91	1.77	1.41	1.06
1.15	1.06	1.25	1.69	1.57	1.32	0.96	1.79	1.45	1.11
0.76	1.14	1.30	1.72	1.61	1.36	1.05	1.82	1.49	1.17
0.36	1.23	1.37	1.73	1.65		1.13	1.85	1.55	1.27
-0.02	1.32	1.42	1.75	1.68	1.43			1.59	1.34
-0.41	1.38	1.46	1.77	1.74	1.48			1.61	1.40
-0.81	1.40	1.48	1.79	1.76	1.52				

c) Case 3b

TABLE BV. Dimensionless Tracer Particle Data

l	a	b	c	d
3.00	0.51	1.03	0.90	1.11
2.33	0.53	1.09	0.96	1.23
1.94	0.56	1.13	1.00	1.29
1.55	0.59	1.17	1.04	1.35
1.15	0.64	1.22	1.09	1.40
0.76	0.69	1.28	1.15	1.49
0.36		1.34	1.22	1.57
-0.02		1.38	1.29	1.61
-0.41		1.41	1.33	1.63
-0.81			1.34	

d) Case 4b

Table BVI. Force Data

POSITION					RATIO	WIRE DRAG	SPHERE DRAG	SCALED DRAG
0.0000000					0.8592101	115.4705548	145.1338196	1.0075496
0.5000000					0.8643479	121.6144104	146.6774139	1.0197977
1.0000000					0.8734416	130.8156210	145.8559113	1.0187165
1.5000000					0.8857660	145.0243866	144.2695007	1.0021696
2.0000000					0.8907718	151.8056946	144.1972656	1.0102037
2.5000000					0.9134011	157.7586821	141.1591140	1.0058681
3.0000000					0.8962558	163.6932731	144.7161560	1.0169425
3.5000000					0.9009537	169.5796051	148.2138715	1.0432590
4.0000000					0.9027001	175.4476776	151.7422791	1.0695907
4.5000000					0.9105114	182.8828430	150.1463165	1.0613386
5.0000000					0.9134511	188.6383667	155.6003326	1.1019882
5.5000000					0.9158040	204.1658752	157.1350220	1.1175920
6.0000000					0.9176359	210.0653229	159.0454712	1.1314925
6.5000000					0.9195761	215.7368927	160.7393927	1.1457459
7.0000000					0.9219070	221.3805389	162.5041064	1.1607633
7.5000000					0.9244419	238.1445160	172.2160070	1.2347220
8.0000000					0.9271750	243.6769562	174.1232452	1.2501860
8.5000000					0.9300495	249.1817322	177.2821960	1.2750651
9.0000000					0.9330921	254.6588898	173.9883728	1.2511185
9.5000000					0.9362711	260.1084290	180.0417175	1.2980825
10.0000000					0.9395703	265.5304565	181.2674713	1.3095845
10.5000000					0.9429825	270.9248962	180.1708221	1.3019138
11.0000000					0.9465489	276.2917480	196.6543289	1.4206003
11.5000000					0.9502489	281.6310059	198.5355835	1.4417586
12.0000000					0.9541002	286.9426612	200.6450348	1.4606395
12.5000000					0.9580908	292.2267151	209.7863892	1.5214727
13.0000000					0.9622018	297.4831450	212.9212189	1.5512924
13.5000000					0.9664000	302.7225342	215.0654144	1.5705969
14.0000000					0.9707754	307.9445931	225.2175751	1.6464849
14.5000000					0.9753264	313.1497192	233.3750458	1.7073341
15.0000000					0.9800361	318.3379211	244.3234253	1.7889594
15.5000000					0.9850059	323.5091858	259.6611023	1.9043543
16.0000000					0.9901223	328.6637329	273.0101318	2.0043905
16.5000000					0.9954422	333.8013611	352.0793457	2.5931966
17.0000000					1.0010111	338.9388672	384.1093445	2.8131577
17.5000000					1.0067106	344.0612793	426.0946655	3.1300914
18.0000000					1.0126273	349.1685791	448.1750183	3.2916015
18.5000000					1.0187531	354.2607422	450.2449951	3.3076843
19.0000000					1.0250907	359.3376465	449.3476563	3.3064139
19.5000000					1.0316277	364.3993225	440.4083118	3.2400527
20.0000000					1.0383775	369.4457703	440.6550903	3.2418911
20.5000000					1.0453157	374.4770203	397.1243591	2.9438624
21.0000000					0.0000000	0.0000000	0.0000000	0.0000000
97.0000031					0.0000000	0.0000000	0.0000000	0.0000000
139.3999939					0.0000000	0.0000000	0.0000000	0.0000000

a) Case 1s.

Table BVI. Force Data

POSITION				WIRE DIA IN.	RATIO	WIRE DRAG	SPHERE DRAG	SCALED DRAG
0.0000000				1.9385750	0.9535655	110.6095352	145.1452179	1.0076188
0.5000000				4.1010650	0.8607503	116.7407761	142.5019226	0.9907669
1.0000000				4.3823277	0.8671179	122.8434525	141.8598038	0.9877991
1.5000000				4.6113081	0.8727900	128.9175415	142.9451904	1.0685908
2.0000000				5.0511301	0.8825544	140.9302856	140.3881073	0.9820191
2.5000000				5.2816516	0.8867705	146.9689789	139.4211273	0.9767435
3.0000000				5.5030139	0.8905220	152.9293365	138.5208618	0.9722703
3.5000000				5.7271484	0.8941565	158.9612976	135.6819305	0.9514577
4.0000000				5.9477062	0.8974705	164.7650146	137.0980225	0.9648858
4.5000000				6.1654340	0.9004740	170.6404572	136.4813843	0.9620381
5.0000000				6.6113720	0.9060131	182.3068237	137.1889954	0.9690870
5.5000000				6.8352051	0.9110138	193.8606873	136.5693359	0.9685892
6.0000000				7.0552063	0.9153981	194.5955811	138.0301819	0.9806646
6.5000000				7.2719483	0.9193247	206.3023987	136.8702130	0.9738740
7.0000000				7.7166321	0.9260319	210.9813538	137.6413147	0.9791123
7.5000000				7.9329834	0.9293607	216.6123853	137.2119598	0.9791978
8.0000000				8.1475372	0.9324178	222.2556305	139.0622102	0.9919829
8.5000000				8.5713654	0.9380459	233.9503113	146.8572388	1.0545877
9.0000000				8.7810287	0.9407799	244.4705048	144.7714691	1.0412384
9.5000000				8.9894409	0.9433220	249.9550323	150.0268250	1.0807296
10.0000000				9.1965332	0.9457459	255.4119263	144.7742615	1.0465115
10.5000000				9.6077881	0.9505192	260.8413391	156.1470795	1.1283582
11.0000000				9.8111877	0.9527512	266.2431641	155.0066071	1.1218829
11.5000000				10.0099487	0.9550591	271.6175842	161.1599426	1.1682603
12.0000000				10.2141418	0.9573016	276.9644775	161.2308478	1.1710505
12.5000000				10.6173553	0.9617182	287.5763550	171.5911281	1.2505285
13.0000000				10.8155518	0.9637324	292.9413391	177.9192657	1.2979479
13.5000000				11.0085297	0.9656295	296.1012390	184.1338196	1.3446943
14.0000000				11.2437588	0.9681446	299.8535767	185.4254150	1.3555930
14.5000000				11.3955078	0.9694946	303.2294807	186.4441071	1.3644743
15.0000000				11.5248871	0.9706420	306.7445374	200.6413269	1.4699361
15.5000000				11.6885967	0.9721006	310.1248856	209.4114075	1.5314578
16.0000000				11.8103247	0.9731794	313.6290283	222.9956696	1.6321949
16.5000000				11.9518433	0.9744256	317.0480042	235.1837616	1.7205172
17.0000000				12.0912476	0.9755951	320.4621277	247.3631897	1.8099764
17.5000000				12.2247314	0.9767004	323.8501892	261.5195508	1.9263170
18.0000000				12.4464722	0.9784927	328.9153137	311.6708069	2.2992613
18.5000000				12.5610962	0.9793982	330.6213379	333.6759949	2.4629176
19.0000000				12.6577759	0.9801847	332.1037415	347.7116699	2.5678930
19.5000000				12.7291565	0.9807620	333.9833679	363.7119136	2.6876464
20.0000000				12.7991562	0.9813267	335.6601868	383.7750854	2.8328705
20.1666667				12.7991562	0.9813267	337.1305664	397.7763062	2.9423571
20.3333333				12.7991562	0.9813267	339.0046692	415.8103638	3.0774555
20.5000000				12.7991562	0.9813267	350.6727600	421.8774414	3.1219927
20.6666667				12.7991562	0.9813267	342.1372498	436.7477501	3.1617558
20.8333333				12.7991562	0.9813267	343.9990234	420.0988159	3.1141708
21.0000000				12.7991562	0.9813267	347.3103943	404.4456787	3.0013621
21.3333333				0.0000000	0.0000000	0.0000000	0.0000000	0.0000000
22.0000000				0.0000000	0.0000000	0.0000000	0.0000000	0.0000000

b) Case 1b.

Table BVI. Force Data

POSITION	WEIGHT	DIST TO WATER	TOTAL LOAD	WIRE LEN IN.	RATIO	WIRE DRAG	SPHERE DRAG	SCALED DRAG
0.0000000	11.5000000	35.6129000	231.6500000	4.1700000	0.8615751	118.3130401	145.9326019	1.0077106
0.5000000	10.7000000	34.9600000	215.4000000	4.4100000	0.8567845	124.5010605	142.1039429	0.9827506
1.0000000	10.1000000	32.9600000	204.0000000	4.6100000	0.8579864	130.7908630	141.5610461	0.9818158
2.0000000	10.0500000	31.6200000	203.0000000	4.5900000	0.8611252	129.9659729	141.4441071	0.9841174
2.5000000	10.0500000	30.6700000	203.0000000	4.5900000	0.8687253	131.8106506	136.2548170	0.9494512
3.0000000	10.0000000	29.7200000	201.0000000	4.5600000	0.8691376	131.0106506	136.2548170	0.9494512
3.5000000	9.7000000	28.7900000	195.0000000	4.4700000	0.8647895	131.0106506	141.6925098	0.9882778
4.0000000	9.7000000	27.8400000	195.0000000	4.4700000	0.8629153	127.0144958	138.8185468	0.9704008
4.5000000	9.7000000	26.9000000	195.0000000	4.4700000	0.8610009	122.9737091	140.1663361	0.9811751
5.0000000	9.6000000	25.9500000	193.0000000	4.4300000	0.8613210	120.9065410	137.6173584	0.9634010
5.5000000	9.5000000	25.0000000	191.0000000	4.3900000	0.8607777	118.8869916	136.5488281	0.9558762
6.0000000	9.4500000	24.0500000	190.0000000	4.3700000	0.8577084	116.8611371	136.0771637	0.9525740
6.5000000	9.4000000	23.1000000	189.0000000	4.3500000	0.8541191	114.8352778	134.5272491	0.9417091
7.0000000	9.3500000	22.1500000	188.0000000	4.3300000	0.8504298	112.8094186	132.9773345	0.9308441
7.5000000	9.3000000	21.2000000	187.0000000	4.3100000	0.8466404	110.7835594	131.4274199	0.9199791
8.0000000	9.2500000	20.2500000	186.0000000	4.2900000	0.8427510	108.7577002	129.8775053	0.9091141
8.5000000	9.1500000	19.3000000	184.0000000	4.2500000	0.8347722	106.7318410	128.3275907	0.8982490
9.0000000	9.0500000	18.3500000	182.0000000	4.2100000	0.8267934	104.7059818	126.7776761	0.8873840
9.5000000	8.9500000	17.4000000	180.0000000	4.1700000	0.8188145	102.6801226	125.2277615	0.8765190
10.0000000	8.8500000	16.4500000	178.0000000	4.1300000	0.8108357	100.6542634	123.6778469	0.8656540
10.5000000	8.7500000	15.5000000	176.0000000	4.0900000	0.8028569	98.6284042	122.1279323	0.8547889
11.0000000	8.6500000	14.5500000	174.0000000	4.0500000	0.7948780	96.6025450	120.5780177	0.8439239
11.5000000	8.5500000	13.6000000	172.0000000	4.0100000	0.7868992	94.5766858	119.0281031	0.8330589
12.0000000	8.4500000	12.6500000	170.0000000	3.9700000	0.7789204	92.5508266	117.4781885	0.8221939
12.5000000	8.3500000	11.7000000	168.0000000	3.9300000	0.7709415	90.5249674	115.9282739	0.8113288
13.0000000	8.2500000	10.7500000	166.0000000	3.8900000	0.7629627	88.4991082	114.3783593	0.8004638
13.5000000	8.1500000	9.8000000	164.0000000	3.8500000	0.7549839	86.4732490	112.8284447	0.7895988
14.0000000	8.0500000	8.8500000	162.0000000	3.8100000	0.7470050	84.4473898	111.2785301	0.7787338
14.5000000	7.9500000	7.9000000	160.0000000	3.7700000	0.7390262	82.4215306	109.7286155	0.7678687
15.0000000	7.8500000	6.9500000	158.0000000	3.7300000	0.7310474	80.3956714	108.1787009	0.7570037
15.5000000	7.7500000	6.0000000	156.0000000	3.6900000	0.7230685	78.3698122	106.6287863	0.7461387
16.0000000	7.6500000	5.0500000	154.0000000	3.6500000	0.7150897	76.3439530	105.0788717	0.7352737
16.5000000	7.5500000	4.1000000	152.0000000	3.6100000	0.7071109	74.3180938	103.5289571	0.7244086
17.0000000	7.4500000	3.1500000	150.0000000	3.5700000	0.6991320	72.2922346	101.9790425	0.7135436
17.5000000	7.3500000	2.2000000	148.0000000	3.5300000	0.6911532	70.2663754	100.4291279	0.7026786
18.0000000	7.2500000	1.2500000	146.0000000	3.4900000	0.6831744	68.2405162	98.8792133	0.6918136
18.5000000	7.1500000	0.3000000	144.0000000	3.4500000	0.6751955	66.2146570	97.3292987	0.6809485
19.0000000	7.0500000	-0.6500000	142.0000000	3.4100000	0.6672167	64.1887978	95.7793841	0.6700835
19.5000000	6.9500000	-1.6000000	140.0000000	3.3700000	0.6592379	62.1629386	94.2294695	0.6592185
20.0000000	6.8500000	-2.5500000	138.0000000	3.3300000	0.6512590	60.1370794	92.6795549	0.6483535
20.5000000	6.7500000	-3.5000000	136.0000000	3.2900000	0.6432802	58.1112202	91.1296403	0.6374884
21.0000000	6.6500000	-4.4500000	134.0000000	3.2500000	0.6353014	56.0853610	89.5797257	0.6266234
21.5000000	6.5500000	-5.4000000	132.0000000	3.2100000	0.6273225	54.0595018	88.0298111	0.6157584
22.0000000	6.4500000	-6.3500000	130.0000000	3.1700000	0.6193437	52.0336426	86.4798965	0.6048934
22.5000000	6.3500000	-7.3000000	128.0000000	3.1300000	0.6113649	50.0077834	84.9299819	0.5940283
23.0000000	6.2500000	-8.2500000	126.0000000	3.0900000	0.6033860	47.9819242	83.3800673	0.5831633
23.5000000	6.1500000	-9.2000000	124.0000000	3.0500000	0.5954072	45.9560650	81.8301527	0.5722983
24.0000000	6.0500000	-10.1500000	122.0000000	3.0100000	0.5874284	43.9302058	80.2802381	0.5614333
24.5000000	5.9500000	-11.1000000	120.0000000	2.9700000	0.5794495	41.9043466	78.7303235	0.5505682
25.0000000	5.8500000	-12.0500000	118.0000000	2.9300000	0.5714707	39.8784874	77.1804089	0.5397032
25.5000000	5.7500000	-13.0000000	116.0000000	2.8900000	0.5634919	37.8526282	75.6304943	0.5288382
26.0000000	5.6500000	-13.9500000	114.0000000	2.8500000	0.5555130	35.8267690	74.0805797	0.5179732
26.5000000	5.5500000	-14.9000000	112.0000000	2.8100000	0.5475342	33.8009098	72.5306651	0.5071081
27.0000000	5.4500000	-15.8500000	110.0000000	2.7700000	0.5395554	31.7750506	70.9807505	0.4962431
27.5000000	5.3500000	-16.8000000	108.0000000	2.7300000	0.5315765	29.7491914	69.4308359	0.4853781
28.0000000	5.2500000	-17.7500000	106.0000000	2.6900000	0.5235977	27.7233322	67.8809213	0.4745131
28.5000000	5.1500000	-18.7000000	104.0000000	2.6500000	0.5156189	25.6974730	66.3310067	0.4636480
29.0000000	5.0500000	-19.6500000	102.0000000	2.6100000	0.5076400	23.6716138	64.7810921	0.4527830
29.5000000	4.9500000	-20.6000000	100.0000000	2.5700000	0.4996612	21.6457546	63.2311775	0.4419180
30.0000000	4.8500000	-21.5500000	98.0000000	2.5300000	0.4916824	19.6198954	61.6812629	0.4310530
30.5000000	4.7500000	-22.5000000	96.0000000	2.4900000	0.4837035	17.5940362	60.1313483	0.4201879
31.0000000	4.6500000	-23.4500000	94.0000000	2.4500000	0.4757247	15.5681770	58.5814337	0.4093229
31.5000000	4.5500000	-24.4000000	92.0000000	2.4100000	0.4677459	13.5423178	57.0315191	0.3984579
32.0000000	4.4500000	-25.3500000	90.0000000	2.3700000	0.4597670	11.5164586	55.4816045	0.3875928
32.5000000	4.3500000	-26.3000000	88.0000000	2.3300000	0.4517882	9.4905994	53.9316899	0.3767278
33.0000000	4.2500000	-27.2500000	86.0000000	2.2900000	0.4438094	7.4647402	52.3817753	0.3658628
33.5000000	4.1500000	-28.2000000	84.0000000	2.2500000	0.4358305	5.4388810	50.8318607	0.3549978
34.0000000	4.0500000	-29.1500000	82.0000000	2.2100000	0.4278517	3.4130218	49.2819461	0.3441327
34.5000000	3.9500000	-30.1000000	80.0000000	2.1700000	0.4198729	1.3871626	47.7320315	0.3332677
35.0000000	3.8500000	-31.0500000	78.0000000	2.1300000	0.4118940	-0.6387966	46.1821169	0.3224027
35.5000000	3.7500000	-32.0000000	76.0000000	2.0900000	0.4039152	-2.6646558	44.6322023	0.3115376
36.0000000	3.6500000	-32.9500000	74.0000000	2.0500000	0.3959364	-4.6905150	43.0822877	0.3006726
36.5000000	3.5500000	-33.9000000	72.0000000	2.0100000	0.3879575	-6.7163742	41.5323731	0.2898076
37.0000000	3.4500000	-34.8500000	70.0000000	1.9700000	0.3799787	-8.7422334	39.9824585	0.2789425
37.5000000	3.3500000	-35.8000000	68.0000000	1.9300000	0.3719999	-10.7680926	38.4325439	0.2680775
38.0000000	3.2500000	-36.7500000	66.0000000	1.8900000	0.3640210	-12.7939518	36.8826293	0.2572125
38.5000000	3.1500000	-37.7000000	64.0000000	1.8500000	0.3560422	-14.8198110	35.3327147	0.2463474
39.0000000	3.0500000	-38.6500000	62.0000000	1.8100000	0.3480634	-16.8456702	33.7828001	0.2354824
39.5000000	2.9500000	-39.6000000	60.0000000	1.7700000	0.3400845	-18.8715294	32.2328855	0.2246174
40.0000000	2.8500000	-40.5500000	58.0000000	1.7300000	0.3321057	-20.8973886	30.6829709	0.2137523
40.5000000	2.7500000	-41.5000000	56.0000000	1.6900000	0.3241269	-22.9232478	29.1330563	0.2028873
41.0000000	2.6500000	-42.4500000	54.0000000	1.6500000	0.3161480	-24.9491070	27.5831417	0.1920223
41.5000000	2.5500000	-43.4000000	52.0000000	1.6100000	0.3081692	-26.9749662	26.0332271	0.1811572
42.0000000	2.4500000	-44.3500000	50.0000000	1.5700000	0.3001904	-29.0008254	24.4833125	0.1702922
42.5000000	2.3500000	-45.3000000	48.0000000	1.5300000	0.2922115	-31.0266846	22.9333979	0.1594272
43.0000000	2.2500000	-46.2500000	46.0000000	1.4900000	0.2842327	-33.0525438	21.3834833	0.1485621
43.5000000	2.1500000	-47.2000000	44.0000000	1.4500000	0.2762539	-35.0784030	19.8335687	0.1376971
44.0000000	2.0500000	-48.1500000	42.0000000	1.4100000	0.2682750	-37.1042622	18.2836541	0.1268321
44.5000000	1.9500000	-49.1000000	40.0000000	1.3700000	0.2602962	-39.1301214	16.7337395	0.1159670
45.0000000	1.8500000	-50.0500000	38.0000000	1.3300000	0.2523174	-41.1559806	15.1838249	0.1051020
45.5000000	1.7500000	-51.0000000	36.0000000	1.2900000	0.2443385	-43.1818398	13.6339103	0.0942370
46.0000000	1.6500000	-51.9500000	34.0000000	1.2500000	0.2363597	-45.2076990	12.0839957	0.0833719
46.5000000	1.5500000	-52.9000000	32.0000000	1.2100000	0.2283809	-47.2335582	10.5340811	0.0725069
47.0000000	1.4500000	-53.8500000	30.0000000	1.1700000	0.2204020	-49.2594174	8.9841665	0.0616419
47.5000000	1.3500000	-54.8000000	28.0000000	1.1300000	0.2124232	-51.2852766	7.4342519	0.0507768
48.0000000	1.2500000	-55.7500000	26.0000000	1.0900000	0.2044444	-53.3111358	5.8843373	0.0399118
48.5000000	1.1500000	-56.7000000	24.0000000	1.0500000	0.1964655	-55.3369950	4.3344227	0.0290468
49.0000000	1.0500000	-57.6500000	22.0000000	1.0100000	0.1884867	-57.3628542	2.7845081	0.0181817
49.5000000	0.9500000	-58.6000000	20.0000000	0.9700000	0.1805079	-59.3887134	1.2345935	0.0073167
50.0000000	0.8500000	-59.5500000	18.0000000	0.9300000	0.1725290	-61.4145726	-0.3153211	-0.0035483
50.5000000	0.7500000	-60.5000000	16.0000000	0.8900000	0.1645502	-63.4404318	-1.8652357	-0.0144133
51.0000000	0.6500000	-61.4500000	14.0000000	0.8500000	0.1565714	-65.4662910	-3.4151503	-0.0252784
51.5000000	0.5500000	-62.4000000	12.0000000	0.8100000	0.1485925	-67.4921502	-4.9650649	-0.0361434
52.0000000	0.4500000	-63.3500000	10.0000000	0.7700000	0.1406137	-69.5180094	-6.5149795	-0.0470084
52.5000000	0.3500000	-64.3000000	8.0000000	0.7300000	0.1326349	-71.5438686	-8.0648941	-0.0578735
53.0000000	0.2500000	-65.2500000	6.0000000	0.6900000	0.1246560	-73.5697278	-9.6148087	-0.0687385
53.5000000	0.1500000	-66.2000000	4.0000000	0.6500000	0.1166772	-75.5955870	-11.1647233	-0.0796035
54.0000000	0.0500000	-67.1500000	2.0000000	0.6100000	0.1086984	-77.6214462	-12.7146379	-0.0904686
54.5000000	0.0000000	-68.1000000	0.0000000	0.5700000	0.1007195	-79.6473054	-14.2645525	-0.1013336
55.0000000	0.0000000	-69.0500000	0.0000000	0.5300000	0.0927407	-81.6731646	-15.8144671	-0.1121986
55.5000000	0.0000000	-70.0000000	0.0000000	0.4900000	0.0847619	-83.6990238	-17.3643817	-0.1230637
56.0000000	0.0000000	-70.9500000	0.0000000	0.4500000	0.0767830	-85.7248830	-18.9142963	-0.1339287
56.5000000	0.0000000	-71.9000000	0.0000000	0.4100000	0.0688042	-87.7507422	-20.4642109	-0.1447937
57.0000000	0.0000000	-72.8500000	0.0000000	0.3700000	0.0608254	-89.7766014	-22.0141255	-0.1556588
57.5000000	0.0000000	-73.8000000	0.0000000	0.3300000	0.0528465	-91.8024606	-23.5640401	-0.1665238
58.0000000	0.0000000	-74.7500000	0.0000000	0.2900000	0.0448677	-93.8283198	-25.1139547	-0.1773888
58.5000000	0.0000000	-75.7000000	0.0000000	0.2500000	0.0368889	-95.8541790	-26.6638693	-0.1882539
59.0000000	0.0000000	-76.6500000	0.0000000	0.2100000	0.0289100	-97.8800382	-28.2137839	-0.1991189
59.5000000	0.0000000	-77.6000000	0.0000000	0.1700000	0.0209312	-99.9058974	-29.7636985	-0.2099839
60.0000000	0.0000000	-78.5500000	0.0000000	0.1300000	0.0129524	-101.9317566	-31.3136131	-0.2208490
60.5000000	0.0000000	-79.5000000	0.0000000	0.0900000	0.0049735	-103.9576158	-32.8635277	-0.2317140

c) Case 2s.

Table BVI. Force Data

POSITION	HEIGHT	DIST TO INTER	TOTAL FORCE	WIRE FIN IN.	RATIO	WIRE DRAG	SPHERE DRAG	SCALED DRAG
0.0000000	18.3[illegible]	31.0[illegible]	245.[illegible]	5.0[illegible]	0.87[illegible]	137.9311371	141.3054967	1.0078386
0.5000000	18.2[illegible]	30.1[illegible]	252.[illegible]	5.0[illegible]	0.8827764	138.6911847	142.6411580	1.0189624
1.0000000	17.4[illegible]	27.[illegible]	269.[illegible]	5.[illegible]	0.8949014	155.8050537	140.8077626	1.0117110
1.5000000	17.5[illegible]	26.4673824	275.[illegible]	5.[illegible]	0.8774907	161.4541626	144.6958521	1.0400274
2.0000000	17.[illegible]	25.[illegible]	297.[illegible]	6.[illegible]	0.8986077	176.2357025	145.5560760	1.0512207
2.5000000	16.[illegible]	22.[illegible]	301.[illegible]	6.[illegible]	0.9092140	181.7744293	145.3572998	1.0514392
3.0000000	16.[illegible]	21.[illegible]	309.[illegible]	6.[illegible]	0.9180000	189.2857056	146.2870789	1.0598146
3.5000000	16.[illegible]	20.[illegible]	322.[illegible]	7.[illegible]	0.9317641	200.2259521	147.1058502	1.0611409
4.0000000	16.[illegible]	19.[illegible]	326.[illegible]	7.[illegible]	0.9277849	205.6549835	145.0297394	1.0557234
4.5000000	15.[illegible]	17.[illegible]	338.[illegible]	7.[illegible]	0.9390625	211.0567627	150.1859028	1.0964806
5.0000000	15.[illegible]	17.[illegible]	346.[illegible]	8.[illegible]	0.9348337	216.4112244	144.4084412	1.0538148
5.5000000	15.[illegible]	16.[illegible]	352.[illegible]	8.[illegible]	0.9241761	227.0985870	149.6999512	1.0966752
6.0000000	15.[illegible]	16.[illegible]	362.[illegible]	8.[illegible]	0.9261545	232.3915100	155.7774780	1.1426551
6.5000000	15.[illegible]	15.[illegible]	369.[illegible]	8.[illegible]	0.9278638	237.6573486	155.9248047	1.1459366
7.0000000	15.[illegible]	15.[illegible]	373.[illegible]	9.[illegible]	0.9291151	242.8961029	154.1283264	1.1345481
7.5000000	14.[illegible]	13.[illegible]	386.[illegible]	9.[illegible]	0.9307104	248.1079102	162.4291455	1.1900073
8.0000000	14.[illegible]	13.[illegible]	392.[illegible]	9.[illegible]	0.9320068	253.2927094	162.7000656	1.2021629
8.5000000	14.[illegible]	13.[illegible]	401.[illegible]	9.[illegible]	0.9331704	258.4506226	167.1536407	1.2363756
9.0000000	14.[illegible]	12.[illegible]	405.[illegible]	10.[illegible]	0.9340216	263.5816650	165.4785461	1.2259606
9.5000000	13.[illegible]	11.[illegible]	425.[illegible]	10.[illegible]	0.9369723	273.7631836	176.3512268	1.3107423
10.0000000	13.[illegible]	11.[illegible]	442.[illegible]	10.[illegible]	0.9388069	278.8138428	188.8547876	1.4058776
10.5000000	13.[illegible]	10.[illegible]	446.[illegible]	10.[illegible]	0.9391127	283.8372991	189.2932587	1.4115052
11.0000000	13.[illegible]	10.[illegible]	471.[illegible]	11.[illegible]	0.9402117	288.8350220	207.9276367	1.5522319
11.5000000	12.[illegible]	9.[illegible]	482.[illegible]	11.[illegible]	0.9412859	293.8056946	214.3322449	1.6034223
12.0000000	12.[illegible]	9.[illegible]	498.[illegible]	11.[illegible]	0.9419578	298.7014404	227.8878479	1.7066842
12.5000000	11.[illegible]	8.[illegible]	512.[illegible]	11.[illegible]	0.9426178	300.3922729	239.0316162	1.7920926
13.0000000	11.[illegible]	8.[illegible]	531.[illegible]	11.[illegible]	0.9437291	303.6573279	255.3612061	1.9166069
13.5000000	10.[illegible]	7.[illegible]	542.[illegible]	11.[illegible]	0.9439215	306.9277649	263.7049103	1.9813824
14.0000000	10.[illegible]	7.[illegible]	591.[illegible]	11.[illegible]	0.9444431	310.1931665	311.9627380	2.3465438
14.5000000	9.[illegible]	6.[illegible]	601.[illegible]	12.[illegible]	0.9448884	311.8043823	322.1112249	2.4242067
15.0000000	8.[illegible]	6.[illegible]	622.[illegible]	12.[illegible]	0.9451107	313.4230042	340.2351990	2.5620039
15.5000000	[illegible]	5.[illegible]	636.[illegible]	12.[illegible]	0.9454486	315.0396061	358.3522949	2.6999015
16.0000000	7.[illegible]	5.[illegible]	657.[illegible]	12.[illegible]	0.9457451	316.6481934	376.4640503	2.8379104
16.5000000	7.[illegible]	-0.[illegible]	670.[illegible]	12.[illegible]	0.9460399	318.2611694	392.5688171	2.9609375
17.0000000	6.[illegible]	-0.[illegible]	695.[illegible]	12.[illegible]	0.9463318	319.8603777	410.6628723	3.0971089
17.5000000	6.[illegible]	-0.[illegible]	713.[illegible]	12.[illegible]	0.9466205	321.4719849	424.3672017	3.2043004
18.0000000	5.[illegible]	-1.[illegible]	714.[illegible]	12.[illegible]	0.9469069	323.0730591	430.9044800	3.2554317
18.5000000	5.[illegible]	-1.[illegible]	713.[illegible]	12.[illegible]	0.9471914	324.6711426	431.0615540	3.2735262
18.3333333	5.[illegible]	-1.[illegible]	713.[illegible]	12.[illegible]	0.9474714	326.2631531	427.2645264	3.2314959
18.5000000	6.[illegible]	-1.[illegible]	712.[illegible]	12.[illegible]	0.9477704	327.8585815	419.4443360	3.1743774
97.9000031	0.1[illegible]	1.0[illegible]	0.0[illegible]	6.0[illegible]	0.0000000	0.0000000	0.0000000	0.0000000
139.1000030	0.1[illegible]	0.0[illegible]	0.0[illegible]	0.0[illegible]	0.0000000	0.0000000	0.0000000	0.0000000

d) Case 2b.

Table BVI. Force Data

7.7250	0.0997	0.0041	24.0000	0.3760	
14	14				
0.3333	15.2200	15.2694			
0.0010	25.2000	1.0774	15.0000	1.0150	
0.0300	1.0001	33.6611			
0.47705+07					

POSITION	WEIGHT	DIST TO INTER	TOTAL FLIGHT	WIRE LEN IN.	RATIO	WIRE DRAG	SPHERE DRAG	SCALED DRAG
0.0000000	12.0000000	11.9793789	461.7099915	6.2141981	0.9225189	174.2174088	305.0079346	1.0069791
0.3333000	12.4500391	11.9615566	470.9916077	6.3711666	0.9229087	178.3981171	308.5411682	1.0202208
0.6667000	12.1999634	11.9439245	479.7790035	6.5116099	0.9213020	182.5581055	312.0661792	1.0315969
1.0000000	12.1999634	11.9263855	488.1217432	6.6490672	0.9236582	186.6974792	309.7625122	1.0224398
1.3330000	12.0000000	10.7101176	466.9556265	6.4585085	0.9241106	190.8162384	314.4588318	1.0446389
1.6667000	11.7000000	10.3342509	497.9721069	7.0065347	0.9247096	194.9144745	320.3530579	1.0658771
2.0000000	11.5000067	10.0726772	508.9660400	7.1643218	0.9248991	198.9921722	322.6722900	1.0752815
2.3330000	11.1000160	9.7659596	518.7630615	7.3211174	0.9253022	201.0493927	334.4150085	1.1161507
2.6667000	11.1000320	9.4599001	528.0610596	7.4790654	0.9252059	207.0861511	331.2480774	1.1073008
3.0000000	11.1000064	9.1549058	536.8072266	7.6380774	0.9261094	211.1025045	334.0335999	1.1183621
3.3330000	10.9000092	8.8519015	545.0072266	7.7980220	0.9264134	215.0984497	340.1543396	1.1411112
3.6667000	10.7000000	8.5508156	552.6580505	7.9592317	0.9269171	219.0740509	344.7727356	1.1579471
4.0000000	10.3999996	8.1955643	559.1138428	8.1015984	0.9271302	221.0291274	346.1412781	1.1650468
4.3330000	10.1000092	7.8863831	556.1365112	8.2618167	0.9277225	226.9642792	349.5981140	1.1778572
5.0000000	9.7999878	7.5717945	568.1760254	8.5171184	0.9283300	230.8789673	353.9294739	1.1943339
5.3330002	9.6500092	7.2600479	566.8258057	8.5729160	0.9291242	234.7734680	354.9559631	1.1990928
5.6667000	9.5999718	6.9499922	572.2918701	8.7281771	0.9295211	238.6477356	355.1402283	1.2022448
6.0000000	9.3999996	6.6419983	584.3560486	8.8836231	0.9253219	242.5018311	363.4747620	1.2323846
6.3330002	9.1500000	6.3359528	590.1424255	9.0380211	0.9297287	246.3357697	365.8478868	1.2424071
6.6667004	9.1500034	6.0299835	596.5955200	9.1925659	0.9301106	250.1496429	368.9554749	1.2549510
7.0000000	8.9500122	5.7212782	609.6110001	9.3480988	0.9305027	254.1434662	378.9160217	1.2895229
7.3330002	8.3500366	5.4060669	622.9620056	9.5009613	0.9308930	257.7171936	388.2926074	1.3206658
7.6667004	8.3500366	5.0996399	626.0163574	9.6542196	0.9312810	261.4709473	390.2744141	1.3318155
8.0000000	7.6500244	4.7991798	634.0020447	9.8082790	0.9316671	265.2046814	394.8663635	1.3516970
8.3330002	7.1999634	4.4874591	644.0019531	9.9615936	0.9320511	268.9185486	399.4732056	1.3696566
8.6667004	6.7000000	4.1761323	654.3955078	10.1146612	0.9324325	272.6124573	409.8025513	1.4073311
9.0000000	6.3000000	3.8709655	665.2744141	10.2674828	0.9328116	276.2864990	425.1170850	1.4623433
9.3330002	6.1000000	3.5655239	676.6274414	10.4206543	0.9331886	279.9407043	435.9593201	1.5019870
9.6667004	5.5000000	3.2604368	688.4974365	10.5723906	0.9335631	283.5750122	448.7475281	1.5343799
10.0000000	5.1000000	2.9554178	700.8616943	10.7244759	0.9339348	287.1896362	465.2555542	1.6081066
10.3330002	5.0000000	2.6504211	713.6838989	10.8763132	0.9343051	290.7844543	485.1089172	1.6794449
10.6667004	4.1999998	2.3534698	725.9977722	11.0279064	0.9346849	294.3595886	512.5603638	1.7773621
11.0000000	3.3000000	2.0491371	738.0021973	11.1792336	0.9350494	297.9150391	546.4603271	1.8970950
11.3330002	2.4000001	1.7446075	810.1582031	11.3303547	0.9353970	301.4507446	581.0125732	2.0212701
11.6667004	1.5000000	1.4411115	859.2529297	11.4813107	0.9357561	304.9669189	615.5790405	2.1450169
12.0000000	0.1410000	1.1421131	882.1729736	11.6000000	0.0000000	0.0000000	0.0000000	0.0000000
112.4000015	0.1504000	0.0000000	0.0000000	0.0000000	0.0000000	0.0000000	0.0000000	0.0000000

e) Case 3s.

Table BVI. Force Data

POSITION	HEIGHT	DIST TO INTER	TOTAL FORCE	WIRE LED IN.	RATIO	WIRE DRAG	SPHERE DRAG	SCALED DRAG
0.0000000	27.7500000	13.0413519	415.6954346	3.4881592	0.9174027	95.7923201	337.2471924	1.1210817
1.0000000	23.0000000	12.0961876	429.7750244	3.9230342	0.9178018	107.4566509	317.8763733	1.1417491
2.0000000	24.0000000	12.0822460	456.8556213	4.1624425	0.9185469	118.0567958	362.5582225	1.1627816
3.0000000	21.5000000	11.7121116	456.5161438	4.2958762	0.9193445	130.2034875	337.0527354	1.1842679
4.0000000	21.5000000	11.2121116	456.5161438	4.4348145	0.9202129	141.4714203	331.6554871	1.1360019
5.0000000	21.4500000	10.3409119	456.1656494	4.7434311	0.9212214	152.4831299	308.8547668	1.2003666
6.0000000	22.4400005	9.4739990	457.5000000	5.0681224	0.9222417	163.3480377	351.8210022	1.2232093
7.0000000	21.1000000	8.6181416	457.8458252	5.4100361	0.9232069	174.0481415	358.9891968	1.2466164
8.0000000	23.2500000	7.7310276	515.2156372	6.5276489	0.9245852	184.5984230	364.0861511	1.2701659
9.0000000	21.0500000	6.8356934	527.7990723	6.5574404	0.9254502	194.9755859	381.7799072	1.3380845
10.0000000	21.2000000	6.0662537	554.1867981	7.3830318	0.9265491	205.2043762	391.1561584	1.3491799
11.0000000	23.1000004	5.1706238	585.5000000	7.9066492	0.9276366	215.2775574	413.1103210	1.4614806
12.0000000	22.5400009	4.2413712	661.1992188	8.2282715	0.9287171	225.1957703	441.1320496	1.5750805
13.0000000	22.7000008	3.3136368	646.8994751	8.6479645	0.9297970	234.9598083	497.5515137	1.7768872
14.0000000	22.2000008	2.4772871	701.2196045	9.0656586	0.9308435	244.5703735	594.1896484	2.0969412
15.0000000	21.7500000	1.6462317	791.6995850	9.4813919	0.9318864	254.0281982	735.9071655	2.6512526
16.0000000	21.1000004	1.0195474	962.1001587	9.8951492	0.9329092	263.3140259	900.1837158	3.5509517
17.0000000	20.5000000	0.1567707	1180.0056152	10.3069057	0.9339159	272.4885864	1199.8638916	4.3677831
18.0000000	20.0450000	-0.2755005	1374.8955078	10.7167053	0.9349248	281.4925232	1617.7543945	5.8992829
19.0000000	0.1615000	-1.4499971	1790.7700000	11.1245117	0.0000000	0.0000000	0.0000000	0.0000000
112.4000015	0.1750000	0.0000000	0.0000000	0.0000000	0.0000000	0.0000000	0.0000000	0.0000000

f) Case 3b.

Table BVI. Force Data

POSITION	HEIGHT	DIST TO INTER	TOTAL [illegible]	WIRE LEN IN.	RATIO	WIRE DRAG	SPHERE DRAG	SCALED DRAG
0.0000000	31.7959900	13.6300000	414.7661163	5.8251696	0.9134041	134.5559998	291.1908875	0.9731415
1.0000000	31.7510000	13.0861777	426.1455753	5.6778271	0.9199574	141.7521564	298.2717830	0.9924908
2.0000000	31.7060000	12.5423254	437.5251677	5.5368550	0.9265202	148.8976298	303.2821960	1.0120459
2.5000000	31.6490906	12.0017172	449.0033779	5.4038565	0.9331515	155.9775218	308.3728943	1.0310061
3.0000000	31.6220000	11.4623286	460.5222000	5.2908293	0.9398218	162.9970856	322.2625122	1.0811914
4.0000000	31.5650000	10.9242239	472.0425931	5.1771765	0.9464350	169.9563904	330.4818726	1.1117710
4.5000000	31.5080004	10.3872257	483.5606934	5.0647350	0.9530871	176.8556366	328.2300720	1.1071972
5.0000000	31.4510000	9.8513447	495.0805969	4.9535054	0.9597747	183.6950073	323.9865417	1.0958594
6.0000000	31.3370000	9.3165971	506.6017761	4.8434991	0.9664941	190.4746399	325.4275891	1.1019773
7.0000000	31.2230000	8.7829567	518.1227319	4.7345456	0.9732419	197.1947327	335.3056946	1.1403576
8.0000000	31.1090000	8.2503907	529.6407031	4.6265870	0.9800150	203.8553925	344.4431763	1.1746507
8.5000000	31.0520000	7.7204700	535.6745850	4.5196233	0.9868099	210.4568129	344.8955994	1.1794125
9.0000000	30.9950000	7.1896051	544.4913712	4.4136658	0.9936268	216.9991608	347.7217712	1.1923805
9.5000000	30.9380000	6.6577969	555.0109863	4.3087158	1.0004623	223.4826202	353.2051392	1.2145374
10.0000000	30.8810000	6.1250000	565.5300000	4.2047500	1.0073125	229.9072723	356.5757751	1.2295325
11.0000000	30.7670000	5.0631761	586.6494141	4.0000000	1.0211211	242.5810242	369.9026794	1.3519670
11.5000000	30.7100000	4.5341172	597.2091064	3.9000000	1.0280000	248.8830986	400.4686584	1.3924817
12.0000000	30.6530000	4.0059766	607.7688599	3.8000000	1.0348750	255.0216980	409.1178601	1.4231176
12.5000000	30.5960000	3.4788086	618.3287354	3.7000000	1.0417500	261.1550598	411.7099609	1.5165586
13.0000000	30.5390000	2.9526118	628.8887329	3.6000000	1.0486250	267.2106211	452.3765381	1.5861217
13.5000000	30.4820000	2.4273438	639.4487305	3.5000000	1.0555000	273.2485962	406.6567993	1.7465012
14.0000000	30.4250000	1.9030118	650.0087280	3.4000000	1.0623750	279.2090759	535.2145996	1.8874350
14.5000000	30.3680000	1.3796387	660.5687256	3.3000000	1.0692500	285.1123047	596.5450439	2.1097078
15.0000000	30.3110000	0.8572266	671.1287231	3.2000000	1.0761250	290.9583740	703.9102173	2.4965191
15.5000000	30.2540000	0.3357422	681.6887207	3.1000000	1.0830000	296.7474670	868.0503333	3.0164547
16.0000000	30.1970000	0.1848633	692.2487183	3.0000000	1.0898750	302.4797974	1008.2077637	3.5962958
16.5000000	30.1400000	-0.0344727	702.8087158	2.9000000	1.0967500	308.1555176	1153.5306396	4.1265182
17.0000000	30.0830000	-0.0344904	713.3687134	2.8000000	1.1036250	313.7746582	1233.1589355	4.4241166
22.0000000	0.1611328	-1.0844238	1470.2990723	0.0000000	0.0000000	0.0000000	0.0000000	0.0000000
112.4000015	0.1040000	0.0000000	0.0000000	0.0000000	0.0000000	0.0000000	0.0000000	0.0000000

g) Case 4s.

Table BVI. Force Data

POSITION	HEIGHT	DIST TO INTER	TOTAL FORCE	WIRE LEN PL.	RATIO	WIRE DRAG	SPHERE DRAG	SCALED DRAG
0.0000000	12.8999996	13.5560057	445.9900000	5.6670611	0.9212173	164.3718548	294.2923809	0.9391119
1.0000000	12.5000000	13.1864091	452.1900000	5.8911674	0.9213426	170.5373840	295.2884521	0.9458161
1.5000000	12.1000002	12.8556229	455.5000000	6.1158411	0.9222291	176.6636658	297.3097229	0.9526487
2.0000000	11.6999998	12.5097212	466.6722900	6.3397211	0.9228358	182.7502747	298.8562317	0.9595702
2.5000000	11.2999992	11.7631006	471.9629900	6.5627686	0.9233789	188.7971649	300.4299927	0.9666079
3.0000000	11.0000002	11.3164148	484.1106639	6.7857411	0.9219377	194.8044891	305.3825989	0.9845682
3.5000000	10.6999998	10.8719196	486.3300171	7.0078626	0.9242127	200.7722778	301.2090759	0.9731188
4.0000000	10.3999996	10.4277992	494.6412659	7.2299255	0.9250665	206.7006378	304.2987061	0.9851158
4.5000000	10.0000000	9.9868813	501.6259155	7.4511719	0.9261481	212.5896301	305.5496216	0.9912375
5.0000000	10.0000000	9.5438843	512.2490234	7.6720734	0.9277705	218.4391632	310.8281186	1.0104585
5.5000000	10.0000000	9.1017132	518.9113159	7.8925000	0.9287705	224.2490082	311.9197388	1.0141189
6.0000000	10.0000000	8.6591257	527.1248779	8.1125879	0.9273392	230.0211334	314.7118225	1.0223546
6.5000000	10.0000000	8.2173576	532.9554443	8.3321562	0.9279044	235.7515717	319.2745972	1.0444297
7.0000000	10.0000000	7.7753973	540.2044678	8.5512648	0.9286626	241.4471436	322.9447632	1.0586504
7.5000000	9.9999999	7.3336742	550.4200439	8.7699356	0.9298302	247.1017456	321.8121387	1.0571698
8.0000000	9.9999998	6.8909538	559.1718750	8.9881096	0.9295859	252.7175446	325.1094177	1.0708916
8.5000000	9.9999997	6.4484524	569.7129517	9.2059411	0.9301444	258.2946472	327.2273865	1.1124665
9.0000000	9.9999996	6.0060758	580.2745361	9.4231157	0.9306959	263.8331604	327.9957886	1.1471108
10.0000000	9.9999995	5.1212811	601.4690308	9.8570900	0.9319437	274.7944946	326.6745605	1.1771888
10.5000000	9.9999993	4.6790771	614.1754227	9.8502808	0.9317875	274.7944946	361.2550209	1.1993229
11.0000000	9.9999992	4.2411232	625.2814941	10.0721855	0.9324268	280.2176514	367.1983643	1.2216449
11.5000000	9.9999991	3.8010693	634.5577393	10.2938766	0.9328616	285.6024170	377.2109070	1.2576315
11.6407204	9.9999990	3.6599998	645.5371704	10.3650665	0.9311917	290.9490662	387.9220276	1.3295175
12.0000000	9.9999989	3.4630001	648.4602661	10.4171259	0.9339169	296.2575073	414.5402527	1.3880070
12.5000000	9.9999988	3.2230307	709.6826172	10.5111359	0.9344174	301.5279541	435.0666973	1.4598550
12.6407204	9.9999987	2.5999999	752.5590820	11.1547226	0.9349734	306.7603455	464.4187817	1.5617706
13.0000000	9.9999986	2.1629884	785.5806152	11.3790369	0.9354629	311.9548950	504.8744507	1.7014024
13.5000000	9.9999985	1.7049999	829.6029053	11.5706214	0.9359679	317.1116638	546.1403320	1.8451166
72.0000000	0.1419696	1.4182970	885.9500122	11.7828903	0.9364778	322.2307129	600.9883228	2.0340006
112.4000015	0.1508008	0.0000000	0.0000000	0.0000000	0.0000000	0.0000000	0.0000000	0.0000000

h) Case 4b.

Chapter IV

The Effect of London-van der Waals Dispersion Forces on the Motion of a Sphere Normal to a Deformable Fluid-Fluid Interface

I. Introduction

Previously in this work, several aspects of the problem of a sphere moving normal to a deformable fluid-fluid interface hve been studied by a numerical technique. Two different types of sphere motion were considered in Chapter II, and two limiting cases for the dynamics of the interface were given in Chapter III. All these solutions have in common the fact that even without the limitations imposed by difficulties in achieving convergence for the numerical scheme, none could solve for the flow of a fluid reaching zero thickness. This final stage of the breakthrough process is fundamentally a molecular process, and so, cannot be treated in the continuum framework of the previous chapters. In this chapter, however, we begin consideration of molecular forces in a numerical scheme used previously.

Specifically, we begin by treating London-van der Waals dispersion forces; this is a force which results from the induced dipoples between two separated molecules. Although calculations of the exact quantitative force between bodies requires a detailed understanding of the molecular environment, researchers have used a single parameter, A, the London-van der Waals constant, to describe the attraction between particles from induced dipoles. Hamaker (1937) used this approach to find the attraction between two spheres and the attraction of a sphere to an infinite plane wall, all in a vacuum. By devising a mixing rule for combining the A's for the various materials, Hamaker also solved the problem for bodies separated by a continuous medium. Hamaker's results have been widely applied to problems involving colloidal forces, for exampl, Spielman and Cukor (1973), Zeichner and Schowalter (1977), to name only two. These solutions apply integrated forms of the London-van der Waals point force to discrete bodies, but applications also exist for dispersion forces acting on infinite interfaces between two fluids. Maldarelli and Jain (1982) provide a review of the work done on thin films in the regime where London-van der Waals forces are significant. Although the dispersion force is a body-

force depending on the entire volume of the materials involved, some workers in the field treat this force, which only exists when at least two interfaces exist between materials, as an interfacial effect. Maldarelli and Jain outline two approaches to treating London-van der Waals effects. The first is the "body force method" in which the dispersion forces are included in the differential equations of motion as the gradient of the London-van der Waals potential. Felderhoff (1968) treats the problem of a thinning liquid film via this method. An alternative approach, and the one that proves more convenient for application in our problem, is termed the disjoining pressure approach. In the disjoining pressure treatment, an additional term, the disjoining pressure, is added to the normal stress boundary condition to account for the attraction across two liquid boundaries. There is no added force from two materials separated by a single boundary, that is, in contact. Interfacial tension is defined to include all excess thermodynamic properties from materials in contact. Ivanov, Radoev, Manev, and Scheludko (1969) apply this technique to the stability of thin liquid films.

Just as lubrication analysis is able to provide an accurate solution to the film drainage problem with better numerical convergence than the boundary integral technique we employ, the thin film analysis performed by Ivanov *et al.*, among others, using either the body force or disjoining pressure approach is able to give an accurate representation for the collapse of these thin films under the action of dispersion forces. In the context of particle/interface interactions, however, the problem with studying thin films through any of these thin film analyses is that there is no "a priori" basis to determine whether a thin film will actually occur, for a given physical system, due to the motion of a sphere toward the interface from "far out" in the fluid.

It is therefore fortunate that the problem of sphere motion toward an interface in the presence of London-van der Waals forces can be studied without necessity

for any assumptions about the interface shape. This is because the description of London-van der Waals forces through a disjoining pressure contribution to the normal stress balance can be adapted directly to the same boundary integral solution scheme that was described in the preceeding chapters. In particular, the attraction of fluid I to the sphere from dispersion forces causes an added discontinuity in the stress across the interface. By adding the dispersion force to the normal stress jump, the differential equations of motion remain unaffected by the inclusion of London-van der Waals forces, and the point force solutions of the previous chapters still apply; it is only the boundary conditions which are applied to the integral form of the solution that are altered. In the present work, the local dispersion force on the interface is evaluated by analytically integrating over the volume of fluid behind the interface for a given sphere-interface configuration.

This chapter reports on the derivation of the dispersion force at a deformed interface near a solid sphere, and the modifications to the numerical technique of Chapter II that are necessary to include the disjoining pressure in the normal stress jump boundary condition. Six sample numerical calculations were performed; three for the case of a constant sphere velocity, and three for a constant applied body force on the sphere. The cases chosen are for the situation where characteristic interfacial tension, gravity, viscous forces, and the disjoining pressure are all of equal magnitude. The range of viscosity ratios chosen for calculation, $0 - 10$, essentially spans all variation associated with changes in λ.

II. Mathematical Formulation

In order to include the effect of London-van der Walls dispersion forces on the motion of the sphere-interface system, we modify the numerical method described in Chapter II to include these attractive forces in the normal stress boundary condition

through the so-called "disjoining pressure approach." As was the case in the previous chapters, the Reynolds number, $Re = \rho_i U a/\mu_i$, is small enough that Stokes equation describes the flow in both fluids. The governing equations and boundary conditions are:

$$\begin{aligned} 0 &= -\nabla p_1 + \lambda \nabla^2 \mathbf{u}_1 \\ 0 &= \nabla \cdot \mathbf{u}_1 \qquad\qquad \text{in fluid 1,} \end{aligned} \tag{1}$$

$$\begin{aligned} 0 &= -\nabla p_2 + \nabla^2 \mathbf{u}_2 \\ 0 &= \nabla \cdot \mathbf{u}_2 \qquad\qquad \text{in fluid 2.} \end{aligned} \tag{2}$$

with

$$\mathbf{u}_1, \mathbf{u}_2 \rightarrow 0 \qquad\qquad \text{as } |\mathbf{x}| \rightarrow \infty \ , \tag{3}$$

and at the interface $\mathbf{x} \in S_I \mathbf{u}_1 = \mathbf{u}_2$,(4)

$$\mathbf{n} \cdot \mathbf{u}_1 = \mathbf{n} \cdot \mathbf{u}_2 = \frac{1}{|\nabla H|} \frac{\partial f}{\partial t} \quad . \tag{5}$$

Here the interface shape is denoted as $z = f(r,t)$, and the outward pointing normal $\mathbf{n}$ at the interface is $\mathbf{n} = \nabla H/|\nabla H|$ with $H \equiv z - f(r,t) = 0$. On the sphere, we apply either the boundary condition for constant velocity,

$$\mathbf{u}_2 = \mathbf{i}_z \qquad \mathbf{x} \in S_P \ , \tag{6a}$$

or the constant force condition which will be given after the form for the disjoining pressure has been derived. All of the equations and boundary conditions above are the same as those for the problems treated in Chapters II and III. The final boundary condition, the stress jump at the interface, though, now takes the form:

$$(\mathbf{n} \cdot \mathbf{T}_1 - \mathbf{n} \cdot \mathbf{T}_2) = -\gamma (\nabla \cdot \mathbf{n})\mathbf{n} + (\rho_2 - \rho_1) g a^2 f \mathbf{n} + \Pi(h)\mathbf{n} \quad . \tag{7}$$

$\Pi(h)$ is the disjoining pressure at a point on the interface (whose distance to the center of the sphere is h for the given sphere-interface configuration) due to the London-van der Waals attraction between the sphere and the mass of fluid I beyond the fluid I-fluid II interface. In order to get an expression for $\Pi(h)$, we begin by considering the London-van der Waals potential between two points of matter. The potential for a molecule at position r given a molecule at the origin is

$$E(r) = \frac{-A_{12}}{r^6} \quad . \tag{8}$$

Where A_{12} is the van der Waals constant whose value depends on the two materials involved and the intervening medium. If molecules 1 and 2 are separated by a third material rather than a vacuum, a mixing rule such as the one given by Hamaker (1937) must be used to get the value of A_{12}. The force between these two molecules is then given by the negative gradient of the potential.

$$F(r) = -\nabla E(r) = \frac{-6A_{12}}{r^7}\, i_r \tag{9}$$

To get the force at a point r due to a sphere of radius a and molecular density q_1, whose center is located at the origin, Eq. (9) is integrated over the volume of the sphere. With $r' = (R - r)$

$$\begin{aligned} F(r) &= \int_{|R|\leq a} \frac{-6A_{12}q_1}{|r'|^7} dR \\ &= \frac{\pi A_{12} q_1}{2r^2}\left[\frac{1}{(r-a)^2} - \frac{1}{(r+a)^2} - \frac{r^2+a^2}{2(r-a)^4} + \frac{r^2+a^2}{2(r+a)^4}\right]. \end{aligned} \tag{10}$$

The disjoining pressure on a differential segment of the interface located a distance l_c from the sphere center is the attractive force from the mass of fluid I lying behind this differential area of the interface divided by its area. In spherical coordinates, this can be written:

$$\Pi(l_c) = \frac{\int_{l_c}^{l_e} q_2 r^2 F(r) \sin\phi \, d\phi \, d\theta \, dr}{l_c^2 \sin\phi \, d\phi \, d\theta}$$

$$= \frac{\Lambda_{12} q_1 q_2 \pi}{4} \left[\frac{1}{r+a} - \frac{1}{r-a} + \frac{a}{(r+a)^2} + \frac{a}{(r-a)^2} \right.$$

$$\left. - \frac{2a^2}{3} \frac{1}{(r+a)^3} + \frac{2a^2}{3} \frac{1}{(r-a)^3} \right|_{l_c}^{l_e} i_r \qquad (11)$$

The upper limit of integration, l_c, will be ∞ for points on the interface above the center of the sphere, and the point where the line $O\bar{l}_c$ meets the interface again for l_c below the sphere center. Letting the area on the interface go to 0 by $d\phi,\ d\theta \to 0$, and substituting Eq. (11) into the normal stress boundary condition, and non-dimensionalizing with respect to the characteristic length a, and the characteristic stress $\mu U/a$, we obtain the final form for the normal stress jump is

$$\mathbf{F}(f) \equiv (\lambda \mathbf{n} \cdot \mathbf{T}_1^I - \mathbf{n} \cdot \mathbf{T}_2^I) = -\frac{1}{Ca} (\nabla \cdot \mathbf{n}) \mathbf{n} + \frac{1}{Cg} f \mathbf{n} + \frac{1}{Cl} \Pi \cdot \mathbf{n} \quad , \qquad (12)$$

where $Cl = 4\mu U a^2 / \pi \Lambda_{12} q_1 q_2$ and $\Pi(l_c)$ is

$$\Pi(l_c) = \frac{1}{r^2} \left[\frac{1}{r+1} - \frac{1}{r-1} + \frac{1}{(r+1)^2} + \frac{1}{(r-1)^2} \right.$$

$$\left. - \frac{2}{3} \frac{1}{(r+1)^3} + \frac{2}{3} \frac{1}{(r-1)^3} \right|_{l_c}^{l_e} i_r \qquad (13)$$

The term $\Lambda_{12} q_1 q_2 \pi^2$ is known as the Hamaker constant, and is of the order 10^{-12}-10^{-13} erg. The new form of the normal stress jump, Eq. (12), applies to both the problem of a constant applied body force on the sphere, and a sphere moving with constant velocity. Unlike the modification to the stress jump for an immobile interface of Chapter III, no additional variables or constraints are added by including the disjoining pressure.

In this chapter, Eqs. (1) and (2) are solved subject to the boundary conditions Eq. (3), (4), (5), (6), and (12) using the boundary integral technique described

in Chapter II. The collocation assumption that is applied in Chapters II and III to the unknowns $\mathbf{u}$ and $\mathbf{T}\cdot\mathbf{n}$ and the interface shape functions $\nabla\cdot\mathbf{n}$ and f is applied here to the disjoining pressure as well. $\Pi(l_c)$ is calculated at the center of each interface segment, and this value is assumed to be the disjoining pressure over the entire portion of the interface. This allows us to withdraw $\mathbf{F}(f)$ from the integral and maintain the system of linear equations which were derived for the earlier problems.

The attractive London-van der Waals force acts on the sphere as well as fluid I; so the total force on the sphere is now the sum of the stress due to fluid II and the body force resulting from attraction to fluid I. In dimensionless terms, the force which must be applied in the positive z direction to the sphere so that the velocity remains constant is

$$F_{sphere} = -\frac{1}{3}\int_0^{\pi} T_{nz}^P \sin\phi\, d\phi - \frac{Nu_{Disp}}{3}\int_0^{\infty} \Pi(l_c)\,\eta_r\,(1+f'^2)^{1/2}\,d\eta_r \quad . \qquad (14)$$

With the gradient of the interface shape function, f', and the position on the interface, η_r, defined as in Chapter II, Eq. (14) is used to get the total force on the sphere for constant velocity calculations, and also forms the basis for application of the constant force condition on the sphere when that is relevant. The basis for calculation in the constant force problem is that without the presence of the interface, the normalized force on the sphere is 1. For the case of a particle settling in a constant gravitational field, the normalization constant is Stokes drag for the settling velocity. In the problem under consideration here, where in addition to the constant body force force on the sphere, there is the variable dispersion force, the constant body force condition on the sphere surface is:

$$-\int_0^{\pi} \mathbf{T}_{nz}^P sin\phi\, d\phi = 3 + Nu_{Disp}\int_0^{\infty} \Pi(l_c)\,\eta_r\,(1+f'^2)^{1/2}\,d\eta_r \quad . \qquad (6b)$$

This equation completes the system of equations for the constant force calculations. The details of applying the boundary integral method and solving the resulting sys-

tem of linear algebraic equations is essentially identical to the procedure described in Chapter II, and so is not repeated here.

III. Numerical Results

Numerical results for the problem of a sphere moving normal to a deformable interface subject to a London-van der Waals type dispersion force are presented in this section for cases with a dimensionless dispersion number equal to unity, that is, $Cl = 4\mu_2 U a^2/\pi A_{12} q_1 q_2 = 1$. This value is typical of micron sized particles in water settling under gravity. However, $Cl = 1$ was not chosen to represent a particular physical system, but because when coupled with $Ca = Cg = 1$, we have a system with all characteristic restoring forces at the interface equal in magnitude to the force of deformation. Furthermore, referring to the results in Chapter II, the $Ca = Cg = 1$ cases in the absence of London-van der Waals forces, resulted in tails behind the sphere of various widths, and a range of behavior of the film in front of the sphere from a stable thick film for $\lambda = 0$, to a continuosly thinning film for $\lambda = 10$. These factors combine to create a situation where the presence of dispersion forces could increase the rate of film drainage to the point where breakthrough occurs before tails form. In the present study, calculations were performed for three values of λ; as discussed in Chapter II, this is the parameter which controls the thickness of the film in front of the sphere, and is hence most likely to illustrate a changing role for Cl. A complete span of the parameter space will be presented in Geller and Leal (1986). In order to obtain experimentally a value of $Ca = 1$ simultaneously with $Cl = 1$ and a particle in the range $10\,\mu m$, the interfacial tension would have to be extremely small. Alternatively for $\gamma \sim O(10)$, the particle diameter must be in the range $1 - 0.1\mu m$. However the results reported accurately represent the physics of a system where capillary effects are of the same order as dispersion forces

acting over a distance $O(10)$. The same numerical parameters, sphere and interface segment distribution, time step, and starting sphere position, used in Chapter II are employed for the calculations performed for this chapter. This way any changes associated with the different numerical scheme will be minimzed.

We begin with a discussion of the constant velocity results. In Chapter II, the case $\lambda = 1,\ Ca = 1,\ Cg = 1$ formed the basis of comparison for the calculations which followed. The interface shapes for this calculation are again presented here for reference, Fig. 1. Now, however, the set of parameters reads $(1, 1, 1, \infty)$ for $(\lambda,\ Ca,\ Cg,\ Cl)$ with Cl added to the set. As shown clearly in Fig. 1, this is a case which displays a long, slender tail behind the sphere. In Fig. 2 we compare the interface shapes for the two cases $(1, 1, 1, 1)$ and $(1, 1, 1, \infty)$. For the early stages, the sphere is far enough from the interface, $l = 1, 2$, that London-van der Waals forces have a negligible effect. However, when the sphere stradles the interface, $l = 0$, the London-van der Waals attraction between the sphere and interface is large enough that the interface lies closer than to the sphere than was observed for the $Cl = \infty$ calculation. This reduction in interface motion is observable out to a distance of $R \approx 3$ on the interface (mainly as an indirect consequence of the change in shape closer to the centerline, though). As the sphere continues to move, the attractive forces grow rapidly and the interface dips down at the centerline to contact the sphere. Breakthrough in this case occurs shortly after the sphere is in the position of the last interface shape, $l = -0.375$. Breakthrough is defined here as the point in the calculation which gives a positive sphere-interface separation but for which the next time step results in the interface crossing the surface of the sphere. In fact, for any choice of Cl, there will be a point in the caculation where London-van der Waals forces will be of equal magnitude to capillary forces, and then grow larger as the fluid film thins. The capillary forces remain $O(Ca)$ throughout the calculation whereas the dispersion force is of $O(Cl\,1/\epsilon), \epsilon = 1 - l_c$, as the sphere moves, ϵ

approaches 0 and thus these forces will always come to dominate the system. For these preliminary calculations, it was thought best to choose a value for Cl which would lead to effects distinct from the $Cl = \infty$ calculations easily resolved by our numerical method, even though the set of parameters chosen might not represent a typical physical system.

Of course, the numerically calculated breakthrough point must not depend on the numerical parameters of the calculation. Given our definition of breakthrough, the parameter likely to have the most impact on the calculated breakthrough point is the time step for values of the time step, Δt, typically used in the calculations. For the $(10, 1, 1, 1)$ calculation discussed later in this section, breakthough was predicted to occur at $l = 0.525$ with $\Delta t = 0.05$. As a test case the calculation was repeated for Δt an order of magnitude smaller than the usual value, $\Delta t = 0.005$, and again breakthrough took place at $l = 0.525$. The $\lambda = 10$ calculation was chosen for this trial because it produced the most rapid collapse of the fluid film. Thus, the time scale associated with the growth of disjoining pressure effects, $a/(dl_c/dt)$, will be shortest for this calculation, and in the region near breakthrough where dispersion forces dominate, this situation will require the smallest Δt.

In Chapter II, it was explained that calculations for $Cl = \infty$ with a constant sphere velocity will always exhibit tails behind the sphere provided the calculation continues for long enough time. The combination of purely hydrodynamic forces plus constant interfacial tension in these cases cannot result in breakthrough as there is no mechanism to overcome the force in the lubrication layer between the sphere and interface which becomes infinitely large as the film thickness goes to 0. The action of dispersion forces present in the $Cl \neq \infty$ case provides such a mechanism to overcome the lubrication forces: first through the variation in $\Pi(l_c)$ along the interface which causes a pressure driven outflow of fluid from the film; and second, through the London-van der Waals attraction of the sphere to the interface

reduces the total force on the sphere as it drives fluid from the gap. Fig. 3 shows the hydrodynamic drag and total force on the sphere for the $(1,1,1,1)$ calculation, and the drag on the sphere for the $(1,1,1,0)$ calculation for reference. This figure shows that the drag on the sphere grows rapidly as the separation between the sphere and interface decreases. This drag force on the sphere, however, is more than offset by the London-van der Waals attraction between the body and the interface. Shortly before breakthrough, the total force even becomes negative indicating London-van der Waals forces more than overcome the hydrodynamic drag. To maintain constant velocity, a force must be applied opposite to the direction of sphere motion.

Figs. 4 and 5 show the same type of behavior for the $\lambda = 10$ calculation. Again, breakthrough occurs via a film drainage mechanism before tails can be formed behind the sphere. The larger fluid I viscosity in this calculation slows the motion of the interface away from the approaching sphere. This results in the more rapid growth of the disjoining pressure, and sudden collapse of the fluid film. At the sphere position $l = 1.5$, there is only a slight difference in the force on the sphere with or without dispersion forces. Even as close to the interface as $l = 1.0$, the force in the $Cl = 1$ calculation is only $\approx 20\%$ lower than for the calculation where disjoining pressure was not included; in addition, the interface shapes for the two calculations are virtually identical. As the sphere continues to move toward the interface, however, London-van der Waals forces rapidly dominate the flow, lowering the drag on the sphere and accelerating the rate of film drainage until breakthrough occurs at $l = 0.525$.

The final constant velocity calculation was for an inviscid upper fluid. This case $\lambda = 0$, produced the widest gap between the sphere and interface for each sphere position in the $Cl = \infty$ calculation as shown in Fig. 6 of Chapter II. Once established, this film was shown by calculation to be stable and to thin only very slowly. The calculations performed here for $Cl = 1$, $\lambda = 0$, $Ca = 1$, $Cg = 1$

and illustrated in Fig. 6 show that even this relatively thick film could not reduce the London-van der Waals attraction to the point where film thinning was retarded enough to allow tails to form. Once the film in front of the sphere begins to collapse, this case closely resembles the previous two constant velocity calculations.

The results for the set of calculations performed for decreasing λ leads us to hypothesize about London-van der Waals effects for more realistic values of Cl, i.e., $Cl = 10^2 - 10^6$. For cases with Cl in this range, the contribution to the normal stress jump from the disjoining pressure will be very small, and the solution will resemble the $Cl = \infty$ results until the sphere-interface separation reaces $O(\nu^{-1})$. From that point in the calculation, the London-van der Waals force will grow rapidly, and the point on the interface nearest the sphere will quickly make contact for breakthrough. In most calculations, this point on the interface will be at the centerline, but for some sets of the dimensionless parameters, e.g., $\lambda = 0.022$, $Ca = 0.465$, $Cg = 0.089$, the closest point moves from the centerline to a dimple away from $R = 0$. In such cases, if teh magnitude of Cl is large enough that London-van der Waals froces do not become relevant until after the dimple has formed, breakthrough will occur around a ring away from the centerline. In some cases, Cl may be so large that the disjoining pressure is not significant until the film drainage process is well under way and a thin film has formed. Then random disturbances in the film wil cause a point on the interface to fall close enough that London-van der Waals forces become significant for that point only and breakthrough occurs through what appears to be a growing instability

Calculations were also performed for the same sets of parameters for the constant force type problem. In Chapter II, we were unable to calculate near the point of breakthrough owing to dificulties with convergence of the numerical scheme particularly with the time stepping procedure, for small boundary separations. This problem is removed for the $Cl = 1$ calculations as the dominant term is now the

attractive dispersion force rather than the hydrodynamic drag in the thin film. The interface shape results displayed in Figs. 8, 9, and 10 for the three constant force calculations $Ca = 1,\ Cg = 1,\ Cl = 1;\ \lambda = 0,\ 1,\ 10$ respectively show the same qualitative behavior as the constant velocity results; early deformation of the interface is followed by rapid collapse of the fluid film under the force of the disjoining pressure. As was the case for the constant velocity calculations, the viscosity ratio does influence the position of the sphere at breakthrough, shortening the distance from $l = -0.7129$ for $\lambda = 0$ to $l = -0.5886$ for $\lambda = 1$ to the position farthest out in fluid II, $l = 0.5807$ for $\lambda = 10$. Although the sphere breaks through further out in fluid II for larger values of λ, the time required for breakthrough actually increases as λ is increased in the calculations. This is explained through reference to the data shown in Figs. 11, 12, and 13. The sphere velocity decreases with increasing viscosity ratio and the time added to acheive breakthrough due to the increased slowing of the sphere for higher λ is not offset by the more rapid growth of the London-van der Waals dispersion force resulting from smaller sphere-interface separations in these systems. Finally, the total force on the sphere is shown in Fig. 14. This force is equal to the constant body force due to the bouyancy of the sphere, equal to 1, and the growing London-van der Waals dispersion force. The force remains near unity in all cases until the sphere is near the interface after which the force grows rapidly.

IV. Conclusions

The results of this chapter demonstrate that when dispersion forces are equal in magnitude to viscous, capillary and gravitational forces, no tails are formed behind the sphere; breakthrough always occurs at the front of the sphere. However, unlike film drainage results from Chapter II and the theories described in Chapter I, the breakthrough process for the $Cl = O(1)$ systems is a relatively rapid one, with

London-van der Waals dispersion forces causing a pressure driven outflow of fluid from the film and an attraction of the interface to the sphere both accelerating the process. For cases $\nu \gg 1$, the London-van der Waals effects will be delayed until the sphere-interface separation is $O(Cl^{-1})$, after this point, the growth of the disjoining pressure will lead to rapid breakthrough. The constant force calculations do not produce the same deceleration of the sphere which leads to large effective values for Ca and Cg in the $Cl = \infty$ calculations of Chapter II. In the results from the calculations with $Cl = 1$, the sphere does not slow down to a large extent, and as it approaches the interface, rapidly speeds up to breakthrough.

References

Charles, G.E. and Mason, S.G. 1960 The coalescence of liquid drops with flat liquid/liquid interfaces. *J. Coll. Sci.* **15**, 236.

Felderhoff, B.U. 1968 Dynamics of free liquid films. *J. Chem. Phys.* **49**, 44.

Geller, A.S. and Leal, L.G. 1986 The effect of London-van der Waals dispersion forces on the motion of a sphere normal to a deformable fluid-fluid interface. In preparation.

Hamaker, H.C. 1937 The London-van der Waals attraction between spherical particles. *Physica* **4**, 1058.

Ivanov, I., Radoev, B., Manev, E., and Scheludko, A. 1970 Theory of the critical thickness of systems of thin liquid films. *Trans. Faraday Soc.* **66**, 1262.

Maldarelli, C. and Jain, R. 1982 The linear, hydrodynamic stability of an interfacially perturbed, transversely isotropic, thin,planar viscoelastic film. I. General formulation and a derivation of the dispersion equation. *J. Coll. and Interface Sci.* **90**, 233.

Spielman, L.A. and Cukor, P.M. 1973 Deposition of Non-Brownian particles under colloidal forces. *J. Coll. and Interface Sci.* **43**, 51.

Zeichner, G.R. and Schowalter, W.R. 1977 Use of trajectory analysis to study stability of colloidal dispersions in flow fields. *A. I. Ch. E. Journal* **23**, 243.

Figure Captions

Figure 1: Interface shape as a function of sphere position (drawn in a reference frame in which the sphere is fixed) for $\lambda = 1$, $Ca = 1$, $Cg = 1$, $Cl = \infty$. Sphere initially at $l_0 = 3$. Constant velocity case.

Figure 2: Interface shape as a function of sphere position for $\lambda = 1$, $Ca = 1$, $Cg = 1$; —— shapes for $Cl = 1$; – – – $Cl = \infty$ Sphere initially at $l_0 = 3$. Constant velocity case.

Figure 3: Drag ratio as a function of sphere position for $\lambda = 1$, $Ca = 1$, $Cg = 1$; —— hydrodynamic stress for $Cl = 1$; – – – hydrodynamic stress and total force for $Cl = \infty$; - - - total force on sphere for $Cl = 1$.

Figure 4: Interface shape as a function of sphere position for $\lambda = 10$, $Ca = 1$, $Cg = 1$; —— shapes for $Cl = 1$; – – – $Cl = \infty$ Sphere initially at $l_0 = 3$. Constant velocity case.

Figure 5: Drag ratio as a function of sphere position for $\lambda = 10$, $Ca = 1$, $Cg = 1$; —— hydrodynamic stress for $Cl = 1$; – – – hydrodynamic stress and total force for $Cl = \infty$; - - - total force on sphere for $Cl = 1$.

Figure 6: Interface shape as a function of sphere position for $\lambda = 0$, $Ca = 1$, $Cg = 1$; —— shapes for $Cl = 1$; – – – $Cl = \infty$ Sphere initially at $l_0 = 3$. Constant velocity case.

Figure 7: Drag ratio as a function of sphere position for $\lambda = 0$, $Ca = 1$, $Cg = 1$; —— hydrodynamic stress for $Cl = 1$; – – – hydrodynamic stress and total force for $Cl = \infty$; - - - total force on sphere for $Cl = 1$.

Figure 8: Interface shape as a function of sphere position for $\lambda = 0$, $Ca = 1$, $Cg = 1$, $Cl = 1$. Sphere initially at $l_0 = 3$. Constant force problem.

Figure 9: Interface shape as a function of sphere position for $\lambda = 1$, $Ca = 1$, $Cg = 1$, $Cl = 1$. Sphere initially at $l_0 = 3$. Constant force problem.

Figure 10: Interface shape as a function of sphere position for $\lambda = 10$, $Ca = 1$, $Cg = 1$, $Cl = 1$. Sphere initially at $l_0 = 3$. Constant force problem.

Figure 11: Sphere velocity as a function of sphere position for $\lambda = 0$, $Ca = 1$, $Cg = 1$; —— $Cl = 1$; - - - $Cl = \infty$.

Figure 12: Sphere velocity as a function of sphere position for $\lambda = 1$, $Ca = 1$, $Cg = 1$; —— $Cl = 1$; - - - $Cl = \infty$.

Figure 13: Sphere velocity as a function of sphere position for $\lambda = 10$, $Ca = 1$, $Cg = 1$; —— $Cl = 1$; - - - $Cl = \infty$.

Figure 14: Total force on sphere as a function of sphere position for $\lambda = 0$, 1, and 10 $Ca = 1$, $Cg = 1$, $Cl = 1$. Constant force problem.

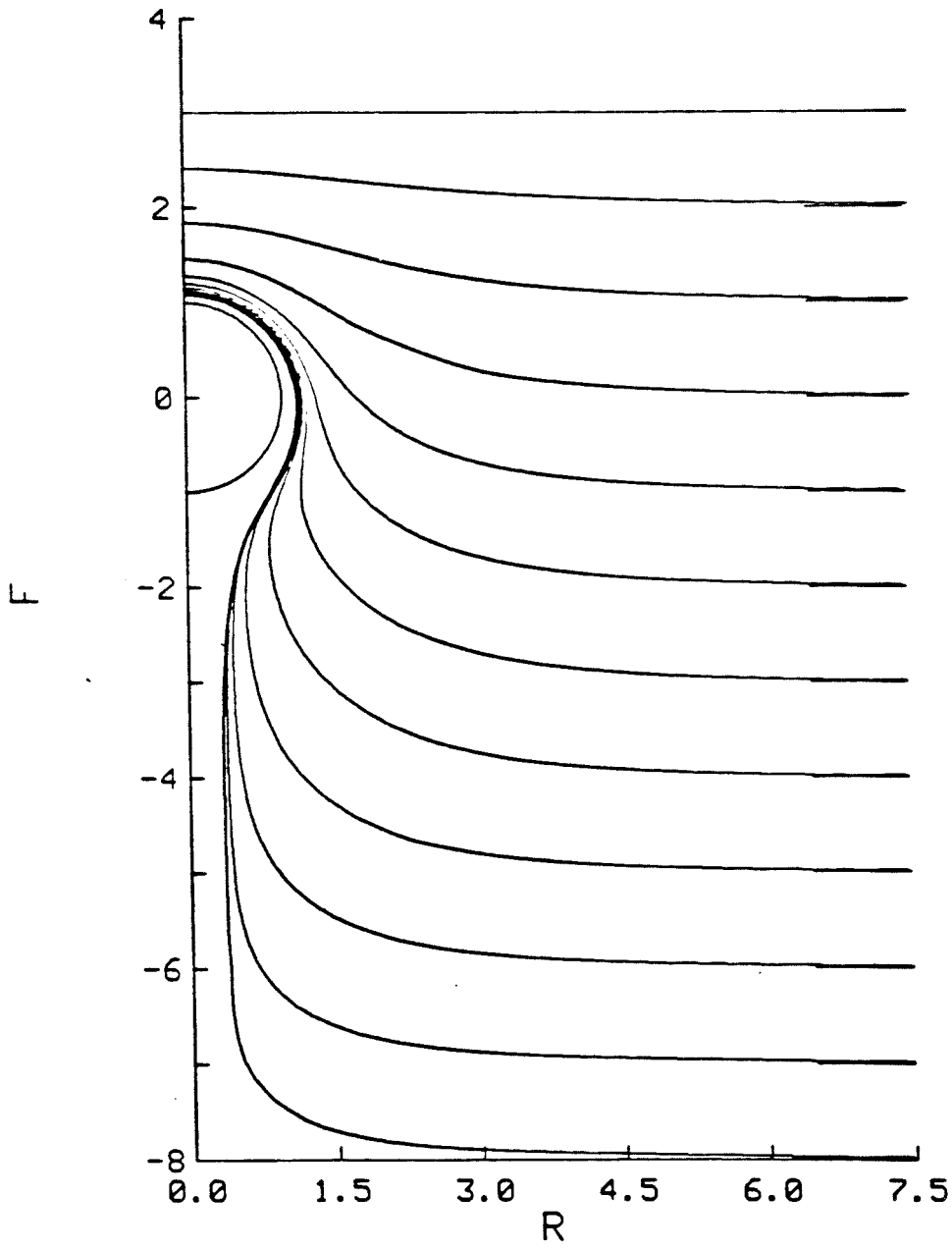

Figure 1.

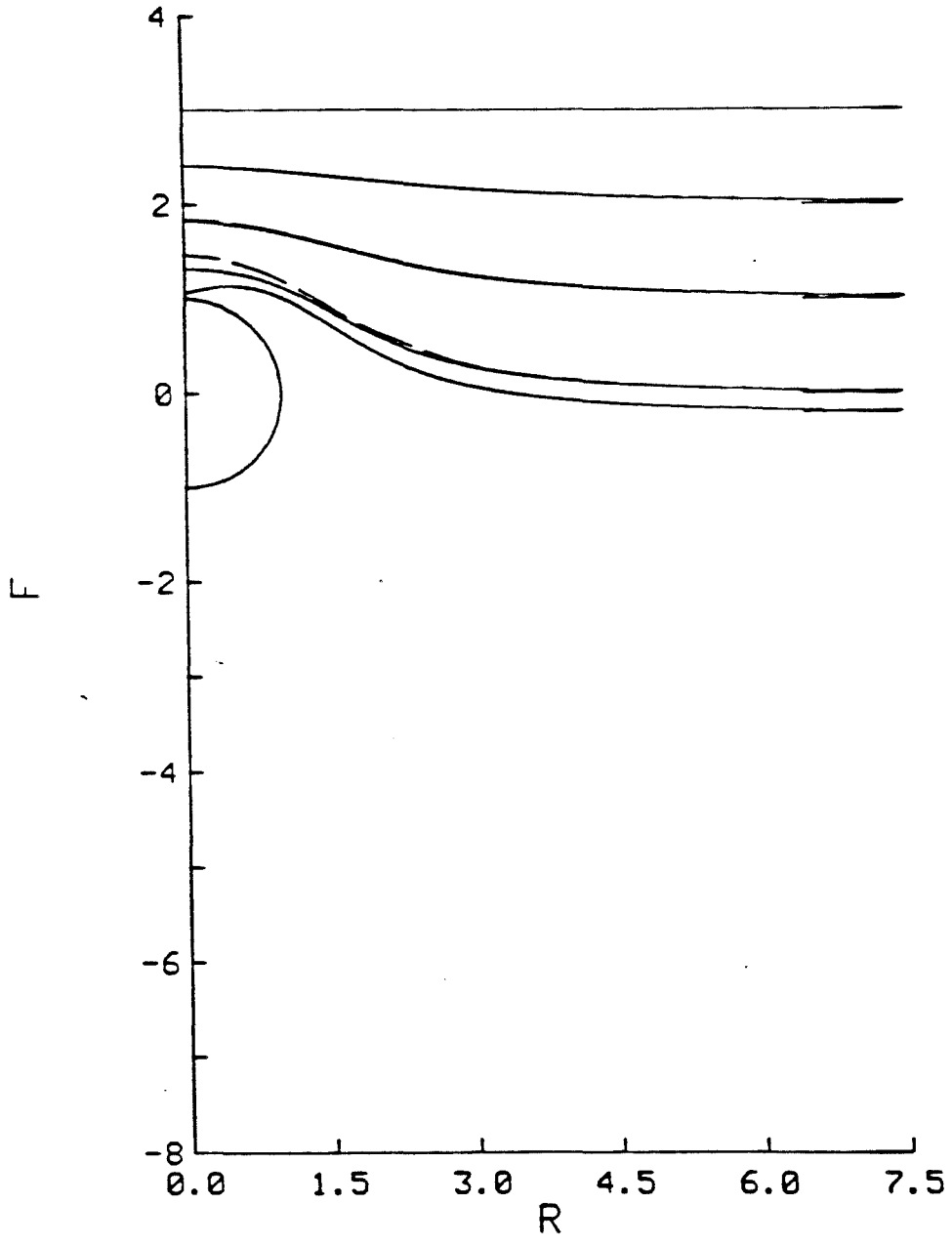

Figure 2.

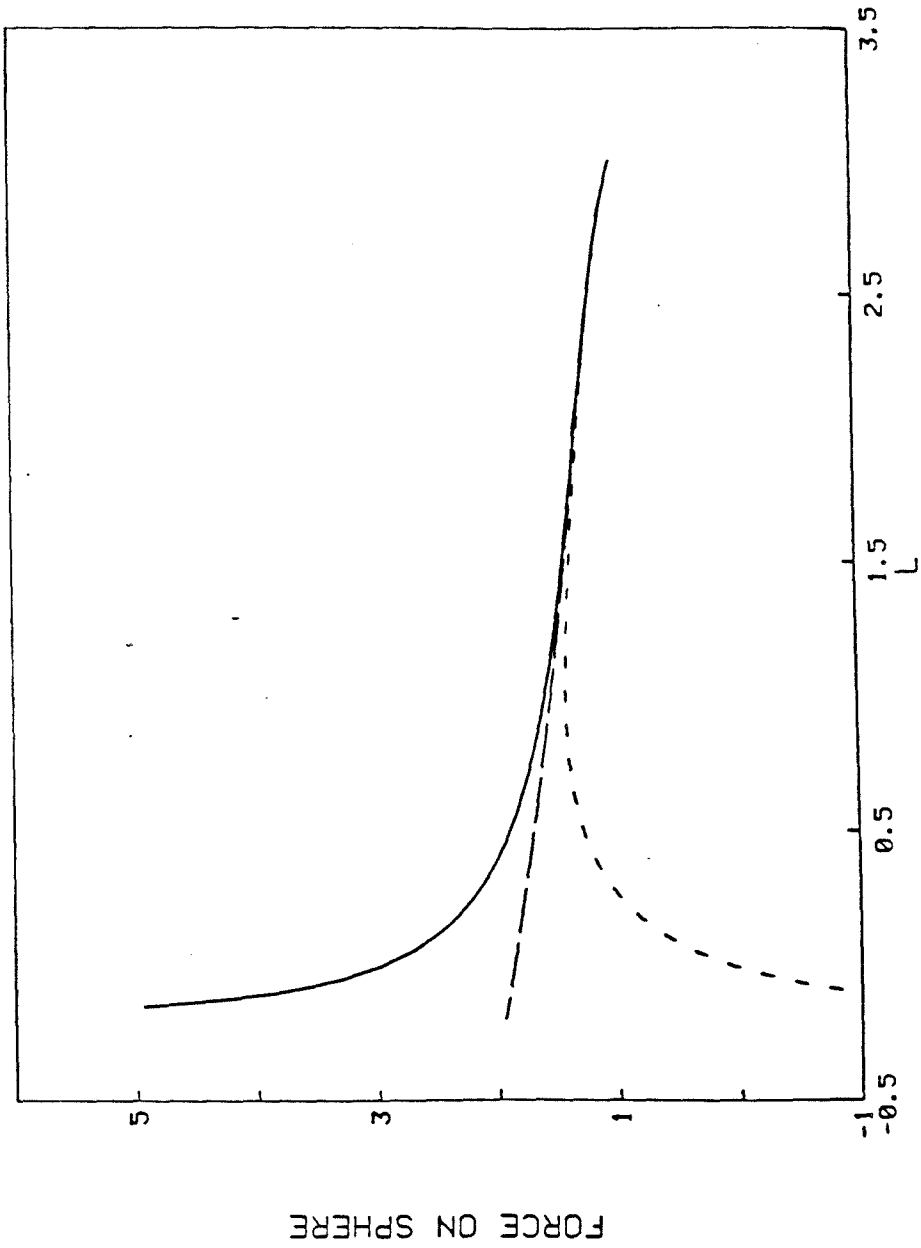

Figure 3.

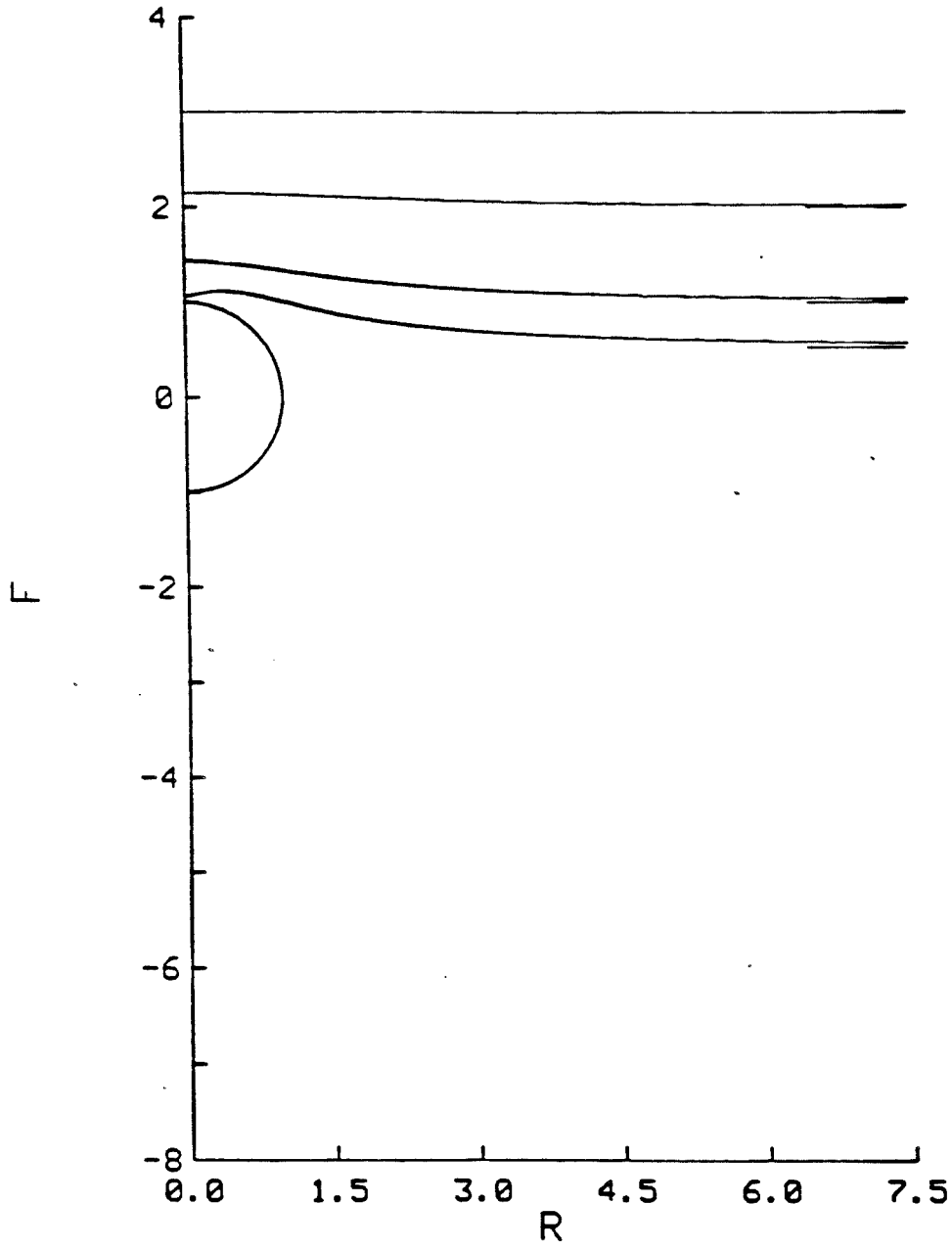

LAMBDA = 10.000 CA = 1.000 CG = 1.000

Figure 4.

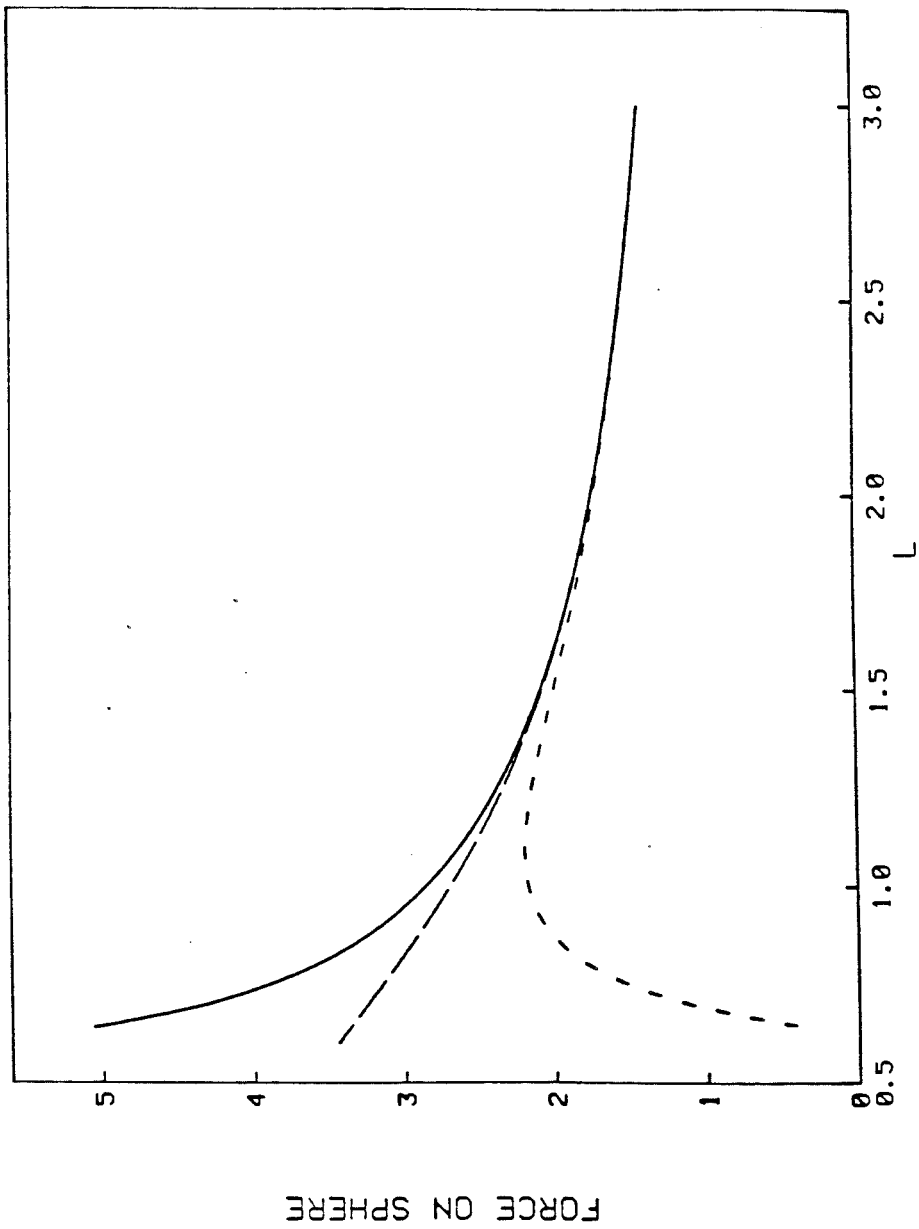

Figure 5.

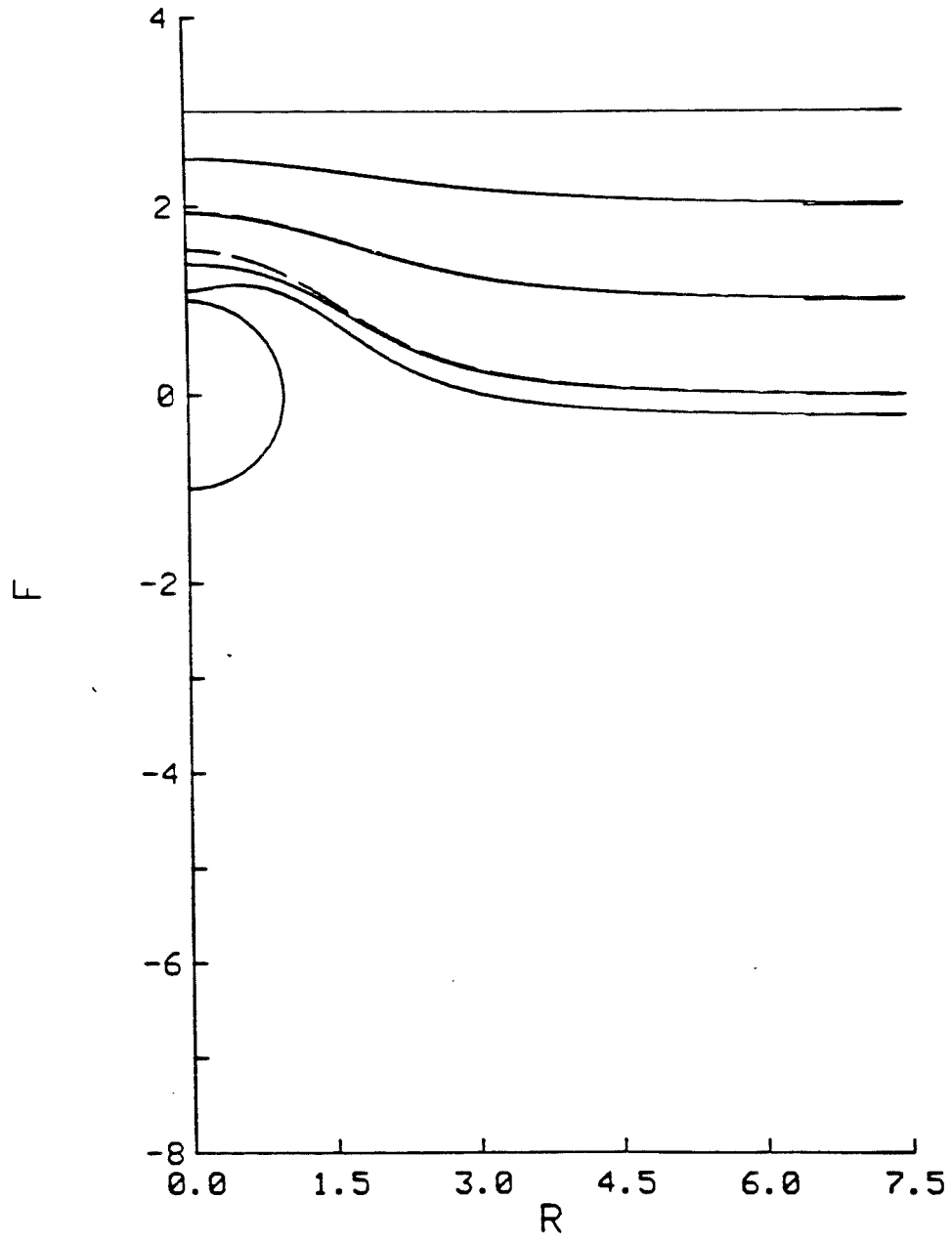

LAMBDA = 0.000 CA = 1.000 CG = 1.000

Figure 6.

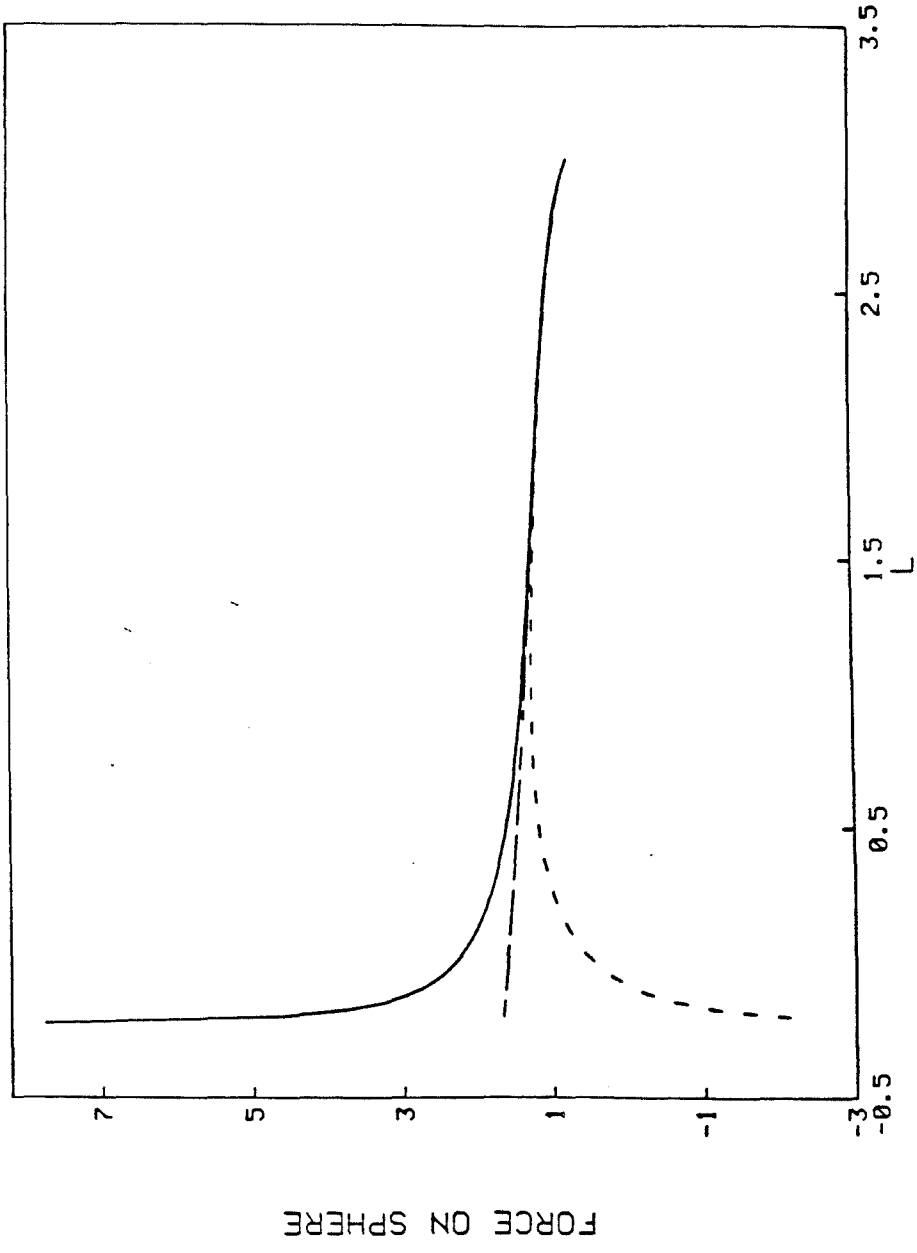

Figure 7.

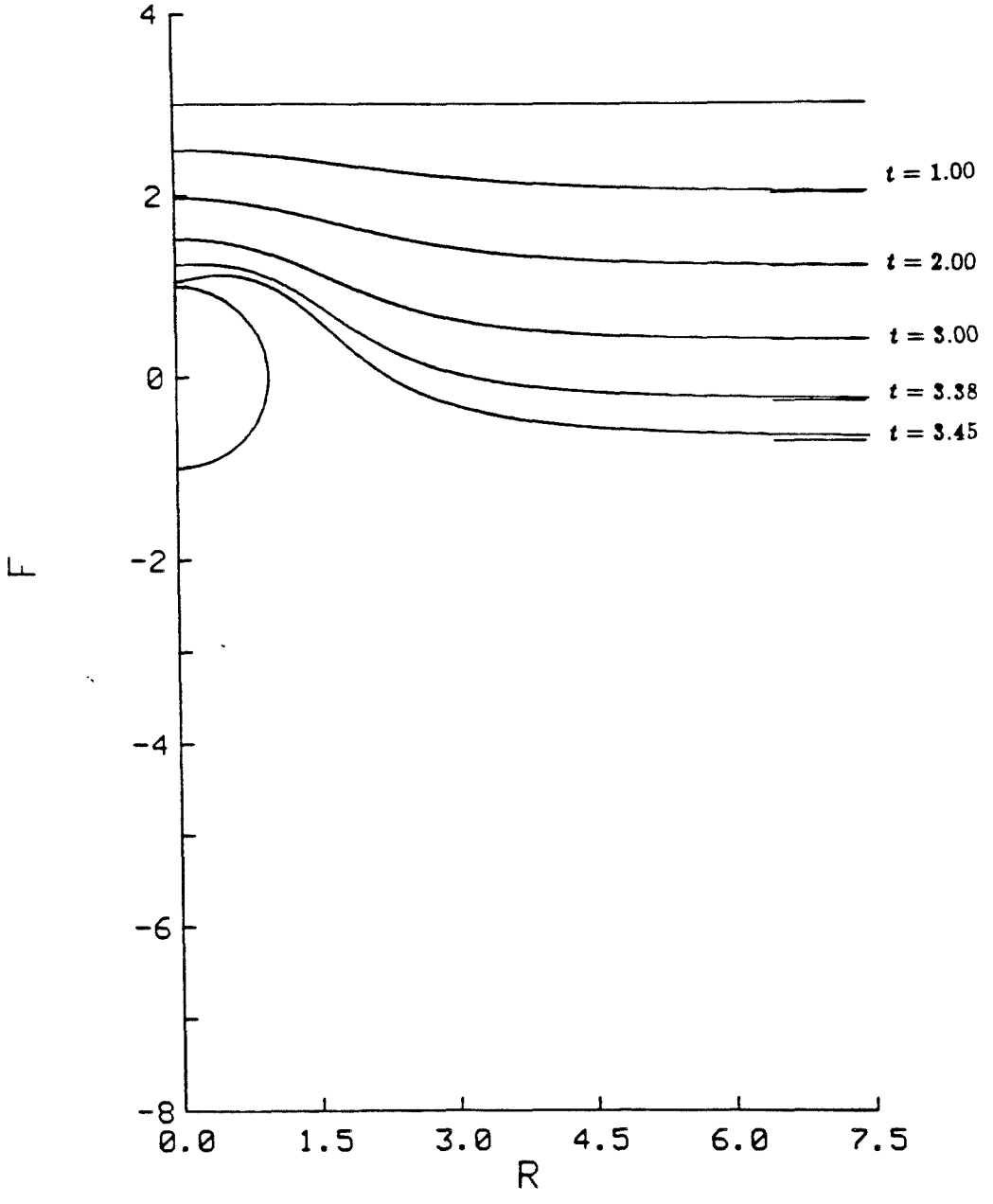

LAMBDA = 0.000 CA = 1.000 CG = 1.000

Figure 8.

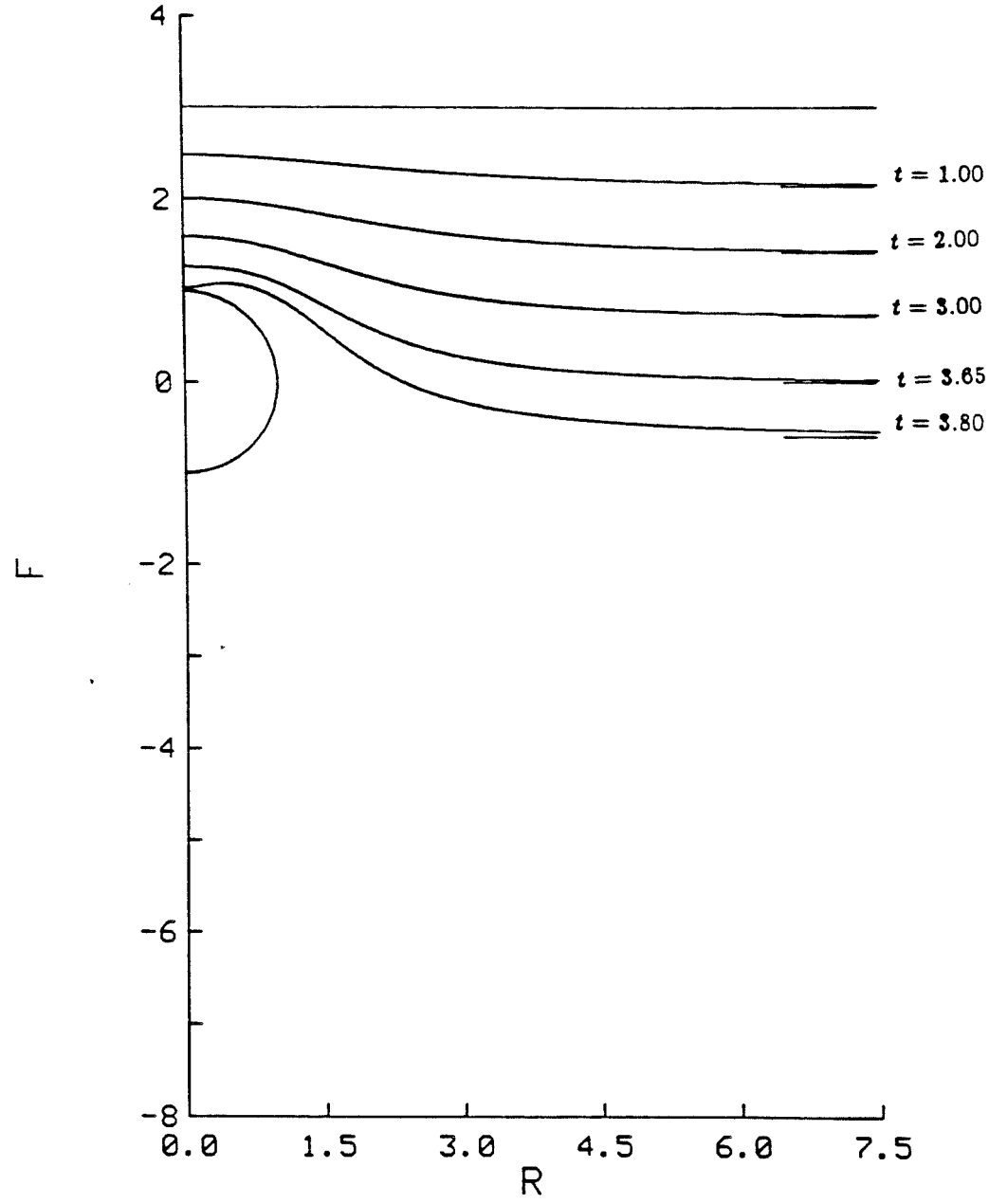

LAMBDA = 1.000 CA = 1.000 CG = 1.000

Figure 9.

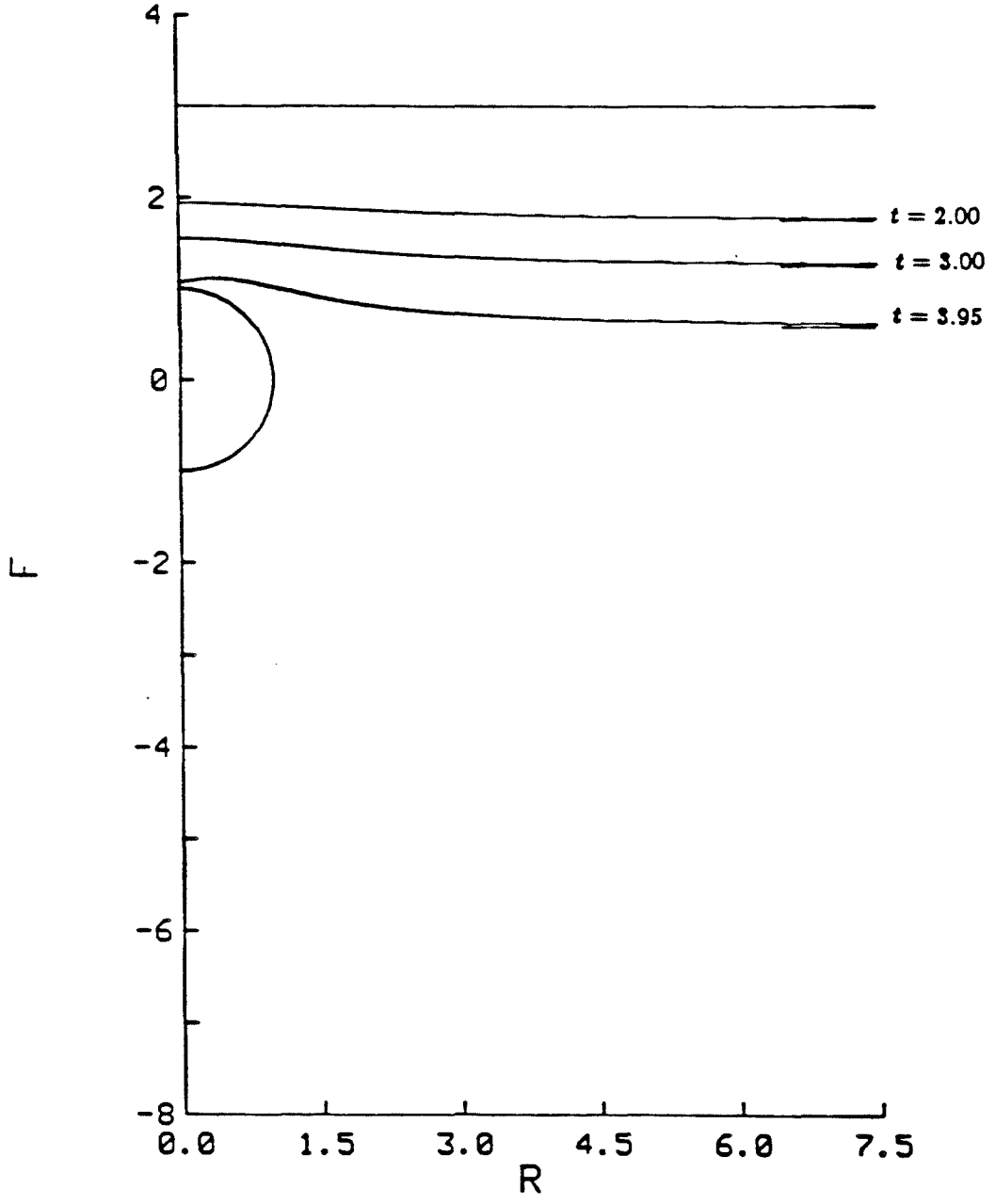
4
2
0
-2
-4
-6
-8
F
0.0
1.5
3.0
4.5
6.0
7.5
R
t = 2.00
t = 3.00
t = 3.95
LAMBDA = 10.000
CA = 1.000
CG = 1.000

Figure 10.

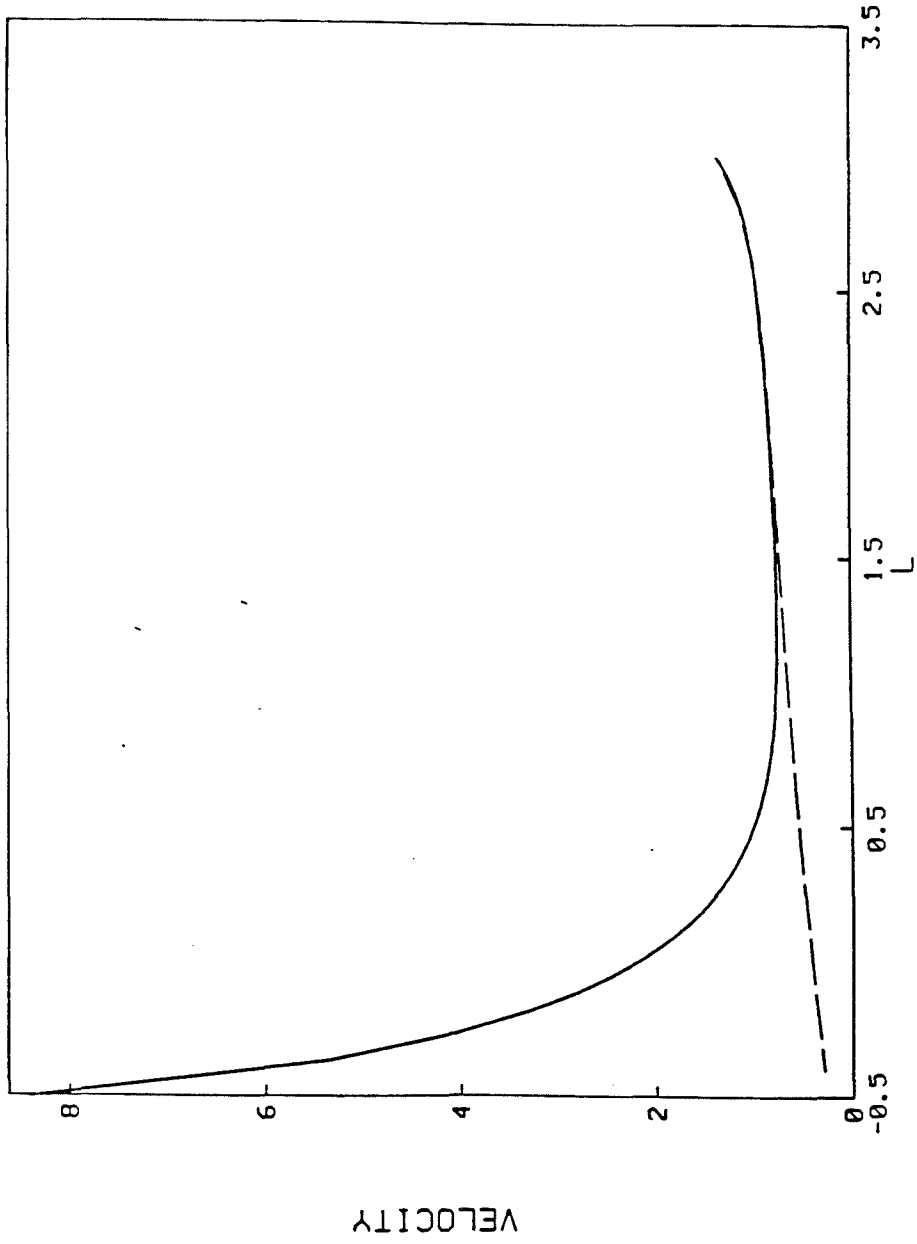

Figure 11.

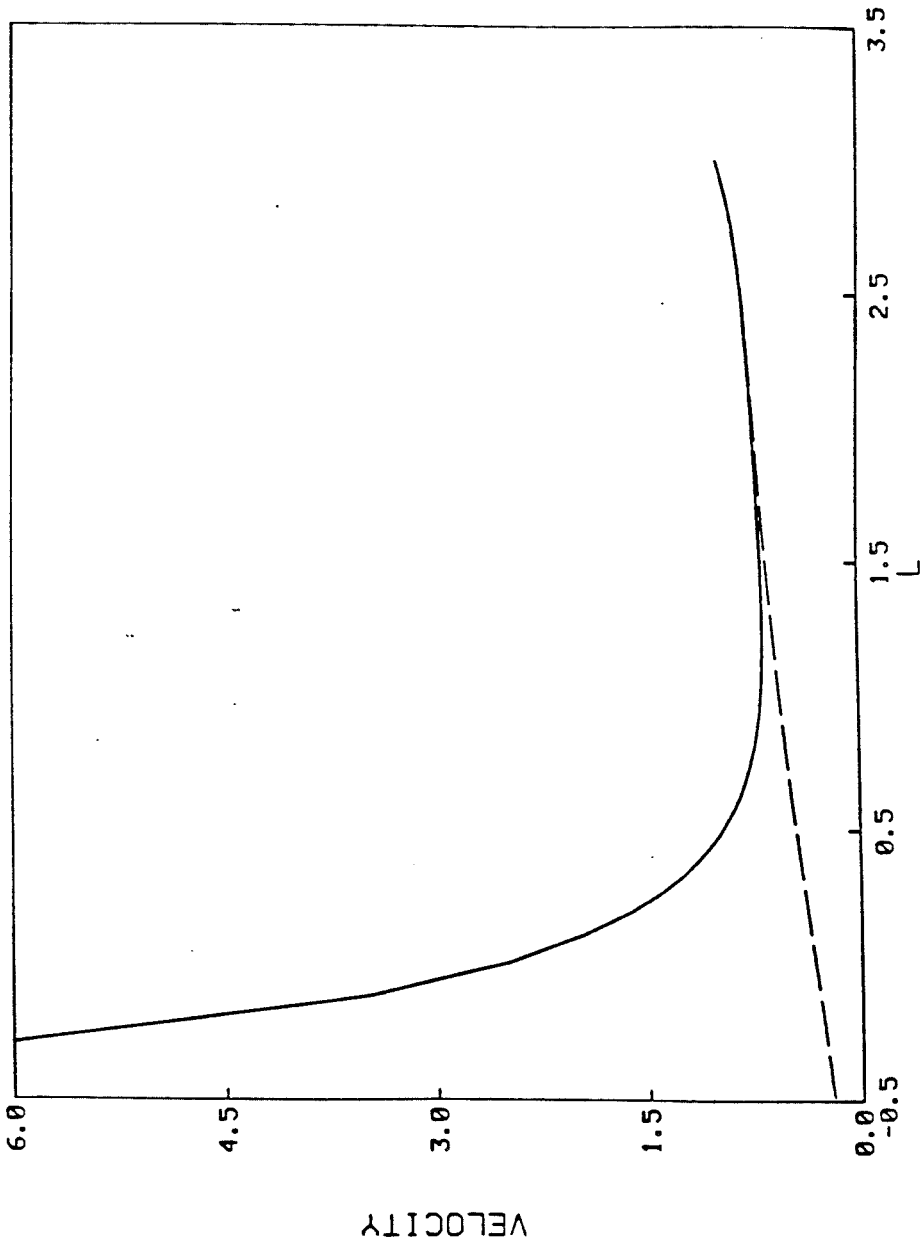

Figure 12.

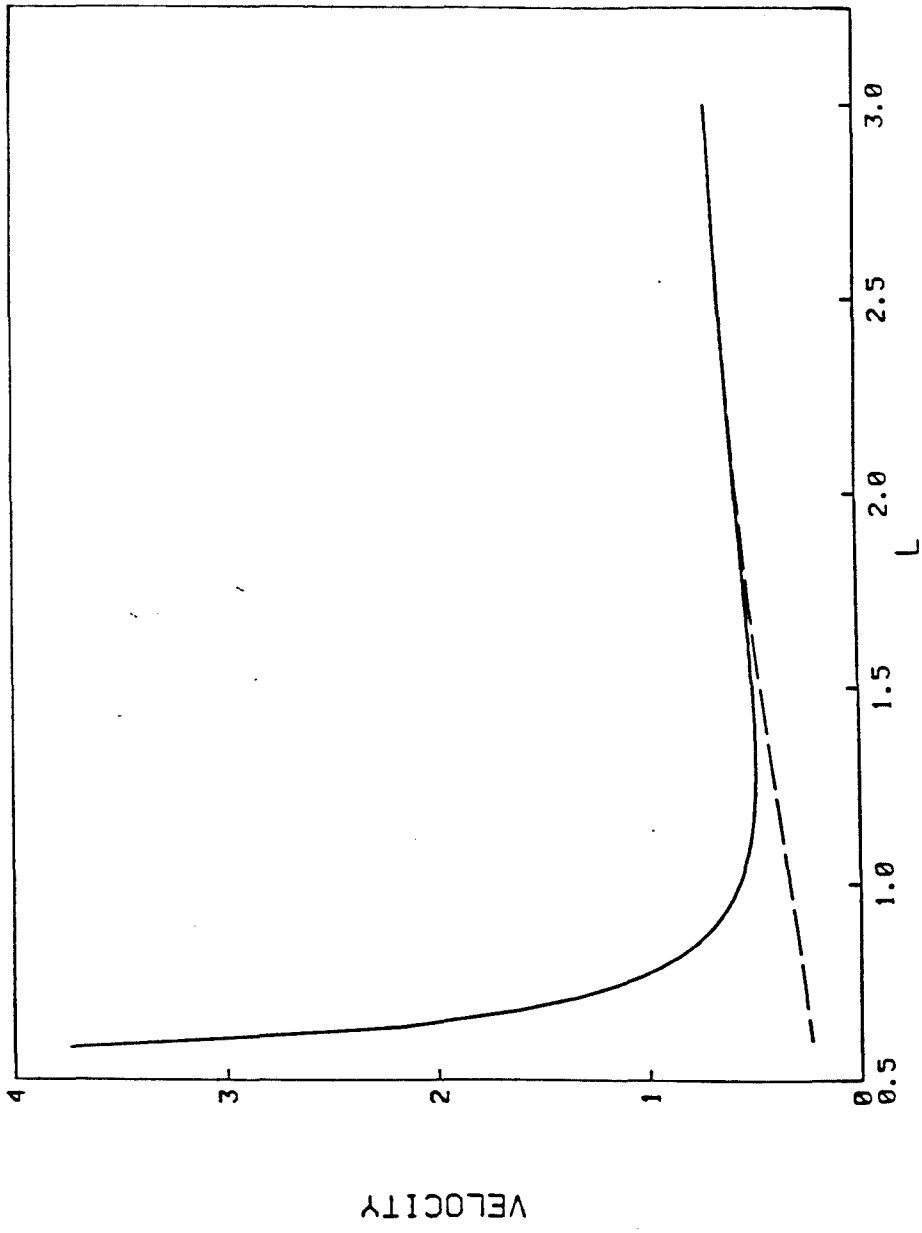

Figure 13.

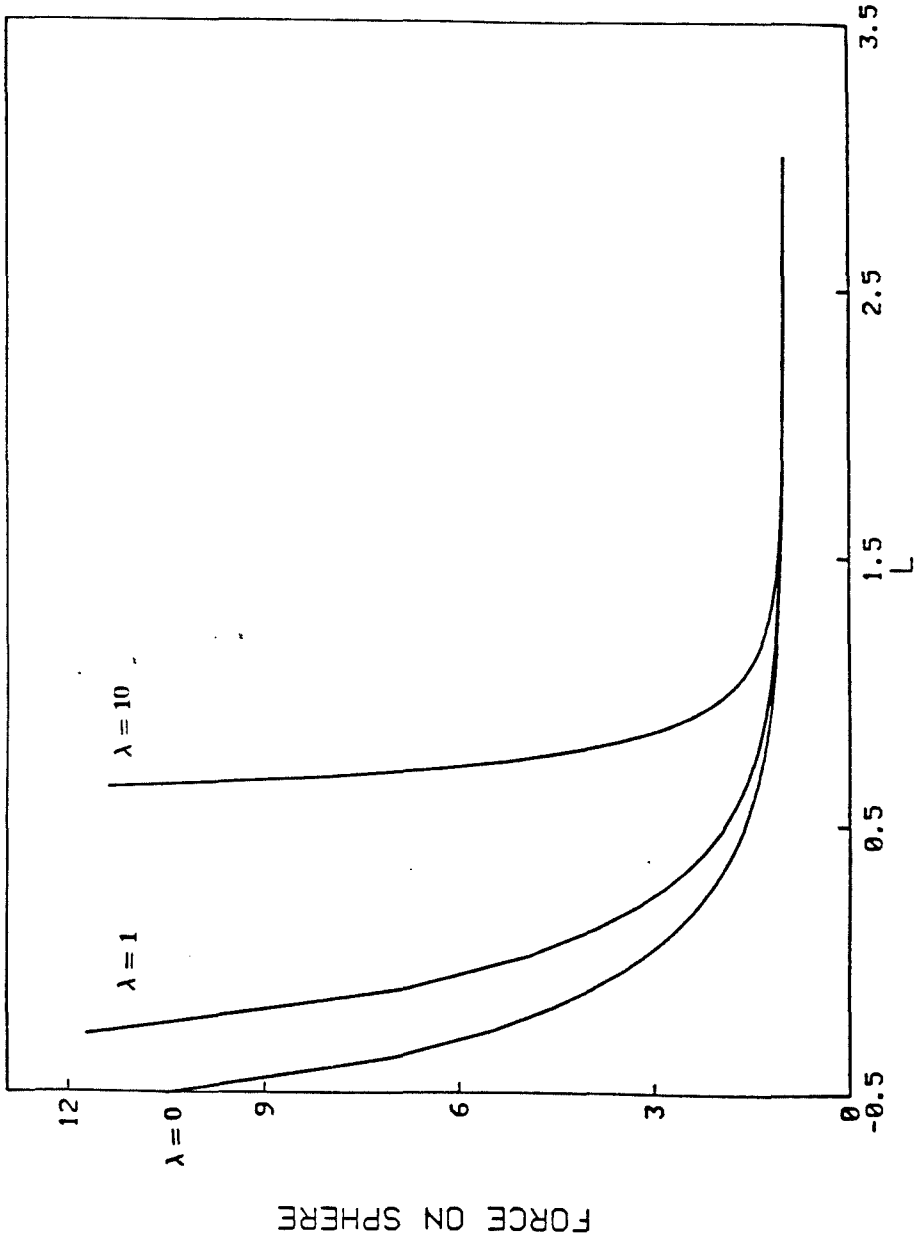

Figure 14.